IMAGING AND SPECTROSCOPY OF NANOSTRUCTURED SURFACES

by

CHRISTOPHER PAUL JONES

A thesis submitted to the
University of Birmingham
for the degree of
DOCTOR OF PHILOSOPHY

Nanoscale Physics Research Laboratory
School of Physics and Astronomy
College of Engineering and Physical Sciences
The University of Birmingham
June 2010

Abstract

STM measurements of large size selected clusters of Pd on HOPG show that the aspect ratio increases with increasing cluster size. The non-spherical nature of these clusters is traced back to the aggregation regime in the gas condensation cluster source. The size and temperature of the clusters create a slow coalescence process that leads to non-spherical clusters.

The molecule methylphenyldisulphide is studied on Si(111)-7x7 by STM. The molecule is found to bond either as an intact molecule or as fragments after fission of the disulphide bond upon landing. The molecule exhibits a 2:1 preference for the middle adatom of the 7x7 unit cell suggesting it enters a precursor state before adsorbing on the surface.

The new SPEAR technique uses an STM tip to collect photoelectrons generated at a surface. The detection of a photocurrent with a W tip is demonstrated. In the case of a bare HOPG surface electronic states of the tip are resolved. However, the large signal generated by photoelectrons from the tip restricts the resolution of states of the surface. To resolve spectra on the nanometre scale a coaxial tip is required, this is demonstrated through the use of simulations.

Acknowledgements

I would like to thank Professor Richard Palmer, Dr Peter Sloan, Dr Wolfgang Theis, Dr George Barreto, Dr Sung-Jin Park and James Lawton all of whom have helped in one way or another over the course of my PhD. I would also like to thank everyone I've known at NPRL both past and present for making it a pleasant place to be. Finally, thank you to my girlfriend, Charlotte, and my parents, Kenneth and Elaine.

Contents

Chapter 1

Introduction and Background

1.1 Introduction

Physics at the nanoscale is not yet fully understood, as an example consider clusters of atoms or molecules ranging in size from a few atoms or molecules to a few tens of thousands of atoms or molecules. A cluster will resemble the properties of the free atom or molecule when very small and will resemble the properties of the bulk equivalent when very large.[1–6] In between these size limits a cluster might have very different properties, due to the quantum confinement of electrons in different dimensions, as its size and structure changes, for example see figures 1.1 and 1.2.[2–7] The size limits involved are generally not well known and how the properties change with structure is not yet well understood. Therefore, there is a large push in research to better understand and predict these properties.[1, 6, 7]

An example of this discrepancy between bulk and nanoscale properties is the widely documented use of gold as a catalyst.[8–10] Bulk gold may be considered inert but

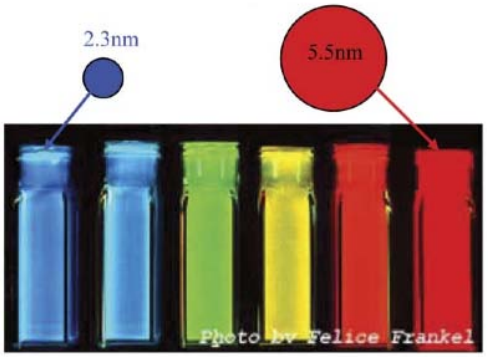

FIGURE 1.1: A colour photograph of the fluorescence of CdSe nanoparticles or clusters from size 2.3 nm to 5.5 nm. The optical properties of these clusters changes with size. Image from reference [5]

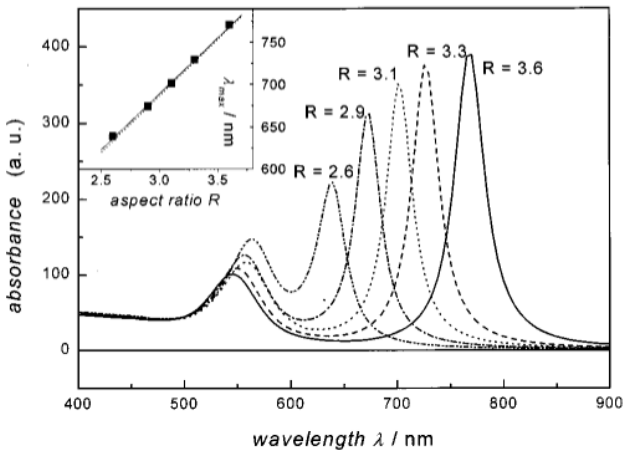

FIGURE 1.2: The calculated absorption spectra of Au nanorods, non-spherical clusters of Au, of different aspect ratios. The absorption peak is seen to shift with increasing aspect-ratio. Inset is a plot of the calculated longitudinal plasmon band as a function of aspect ratio. From reference [2]

a 5 nm cluster of gold is reactive.[8–10] A gold cluster has many low-coordination sites such as edges and corners where reactants can be adsorbed. Furthermore, a gold cluster may allow reactants to move around therefore maximising interactions: exactly the purpose of a catalyst.[10–12] However, such is the complex nature of nanoscale systems that these simple pictures rarely tell the whole story, for example although gold becomes more reactive as the cluster size is reduced, palladium does just the opposite.[10–12]

The challenge of understanding the properties of nanoscale systems requires an ability to obtain information on the morphological and electronic structure of such systems. The issue being that, in general, the ability to map electronic structure is limited in scanning probe instruments that can resolve real space morphology, such as the Scanning Tunnelling Microscope (STM) or Atomic Force Microscope (AFM).[13] On the other hand, techniques like Electron Energy Loss Spectroscopy (EELS) and Photoelectron Spectroscopy (PES) can provide energetically well resolved information on electronic structure but, in general, do not provide spatial resolution and the spectra acquired are an ensemble average of the whole surface and must be interpreted as such.[14–19] This means that whilst it is possible to get atomic resolution on almost any nanoscale system with the correct choice of microscope, and spectroscopy techniques exist to resolve individual energy levels in a system, it is non-trivial to obtain an image of a sample and get information on electronic structure from a specific area in the nanometre range.

One technique that offers the ability to perform spatially resolved spectroscopy of electronic states is Scanning Tunnelling Spectroscopy (STS). Measurements of local I(V) curves at constant tip-sample distance can be done over every pixel in

an STM image which allows atomic resolution spectroscopic studies.[20] A normal image is taken, but, at each required point, the feedback loop of the STM is switched off, and the applied sample bias voltage is linearly ramped between two pre-selected values while moitoring the current at a fixed tip height, producing an I(V) surve or spectrum. After the I(V) curve has been taken the feedback loop is switched back on and normal imaging is continued. By acquiring I(V) curves quickly, while scanning at low speed, it is possible to obtain a constant current topography and spatially resolved I(V) spectra simultaneously.[13] However, STS has three main limitations. (1) The STS spectra are a convolution of the electronic states of the tip and sample. (2) The electronic states probed are those that protrude significantly into the vacuum and overlap with the wave functions of the tip further complicating STS interpretation. (3) The range of states available is limited to a few volts either side of the Fermi level.[13]

Recently many advancements have been made in photoelectron spectroscopy. For instance, the photoemission signal of silver clusters on a graphite substrate, was separated from the substrate signal, by the resonant excitation of the silver cluster surface plasmon with femto-second radiation.[21, 22] In Photoemission Electron Microscopy (PEEM) photoelectrons produced by a specific ionisation energy are accelerated by electric lenses to magnify the electron image produced. A spectral map of the surface is produced with typical resolutions on the order of 0.5 μm but the ability to resolve down to 20 nm has been reported.[23–25]

A prime candidate to combine real space imaging with electronic spectroscopy is the laser assisted STM. The primary idea behind the majority of laser assisted STM systems is to couple laser light into the tunnelling junction modifying the

behaviour of the tunnelling current.[26] Added to the dependence on voltage and barrier width are non-linear terms that depend upon the tip, sample and the laser.[26] It is in this way that information like chemical composition or energy resolution can be obtained.[26–30] However, these non-linear terms make interpretation of the results extremely complicated. Moreover, applying laser radiation in the tip sample region creates heating effects.[30, 31] These heating effects can potentially damage the experimental set-up, for example, thermal expansion of the tip can be expected to complicate matters by producing a varying probe size and a varying barrier width.[30, 31]

Instead of modifying the tunnel junction response, an excitation source, like a laser, can instead be used to produce photoelectrons which can be detected with an STM tip.[32–37] An ordinary STM tip cannot readily be used as an energy analyser, an alternative approach is to use synchrotron radiation with the ability to cycle through highly defined photon energies and obtain spectra as a function of photon energy. This approach is both expensive and time consuming.[33] Some of these approaches have been successful in showing a contrast between chemicals on the surface but none so far have shown energy resolution.[32, 33, 37] Two of the most recent examples are the NanoXAS instrument proposed by Schmid et al. and the nanoscale chemical imaging demonstrated by Okuda et al.[37, 38]

The NanoXAS instrument of Schmid et al. uses an X-ray beam produced at a synchrotron facility and focusses this beam onto the back of a sample by the use of a Fresnel zone plate.[38] Photoelectrons are measured by a coaxial Si tip. Schmid et al. suggest that in order to avoid electrons far from the tip being detected, a very small tip radius is required along, with very effective shielding.[38] It is suggested

that with careful choices a resolution on the order of the tip radius should be achievable.[38]

The chemical mapping demonstrated by Okuda et al. is not the energy level mapping of conventional PES, but an image contrast related to the chemical composition of a given area. Using synchrotron radiation as the ionisation source it is demonstrated that an ordinary STM tip placed far from the surface will pick up electrons from the whole excitation area.[37] By bringing the tip into tunnelling contact it is suggested that low energy secondary electrons contribute to the tunnelling signal.[37] Changing the energy of the incident radiation to that of the absorption edge for specific elements or chemicals, it is possible to see a contrast difference in images pertaining to an area containing that element or chemical, see figure 1.3.[37]

The ideal situation would be to have a microscope that can provide real-space imaging and spectral mapping, providing information on the energetic structure of a sample with a resolution approaching the nanometre range i.e. to be able to realise the individual energy levels of the band structure of a nanoscale feature, such as molecule or cluster on a surface.

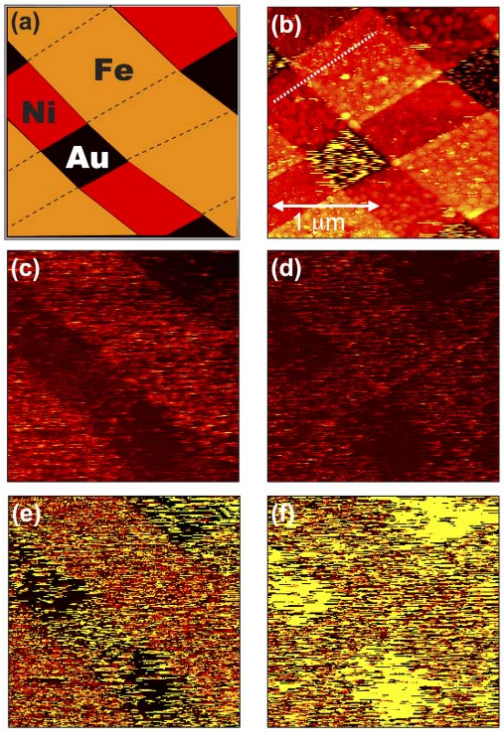

FIGURE 1.3: Images of an Fe, Ni and Au checkerboard by Okuda et al. The images show how the chemical mapping can distinguish individual elements. (a) is a schematic representation of the surface. (b) shows a standard STM image (-5V, 10 pA), (c) and (d) are the chemical mapping images taken with photon energies of 706 eV and 852 eV respectively. An element specific image of Fe, (e), is obtained by dividing the photocurrent image taken at the top of the Fe L_3 absorption edge (706 eV) by that at the bottom of the edge (698 eV). Image (f) is obtained in the same way as (e) but around the Ni L_3 absorption edge (852 and 843 eV). From reference [37]

1.2 Background

1.2.1 Scanning Tunnelling Microscopy (STM)

Scanning tunnelling microscopy is a surface science technique invented in 1982 by Binning and Rohrer.[39] Although there had been similar attempts earlier than 1982,[40] this was the first time atomic resolution imaging had been achieved using the tunnelling of electrons through a vacuum. This earned Binning and Rohrer the Nobel Prize in 1986.[13]

Classically one would expect to require a physical contact between two metallic wires for current to be allowed to flow. This is because there is a potential barrier, between the two wires, which a classical electron cannot pass unless it has the energy to go over. However Quantum Mechanics allows electrons to tunnel through a potential barrier such as the gap between two metallic wires. Consider an electron approaching a potential barrier of width, a, and height V_0 as in figure 1.4

Classically an electron approaching the barrier with energy less than the barrier height would be fully reflected. In Quantum Mechanics the result is quite different.

The time-independent, one-dimensional general expression of Schrödinger's equation has the form,

$$\frac{-\hbar^2}{2m}\frac{\delta^2\Psi}{\delta x^2} = (E - V)\Psi(x) \tag{1.1}$$

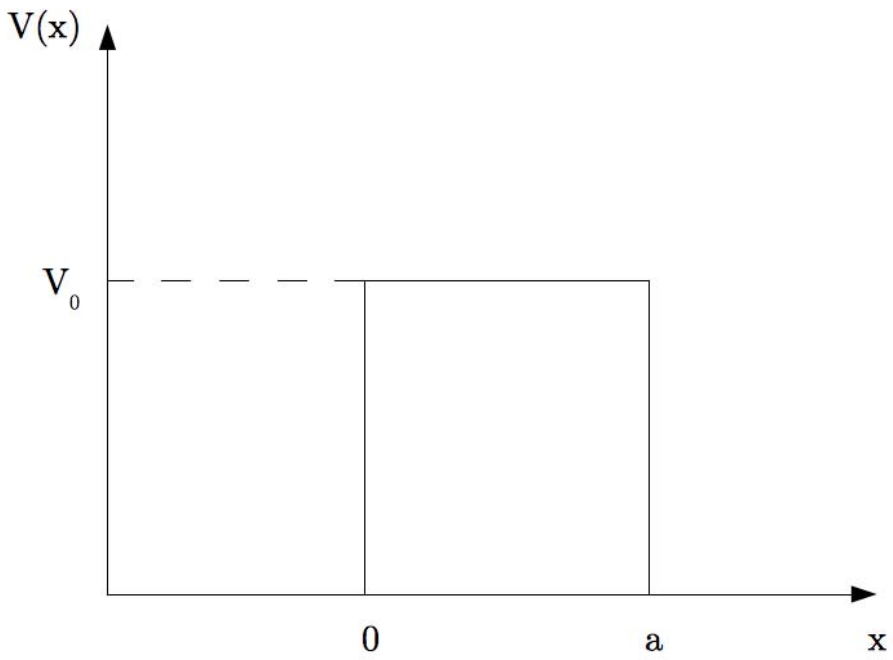

FIGURE 1.4: One dimensional representation af a tunnelling barrier of width, a, and height V_0.

where E is the particle energy, V is the potential at position x, m is the particle mass, $\hbar$ is Planck's constant over 2π and Ψ is the wavefunction. The solution for a free particle has the form,

$$\Psi(x) = Ae^{ikx} + Be^{-ikx} \tag{1.2}$$

where k is given by

$$k = \sqrt{2m\frac{E-V}{\hbar^2}} \tag{1.3}$$

Splitting the space of the problem into three regions a solution for each region can be found, see figure 1.5:

Region One: $x \leq 0$

$$V = 0 \text{ therefore } k = \sqrt{2m\frac{E}{\hbar^2}} \text{ and } \Psi(x) = Ae^{ikx} + Be^{-ikx}$$

Region Two: $0 \leq x \leq a$

$$V = V_0 \text{ therefore } k = \sqrt{2m\frac{E - V_0}{\hbar^2}}$$

$$\text{let } \kappa = \sqrt{2m\frac{E + V_0}{\hbar^2}} \text{ such that } \Psi(x) = Ce^{\kappa x} + De^{-\kappa x}$$

Region Three: $x \geq a$

$$V = 0 \text{ therefore } k = \sqrt{2m\frac{E}{\hbar^2}} \text{ and } \Psi(x) = Fe^{ikx} \text{ (there is no reflectance term)} \tag{1.4}$$

In Quantum Mechanics we see that there exists a solution inside the barrier and therefore there also exists a finite chance of the electron passing through the barrier and appearing on the other side, this is known as tunnelling.

Applying the boundary conditions, such that the wavefunction, $\Psi(x)$, and it's derivative, $\acute{\Psi}(x)$, are continuous at the boundaries, yields the following set of equations

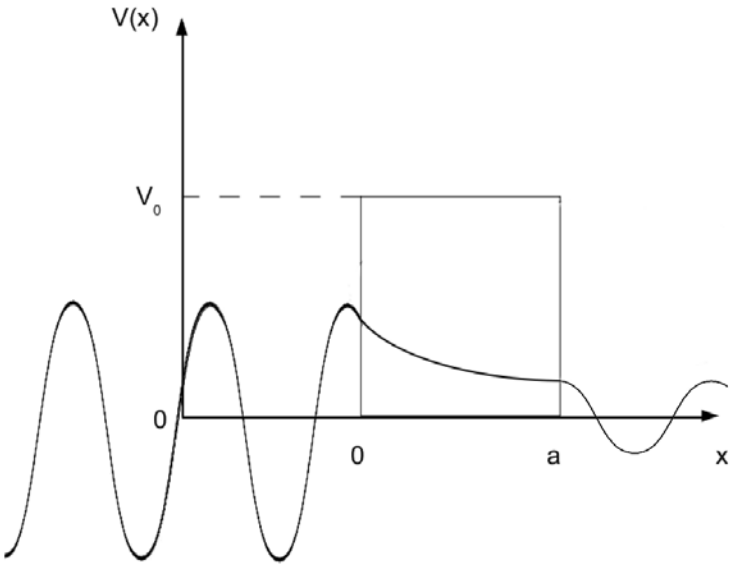

FIGURE 1.5: Wavefunction of a particle reaching a potential barrier and passing through. A particle has a probability of tunnelling through a barrier and being detected on the other side, note that the wavefunction decays in the barrier and the amplitude is lessened on the other side.

$$\begin{aligned} A + B &= C + D \\ A - B &= \frac{\kappa}{ik}(C - D) \\ Ce^{\kappa a} + De^{-\kappa a} &= Fe^{ika} \\ Ce^{\kappa a} - De^{-\kappa a} &= \frac{ik}{\kappa}Fe^{ika} \end{aligned} \tag{1.5}$$

From the set of equations 1.5 the ratio of the amplitude of the incoming and outgoing waves can be found, that is the ratio of F/A. This ratio gives us the transmission probability, $|F^2|/|A^2|$.

$$\frac{F}{A} = \frac{4i\kappa k}{(2i\kappa k + \kappa^2 - k^2)e^{-\kappa a} + (2 - \kappa k - \kappa^2 + k^2)e^{\kappa a}} e^{-ika} \tag{1.6}$$

which leads to a transmission probability

$$\frac{|F|^2}{|A|^2} = \frac{16\kappa^2 k^2}{(\kappa^2 + k^2)^2} e^{-2\kappa a} = \frac{16E(V_0 - E)}{V_0^2} e^{-2\sqrt{\frac{2m}{\hbar^2}(E + V_0)}a} \tag{1.7}$$

According to equation 1.7 the tunnelling probability is exponentially dependent on the barrier width, as in figure 1.5. It is this property that is exploited in STM to give atomic resolution surface mapping. In an STM the tunnelling barrier is the distance between a sample and a sharp metal tip.

When a sharp metal tip is positioned a few $\mathring{A}$ away from a sample surface, a tunnelling current is detected that is proportional to the tunnelling probability, and thus exponentially dependent on the tip sample distance. If a tip is scanned over the surface of a sample at a constant height, a change in tunnelling current will be measured corresponding to the change in the real tip-sample distance which follows the atomic corrugation of the surface. A schematic of an STM system is shown in figure 1.6.

As the current is exponentially dependent on the tip-sample distance, the STM is very sensitive to changes in distance and can measure atomic scale structure, but, as shown in figure 1.7, an STM image is a convolution of the geometric properties of both the tip and the sample.

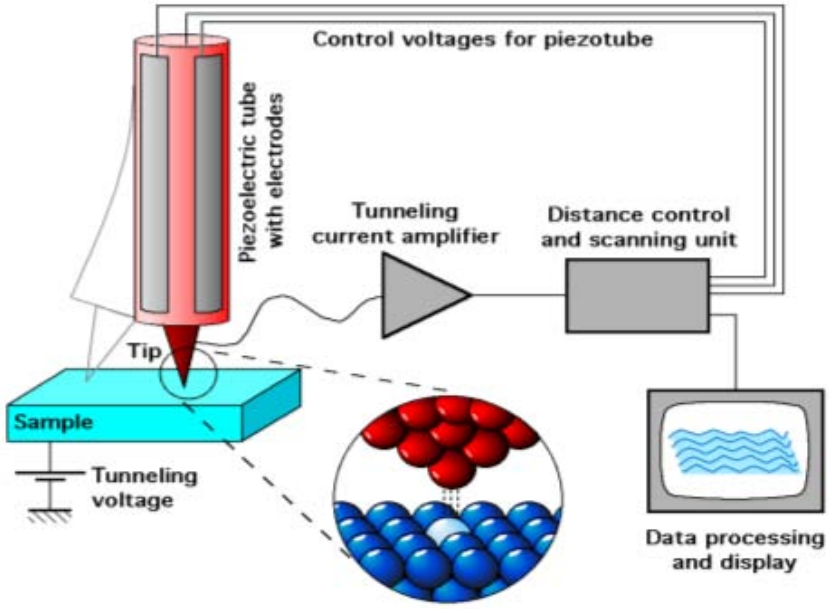

FIGURE 1.6: Schematic of a scanning tunnelling microscope. A sharp metal tip scans a metallic surface. By the use of a current amplifier and some electronics to control the tip's movement, a topographic image of a surface can be produced. From reference [41]

To produce a measurable electron tunnelling current a small voltage difference, ΔV, is applied between the tip and the sample. This offsets the energy levels of the tip and sample such that electrons at or near the Fermi level can flow to the unoccupied states made available, see figure 1.8. [43]

In figure 1.8 the energy levels of both the tip and the sample are represented by square wells for simplicity, this is not the case in reality. Imagine that instead of the square wells of figure 1.8 there is now some structure, as shown in figure 1.9. The density of states (DOS) in this image is given by the number of electrons that sit in an energy range, such as that marked by the red box in figure 1.9, divided by the magnitude of the energy range.[13, 44]

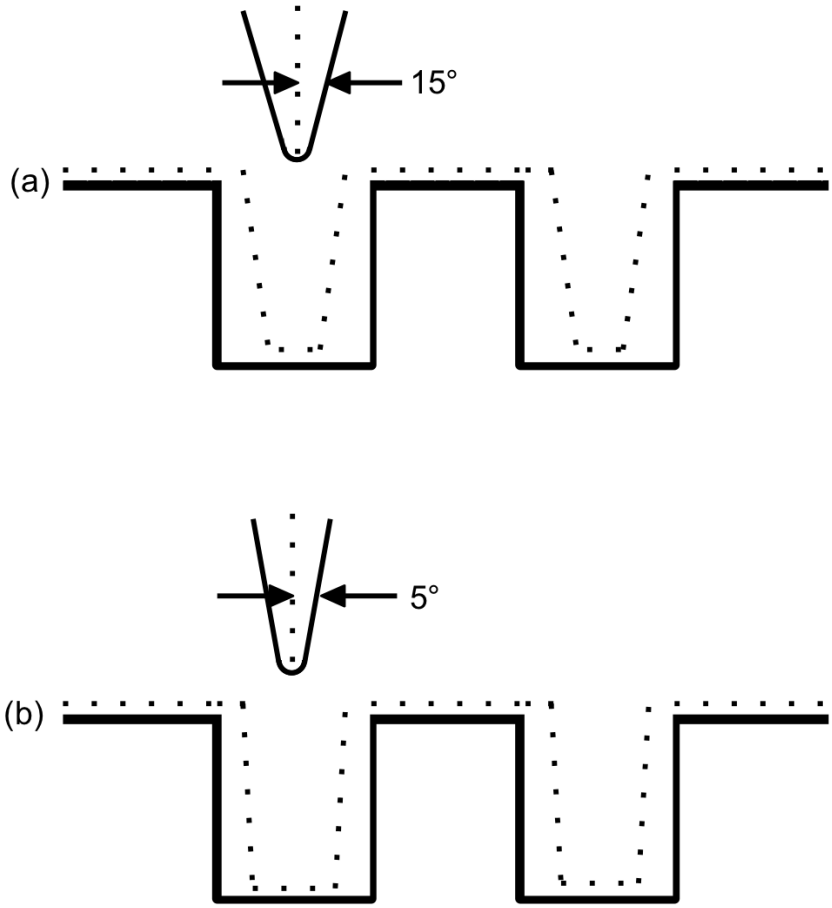

FIGURE 1.7: The effect of tip geometry on the measured profile of grooves 0.75 μm wide and 1.00 μm deep using: (a) tip with radius 500 $\mathring{A}$ radius of curvature with 15° cone half angle and (b) tip with 500 $\mathring{A}$ radius of curvature with 5° cone half angle. The dotted lines indicate the flight path of the tip. Figure adapted from reference [42]

If a sample is brought into tunnelling distance with a tip and a small bias is applied, it can be seen from figure 1.9 that the tunnelling current is now a function of the density of states (DOS), as well as the geometry of the system.

For a given voltage, V, the tunnelling current is proportional to the integral of the density of states of the sample. By varying the bias voltage it should be possible to map out the density of states of the sample, however, the density of states of the tip is also clearly involved. It is important to remember that, whilst STM

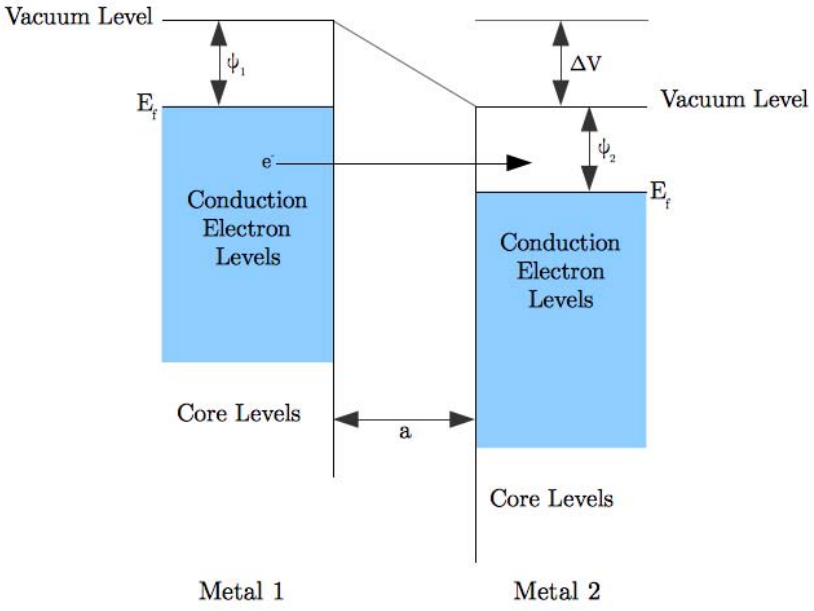

FIGURE 1.8: Energy level diagram for two metals separated by a distance, a, with a bias,ΔV, applied between them which, combined with the workfunctions, ϕ_1 and ϕ_2, acts to offset the Fermi levels. Tunnelling occurs primarily in one direction, as indicated by the arrow, due to the voltage offset.

images are generally interpreted as showing topographic data of the sample, there is in fact a large contribution from the tip shape and from electronic structure of both the tip and the sample.[13]

A formal representation of tunnelling between two metals was formulated by Bardeen in 1961 and can be used to demonstrate the importance of the electronic density of states in scanning tunnelling microscopy.[45] The tunnelling current between the sample and the tip is given by:

$$I = -2q_e\frac{2\pi}{\hbar}|M|^2 \underbrace{(\rho_{sample}(E)f(E))}_{\text{number of filled sample states}} \underbrace{(\rho_{tip}(E+eV)[1-f(E+eV)])}_{\text{number of empty tip states}} \quad (1.8)$$

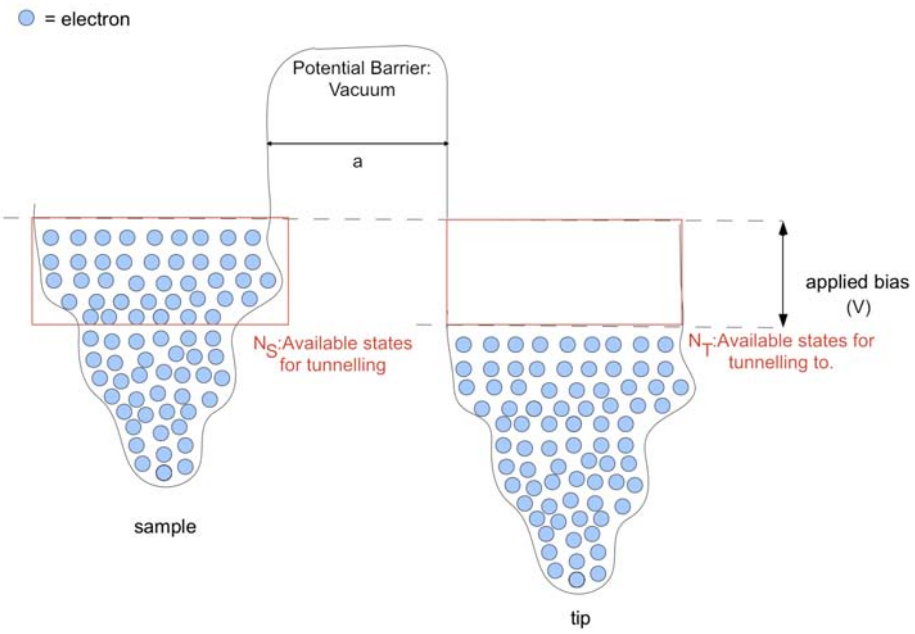

FIGURE 1.9: The total tunnelling current, between a tip and sample separated by a distance, a, is proportional to the density of states of the sample, on the left, available for tunnelling from, N_S, times the number of empty states of the tip, on the right, available for tunnelling to, N_T. Adapted from reference [44]

where q_e is the charge on an electron, f(E) is the Fermi distribution and M is the tunnelling matrix element.[44–46]

Summing over electrons from tip to sample and electrons from sample to tip and integrating over all energies gives:

$$\begin{aligned} I &= -2q_e\frac{2\pi}{\hbar}\int_{-E_f}^{\infty}|M|^2\rho_{sample}(E)\rho_{tip}(E+eV) \\ &\times \{f(E)[1-f(E-eV)]-f(E+eV)[1-f(E)]\}dE \end{aligned} \tag{1.9}$$

This can be simplified by assuming measurements are made at low temperatures and applying, for example, a small negative voltage, V, to the sample:

$$I = -2q_e\frac{2\pi}{\hbar}\int_{-eV}^{0}|M|^2\rho_{sample}(E)\rho_{tip}(E+eV)dE \tag{1.10}$$

An ideal STM tip has a flat density of states over the energy range that measurements will be taken. Making this assumption the density of states of the tip becomes a constant and can be removed from the integral:

$$I = -2q_e\frac{2\pi}{\hbar}\rho_{tip}(0)\int_{-eV}^{0}|M|^2\rho_{sample}(E)dE \tag{1.11}$$

Finally, Bardeen showed that under realistic conditions the wavefunction of the tip and the sample both exponentially fall to zero in the barrier, the density of states of the tip and the sample are independent, and the tunnelling matrix element, M, is independent of energy. Assuming that the barrier is a square barrier and the applied voltage is small compared to the work function, i.e. the height of the barrier, then M is given by:

$$M = e^{-2\frac{z}{\hbar}\sqrt{2m\phi}} \tag{1.12}$$

where m is the electron mass, z is the tip-sample separation and ϕ is the height of the barrier which results from the product of the work functions of both the tip and the sample.[44–46] This gives a tunnelling current that under ideal conditions and with a perfect tip is proportional not only to the negative exponential of the tip-sample distance, which is the assumption in creating an image, but also on the density of states of the sample, as shown in equation 1.13.[44–46]

$$I = \frac{4\pi q_e}{\hbar} e^{-z\sqrt{\frac{8m\phi}{\hbar^2}}} \rho_{tip}(0) \int_{-eV}^{0} \rho_{sample}(E) dE \tag{1.13}$$

1.2.2 Technical Aspects of Scanning Tunnelling Microscopy

Many naturally occurring vibrations e.g. vibrations of a building, acoustic noise or mains hum, will create a larger displacement of the tip than the surface corrugation itself, typically these frequencies range from 1–100 Hz. It is therefore important to make sure the apparatus has good vibration isolation. It is here that Binning and Rohrer succeeded[13, 39, 47]. Initially vibration isolation was supplied by levitating the STM stage, on a superconducting bowl of lead, combined with Eddy current damping[13, 39]. Later a two stage spring system was introduced.[39] It is widely considered advantageous to combine a two stage spring system with eddy-current damping for optimal vibration isolation. A typical system might consist of an STM stage mounted on springs with some viton spacers at the spring mounts, the edge of the STM stage may have copper fins which slide between magnets. As the copper fins move up and down in the magnetic field an induced eddy-current damps their motion and that of the entire system. Typical metal springs have a resonant frequency around 5 Hz which may be excited by ambient noise, but the eddy-current damping system can have a tunable resonance frequency, moving the resonace frequency of the system outside of the range of ambient noise. The eddy-current damping coeeficient, γ is given by equation 1.14.[47, 48] It is also prudent to operate an STM in a sound proof enclosure in a basement in order to minimise acoustic and floor vibrations.[13]

$$\gamma = 9.69 \times 10^{-9} B^2 l S / \rho \tag{1.14}$$

where B is the magnetic field (gauss), l is the thickness (cm) of the copper fins, S is the cross-sectional area (cm^2) and ρ is the resistivity (Ωcm).[48]

It is important to be able to reproducibly create sharp STM tips with a well-known electronic structure. It is also important to understand the electronic structure of the sample. There are several methods of preparing tips which range from mechanical cutting to ion beam milling. The ultimate goal of each method is to reliably reproduce atomically sharp tips with minimal impurities that would effect the electronic properties.[49, 50]

In order to control the placement of the tip over the sample, piezoelectric ceramics are usually employed. A piezoelectric ceramic such as lead-zirconium-oxide (PZT) is a material that will deform when a voltage is applied.[13]

In a single piezoelectric tube, see figure 1.10, with inner and outer electrodes, of length, l, and wall thickness, h, the change in length,$\Delta\ l$, depends on the applied voltage, U, as in Equation 1.15. [13, 39, 51]

$$\Delta l = d_{31}\frac{l}{h}U_p \text{ where } d_{31} \text{ is the relevant piezoelectric coefficient} \tag{1.15}$$

A typical piezoelectric tube has a d_{31} coefficient between 300–600 pm/V which allows repeatable and controlled movement within and below the nm range.

Three piezoelectric tubes of this type can be combined to give full x-y-z movement. Alternatively, one tube can control all three dimensions if the outer electrode is split into four equal parts. Pairs of outer electrodes can cause the tube to bend

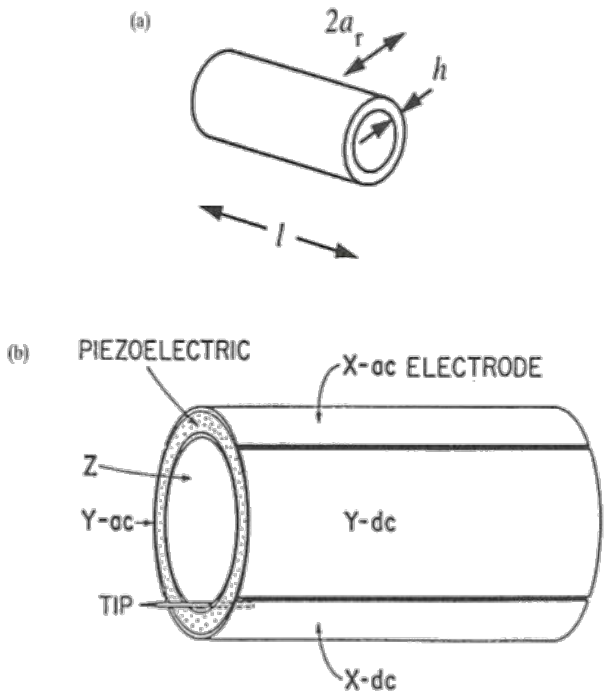

FIGURE 1.10: (a) Piezoelectric tube configuration. (b) STM scanning piezoelectric tube with outside electrode sectioned into four equal parts parallel to the axis of the tube. A voltage applied to a single exterior electrode bends the tube away from that electrode. A voltage applied to the inner tube causes a uniform elongation [51]

in x and y while fixed at one end, allowing scanning of the surface combined with z-motion from the central electrode.[13, 51]

The accuracy of the piezoelectric positioning system is governed by the supply electronics and not by the piezoelectric crystal. The crystal itself could move an infinitesimally small amount given an infinitesimally small change in voltage.

The piezoelectric system can be used to scan a tip over a surface while the current is monitored, using the instantaneous values of the current over different positions of the sample a current image can be obtained. In this case the height is constant and the tip may touch the surface if there is a large change in surface features,

should this happen the tip is likely to be damaged, reducing resolution. It is therefore more common to use a set of electronics, known as a feedback loop or feedback circuit, to monitor the current and attempt to keep it constant by altering the tip-sample distance in real time, this changing tip-sample distance provides a topographic image of the sample, see figure 1.11.

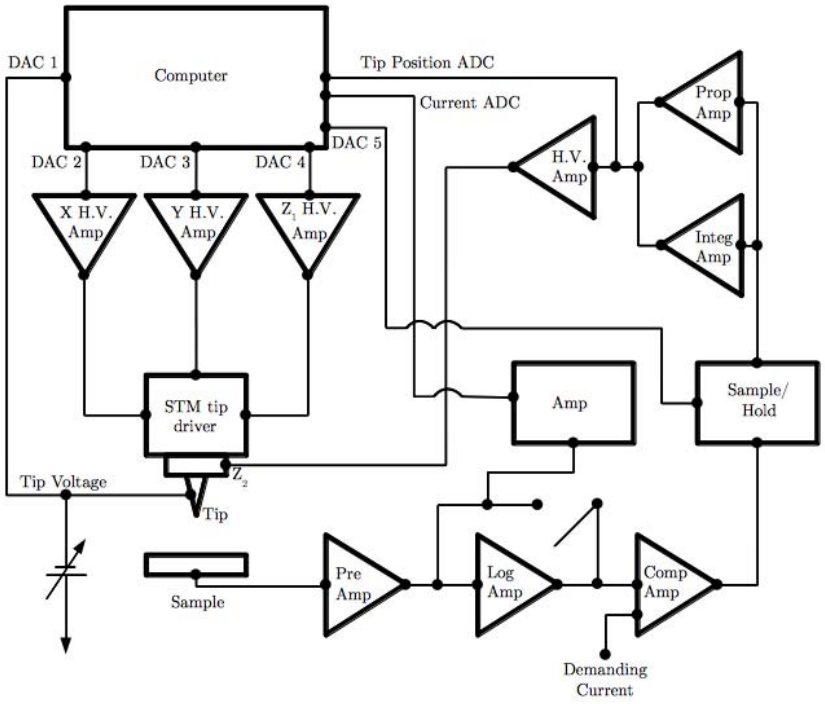

FIGURE 1.11: Block diagram example of STM feedback circuit. The STM tip is mounted on a set of piezo actuators to drive the tip in the x, y and z directions all controlled by computer. While x, y directions are used to scan a surface z is changed in order to keep the current constant. This is done by a feedback loop monitoring the tunnelling current. [13, 52]

The STM electronics are designed to avoid electrical noise and provide precise control and amplification of signal. The tip (or bias) voltage is usually supplied by a computer-controlled digital-to-analogue converter (DAC). The tunnelling current is measured by a pre-amplifier with a gain of between 10^6 and 10^9 VA^{-1} as the tunnelling current is usually in the picoamp regime. The tunnelling signal, which

is exponentially dependent on the tip-sample distance, can be linearised by a logarithmic amplifier to improve the dynamic range. The measured tunnelling current is then compared with the set current and the difference is fed into the feedback circuit. The feedback signal is usually sent to a high-voltage amplifier to drive the z-piezo. Scanning the tip is usually done using separate DACs. [13]

1.2.3 Cluster Formation

As the properties of clusters are dominated by their size and shape it is important to understand the growth processes involved. In this thesis, clusters produced in the gas phase by inert-gas condensation, will be studied.

In gas phase condensation clusters may initially form by the nucleation of atoms, this is likely followed by surface growth of clusters and finally growth may continue via cluster-cluster collisions, as shown in figure 1.12. Temperature and pressure play an important role in the final products available.[53]

If a metal is sputtered by a plasma or charged particle beam the initial products will be a mixture of atoms and small clusters, as shown in figure 1.12(a). The initial growth of these products will be determined by the thermodynamics of the system. The stability of the clusters can be evaluated by size. Following the Gibbs-Kelvin equation, equation 1.16, a nucleus is stable when its critical diameter, d_c, is much smaller than the diameter of a molecule of the product species. Assuming the density of the gas is homogeneous clusters are likely to grow via homogeneous nucleation of atoms in the first instance.[53, 54]

$$d_c = \frac{4\gamma V_{mol}}{K_B T ln(S)} \tag{1.16}$$

where γ is the surface tension, V_{mol} is the molecular volume of the cluster, S is the saturation ratio, T the temperature, and k_B is the Boltzmann constant.[53]

After the initial growth, clusters continue to grow through the addition of atoms to the surface of the cluster, as in figure 1.12(b), or by cluster-cluster collisions,

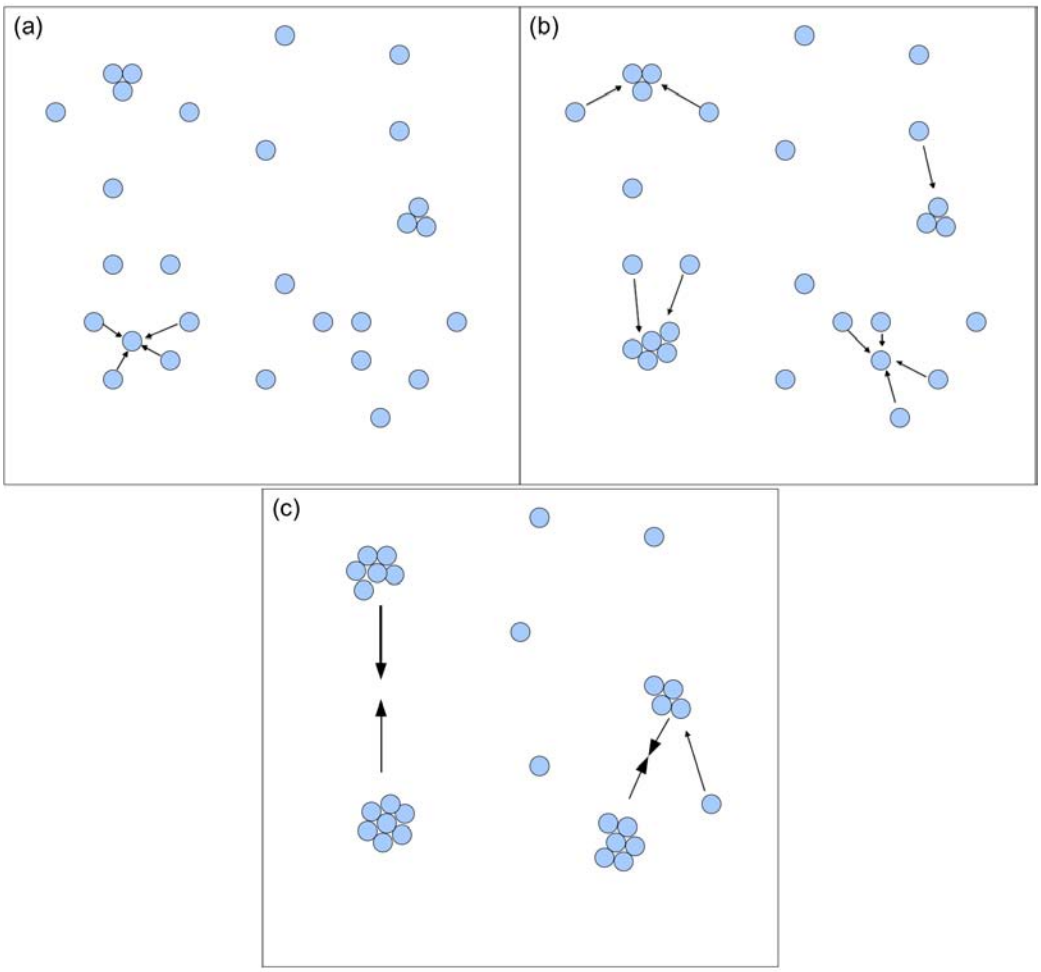

FIGURE 1.12: A schematic of the growth of clusters in the gas phase. (a) Atoms and small clusters are formed by the sputtering of a target material. Atoms nucleate to form small clusters. (b) Some small clusters have formed, which act as seeds for further nucleation, these seeds grow via addition of atoms to their surface. (c) The number of single atoms is depleted over time and the clusters formed will begin colliding with each other and continue to grow in this way.

collisions between clusters are usually followed by coalescence. The most likely growth mode in the early stages is the growth of clusters by the addition of atoms to the surface as the initially formed clusters act as seeds for the remaining vapour.[53, 54] Surface growth may well be the only growth mode if sufficient atoms are available. At the start the cluster diameter should be smaller than the mean free path of the cluster and the rate of change of the cluster diameter at a temperature, T, will be given by equation 1.17

$$\frac{dd_c}{dt} = \frac{2v(p_f - p_c)}{2\pi m k_B T} F_1 \tag{1.17}$$

where v is the volume of the particle being attached to the cluster, p_f is the partial pressure at a distance far from the cluster and p_c is the partial pressure at the cluster surface. F_1 is the Fuchs-Sutugin factor for the free molecule regime, the free molecule regime is defined by the cluster diameter being smaller than the mean free path.[53]

If the cluster diameter becomes larger than the mean free path, the growth is said to be in the continuum regime, the rate of change of cluster diameter is now given by equation 1.18

$$\frac{dd_c}{dt} = \frac{4Dv(p_f - p_c)}{dk_B T} F_2 \tag{1.18}$$

where D is the diffusion coefficient of the gas and F_2 is the Fuchs-Sutugin factor for the continuum regime.[53, 55]

When the gas becomes depleted of atoms, and clusters are the dominant species, as in figure 1.12(c), the growth will become dominated by collisions followed by coagulation or coalescence. Ignoring any initial size or shape distribution, the collisions of the seed clusters can be described by the Brownian motion of monodisperse spheres, and if the cluster diameter is larger than the mean free path, the growth due to coagulation can be described by equation 1.19

$$d_c = d_0(1 + \frac{4k_BTN_0}{3\mu}t)^{\frac{1}{3}} \tag{1.19}$$

where d_c is the diameter at a time, t, and temperature, T. d_0 is the initial cluster diameter, N_0 is the concentration of clusters, and μ is the viscosity of the gas. [53, 55]

If, however, the cluster diameter is smaller than the mean free path, as would normally be the case with metal clusters, the growth is given by equation 1.20 if inhomogeneities in particle size and shape are neglected.

$$d_c^{5/2} = d_0^{5/2} + \frac{10}{\pi}(\frac{6k_BT}{\rho})^{1/2}Vt \tag{1.20}$$

again d_c is the diameter at a time, t, and temperature, T. V is the volume of clusters per unit volume of gas and ρ is the density of clusters.

These equations do not take into account an initial size distribution, a distribution in cluster morphology or indeed forces between clusters such as coulomb forces due to cluster charge. For instance, particle morphology can affect the growth, as agglomerated or non-spherical clusters will undergo more collisions per unit time

than spherical clusters, since, for the same mass, they have more surface area. Therefore when attempting to produce large clusters it is more likely to produce agglomerates. In the collisions-coalescence growth mode, full coalescence has been assumed, but this can only take place if the internal temperature of the cluster is high enough for the cluster to be considered a liquid or glass like state. At lower temperatures, clusters must be considered as solid, and two solid clusters will stick and sinter forming agglomerates rather than spherical clusters.[53, 56, 57]

A more complete picture of the evolution of cluster size is given by a general dynamic equation (GDE), or population balance equation, which can take into account all these factors:

$$\begin{aligned}\frac{\delta n(v)}{\delta t} &= \underbrace{-\Delta n\vec{u}u}_{\text{(a)}} \\ &+ \underbrace{\Delta D\Delta n}_{\text{(b)}} \\ &+ \underbrace{\frac{\delta}{\delta v}(n\frac{dv}{dt})}_{\text{(c)}} \\ &- \underbrace{\Delta\vec{c}n}_{\text{(d)}} \\ &+ \underbrace{\frac{1}{2}\int_0^v \beta(\tilde{v}, v-\tilde{v})n(\tilde{v})n(v-\tilde{v})\ d\tilde{v} - \int_0^\infty \beta(v,\tilde{v})n(v)n(\tilde{v})\ d\tilde{v}}_{\text{(e)}} \\ &- \underbrace{S(v)n(v) + \int_v^\infty \Gamma(v,\tilde{v})Sn(\tilde{v})\ d\tilde{v}}_{\text{(f)}}\end{aligned} \tag{1.21}$$

Each part takes care of a different phenomenon that effects the size distribution function, n, over time, t. $\vec{u}$ is the velocity, D is the diffusion coefficient, v is the

cluster volume, $\tilde{v}$ is the average cluster volume, c the clusters own velocity, β is the collision function, S the rate of fragmentation and Γ the size distribution of fragments.[53, 55]. Part (a) defines convection within the system (b) takes care of the motion of clusters by diffusion, (c) controls the effects of surface growth/ atomic nucleation, (d) external forces such as Van der Waals and Coulomb forces between clusters, (e) the effect of coagulation in the collisions between particles, (f) describes any fragmentation that might occur in collisions. All these terms must be adapted for any particular system, for instance, cluster morphology can be represented by a fractal dimension in the collision function β or, considering a simple case, for a large uniform chamber containing particles larger than their mean free path, coagulation will take place and growth will be driven by diffusion controlled condensation.[55] Even for a simple situation, the result requires non-physical assumptions for direct solutions to be found without resorting to numerical analysis. A discrete solution for all particle sizes below 1 μm would require more than 10^9 differential equations to be solved simultaneously.[53] Therefore computational models consist of a few small particles allowed to evolve over a short time, or two large particles, but the whole growth spectra has not yet been calculated within one simulation.

Studying cluster formation in the gas phase directly is all but impossible. Molecular dynamics (MD) simulations can be used to predict cluster growth in the gas phase in detail, and can give limits on shape and size as a function of temperature, particle density, etc.[53] A simple physical argument in the formation of clusters is that there should be some characteristic times involved in cluster formation,

most importantly perhaps is coalescence time vs collision time.[56, 57] If the coalescence time is defined as the time it takes for two colliding clusters to coalesce to a spherical shape, and the collision time is the time between collisions, which will depend greatly on temperature, pressure and density, then these competing times could decide the final shape of clusters formed. If the coalescence time is short compared to the collision time, the clusters will all be spherical, since, on average, two colliding seed clusters (a doublet), will have formed a sphere before another cluster arrives. If however, the collision time is short in comparison to the coalescence time, clusters should form chains, as there is, on average, not enough time to relax to a spherical shape before another cluster collides.[56–58] The nature of the particles, liquid or solid, changes the simulation parameters, as liquid drops coalesce through viscous flow, whereas solid clusters have a number of competing transport mechanisms.[53, 56, 57, 59, 60] A review of coalescence models by Lunden concluded that the main sintering mechanisms were surface and grain boundary diffusion, with surface diffusion becoming more dominant as the temperature is increased.[60]

The coalescence rate of clusters that have collided in the gas phase is given by:[56]

$$\tau = \frac{3k_B T v_p}{64\pi\sigma D(T) v} \tag{1.22}$$

where, v_p is the particle volume, v is the volume for diffusion, σ is the surface tension and D(T) is the diffusion coefficient at temperature, T. When calculating the coalescence rate for particles of a fixed size all the parameters can be known except the surface tension. Zachariah and Carrier used MD simulations to obtain

a value for the surface tension and calculate the coalescence rate as a function of both cluster size and temperature, the results of which are presented in figure 1.13.[56]

In figure 1.13 coalescence times are seen to increase with both decreasing temperature and increasing cluster size. The temperature dependence will come from the diffusion coefficient, that is how quickly surface diffusion can occur. If this is slower, then the coalescence rate, in total, is slower. The increasing cluster size would also shorten the collision time, therefore, large clusters have an even larger chance of fulfilling the criteria to produce non-spherical shapes, such as agglomerates or chains, rather than spheres.

Simulations carried out by Grigoropoulos et al. show the shapes that can arise for different initial radii and temperature of two colliding Au clusters. Figure 1.14 shows the stages and time duration of the coalescence of two particles with radius 20 $\mathring{A}$ and at a temperature of 895 K, this is close to the melting temperature and the clusters are treated as 'glassy' liquids. In the first stage a neck forms between the two particles following a power law described by equation 1.23. [57]

$$\frac{x}{r_p}^n = \frac{Bt}{r_p^m} \tag{1.23}$$

where r_p is the initial cluster radius, x is the neck radius at a time, t, B is a constant depending on the temperature and m and n are constants that must be calculated. The neck growth does not seem to depend on temperature or cluster size according to these simulations. [57]

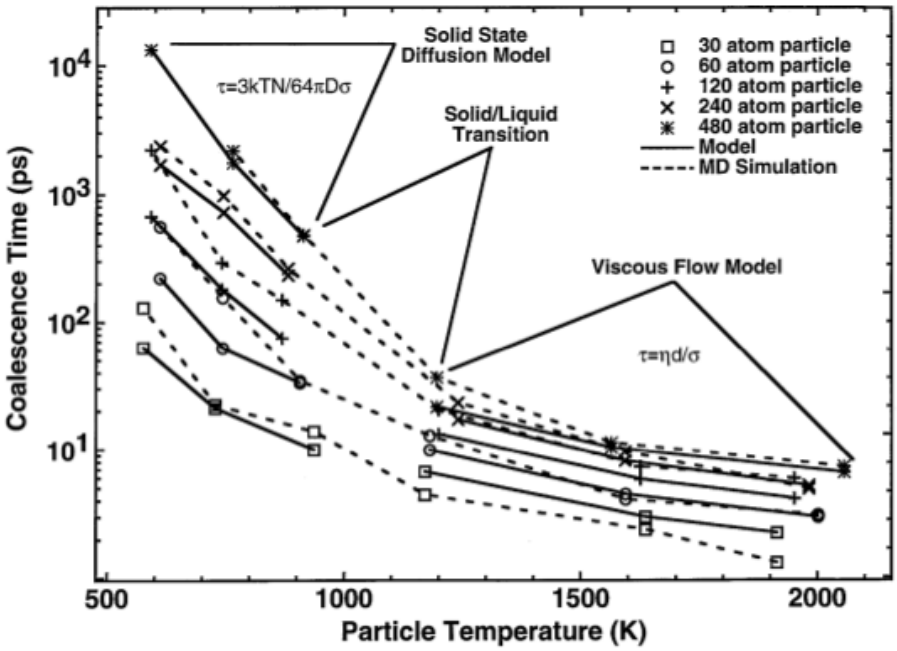

FIGURE 1.13: Coalescence as a function of particle size and temperature. Dotted lines represent MD computations. The solid curves represent viscous and solid state diffusion models. The coalescence time is seen to increase with increasing cluster size approaching the bulk value for the largest clusters. The coalescence time also increases with decreasing temperature due to reduced mobility of surface atoms. The rate of change in coalescence time changes when a cluster becomes solid or liquid as the dominant growth mode changes. From reference [56]

A second stage begins when the neck disappears and the cluster appears as one cluster. The evolution at this stage is much slower, and in this simulation sphericity is not reached. A sphere may be formed in a longer simulation although it appears it would take hundreds of nanoseconds. The dominant growth mechanism in this final stage is claimed to be self diffusion driven by stress gradients resulting from non-perfect sphericity. For liquid like clusters a spherical final state is expected, but in the case of solid clusters, non-spherical final shapes are possible. Solid clusters form crystal structures, unless formed by rapid cooling, Therefore,

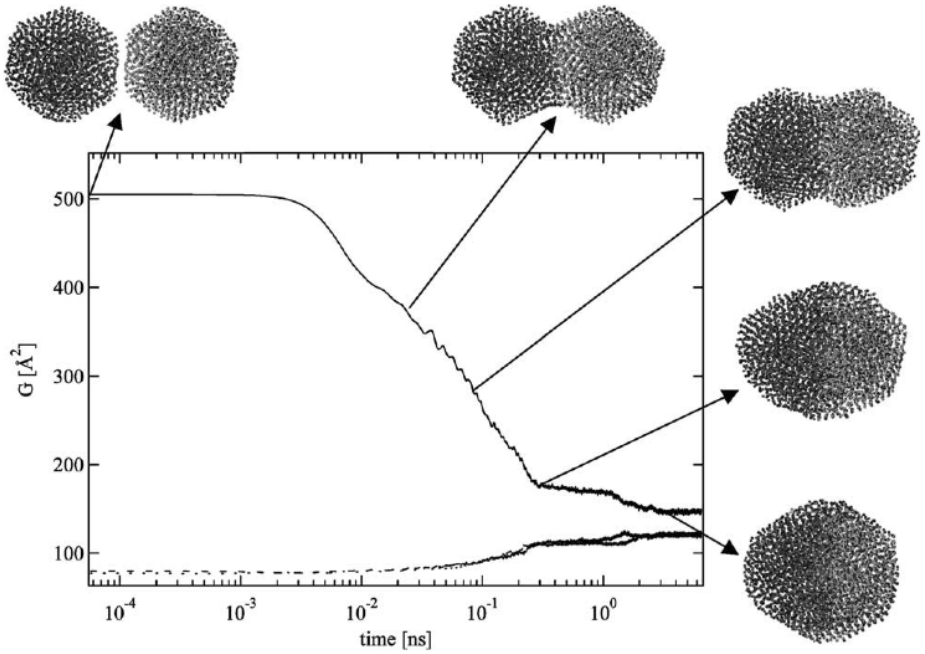

FIGURE 1.14: Simulated time evolution of the gyration radius, G, in x (continuous line), y, z (dashed lines) during the sintering of two Au clusters with radius 20 $\AA$ at temperature 895 K. Also shown is the shape of the cluster formed by the two colliding Au clusters as a function of time. The resultant cluster is still in a non-spherical shape by the end of the simulation, it may be that given more time it would become spherical. From reference [57]

in a solid system, the surface energy gradient driving towards the minimum energy, spherical shape, may not be enough to overcome the crystal structure of the solid.[57, 61]

Figure 1.15 shows two possible collisions between two identical Au clusters with the same size and temperature but different orientation. In (a) the second particle is translated with respect to the original, but in (b) it is also rotated anti-clockwise by 45°. In case (b) the contact area is smaller and this slows down the coalescence process. More strikingly in (b) small lattice rearrangements force the particle into a small rotation, but where the initial lattice arrangement is quite different the effect is far more pronounced. This pronounced rotation causes an actual rotation

in the simulation domain, it is argued that mechanical stresses due to the atomic rearrangement are large enough to cause real rotation of the particle as a whole.[57]

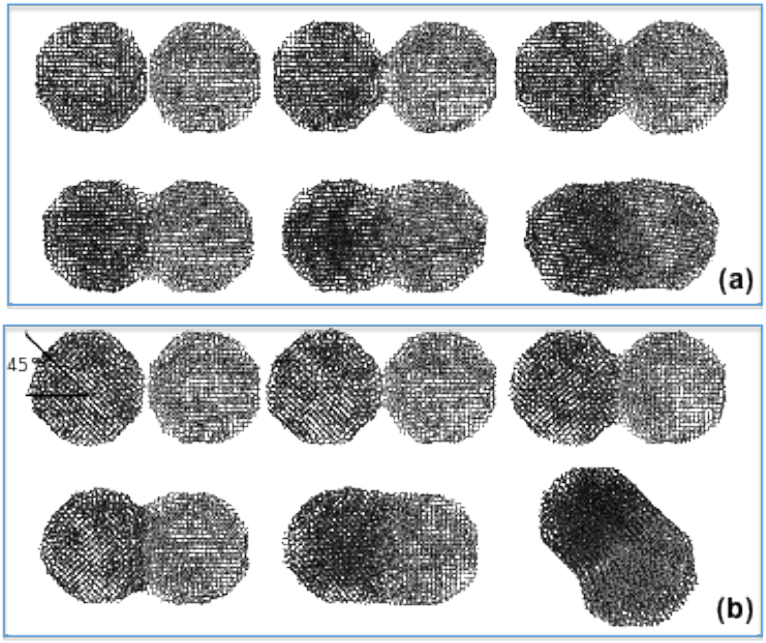

FIGURE 1.15: Comparison of the simulated coalescence of two Au clusters having different initial lattice orientations. Cluster radius is 22.3 $\AA$ with initial temperature of 938 K. In (a) one of the clusters is simply displaced in space with respect to the other, but in (b) a rotation of 45° has been made to one cluster with respect to the other, and the large stresses caused by the lattice mismatch create a rotation of the cluster and slow down the coalescence rate with respect to (a). From reference [57]

To summarise, the gas phase formation of clusters is extremely complex with many factors affecting the final size and shape of products. MD simulations may be used to predict what happens in a system, although they are limited to a small number of clusters, and a small size distribution, it is possible to draw some conclusions from MD simulations and simplistic theories. Larger clusters have higher melting temperatures and higher coalescence rates. Large clusters are therefore more likely to form agglomerates, or non-spherical shapes, rather than spherical clusters as,

particularly for solid clusters, the formation of spherical clusters is a competition between a coalescence rate and collision rate. Whilst it is generally accepted that all clusters should be spherical, as it minimises the surface energy of the cluster, in simulations it is seen that the initial conditions again affect this. It is possible, for large differences between crystal orientation, that the lowest surface energy state will not be for a spherical final product or, that the energy requirements to change shape are too high due to the crystal structure. Therefore in the case of real clusters, produced in the gas phase, a whole range of size and morphology is expected depending on the initial conditions such as density, temperature and pressure.

1.2.4 Molecules on Surfaces

Scanning tunnelling microscopy (STM) has proved to be a useful tool for imaging surfaces with atomic resolution.[46, 62] It has also been demonstrated that the STM can be used to manipulate individual atoms or molecules on surfaces.[63, 64]

Perhaps the most famous example of atomic manipulation is the work of D. Eigler and K. Schweizer who were able to spell out I.B.M. in Xenon atoms using an UHV-STM kept at 4 K, shown in figure 1.16.[64] This lead to an exploration of atomic switches and the hope of creating electronic devices atom by atom. In the particular example by D. Eigler et al. the samples must be kept at 4 K, although some atomic manipulation work has been done at room temperature. In this case the bonding to the surface is strong and no switch-like properties have been observed.[65, 66]

Molecules, however, are more stable at room temperature and by understanding and manipulating electronic structure through choice of molecule and surface there is a chance of finding a useful switch.[63] Many studies of molecules on surfaces have been performed: some with the purpose of finding a molecule suitable for molecular electronics, others purely to study the interaction of the molecule and the surface.[63, 67–70]

Teague and Boland studied the reaction of 1,3-cyclohexadiene (C_6H_8) on the Si(100)-2×1 surface, see figure 1.18. In the work by Teague and Boalnd the aim was to see what bonding configurations resulted and to try to understand the mechanism behind each configuration. It is possible to image unfilled electronic states in the sample, i.e. states above the Fermi level, by applying a negative bias

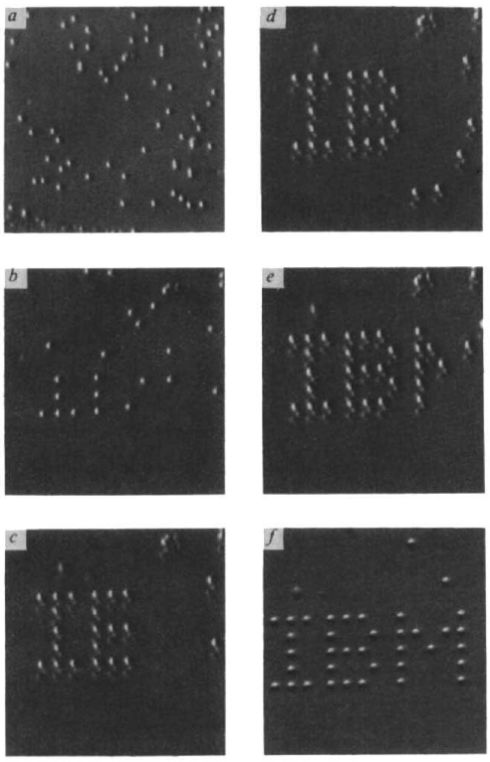

FIGURE 1.16: A sequence of STM images taken during the construction of the I.B.M. logo in Xenon atoms on a Ni(110) surface. From reference [64]

to the tip, equivalent to a positive voltage at the sample, such that electrons tunnel predominantly from filled states in the tip to empty states in the sample. Atomic resolution empty state imaging was performed using an Omicron VT-STM, figure 1.17 shows the different bonding configurations found along with models of what the configuration is believed to be.[71]

By imaging at different voltages it is possible to identify the orientation and bonding mechanisms in various molecules, as demonstrated both by Padowitz and Hamers and also by Andersen et al.[68, 74] Padowitz and Hamers demonstrated that molecules bonding to the surface modify the local electronic structure of the

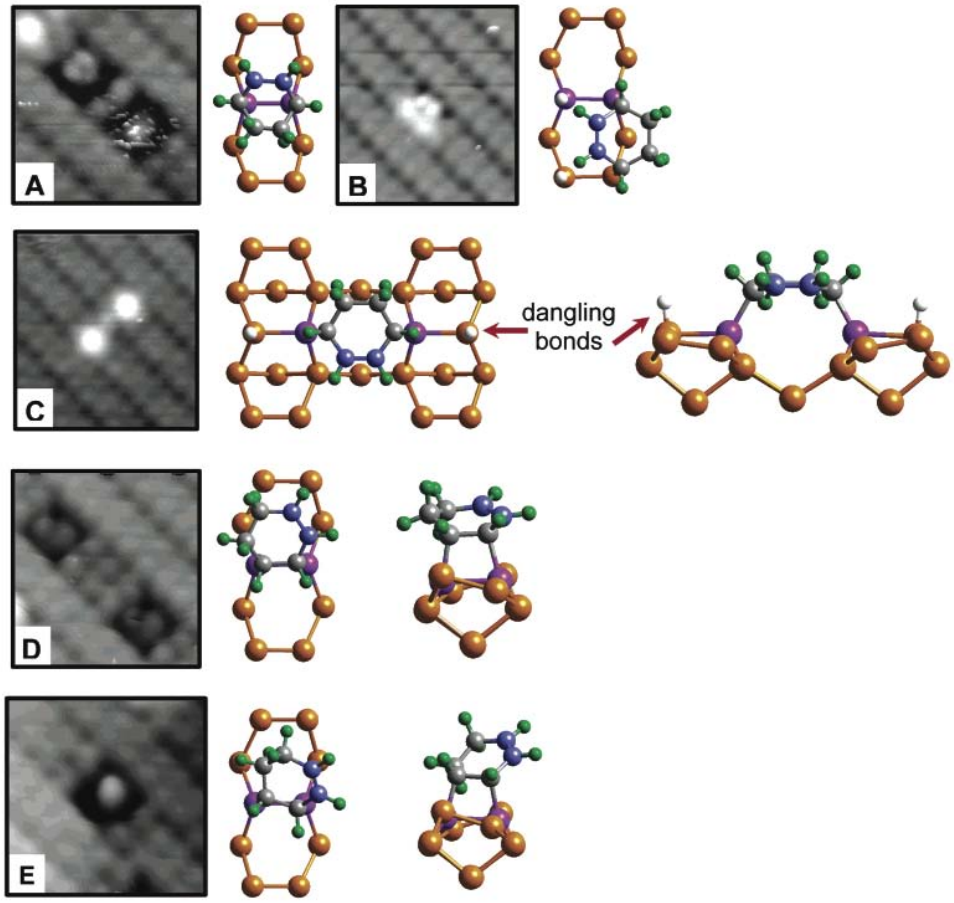

FIGURE 1.17: STM images (≈ 4 nm × 4 nm) of 1,3-cyclohexadiene on the Si(100)-2×1 surface with a tip voltage of -1.3 V. Different reaction products (A-E) are compared to ball-and-stick models. The models show side and top views of the attachment of the 1,3-cyclohexadiene molecule, shown in green and grey, to the underlying Si atoms, shown in yellow. The Si dimer atoms which are bonded to the molecule are shown in purple, the remaining C=C is shown in blue. In the models B and C dangling bonds have been added, in white, for illustration purposes only. From reference [71]

substrate. At small negative bias, molecules were seen as depressions, dark compared to the substrate. At increased negative bias, energy levels in the molecule become available for tunneling, and tunnelling through the molecule is enhanced compared to tunnelling purely involving the substrate, the molecules then appears bright compared to the substrate.[68] Andersen et al. investigated the interaction

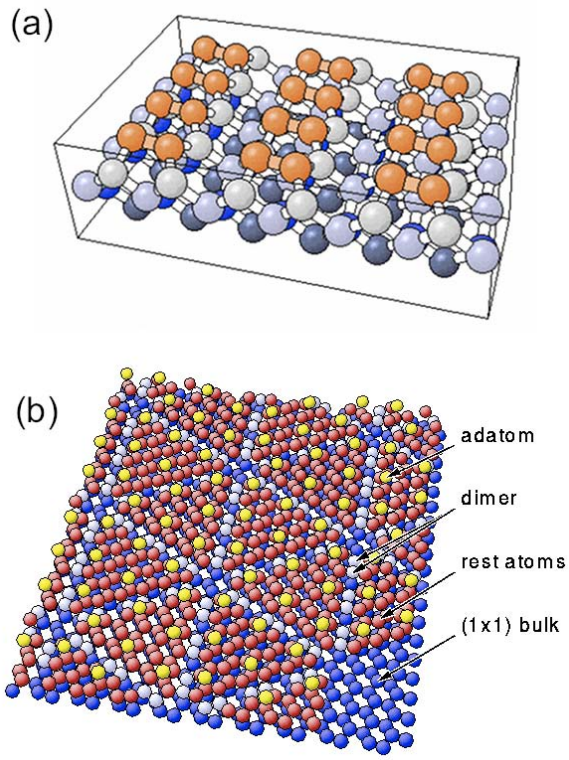

FIGURE 1.18: (a) Schematic of the Si(100)-2×1 surface. The Si atoms of the top layer form a covalent bond in pairs, forming dimers. (b) Schematic of the Si(111)-7×7 surface. The 7×7 unit cell consists of 49 atoms, with the twelve adatoms being the most important feature. The adatoms are the topmost surface atoms and are those generally seen in STM images. Images taken from references[72] and [73]

of 1,1 -dichloroethene with the Si(111)-7×7 surface, see figure 1.18(b). They were able to conclude that the molecule dissociates upon landing, losing both chlorine atoms. This is possible because bright features seen at 1.4 V correspond to chlorine atoms as seen when imaging purely chlorine on Si(111). The rest of the molecule appears dark, much like a defect, for voltages below 1.85 V, above 1.85 V this part of the molecule appears brighter where defects remain dark. This feature, the molecule minus chlorine atoms, has a preference (2:1) for centre (or middle) adatoms compared to corner adatoms. By varying the dose of 1,1 -dichlorethene it was observed that the features which correspond to chlorine atoms do not increase

accordingly, it is therefore possible to conclude that 2-D clusters of the molecule are formed upon further dosing.[74] By varying voltage it is possible to identify various parts of molecules should they dissociate, or split, on the surface. By varying the dose it is possible to draw further conclusions about a molecules bonding dynamics with a given surface.[74]

Work by P. A. Sloan and R. E. Palmer identified desorption and dissociation in the Chlorobenzene molecule by STM on Si(111)-7×7, i.e. the STM can directly influence the molecular state either by splitting it or by changing the way it bonds with the surface. Experiments by Sloan et al. have been aimed at understanding the processes involved in this desorption and dissociation. The dissociation takes place uniquely at the C–Cl bond, meaning the Chlorine atom is ejected from the molecule by the injection of charge from the STM tip. It was found that the molecule is bound to the surface by a di–σ bond between the benzene ring and two silicon surface sites, an adatom and an adjacent rest atom, see figure 1.19.[63, 67, 70, 75]

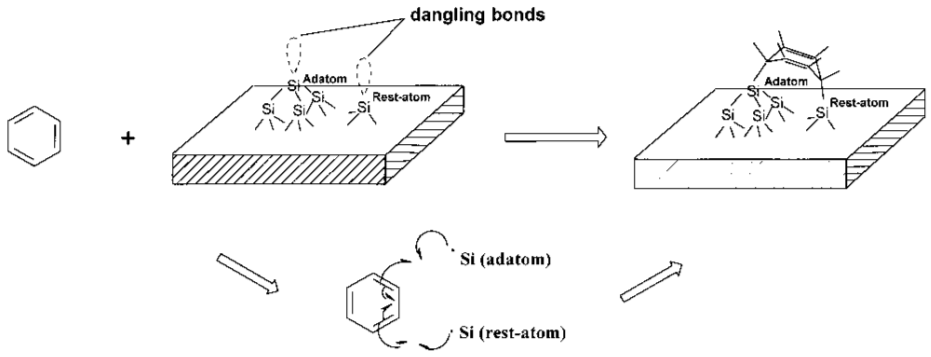

FIGURE 1.19: Schematic model (side view) of the di–σ bonding of the benzene molecule C_6H_6 adsorbed on Si(111)-7×7. From reference [75]

The desorption rate of Chlorobenzene scales approximately linearly with the current (measured at a fixed voltage). This rate is only weakly dependent on the tip-sample distance, meaning it must be almost entirely independent of the electric field, ruling out any electric field mechanism. The same reasoning also rules out a mechanical tip-molecule interaction. The desorption yield is seen to have bias thresholds of +2.5 V and -1.5 V. This all means that the mechanism for desorption is driven by the injection of current into the molecule and not by a field mechanism or mechanical interaction. Comparing the measured desorption thresholds with DFT calculations suggests that for positive bias threshold the electrons are injected into the unoccupied π^* orbitals associated with the adsorbed phenyl ring, and for negative sample bias voltages via hole attachment to the occupied π orbital.[63, 67, 70]

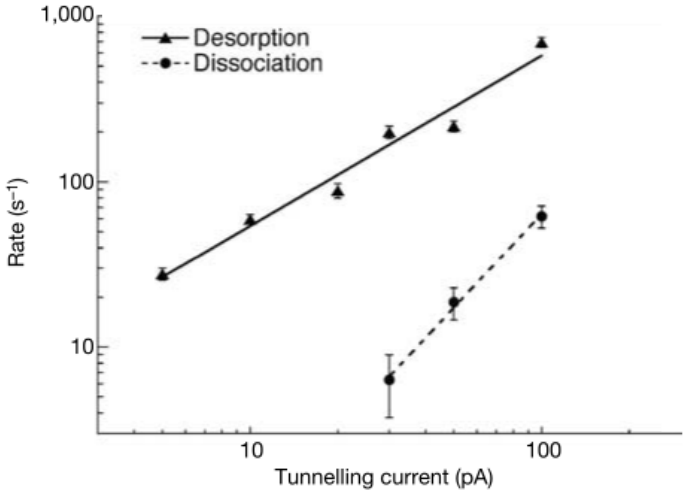

FIGURE 1.20: Rates of desorption (triangles) of C-Cl bond dissociation (circles) for chlorobenzene on Si(111)-7×7 as a function of the tunnelling current (I), with power-law fits, rate $\propto I^N$. For the desorption data N is found to be 0.9 ± 0.1 and for dissociation N is found to be 1.8 ± 0.3 suggesting one electron is required for desorption while two electrons are required for dissociation.(For both desorption and dissociation the voltage was 3 V)[67]

For the dissociation of the Chlorobenzene molecule a threshold voltage is seen at 3 V where the dependence of the dissociation rate on current becomes non-linear, in fact, more like quadratic, see figure 1.20, suggesting a two-electron process. One reason given for the requirement of two electrons is that the thermodynamic dissociation energy (3.6 eV if the Chlorine atom is neutral) exceeds the electron energy (3 eV) while the desorption energy is only 1.0 eV. It is suggested that one electron is required to instigate a vibrational mode, called the C-Cl wag mode, and a second electron can then split the C-Cl bond.[63, 67, 70]

Molecules have been studied on surfaces for possible applications in molecular electronics, or for understanding natural and biological processes. For example, the Sulphur-Sulphur bond is of great importance in biology, it has been found to be involved in a range of biological processes from protein folding to photosynthesis, and it has been suggested that if this bond and the mechanisms of bonding in proteins were better understood then the pharmaceutical industry would be able to prepare better drugs with longer shelf lives.[76–78]

Proteins involving S-S bonds have been studied by Nuclear Magnetic Resonance (NMR)[77] and electron capture dissociation experiments[79, 80] but very little STM work on the S-S bond has been attempted.[81] Electron capture dissociation experiments performed by Zubarev et al. have suggested a one-electron dissociation of the S-S bond using 0.2 eV electrons.[79, 80] An STM investigation of the molecule CH_3SSCH_3 deposited on the Au(111) surface was carried out by Maksymovych et al, see figure 1.21. The deposition was performed at temperatures less than 10 K. The molecule is moved by voltages higher than 0.5 V and dissociates into two CH_3S molecules when voltages above 1 V are used. When warmed to

room temperature, the dissociated products are stabilised by a Au adatom i.e. the structure $CH_3S - Au - SCH_3$ is formed. These new molecules self assemble into chains and these chains are very stable against STM measurements withstanding up to 4.5 V and 20 nA.[81]

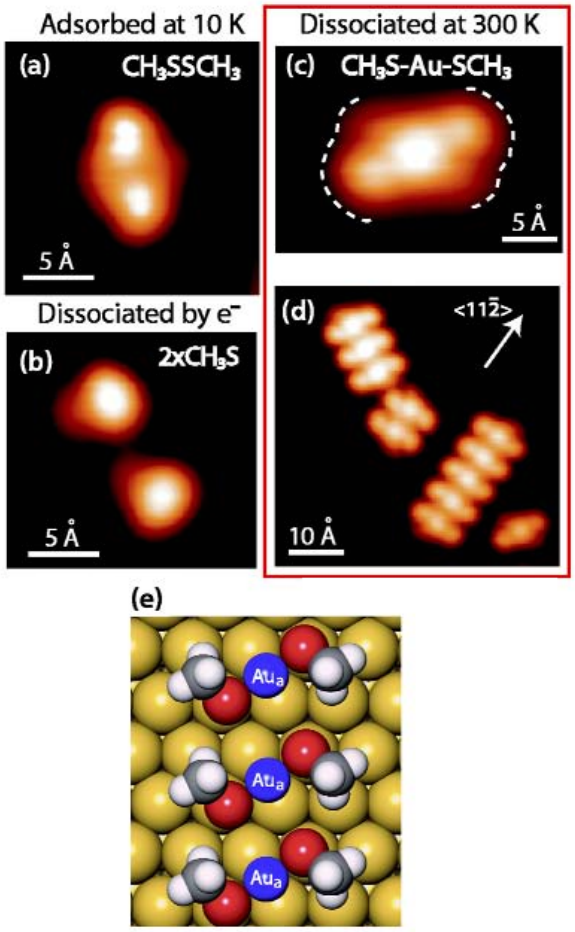

FIGURE 1.21: STM images of the molecule, CH_3S-SCH_3, adsorbed on Au(111). (a) A single CH_3S-SCH_3 molecule at 5 K. (b) Two CH_3S fragments formed by pulsing a single molecule with a 1.0 V pulse at 5 K. (c) A molecule dissociated at room temperature stabalised by a Au adatom. The asymmetrical boundaries of the CH_3S species are marked by dashed white lines. (d) Chains of the CH_3S fragment form after heating the molecule to 300 K. (e) proposed model of the bonding geometry in (c). From reference [81]

1.3 Project Aims

The primary goal was the demonstration of the Scanning Probe Electron AnalyseR (SPEAR) technique. This goal required the completion of a number of sub-goals as outlined below.

- Design and construction of an Ultra High Vacuum system for the SPEAR technique.
- STM studies of nanostructured surfaces that may be suitable and interesting candidates for SPEAR measurements.
- Demonstrate the detection of a photocurrent with an STM tip.
- Demonstrate the ability to obtain photoelectron spectra of large flat samples of HOPG and Au using the SPEAR technique.
- Obtain SPEAR spectra of samples identified as suitable candidates by STM studies.

Two different nanostructured surfaces have been identifed as possible candidates for SPEAR and were studied by STM. These are (1) clusters, formed in a gas-aggregation source, and soft-landed on HOPG and (2) the molecule methylphenyld-isulphide deposited on Si(111)-7×7. Thus section 1.2.3 discussed the gas phase growth of clusters and section 1.2.4 discussed some pertinent data related to molecules similar to methyphenyldisulphide on surfaces.

Chapter 2

Experimental

In this chapter some of the equipment and experimental techniques will be described. The experimental work for this thesis was performed at ultra high vacuum (UHV) pressures in the range of 10^{-10} mbar. The reasons for requiring UHV generally concern noise and contamination; acoustic noise does not propagate through a vacuum, and working in UHV reduces the chance of contamination of a sample by oxygen, water, dust etc. As a UHV system was designed for the SPEAR technique, described in chapter 4, the challenge of achieving UHV will be addressed. The cluster source used to produce clusters for experiments described in chapter 3 will be discussed, the stable deposition of clusters on surfaces in order to study morphology will also be described. Finally, a description of the STM systems, used for the work presented in this thesis, will be given.

2.1 Achieving Ultra High Vacuum (UHV)

Ultra High Vacuum (UHV) is achieved using a combination of pumps, this is because the type of flow changes as the pressure changes. First a roughing pump must reduce the pressure from atmospheric, $\approx$ 1000 mbar, to $\approx$ 0.01 mbar. At this pressure the flow is viscous and collisions between gas molecules are more numerous than between the molecules and the walls of the chamber. The movement of the gas is governed by its viscosity and the pressure gradient between regions in the system i.e. one side of a pump and the other. During viscous flow, molecules tend to move together towards lower pressure regions. A turbomolecular pump is used to get from 0.01 mbar to 10^{-8} mbar, a turbomolecular pump continues to work when the flow has reached the molecular flow regime. In molecular flow, the density of the molecules of a gas is such that they are interacting far more with the walls than with each other. The molecules no longer move in a preferential direction, but are undergoing random thermal motion and bouncing off walls in random directions. The job of a pump at this point is to capture molecules that enter it. Both the roughing pump and the turbomolecular pump contain moving parts which will cause noise in any surface science application, so a further type of pump is required to maintain UHV during experiments. This last type of pump is the ion pump.[17, 19, 82–84] Each type of pump will now be described briefly.

The majority of roughing pumps in use today are rotary-vane pumps.[82] The operation of a rotary-vane pump can be understood by looking at figure 2.1.

Rotary-vane pumps have a cylindrical rotor, mounted off-axis, in a cylindrical or slightly elliptical chamber of a larger diameter. The rotor is mounted such that

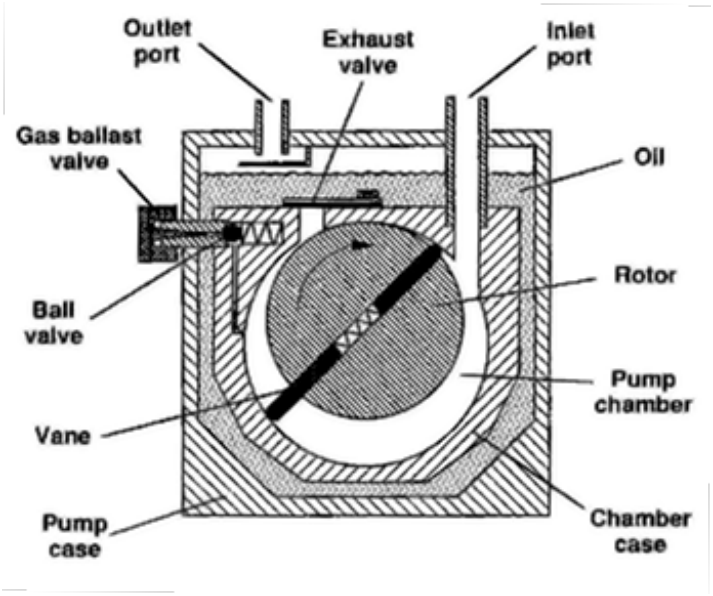

FIGURE 2.1: Schematic of a rotary-vane roughing pump. A rotor is mounted off axis in a chamber larger than the rotor. The rotor houses vanes on springs which create two chambers as the rotor rotates. These vanes act to trap gas entering through the inlet port and compress it until the pressure is high enough to force open the exhaust valve and the compressed gas exits. From reference [82]

it nearly touches the chamber wall at a point along a line between the inlet and outlet ports. The crescent shaped space left is split into two sections by the two vanes. The vanes are held in slots in the rotor and are pushed against the walls with springs.[82, 84]

It is important to remember that no pump 'sucks', all pumps trap gas that has entered either through random motion or through a pressure difference. In the rotary pump, as the rotor turns the upper vane moves past the inlet and gas that has entered the chamber becomes trapped in front of the advancing vane. As the rotor turns the volume which the gas occupies is decreased until the pressure is such that it pushes through the spring loaded exhaust valve.[82, 84]

The turbo-molecular pump (turbo pump) works on a similar principle, with rotating vanes trapping molecules and forcing them in some direction, but the turbo pump is designed to work when there is only molecular flow in the system.[82] A turbo pump looks similar to a turbine engine but functions the opposite way. In a turbine engine expanding gases cause turbine blades to rotate and drive an external device. In a turbo pump the turbine blades are driven by a motor and are designed to collect and compress a gas.[82, 84]

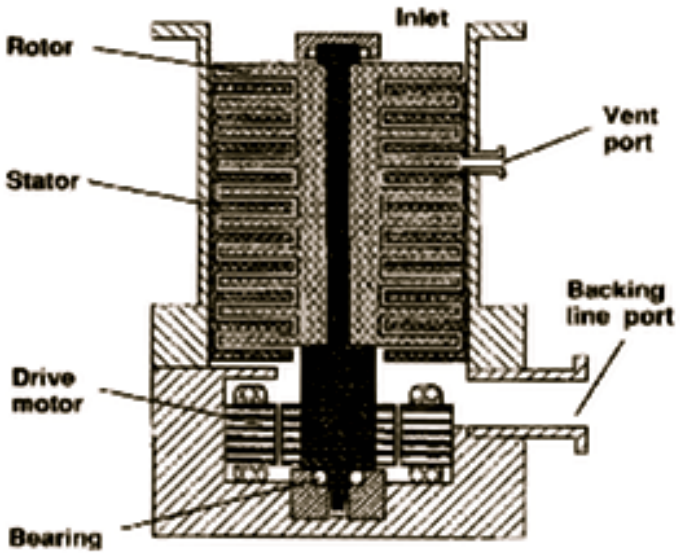

FIGURE 2.2: Schematic of a turbo-molecular pump. The turbo pump is much like a turbine engine, but the other way around. Instead of expanding gas rotating turbine blades, here the rotating rotor, in combination with the stationary blades of the stator, force gas molecules entering in one direction. From reference [82]

A turbo pump's turbine consists of two parts, the rotor which rotates and the stator which remains stationary. The rotor is a set of disks mounted on a shaft driven by the motor. The disks are slotted radially such that each disk looks like a many bladed fan. The stator consists of a matching set of disks interleaved

between the disks of the rotor. These blades extend radially inward from the walls of the pump and are pitched in the opposite sense to those of the rotor.[82, 84]

At the inlet, gas molecules wander into the first rotor disk, due to their own thermal motion. Upon impact with the moving blades the molecules are given a velocity, directed towards the adjacent set of stator blades, which in turn kicks them to the next rotor disk, this process repeats through the pump. The rotor disks transfer the energy required to move the gas molecules through the pump, and the stator disks reduce back diffusion of the molecules. Turbo pumps operate best in the range of molecular flow where the momentum transferred can effectively propel the gas molecules through the pump. At higher pressure, where the flow is viscous, the motion of gas molecules leaving the blades is randomised by scattering with other gas molecules. To maintain the effectiveness of a turbo pump there must be a roughing pump backing it up to maintain molecular flow.[82, 84]

The ion pump has no moving parts and instead uses chemisorption to remove gas molecules. An ion pump utilises highly reactive titanium ions to produce stable products with negligible vapour pressures.[82, 84]

The ion pump consists of a metal case inside of which is an open cylindrical anode with titanium cathode plates located at the opposite ends of the cathode as shown in figure 2.3.

The anode cylinder is maintained at a positive DC potential from 3000-7000 V with respect to the cathodes and the case. A permanent magnet is located outside the case and provides a strong magnetic field parallel to the axis of the anode cylinder.[82, 84]

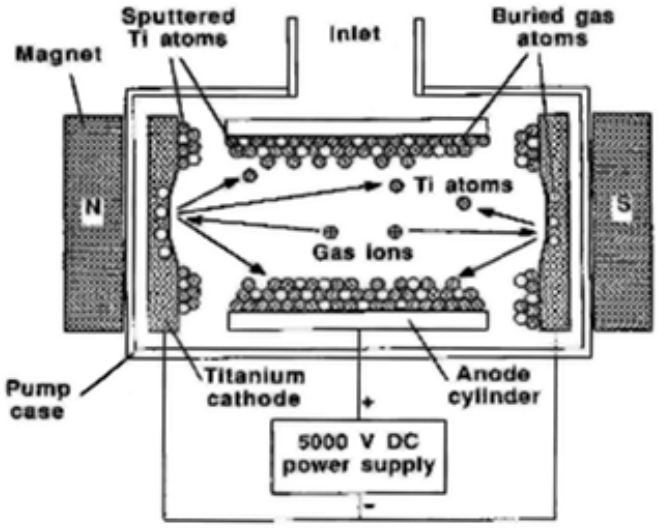

FIGURE 2.3: Schematic of an ion pump. The ion pump consists of an anode, a titanium cathode and large magnets. Sputtered Ti ions capture gas atoms or molecules which enter through the inlet. Primarily the Ti ions react with atoms/molecules and return to the cathode due to the magnets where the captured material is buried by further ions thus reducing the pressure. From reference [82]

The processes that create the pumping effect in an ion pump, for the most part, involve free electrons initially generated by cosmic rays.[82, 84] These electrons are accelerated towards the anode by the potential applied to it. However, the strong magnetic field forces the electrons to follow long spiral paths. This means the electrons are trapped inside the anode cylinder for a significant amount of time, increasing their probability of colliding with any gas molecules present. Such collisions will produce positively charged ions of the molecules and more electrons. The additional electrons become added to the original and a massive amount of electrons, roughly 10^{15} mm^{-3}, can be trapped even at low, 10^{-7} - 10^{-9} mbar, pressure. With such a high number of electrons most gas molecules that enter will be struck by electrons and ionised.[82, 84]

The positive gas ions now formed are drawn directly towards the negative titanium

electrodes as they are heavy enough to not be affected by the magnetic field. Ions under the influence of the large potential gain enough kinetic energy to dislodge titanium atoms from the plates. This ion sputtering process constantly deposits highly reactive titanium ions on the interior surfaces of the pump. It is this deposition of titanium atoms that is the main cause of the pumping action.

Several phenomena are involved in the pumping action of the tion pump and each has a different contribution to different types of gas. Any atom or molecule that comes to rest at a surface where titanium is being deposited will get buried by the sputtered titanium and ultimately all the material pumped by the ion pump will get buried by titanium. Highly reactive gases such as oxygen, nitrogen, carbon monoxide and hydrogen are likely to react with the fresh titanium surfaces forming stable oxides, nitrides, carbides and hydrides. Other less reactive gasses may be more likely to react if they have been ionised by the electron bombardment. Lastly, some positive gas ions may gain enough kinetic energy to penetrate into the cathode plates and implant themselves. This is practically the only mechanism by which the inert gases are pumped.[82, 84]

Pumping alone will not produce UHV as gas molecules become adsorbed onto the surfaces of vacuum chambers whenever they are open to atmosphere. The free molecules are relatively easy to pump out but the adsorbed molecules will be released very slowly into a system. This desorption of molecules from the chamber walls will appear like a leak and limit the ultimate base pressure. The rate of desorption from the walls can be increased exponentially by heating the walls. A few hours pumping at an increased temperature can be equivalent to many hours

pumping at room temperature. UHV systems are enclosed in an oven and baked out for a period of time to improve the ultimate attainable pressure.[82, 84]

The pressure of a vacuum system must be measured at all times, this is usually done by a combination of gauges to cover the full pressure range.

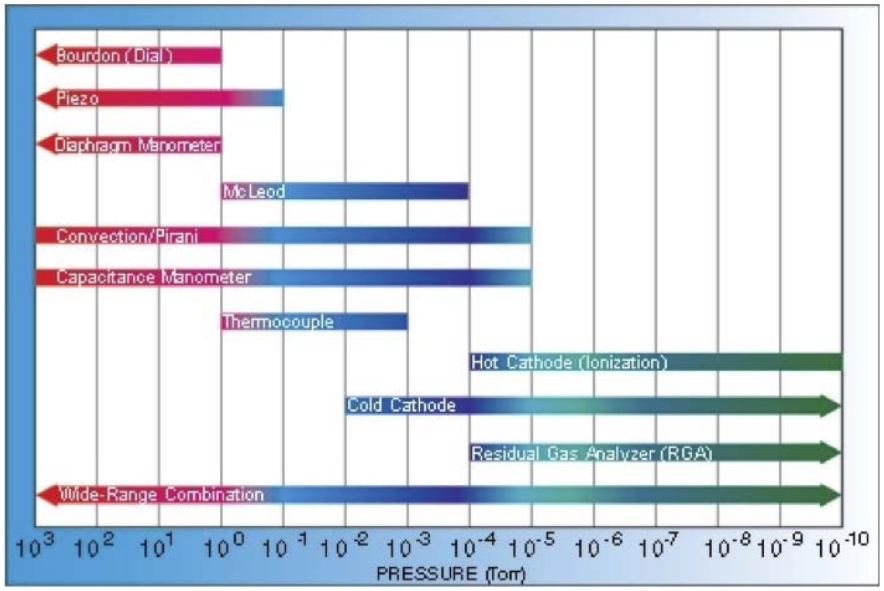

FIGURE 2.4: Pressure range of pressure gauges. The scale here is in Torr, 1 Torr is roughly 1 mbar. The most common way to monitor the pressure in a system is to use a Pirani gauge for high pressures such as in a roughing line. A cold cathode or penning gauge for High Vacuum (HV) such as in a load lock and a hot cathode or ion gauge for UHV. From reference [85]

A Pirani gauge and a hot cathode or ion gauge can cover the full range required and these two gauge types will be discussed here. In a Pirani gauge a heated wire changes temperature with changing pressure. This change in temperature causes the resistance of the wire to change, this change in resistance of the wire is measured as an indicator of the pressure. The gauge tube usually consists of a metal tube with a thin tungsten wire inside, the resistance of tungsten changes rapidly with temperature.[82, 86] Figure 2.5 shows a battery operated Pirani gauge as an example of how the gauge is operated.

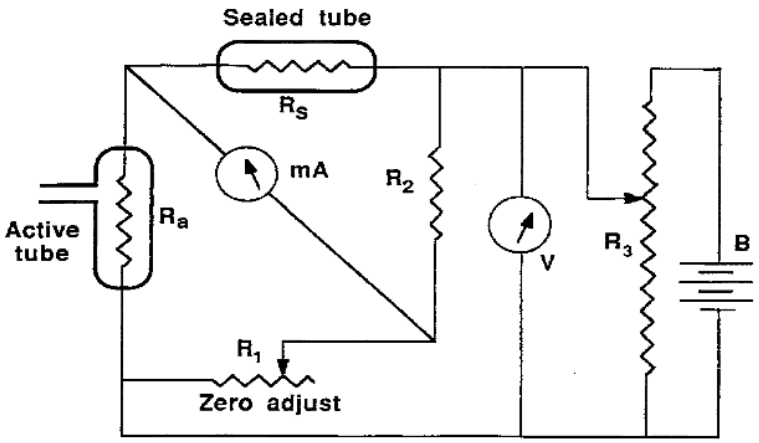

FIGURE 2.5: Schematic of a Pirani gauge. Two tungsten wires are contained within an active tube and a sealed tube. Both wires are kept at a specific temperature. The sealed tube is kept at a constant pressure and is therefore at a constant resistance, while the active tube is exposed to the vacuum being measured and the resistance will vary with the pressure. By balancing the Wheatstone bridge created with these two elements the pressure can be monitored. From reference [82]

Here the active tube with resistance R_a, the sealed compensation tube with resistance R_s and the two resistors R_1 and R_2 form a Wheatstone bridge. The voltage provided by battery, B, causes current to flow through the two parallel branches of the bridge formed by $R_a + R_s$ and $R_1 + R_2$. The current heats the filament in both tubes. To calibrate the device, the bridge is balanced when the active tube is evacuated to a pressure below it's working range. When the pressure is within the normal range, the temperature and resistance of the filament in the active tube unbalances the bridge while the sealed tube remains at a constant resistance. The amount the bridge is unbalanced will vary with pressure giving a corresponding reading. The sealed tube will compensate for changes in ambient temperature.[82, 86]

The ion gauge can be best described by looking at figure 2.6. The filament, F, is

heated to incandescence by the battery or voltage supply, B_1. The electrons emitted by the filament are drawn to the grid, G, a cylinder of wire mesh maintained at a positive potential of roughly 150 V, relative to the filament, by battery B_2. The electrons that travel from the filament to the grid gain sufficient kinetic energy in doing so to ionise any gas molecules present. These ions are collected by the collector, P, usually a thin filament in the centre of the mesh kept at a negative potential of 25-50 V, relative to the filament, by battery B_3. The electron current is measured by the milliammeter in the grid circuit and is kept constant by adjusting resistance at R to change the filament temperature. The ion current is measured with a microammeter. At pressures below 10^{-3} mbar it is unlikely that an electron will collide with more than one ion on its journey from the filament to the grid, therefore, the ratio of the ion current to the electron current is linearly proportional to pressure. The constant of proportionality is a sensitivity factor that is proportional to the ionisation cross-section of the gas molecules.[82, 86]

When designing a vacuum system to obtain UHV pressures, pumps and gauges must be chosen accordingly. The position of pumps on a system is as important as the type and size of pump, this is because the pumping rate is limited not just by the pump but by the port on which it is mounted. Consider a pump mounted to a chamber by a tube, the pump rate, C, will depend on the diameter, D, and length, L, of the tube as follows for (1) viscous flow and for (2) molecular flow.[82, 83]

1. $C = 1.510^9 \frac{D^4}{\eta L} P_{av}$ l/min where η is the viscosity of the gas and P_{av} is the average pressure

2. $C = \frac{0.0121 D^3}{100L + 0.133D}$ l/s

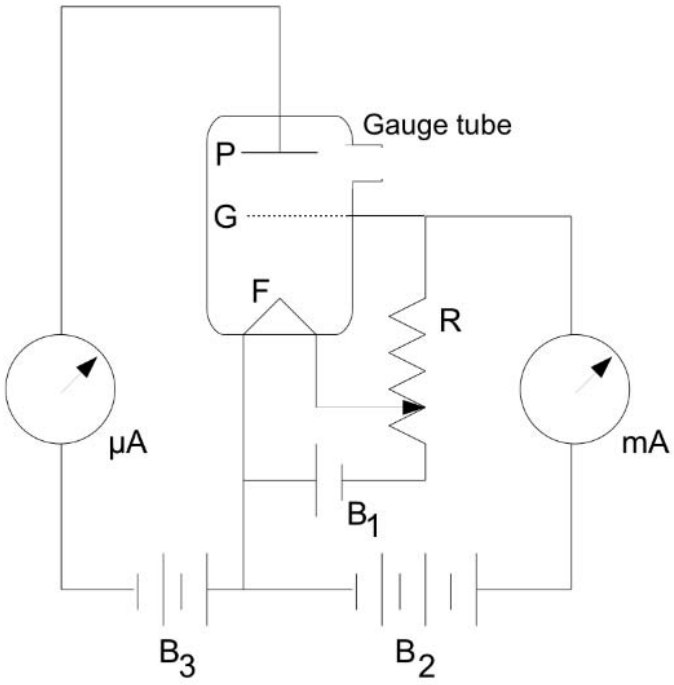

FIGURE 2.6: Schematic of a battery operated ion gauge. Electrons emitted by a filament ionise any atoms or molecules present. These ions are collected by a positive filament and the current is measured by a microammeter. From reference [82]

If a pump is connected directly to a chamber the equations are modified as follows

1. $C \approx 9.42D^2$ l/min
2. $C = \frac{0.12\pi}{4}D^2 = 0.09D^2$ l/s

Consider an ion pump connected to a chamber that houses some equipment, like an STM, by a 6" port, as shown in figure 4.14(a). When using an ion pump the equations for molecular flow are most relevant. For the chamber connected directly to the pump, the pump rate will be 0.0137 ls^{-1}. Now imagine the same chamber connected to the same ion pump via a tube of 6" diameter and, for example, 0.5

m length, as in figure 4.14(b), the pumping rate for this chamber will be 8.562×10^{-7} ls^{-1}. By connecting an ion pump directly to a chamber, pumping speeds can be increased by 10^5, compared to running a single pump for an entire system.

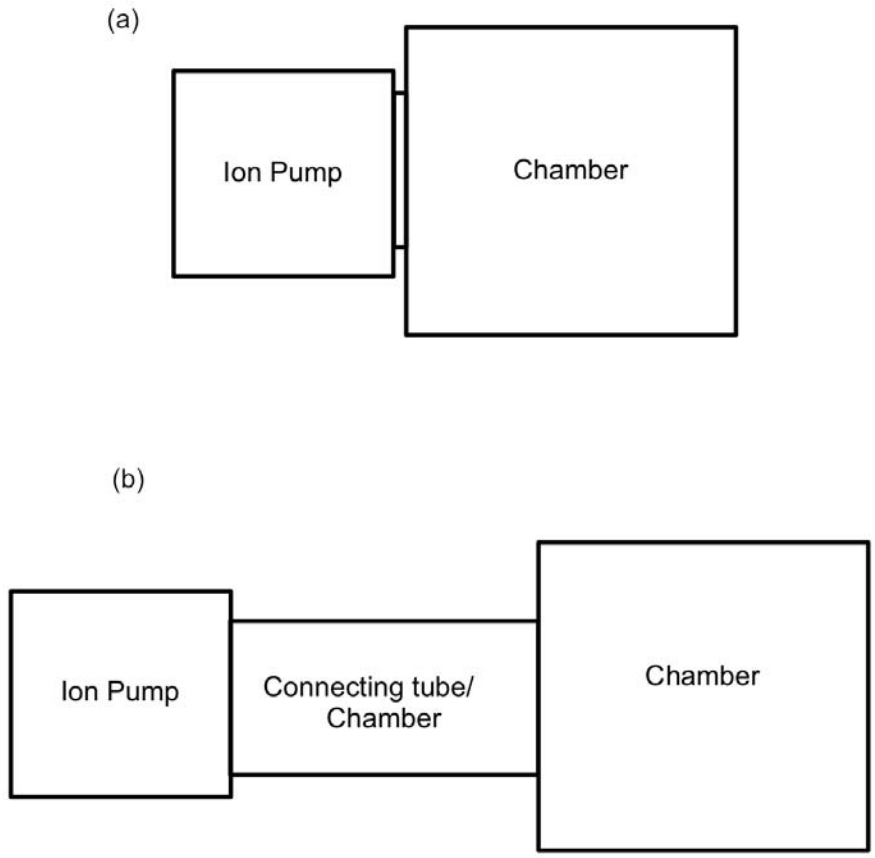

FIGURE 2.7: (a) A chamber directly connected to a pump via a 6" port has a higher pumping speed than (b) a chamber that is connected via another chamber, represented here by a tube. Images are not to scale.

2.2 The Cluster Source

Cluster samples are produced in a Radio Frequency (RF) magnetron sputtering cluster source, which uses a time-of-flight mass filter to select specific cluster masses, and therefore select clusters with a specific number of atoms. All cluster samples, discussed in this thesis, were produced by Dr Feng Yin.

The cluster source, figure 2.8, consists of three main sections (I) cluster production, (II) cluster beam formation (III) mass selection. In phase (I) a magnetron gun (labelled (a) in figure 2.8) combined with the injection of Ar^+ ions produces the initial cluster products. A high voltage RF signal (13.56 MHz) is capacitively coupled to the target material (labelled (d) in figure 2.8) which is otherwise isolated. This RF signal causes both attractive and repulsive phases in the plasma. As electrons in the plasma will be more mobile than positive ions the sample will become more negatively charged and the resultant field induces the sputtering of the target material.[54, 87]

The magnetron gun used is designed to be operated at a pressure of $\approx 10^{-2}$ mbar, the operating pressure of the cluster source is, however, higher at ≈ 1 mbar. At such a high pressure sputtering can occur inside the magnetron gun, therefore, the magnetron gun is protected by a grounded shield (labelled as dark shield (c) in figure 2.8).[54]

The initial products of this sputtering process will be both atoms and small clusters of just a few atoms. These small clusters will act as seeds for further cluster growth whether through surface growth by aggregation of atoms or through collisions with other seed clusters. The growth of larger clusters is mediated by a flow of Helium

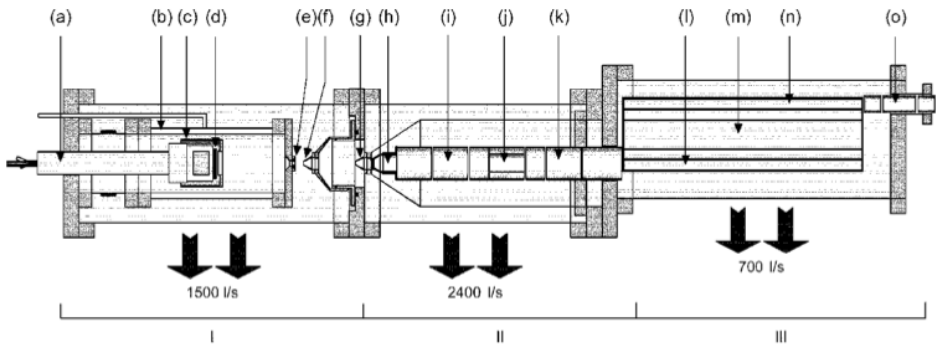

FIGURE 2.8: Schematic of the cluster source showing: (a) magnetron axial mount; (b) liquid nitrogen (lN_2) chamber; (c) dark space shield; (d) sputter target; (e) adjustable nozzle; (f) first skimmer; (g) second skimmer; (h) extraction lens; (i) first einzel lens; (j) deflection plates; (k) second einzel lens; (l) TOF mass filter acceleration region; (m) TOF field-free region; (n) TOF deceleration region; and (o) third einzel lens to focus the cluster beam for deposition into a high vacuum chamber. Figure from reference [54]

gas which is cooled by collisions with the liquid Nitrogen cooled jacket (labelled (b) in figure 2.8).[54, 87]

The clusters produced are focussed into a beam for mass selection through a series of skimmers and lenses. Clusters leave the condensation chamber via the nozzle (labelled (e) in figure 2.8), two skimmers (labelled (f) and (g) in figure 2.8) first create the beam. The beam is then accelerated by the extraction lens (labelled (h) in figure 2.8), the extraction lens is operated at $\approx$ 2 kV. The beam is then focused with a pair of einzel lenses (labelled (i) and (j) in figure 2.8) while a set of deflector plates (labelled (j) in figure 2.8) allows fine adjustment of the beam trajectory before entering the TOF mass selector.[54]

Figure 2.9 shows a schematic of the TOF mass selector. The cluster beam enters the mass selector and a short high voltage pulse applied to plate 1 accelerates the cluster beam vertically. The length of the high voltage pulse is chosen such that no cluster can leave the acceleration region between plates 1 and 2 during

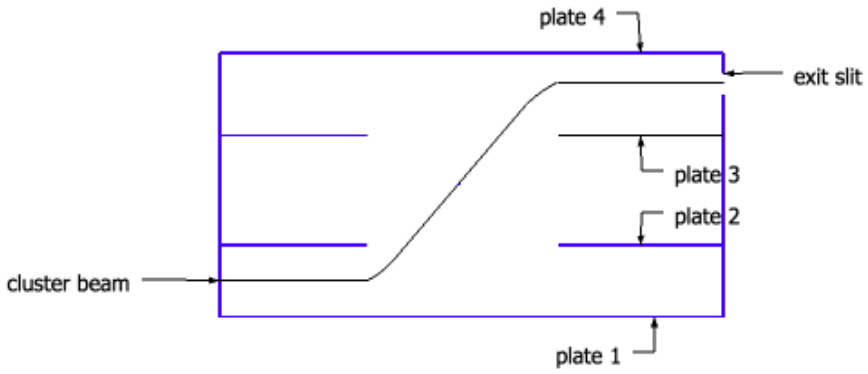

FIGURE 2.9: The TOF mass selector consists of four plates labelled 1-4. Between plates 1 and 2 a voltage is applied to displace the cluster beam, the cluster beam is the allowed to drift in a field free region between plates 2 and 3. Finally plate 4 forces the cluster beam back into its original trajectory and the selected mass passes through the exit slit. Adapted from reference[88]

the pulse, all the clusters should gain the same momentum and all clusters of the same mass will gain the same velocity. The ions pass into a field free region between plates 2 and 3 and are allowed to drift into the region between plates 3 and 4, the difference in velocity between cluster masses will mean different masses reach this region in a different time. When all of the ions of the required mass are calculated to have entered this region, an identical pulse to the one used at plate 1 is applied to plate 4. The clusters should now lose all their vertical velocity and return to their original flight path. The different masses will now be separated in the vertical direction and the selected mass should pass though the exit slit.[88]

The mass resolution of this cluster source can be calculated from the vertical displacement of the different masses and the exit slit width and is given by:

$$R = \frac{m}{\Delta m} = \frac{x}{\Delta x} \tag{2.1}$$

where m is the selected mass,Δ m is the width of the mass range obtained, x is the vertical displacement andΔ x should be a convolution of the cluster beam diameter and the exit slit width.[88] Whilst a value for R, resolution, of 40 should be theoretically achievable experimentally the resolution has been closer to 20 meaning masses of deposited clusters should lie within 5% of the selected mass.[54, 88]

2.3 Cluster Sample Preparation

Clusters can be deposited on practically any type of surface. For STM measurements the sample has to be conducting and generally simple, in terms of ease of preparation and use, but also in terms of the ease with which atomic resolution can be achieved. If atomic resolution can be routinely obtained then the quality of any STM tip can be ascertained before imaging the cluster deposition area itself. In order to study the structure and morphology of individual clusters they have to be immobilized on the surface without appreciably deforming their shape. For these reasons Ar^+ ion sputtered Highly Oriented Pyrolytic Graphite (HOPG) is used as the substrate.

HOPG is easy to prepare, via micro-mechanical cleavage, and is chemically inert. The atomic structure is simple and easily resolved in STM. Clusters, soft landed on a bare HOPG surface, tend to migrate to step edges and form agglomerates, as seen in figure 2.10.[89, 90] To avoid this agglomeration, the surface is sputtered with Ar^+ ions to generate point defects which act as pinning sites for deposited clusters preventing post-deposition agglomeration.[91] In order to preserve their shape the clusters are soft landed by applying a retarding voltage to the HOPG that slows the positively charged clusters. This soft landing allows the clusters to diffuse so that they can find a pinning site. In order to avoid unwanted aggregation during this diffusion process, the density of defects is higher than the density of clusters, both of which can be controlled. This method has been successfully demonstrated using silver clusters by Claeyssens et al.[91]

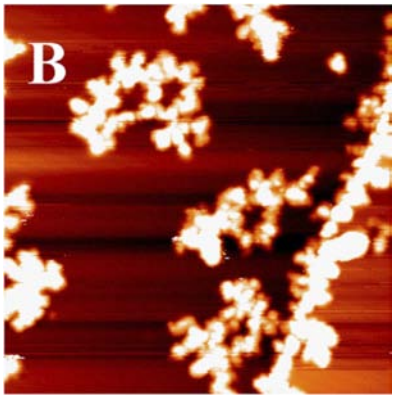

FIGURE 2.10: STM image (100×100 nm^2) of W clusters on HOPG, the W clusters diffuse and form agglomerates especially at step edges where cluster will pin. Image from reference [89]

2.4 STM for the Scanning Probe Electron AnalyseR (SPEAR) and Clusters on Surfaces

The STM chosen for use in the SPEAR system, which will be described in chapter 4, was a Nanograph UHV-STM, this STM was also used for all measurements on clusters. This STM was chosen as its open design gives easy access for light as can be seen in figure 2.11.

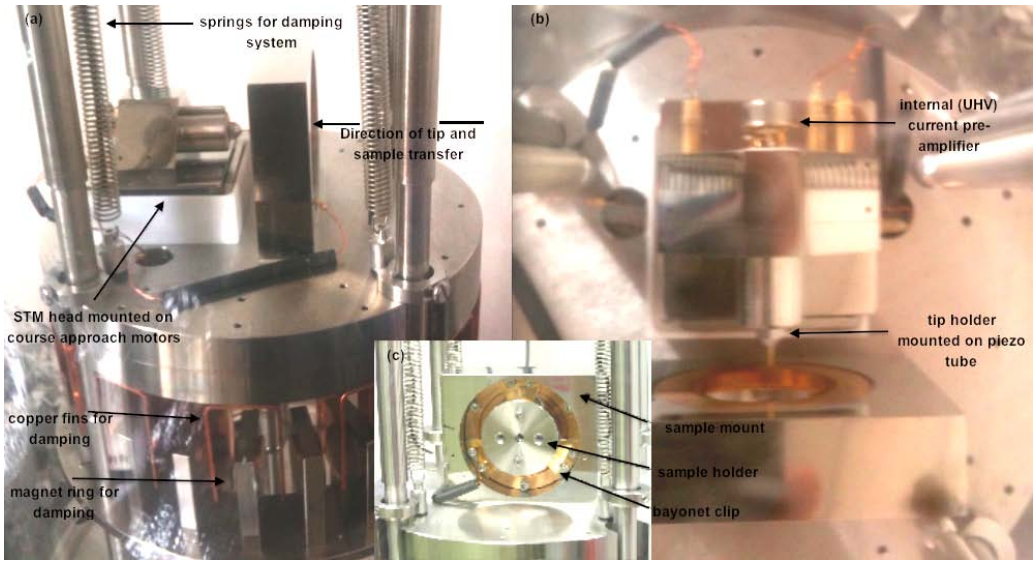

FIGURE 2.11: The Nanograph STM: (a) The spring and eddy current damping system can be seen. The STM head on the left contains all the motors for movement while the sample mount on the right is stationary at all times. (b) A top view of the STM: At the back of the STM head is a current pre-amplifier for amplifying the tunnelling current as soon as possible in vacuum, if the current does not get amplified in the vacuum noise picked up by the wiring in vacuum is also amplified. (c) The back of the sample mount: The locking mechanism involves three wings each with a sapphire bearing to keep the sample holder in place while keeping it electrically isolated and transmitting as little mechanical vibration to the sample as possible.

This STM has a spring and eddy current damping system for vibration isolation. The height of springs must be carefully adjusted for the eddy current damping to be active and these adjustments are only possible out of vacuum.

An RHK SPM-100 controller is used to control the STM. The Nanograph STM employs a single piezoelectric tube for scanning onto which the STM tip is mounted. The scan-head which includes the piezoelectric scanner, tip mount and internal pre-amp, is mounted on top of slip-stick motors which provide movement parallel to the sample surface and movement in the perpendicular direction. The sample is kept in place by sapphire bearings which also keep it electrically isolated from the rest of the STM. Samples and tips are mounted in this system by use of a magnetic transfer arm. The sample mount has a twist lock mechanism using ball bearings, while the tip is mounted on a tip holder that must be screwed into the scan-head. The required bias is applied to the sample and the tunnelling current is measured between the tip and ground as shown in figure 2.12.

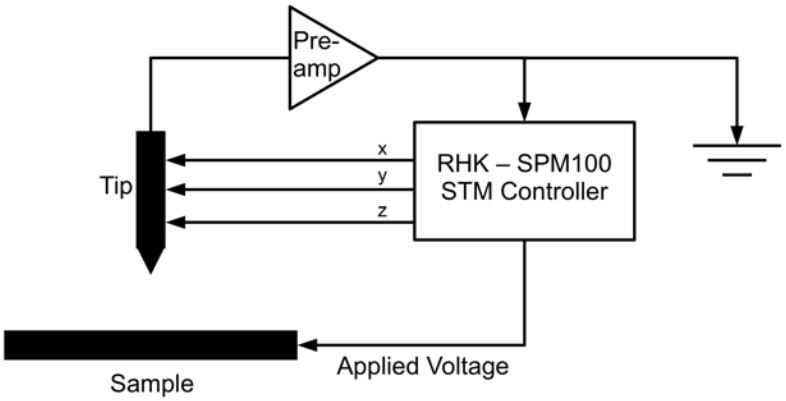

FIGURE 2.12: A simple schematic of the Nanograph STM and RHK control electronics set-up. The bias voltage is applied to the sample and the tunnelling current is measured between the tip and ground via the pre-amplifier shown as pre-amp.

STM measurements of clusters on surfaces were carried out in UHV conditions, the pressure typically being 8×10^{-10} mbar, however, samples were transferred from the cluster source to the STM under ambient conditions, and spent many days in high vacuum, $\approx 10^{-6}$ mbar, in a load-lock. In all cases electrochemically

etched W tips have been used, this electrochemical etching is well documented elsewhere.[49, 50]

2.5 STM of Molecules on Surfaces

The STM used for this set of experiments was an Omicron STM1, shown in figure 2.13. This STM head uses three separate piezos for x, y and z scanning, while the sample is on slip-stick style motors for coarse approach. Samples and tips are transferred by a combination of magnetic transfer arm and 'wobble' stick. A schematic of the system including pumps and valves is shown in figure 2.14. The pressure was 2.5×10^{-10} mbar

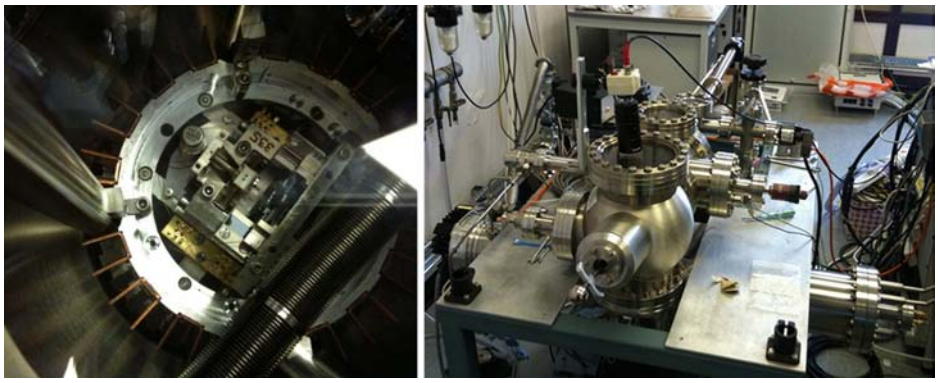

FIGURE 2.13: Omicron STM1 and UHV system that were used. In the left image it is possible to see the three piezoelectric tubes of the scan head. In the right hand image the STM chamber and wobble stick arrangement is visible in the foreground. Behind the STM chamber is the preparation chamber where the heating stage is housed, beyond that the load lock and transfer arm are visible.

The Si surface was cleaned on a specially designed heating stage by direct current resistive heating. To get rid of the oxide layer the sample is heated to 1200 $^{\circ}C$ for 5 - 10 seconds requiring a current of 5 A or more. This is repeated $\approx$ 5 times, reducing the current to $\approx$ 1 A between each step. The final step prepares the Si(111)-7×7 surface, the 1200 $^{\circ}C$ flash is followed by rapid cooling to 960 $^{\circ}C$ ($\approx$ 3.5 A), the melting point of the Si(111) surface, and subsequent slow cooling by 1 $^{\circ}Cs^{-1}$ ($\approx 0.1\ As^{-1}$). The crystal temperature was measured using a pyrometer.

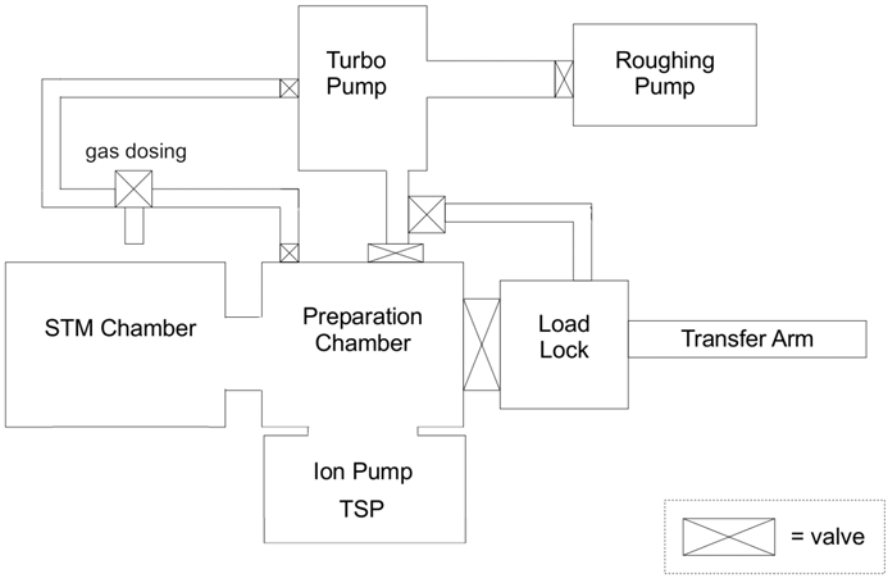

FIGURE 2.14: Schematic diagram for the Omicron STM1 system. The dosing line goes to the preparation chamber however the preparation chamber and STM chamber are directly connected so, as indicated in the diagram, the STM chamber, preparation chamber, ion pump and titanium sublimation pump (TSP) all get dosed with the gas or molecule being used. This diagram is not to scale.

The methylphenyldisulphide sample is in liquid form at room temperature and is purified using a freeze/pump/thaw process. The vacuum test tube containing the methylphenyldisulphide is immersed in liquid nitrogen, LN_2, freezing the sample and the liquid impurities such as water. Gasses dissolved in the sample will be released into the gas phase and are pumped away. Each time the sample thaws the impurities boil off first and a bubbling surface is seen, the freeze-thaw procedure is repeated until no more bubbling is seen and the sample is assumed to be pure. Ideally, mass spectrometry would be used to verify the purity of the sample but this was not available.

Electrochemically etched tips were used, prepared using well known techniques.[49, 50] Tips were cleaned in the load lock by resistive heating, and in the preparation chamber by a radiative heater in order to get rid of all the tungsten oxide and any water.[92, 93] The quality of tips and Si(111) surface prepared was verified by imaging the Si(111) surface. During all imaging the tunnelling current set-point was kept below 100 pA in order to avoid any mechanical interaction between the tip and the molecules being studied. Voltages were typically on the order of 1 V, voltages below 1 V did not allow atomic resolution images.

2.6 Equipment List

2.6.1 Nanograph System

A UHV system was designed by the author for use with the Nanograph STM, described in section 2.4, this system was used for experimental work in chapter 3.1 and chapter 4. Table 2.1 provides a list of equipment and electronics used with this system.

TABLE 2.1: A table of the equipment used for experimental work in chapters 3.1 and 4.

Make	**Model**	**Description**	**Location/Function**
Nanograph		Scanning Tunelling Microscope	STM chamber
RHK	PMC100	Piezoelectric Driver	Controller to run STM
RHK	SPM100	STM Controller	Main controller for STM
SPECS	UVS-300	He Discharge Lamp	Attached to STM chamber
SPECS		UVS-300 Controller	
SRS	SR510	Lock-in Amplifier	For SPEAR Technique
Edwards	RV3	Roughing Pump	Backing for Turbo Pump
Pfeiffer	TMU260	250 ls^{-1} Turbomolecular Pump	Turbo Pump for System
Gamma Vacuum	Titan	300 ls^{-1} Ion Pump	Attached to Preparation Chamber
Varian	Starcell	150 ls^{-1} Ion Pump	STM Chamber
Varian	MiniVac	Ion Pump Controller	Controls Varian Pump
Varian	Dual Controller	Ion Pump Controller	Controls Gamma Vacuum Pump
Pfeiffer	TCP 015	Turbo Pump Controller	
AML	PGC1	Ion Gauge Controller	Two controllers for Ion Guages
AML		Ion Guage	STM Chamber
AML		Ion Guage	Preparation Chamber
AML		Ion Guage	Load Lock
Balzers		Pirani Guage	Roughing Line
Balzers	TPG 252	Guage Controller	Monitor Roughing Line Pressure

2.6.2 Omicron System

The Omicron system was designed by previous users, with some modification and repair required by the author, this system was used for experiments in chapter 3.2.1. Table 2.2 provides a list of equipment and electronics used with this system.

TABLE 2.2: A table of the equipment used for experimental work in chapters 3.1 and 4.

Make	**Model**	**Description**	**Location/Function**
Omicron	STM1	Scanning Tunelling Microscope	STM chamber
RHK	PMC100	Piezoelectric Driver	Controller to run STM
RHK	SPM100	STM Controller	Main controller for STM
Edwards	RV3	Roughing Pump	Backing for Turbo Pump
Leybold	TW300	300 ls^{-1} Turbomolecular Pump	Turbo Pump for System
Varian	Diode	300 ls^{-1} Ion Pump	Connected to Preparation Chamber
Varian	Dual Controller	Ion Pump Controller	Controls Gamma Vacuum Ion Pump
AML		Ion Guage	STM Chamber
AML	PGC1	Ion Gauge Controller	Monitor STM chamber/system pressure
MKS	423 I-mag	Cold Cathode Guage	Load Lock
MKS	943	Cold Cathode Controller	Monitor Load Lock Pressure
Balzers		Pirani Guage	Pressure Measurement for Roughing Line
Balzers	TPG 252	Guage Controller	Used to monitor Roughing Line pressure

Chapter 3

STM Studies of Nanostructured Surfaces

Nanostructured surfaces are surfaces or samples that are modified at the nanoscale either by some lithography process, scanning probe modification or by depositing nanostructures, such as clusters or molecules, which may in turn modify surface properties. In this chapter clusters and molecules deposited on surfaces are characterised and studied by STM.

Size selected clusters were soft landed on HOPG that had been bombarded with Ar^+ ions to produce defects which act as pinning sites preserving the cluster shape, as described in chapter 2.3. The overall shape of Pd and Au clusters is seen to change from spherical shapes to elongated (ellipsoidal) shapes with increasing size. Most likely this phenomenon is traceable to a gas phase aggregation regime in which seed clusters collide to create larger clusters. The shape of metal

nanoclusters, produced by a size-selected cluster beam source, is affected by the growth conditions in the source.

The molecule methylphenyldisulphide ($C_6H_5SSCH_3$) was deposited at different doses on to a Si(111)-7×7 surface. Different surface features are identified and attributed to the bonding of the molecule. The molecule is also seen to bond to the STM tip and is deposited on the surface by the tip.

3.1 Clusters on Surfaces

The properties of clusters depend upon their size and shape, for example the wavelength of light a cluster absorbs, or fluoresces at, is size dependent.[2–7] Certain cluster sizes have also been demonstrated to be effective catalysts but more work is required to discover exactly what makes a good catalyst and optimise cluster samples.[8–11] It has also been demonstrated that non-spherical clusters, produced either by chemical means or by growth on a modified surface, can produce anisotropic optical properties that have potential applications in plasmonics and optical recording.[94, 95] Therefore, if it is possible to precisely control the size and shape of clusters, many advanced applications become available.

Since the discovery of the catalytic activity of Au clusters, catalysis has become a focus of the cluster community.[8–10, 12, 96–99] Palladium has been in use for many years as the catalyst in catalytic converters, more recently research into the catalytic properties of Pd clusters has been spurned on by the possibility of reducing cost and consumption of Pd and by the possibility of using Pd to catalyse other important reactions.[100–102]

Pd and Au clusters not only hold interest for their catalytic properties but also for their optical properties.[99, 103–106] Au clusters have been used for many centuries to colour glass[99], but now, clusters are being used as potential components in biomolecule sensing[107], where the florescence or luminescence must be tuned.[5] There are also potential applications in photonics or as optical recording media[5, 94, 95], where the plasmon modes need to be controlled. The majority of these

size effects arise from the d-band electrons therefore Au, Pd and Ag are regularly used.[2, 4, 104–106, 108–111]

3.1.1 Results and Discussion: Clusters on Surfaces

Palladium (Pd) clusters consisting of 887(±44), 3500(±175) and 4500(±225) atoms were soft landed on Ar^+ ion sputtered HOPG and studied using STM. These samples may be referred to as Pd 887, Pd 3500 and Pd 4500 henceforth. The samples were prepared by Dr Feng Yin as described in chapter 2.3 using the cluster source described in chapter 2.2. Between deposition and imaging the cluster decorated surface was exposed to air both during transport and during storage. It is most likely that the Pd clusters oxidise at their surface. The oxide is an insulator and so prevents STM imaging of the sample with 'normal' STM parameters (0.5 V to 1 V, 0.5 nA to 1 nA), see figure 3.1. Instead higher voltages and lower tunnelling currents are used to prevent direct tip/cluster interaction which degrades the final quality of the image, but does produce stable images. Nonetheless, the fundamental morphologies of the clusters should remain intact. Indeed here the main feature of interest is the cluster aspect ratio (length/width). Figure 3.2 shows STM images of these cluster samples.

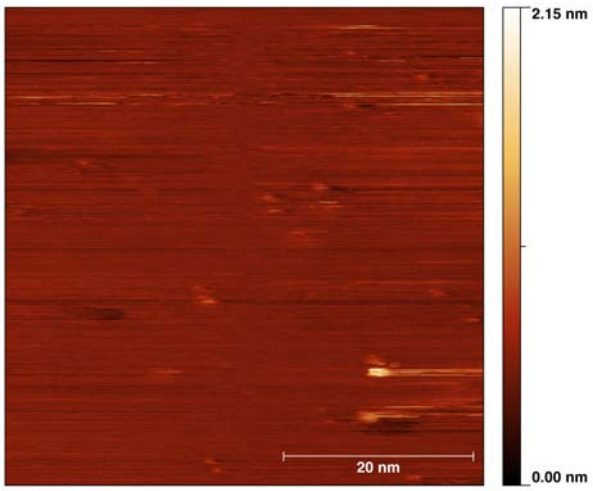

FIGURE 3.1: STM image 50 nm by 50 nm, 0.5 V, 1 nA. Image shows the interaction between the tip and Pd 4500(±225) on HOPG at these STM parameters.

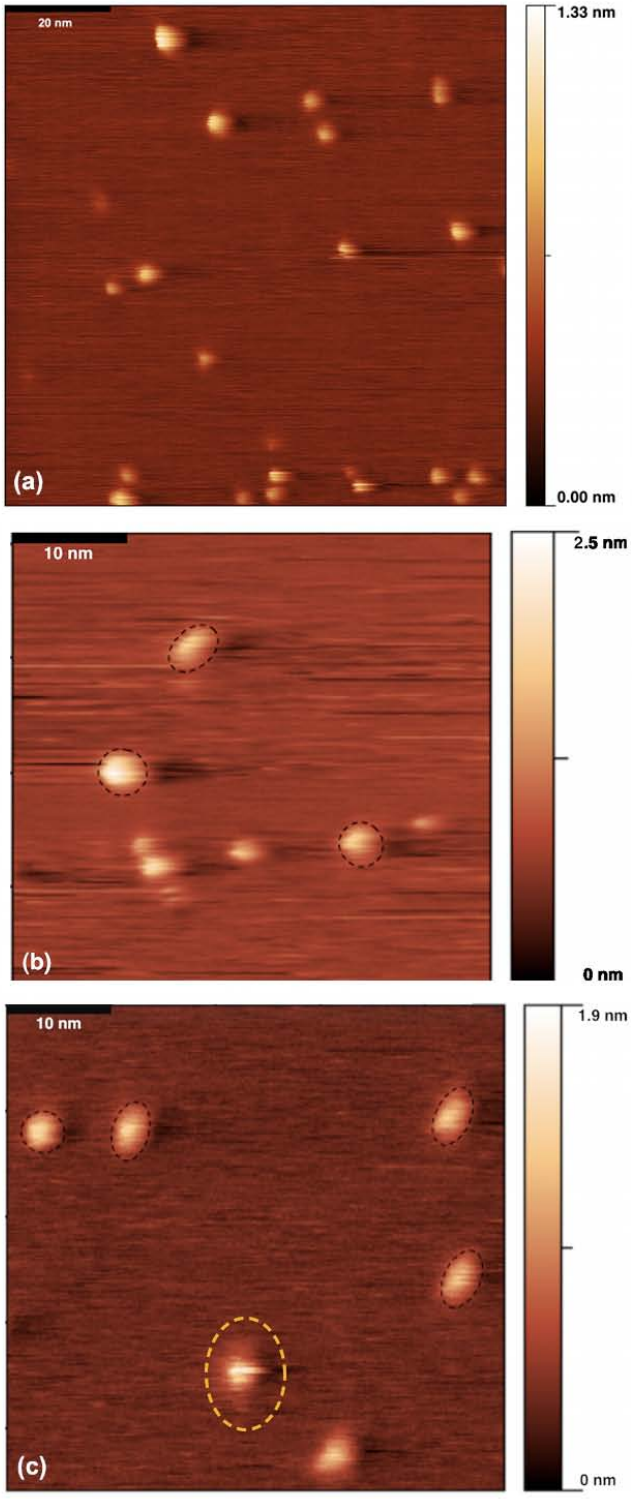

FIGURE 3.2: Example STM images of the three cluster samples. (a) Pd 887(±44) 100 nm by 100 nm, 1.5 V, 0.3 nA (b) Pd 3500(±175), 50 nm by 50 nm, 1.4 V, 0.2 nA (c) Pd 4500(±225), 50 nm by 50 nm, 2.1 V, 0.3 nA. The dotted lines are intended to highlight some typical clusters and their approximate shape.

In figure 3.2 a tip interaction is seen on the top of some clusters. Although unavoidable, the tip interaction sometimes distorts the height. However, the perimeter of the clusters remains stable during scanning and line profiles can still be taken across the clusters to obtain the width and length of clusters, as shown in figure 3.3. A line profile is taken at multiple places on each cluster and the average values are used. Where a clusters shape is clearly affected by a streaking effect due to a tip interaction, such as the cluster highlighted with an orange dashed ring in figure 3.2(c), that cluster is discarded from the data. Despite the problems of tip-cluster interaction, many hundreds of images were taken to ensure good statistics. Despite the need to discard some data, consecutive imaging ensured that the perimeter of clusters could be seen to be stable even if the height was not, see figure 3.4.

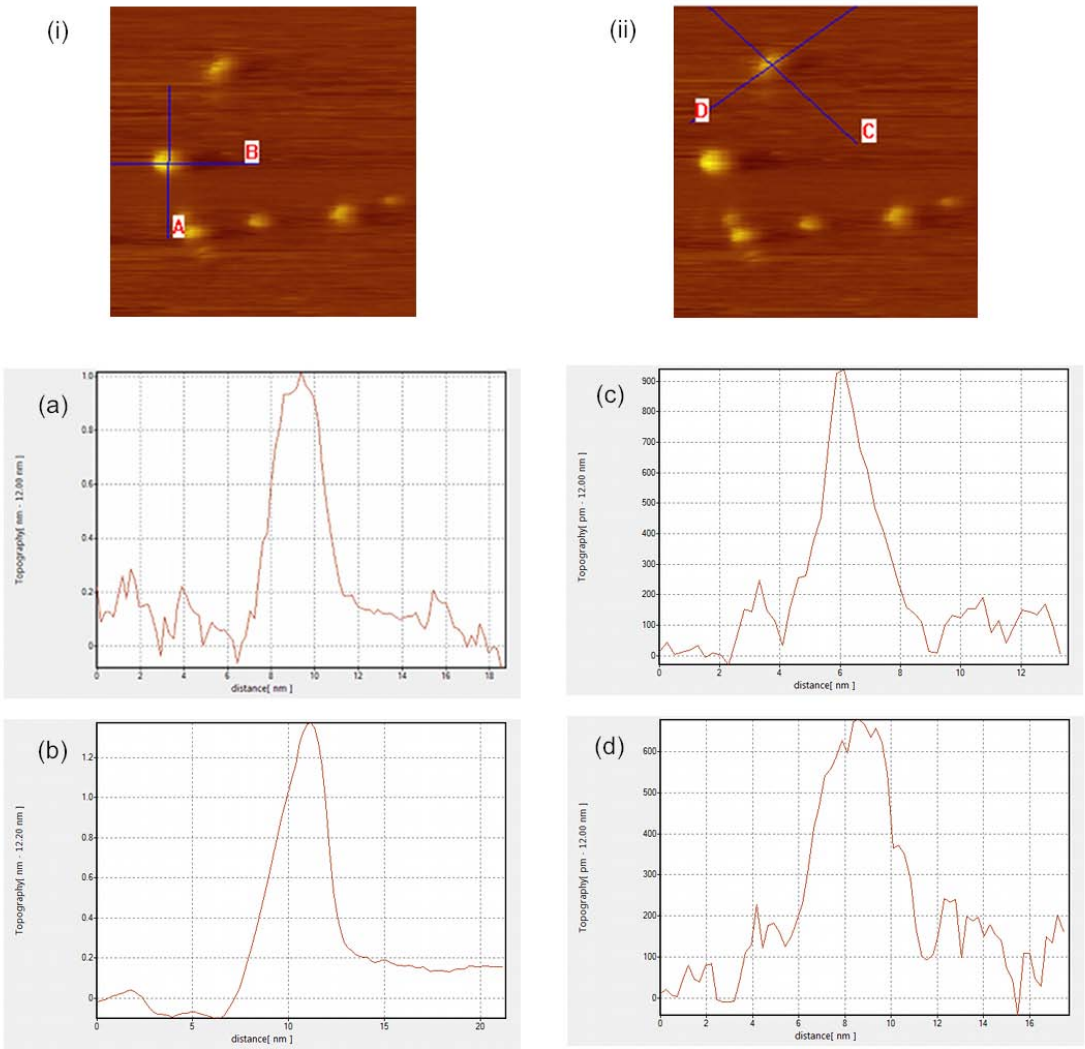

FIGURE 3.3: Line profiles of two clusters from image 3.2(b) showing the difference between an elongated cluster (ii) and a non-elongated cluster (i).

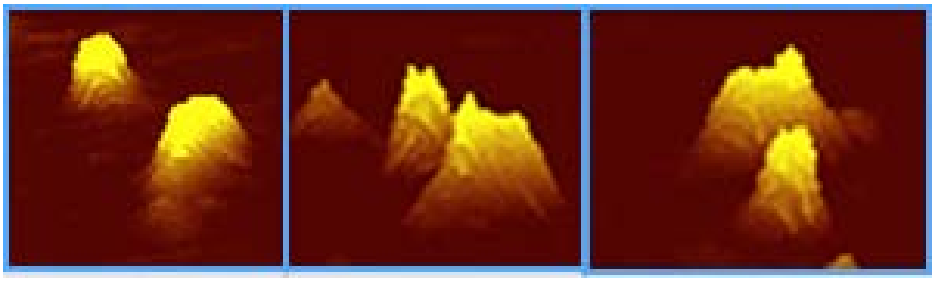

FIGURE 3.4: Three views of two clusters on the HOPG surface, 3-d images taken from three consecutive STM images of scale 50 nm by 50 nm, at 1.5 V and 0.25 nA. The perimeter of these clusters, one elongated and one 'spherical' is stable against scanning, the height information does suggest some tip-cluster interaction.

Image analysis was performed using the Matlab image analysis package. A profile tool was used to manually extract data on heights, widths and lengths from the STM images. The data for Pd 887 was extracted from $\approx$ 100 images, the data for Pd 3500 and Pd 4500 was extracted from $\approx$ 250 images each.

Figure 3.5 shows the distribution of cluster aspect ratios for each of the three sample sizes. The Pd 887 aspect ratio is peaked around 1, which implies a spherical cluster. Both the Pd 3500 and Pd 4500 samples, however, show a discernible shift to non-spherical aspect ratios as shown by figure 3.6.

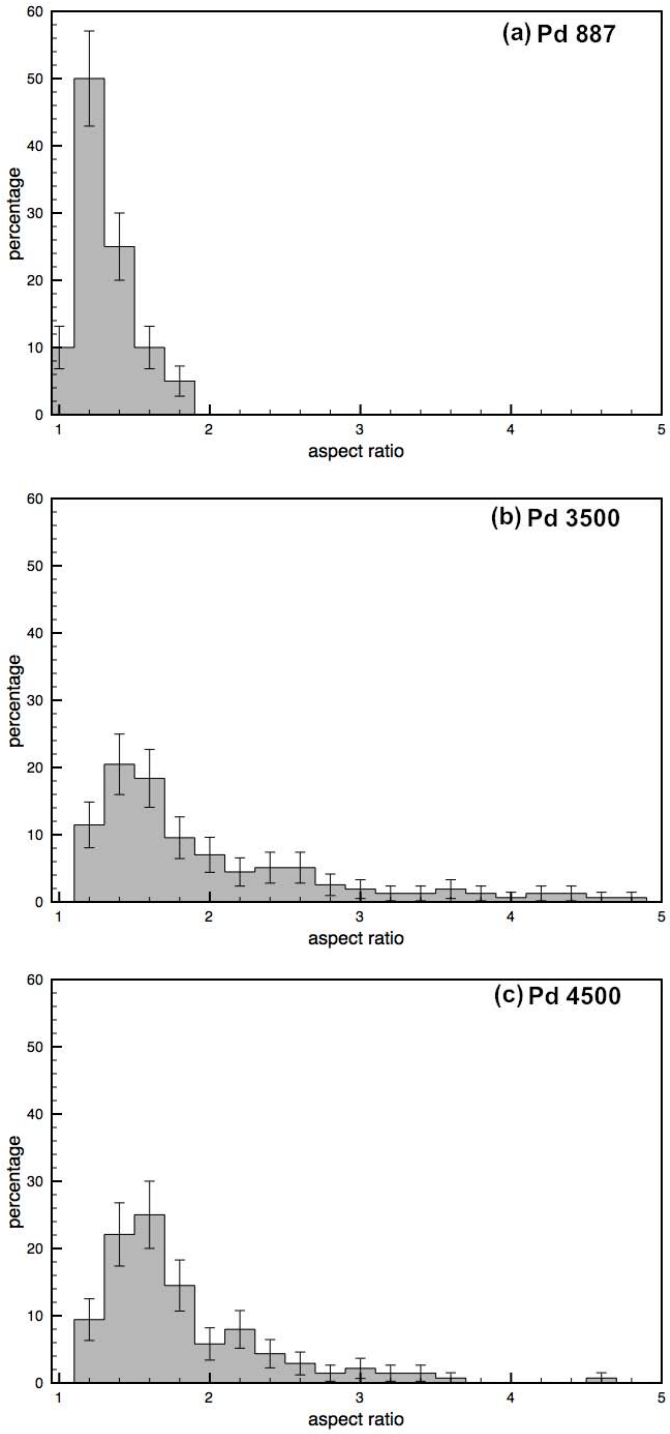

FIGURE 3.5: Distribution of aspect ratios for the three Pd cluster samples. (a) Pd 887(±44): includes data taken from approximately 1000 individual clusters. (b) Pd 3500(±175): includes data taken from approximately 3000 individual clusters. (c) Pd 4500(±225): includes data taken from approximately 3000 individual clusters.

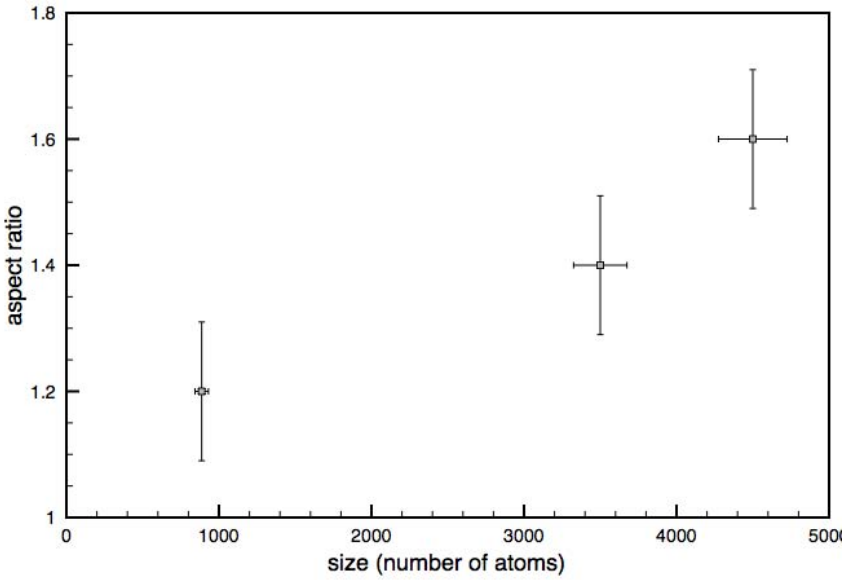

FIGURE 3.6: The mode of the aspect ratio of Pd clusters as a function of cluster size. A trend of increasing aspect ratio with increasing cluster size is observed.

The distribution of aspect ratios for the Pd 3500 and Pd 4500 clusters unambiguously demonstrates non-spherical clusters. Figures 3.7 and 3.8 shows that this phenomenon is not restricted to Pd but is also present in Au clusters.

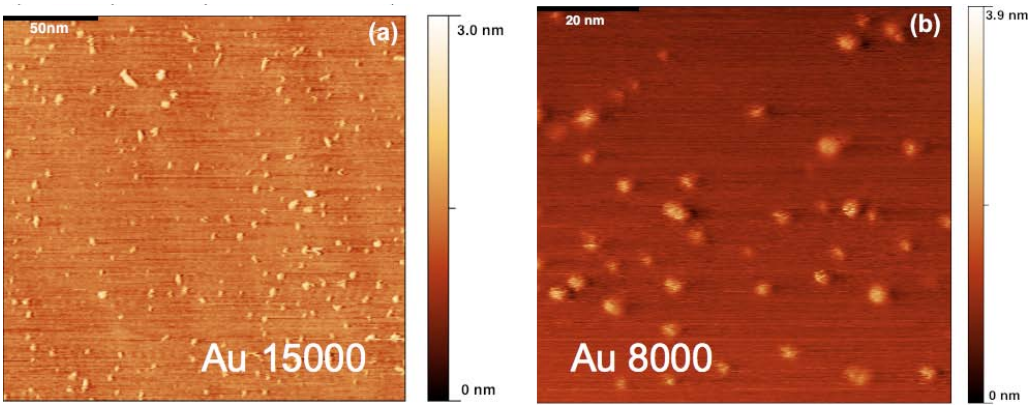

FIGURE 3.7: Two STM images of Au clusters on Ar^+ sputtered HOPG surfaces. (a) Au 15000(±750): 200 nm by 200 nm, 1.1 V, 1.5 nA. (b) Au 8000(±400): 100 nm by 100 nm, 1.2 V, 1.5 nA.

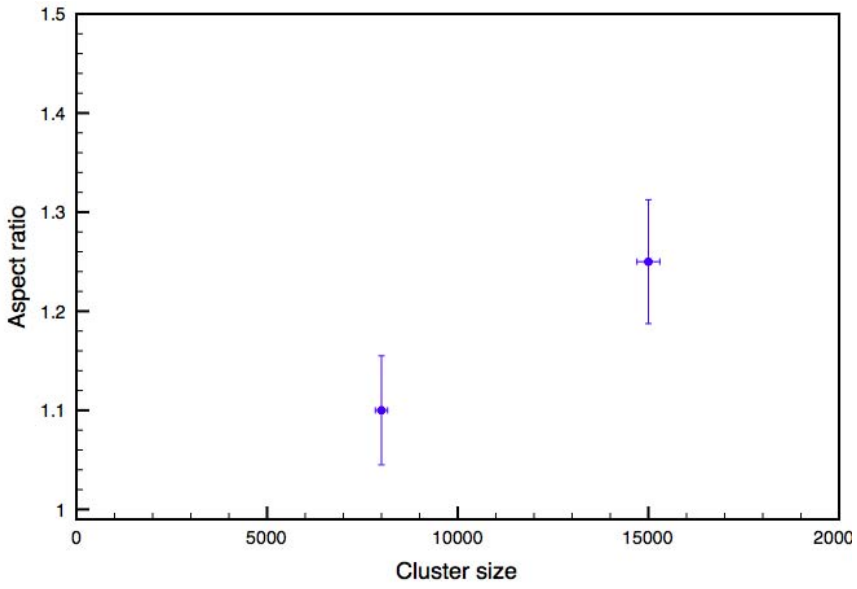

FIGURE 3.8: The mode of the aspect ratio as a function of cluster size for Au clusters. Only two data points are available but it can still be suggested that the aspect ratio is seen to increase with increasing cluster size.

There is clear evidence that non-spherical particles are produced in the cluster source. The clusters are pinned by argon defects and are stable against scanning, therefore, it should not be aggregation on the surface, and, although the mass of these clusters cannot be directly verified by STM due to oxidation, the cluster source size selection regime will give clusters of only one size.[91] Such non-spherical clusters have been seen in High Angle Annular Dark Field (HAADF) measurements performed by David Pearmain.[112, 113] In HAADF the intensity of a signal at a given point is proportional to the Z number, i.e. the nuclear mass at that given point, by integrating the HAADF intensity of a feature it is possible to 'weigh' individual features.[113] By comparing all the objects in a particular cluster sample, the integrated HAADF intensity, and therefore cluster mass, is found to be the same no matter what their shape, therefore this phenomenon is not due to aggregation on the surface.[112, 113]

From chapter 1.2.3 it is known that for gas phase cluster formation a collision rate that is greater than the coalescence rate leads to non-spherical/agglomerated products.[56, 60] Zachariah et al. showed that the coalescence rate of clusters increases with increasing cluster size or decreasing cluster temperature, see figure 1.13 in chapter 1.2.3.[56] The increase in coalescence rate with increasing cluster size may contribute to the increase in non-spherical clusters that are seen.

In order to produce large clusters the cluster source, previously described in section 2.2, is tuned to produce more material in the sputtering process and collisions are encouraged by an increased pressure, see table 3.1. Therefore, collision times are decreased with increasing cluster size.

TABLE 3.1: Cluster source settings, recorded by Dr Feng Yin, used in the formation of three different size of Pd clusters, each cluster size deposited on a separate piece of HOPG.

Size (atoms)	887	3500	4500
Magnetron Power (W)	54	42	42
Pressure (mbar)	0.28	0.38	0.48
Deposition Energy (keV)	0.5	0.5	0.5
Beam Current (pA)	40	17	10

The melting temperature of clusters increases with increasing size until reaching the bulk value.[114] For a Pd sample of 456 atoms the melting temperature is $\approx$ 1000 K, for 1568 atoms the melting point is $\approx$ 1200 K while the bulk melting point of Pd is 1825 K.[114] In the cluster source used for these experiments, the starting temperature of the plasma is $\approx$ 1200 K, but the clusters are quickly cooled by a helium flow during formation. This suggests that for larger clusters the collision products may be solid, even if the balance of collision time and coalescence time favours spherical clusters, non-spherical clusters may form due to the growth mode of solid clusters. In solid clusters the growth, as discussed in chapter 1.2.3, is dominated by the diffusion of atoms through grain boundaries, the energy-gradients that drive this growth may not be enough to overcome the crystal structure of the solid clusters giving rise to non-spherical clusters.[57, 61] Arcidiacono et al. showed that a lattice mismatch between colliding solid, or nearly solid, clusters produced even greater strain during coalescence of the clusters. The strain created by the rearrangement of the crystal structure is enough to induce a rotation of the cluster in free space. This increase in strain will increase the energy required to achieve the lowest energy, spherical, state.[57]

The final shape of clusters produced in a cluster source depends on the settings used and the size of clusters. If high collision rates can be induced then it may be

possible to produce non-spherical clusters for smaller sizes. For larger clusters the percentage of non-spherical particles can be increased or decreased by manipulating the cooling and collision rates. It may be possible to produce different shapes of clusters at different sizes to order, and hence influence the electronic structure of such nanoparticles in more than one-dimension.

Although, due to the oxidation of Pd, the heights of Pd clusters measured by STM will not exactly reflect their true heights, they will however, reveal the distribution of heights. As can be seen in figure 3.9, heights were measured by taking three profiles across each cluster at different places and taking the average value.

The Pd 887 sample has the smallest spread in heights, consistent with a spherical nanoparticle. The measurements of Pd 3500 and Pd 4500 show a much wider height distribution. A wide height distribution is to be expected for a distribution of aspect ratios as the volume must remain constant. However, a constant volume is not observed, see figure 3.10, but, as discussed above, the clusters are not a product of surface aggregation. This volume discrepancy in STM data could arise from inaccurate height measurements due to an oxide layer on the Pd clusters. However this discrepancy could also be explained by the orientation of clusters on the surface, see figure 3.11, clusters that do not lie flat against the surface will present larger volumes than those that do lie flat. It may then be possible to have a distribution of aspect ratios from a single aspect ratio sitting in a variety of orientations.

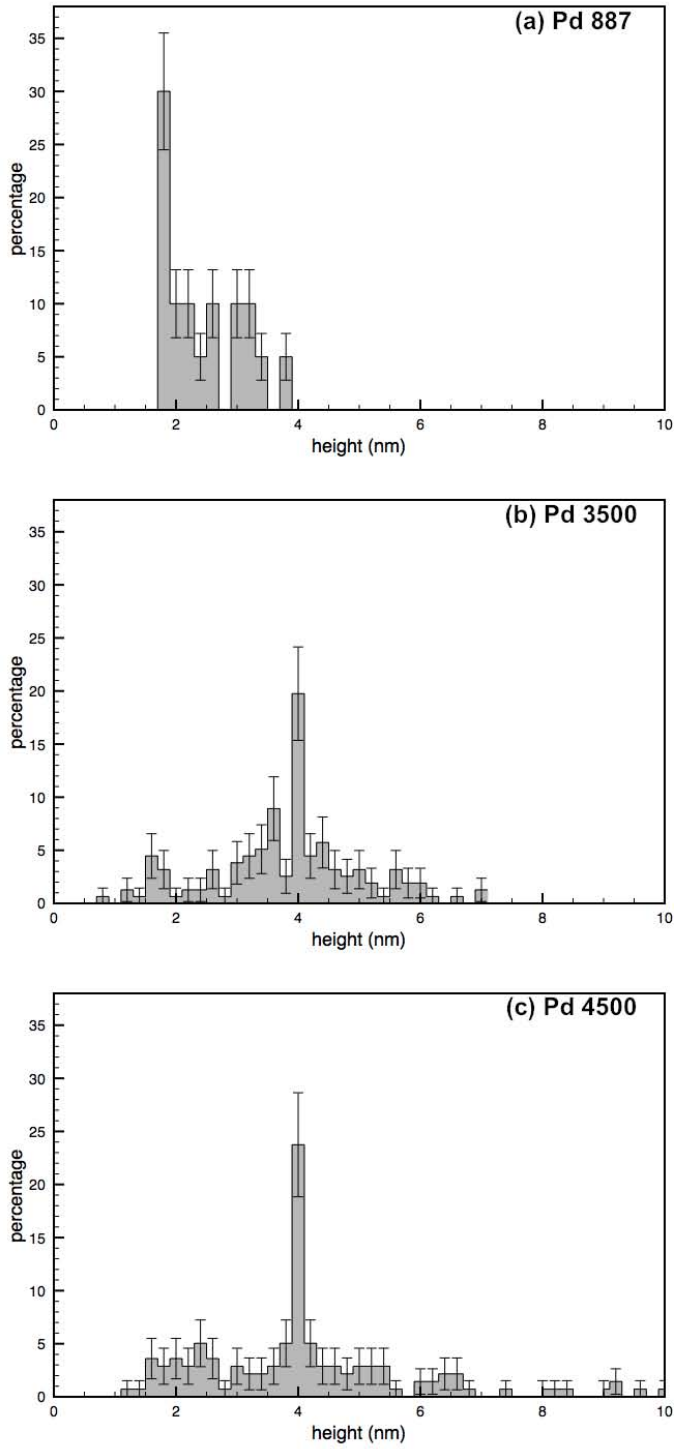

FIGURE 3.9: Distribution of heights for the three Pd cluster samples as measured in the STM. Typical imaging parameters are 1–2.5 V and 0.2–0.7 nA. (a) Pd 887(±44): includes data taken from approximately 1000 individual clusters. (b) Pd 3500(±175): includes data taken from approximately 3000 individual clusters. (c) Pd 4500(±225): includes data taken from approximately 3000 individual clusters.

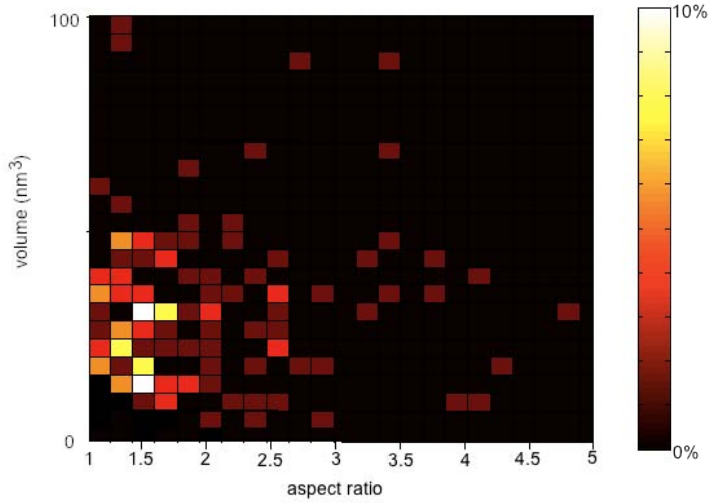

FIGURE 3.10: A plot of volume against aspect ratio for Pd 3500(±175). Data on 3000 clusters have been binned into a histogram of both aspect ratio and height. The colour scale indicates the amount of clusters of a given aspect ratio within a certain volume range. There is a general decrease of volume with increasing aspect ratio but there is also a spread in volume for any given aspect ratio.

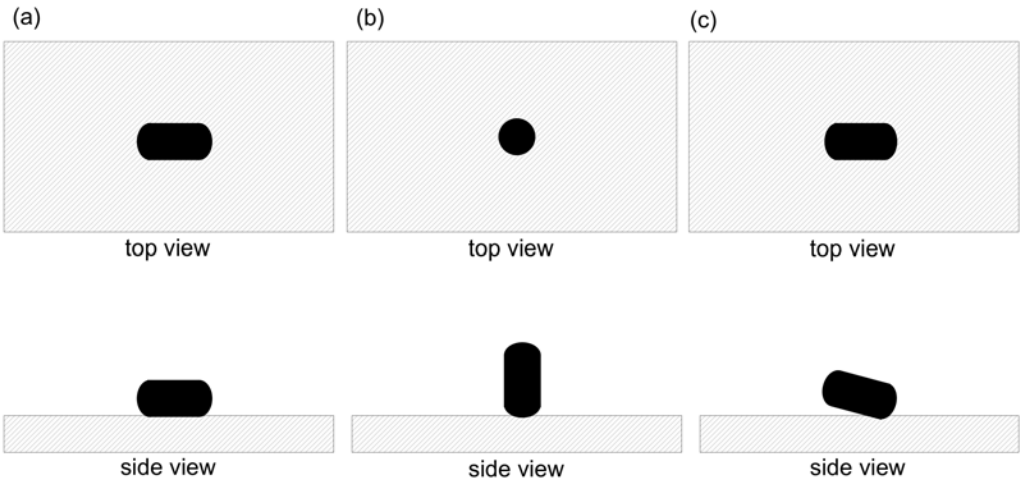

FIGURE 3.11: Schematics of three possible cluster orientations. (a) The cluster lies flat on the surface. (b) The cluster stands up, from a top view or STM image it would appear spherical, but appears higher, the volume would appear the same. (c) The cluster sits at a 15° angle with the surface, perhaps due to the shape of a defect. An aspect ratio lower than the real aspect ratio would be measured by STM. The volume now contains some extra volume from underneath the cluster.

There are three possible scenarios for the relationship between measured cluster volume and measured aspect ratio:

1. There is a real distribution of aspect ratios and all the clusters lie flat against the surface.

2. There is only one aspect ratio but clusters sit with different orientations as in figure 3.11.

3. There is both a real spread in aspect ratio and a variety of orientations.

In scenario 1, a spread in aspect ratios would be seen, but, the measured height would be a simple function of the aspect ratio and would reflect the real height exactly. In scenario 2, where there is only one aspect ratio, the measured height would be proportional to the real height. The measured aspect ratio for scenario 2 would be proportional to the real aspect ratio. Therefore scenario 2 also produces a simple relationship between the measured aspect ratio and measured height. Scenario 3 is more complicated, as there are now two variables affecting the height. The measured aspect ratios and heights for the three scenarios can be calculated by modelling the clusters as dumbbells, that is to say a cylinder with hemi-spherical ends as in figure 3.12. The real volume, V, of the cluster is determined by equation 3.1.

$$V = \frac{4}{3}\pi(\frac{d_a}{2}N^{\frac{1}{3}})^3 \tag{3.1}$$

where d_a is the inter-atomic distance of bulk Pd and N is the number of atoms. From this volume the length of the cylindrical part, l_{cyl}, real width, w_{real}, real

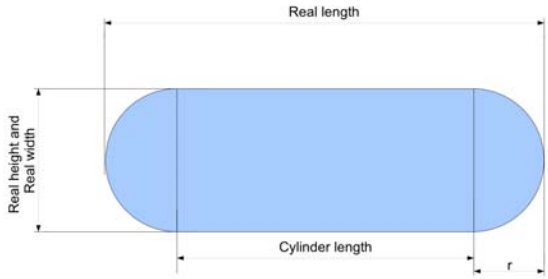

FIGURE 3.12: Clusters were modelled as a cylinder capped by hemispheres of radius, r, in order to determine the nature of the measured heights and aspect ratios observed in the STM data.

length, l_{real}, and real height, h_{real}, can be determined as a function of the aspect ratio, asr_{real}, which may be chosen or may be random depending on the scenario modelled:

$$r = \left(\frac{V}{2asr_{real}\pi - \frac{2}{3}\pi}^{\frac{1}{3}}\right) \tag{3.2}$$

$$w_{real} = 2r$$

$$l_{real} = w_{real} \times asr_{real}$$

$$l_{cyl} = \frac{volume}{\pi r^2} - \frac{4}{3}r$$

The height that would be measured by a perfect STM, h_{meas}, and the aspect ratio that would be measured, asr_{meas}, can then be determined by:

$$h_{meas} = l_{cyl}\sin(\theta) + 2r \tag{3.3}$$

$$asr_{meas} = \frac{l_{cyl}\cos(\theta) + 2r}{2r}$$

Figure 3.13 shows the distribution of simulated measured heights calculated for the three scenarios described above. Only the result of scenario 3 matches the height distributions measured by STM, suggesting that not only is there a real distribution of aspect ratios but the clusters also sit in orientations other than flat.

The spread of volume as a function of aspect ratio produced by scenario 3, see figure 3.14, also closely resembles the STM data, figure 3.10. For scenarios 1 and 2 the height is proportional to the aspect ratio or the cosine of the angle subtended to the surface respectively, therefore a simple volume-aspect ratio relationship is also seen and only scenario 3 can give the spread of volume seen. The comparison of figure 3.10 to figure 3.14 strongly supports the hypothesis that the clusters exhibit both a real distribution of aspect ratio and a real distribution of orientations with respect to the surface.

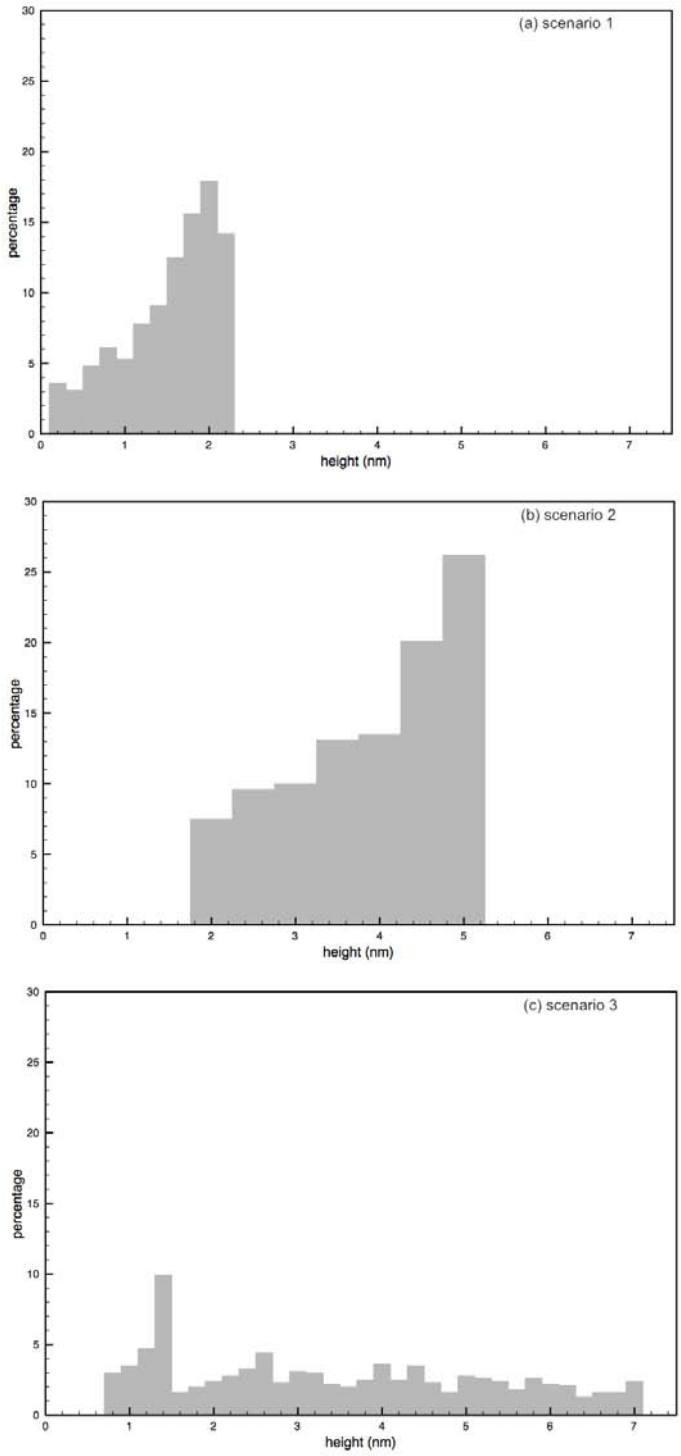

FIGURE 3.13: Height distributions for the model of Pd 3500. (a) Data for scenario 1: 1000 clusters each with an aspect ratio randomly set between one and three. This produces a narrow distribution of heights. (b) Data for scenario 2: 1000 clusters each with the aspect ratio 1.5 but with random orientation w.r.t the surface. Again there is a small spread in heights. (c) Data for scenario 3: 1000 clusters each with a random aspect ratio between one and three and with a random angle w.r.t. the surface. A large spread in aspect ratios is seen.

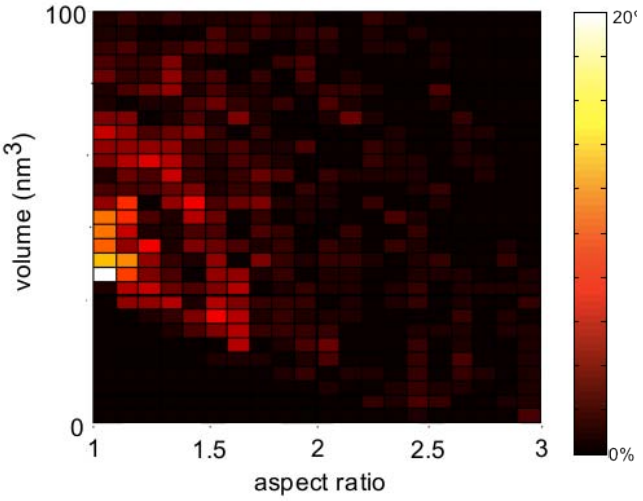

FIGURE 3.14: A plot of volume against aspect ratio for the model of Pd 3500(±175) using scenario 3. Data on 1000 simulated clusters has been binned into a histogram of both aspect ratio and height. The colour scale indicates the amount of clusters of a given aspect ratio within a certain volume range.

3.2 Molecules on Surfaces

In 1983 Binnig, Rohrer, Gerber and Weibel published results of atomic resolution STM of Si(111)-7×7,[62] this was the first time real space imaging of the atomic structure of Si(111)-7×7 had been achieved.[115–117] A six-fold symmetry, as predicted by Low Energy Electron Diffraction experiments, was confirmed.[115–118] This six-fold symmetry can be clearly seen in STM images such as in figure 3.15(a).

The observed structure is best described by the Dimer-Adatom-Stacking (DAS) model proposed by K. Takayanagi et al. in 1985.[118] The DAS model has nine dimer atoms, twelve adatoms and a stacking fault layer to make up the 49 atom structure. The twelve adatoms can be identified in the STM image, figure 3.15(a). Figure 3.15(c) shows a schematic of the DAS model. The 7×7 unit cell consists of two halves, one of which has a stacking fault (the faulted half), the other with no fault (unfaulted half). Each half has nine dangling bonds, one on each of the six adatoms and one on each of the three rest atoms. In addition there is a dangling bond at each corner hole site. These highly reactive dangling bonds provide natural bonding sites, therefore molecules on the Si(111)-7×7 surface predominantly bond at these dangling bond sites.[118, 119] As shown in figure 3.15(c) it is possible to identify the adatoms as either corner or middle. It is the dangling bond sites that make up an STM image of Si(111)-7×7, therefore the STM can identify where a molecule prefers to bond by the change in height, caused by the presence of a molecule, of each dangling bond site. With a positive bias, empty states image, the twelve adatoms are imaged, as seen in figure 3.15(a). If a negative voltage is

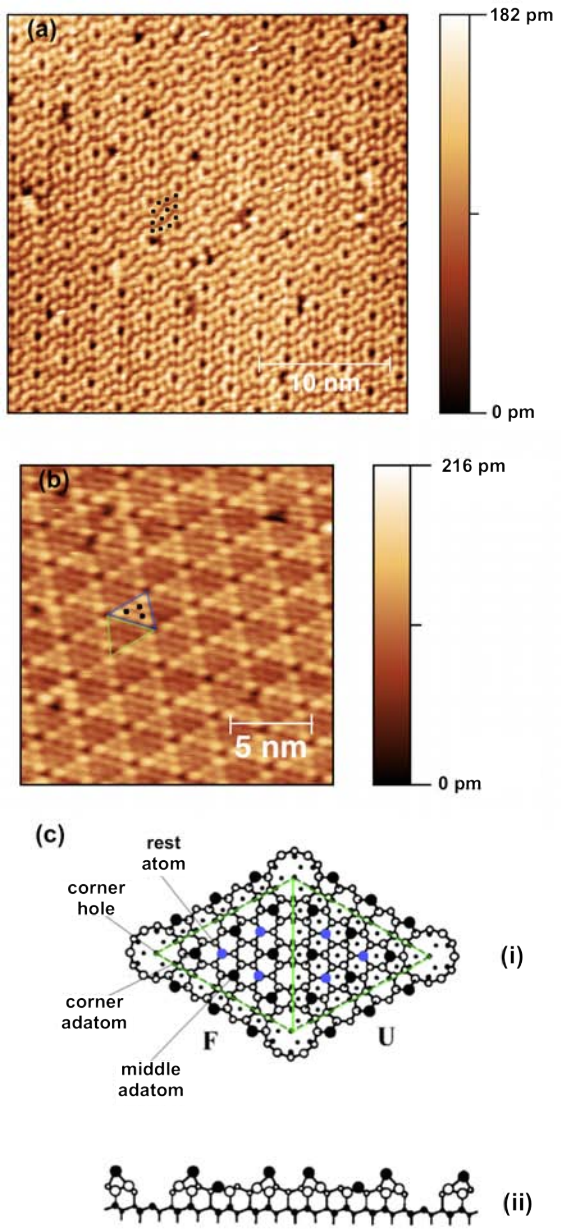

FIGURE 3.15: (a) Empty states STM image of the Si(111)-7×7 reconstruction taken, by the author, using the Omicron STM1 system (25 nm by 25 nm, 1.5 V, 120 pA). The black dots mark the 12 adatoms of the 7×7 unit cell (b) Filled states STM image of the Si(111)-7×7 reconstruction taken using the Omicron STM1 system. The difference between the faulted (blue triangle) and unfaulted (red triangle) half is clear with the unfaulted half appearing higher, i.e. the density of filled states is higher (20 nm by 20 nm,-1.5 V, 120 pA) . The black dots denote the positions of rest atoms in the 7×7 unit cell but the image quality makes resolving the rest atoms from the adatoms difficult. (c) The DAS model of the Si(111)-7×7 surface. (Adapted from reference [118]) (i) Top view. Filled circles mark the adatoms and blue filled circles the rest atoms, the green line marks the two halves of the 7×7 unit cell. In the top view the positions of the 12 adatoms and 6 rest atoms of the top layer are clear, also clear are the hole sites in each corner. (ii) Side view. The 49 atom unit cell, discovered by LEED measurements, is actually two layers, with the 12 adatoms on top. [118][119]

applied, the filled states are imaged, and contributions from the rest atoms are visible, as shown in figure 3.15(b).

The disulphide bond is known to play a key role in protein folding and in the stability of proteins.[120–122] Disulphide bonds are employed in the pharmaceutical industry for the stabilisation of synthesised proteins.[76] Synthesised disulphide bonds tend to suffer from oxidation reactions more than those found in nature, hence a greater understanding of the nature of disulphide bonding is needed.[76, 121, 123]

Many molecules contain a disulphide bond, for this thesis the molecule methylphenyldisulphide ($C_6H_5SSCH_3$), shown in figure 3.16, was chosen for its similarity to the Chlorobenzene molecule. The interaction of the benzene ring, which is similar to the phenyl ring, with the Si(111) surface is well understood thanks to work by Sloan et al.[70] The Si(111)-7×7 surface was dosed with the molecule methylphenyldisulphide at room temperature, as discussed in chapter 2.5 and, by varying the imaging voltage and dose parameters, the range of products produced upon reaction with the surface is examined.

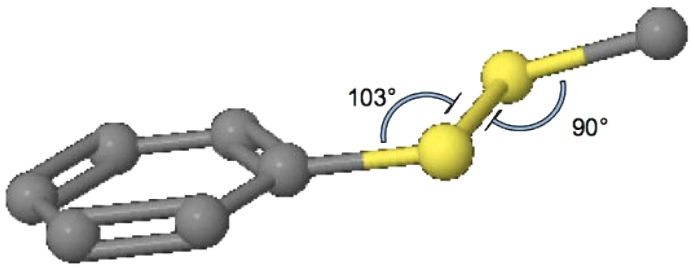

FIGURE 3.16: A 3D model of a methylphenyldisulphide $C_6H_5SSCH_3$ molecule. Carbon atoms are grey, the Sulphur atoms are yellow and Hydrogen atoms are not shown. The C-S bond length is 1.8 Åand the S-S bond length is 2.05 Å.[124]

3.2.1 Results and Discussion: Adsorption of Methylphenyldisulphide on Si(111)-7×7

After repeated freeze/pump/thaw cycles, as described in chapter 2.5, the molecule, methylphenyldisulphide (MPDS), was backfilled into the UHV system using a leak valve, see figure 2.14 in chapter 2.5.

Figure 3.17 shows a typical STM image (25 nm by 25 nm, 1.5 V, 120 pA) taken after the system was dosed with MPDS. Two features stand out, darkened adatoms and bright features.

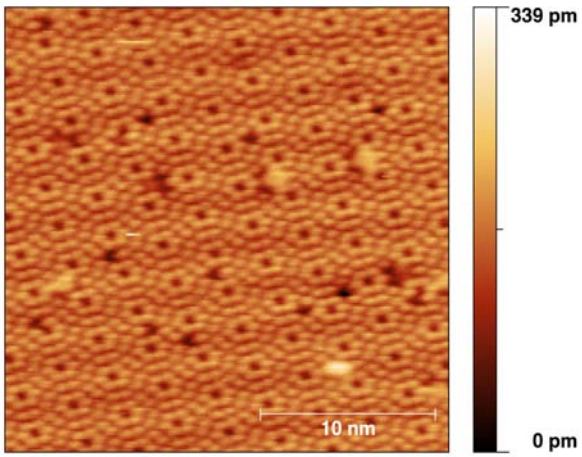

FIGURE 3.17: STM image of Si(111)-7×7 dosed with the molecule methylphenyldisulphide.

Comparing to published work of similar molecules it would be expected that either the whole molecule will bond to the surface through the phenyl ring, as chlorobenzene bonds through the benzene ring,[70, 125] or the disulphide bond will split and the two products, $C_6H_5 - S$ and $S - CH_3$, will bond via the sulphur atoms which has been observed with diphenyldisulphide as discussed in chapter 1.2.4.[81]

In the case of a split disulphide bond the $C_6H_5 - S$ product may bond through the phenyl ring.[70, 125]

Before characterising the molecule on the surface it is important to characterise the surface itself. In the reconstructed surface it is not uncommon for atoms to be missing from the surface layer, these are defects in the surface and appear as dark spots where a bright atom is expected according to the Si(111)-7×7 reconstruction, see figure 3.15. If a molecule bonds to an atom on the surface it is likely to make that atom appear darker. It is therefore important to know the density of defects before introducing the molecule to the system. This has been done by manually counting defects on 20 images each with a scan size of 60 nm by 60 nm. The result is that 0.098 defects per unit cell are expected for this particular Si sample. There is no preference for defects to be on either corner or middle adatoms.

Upon dosing the system with the methylphenyldisulphide molecule six features can be seen on the Si surface:

1. Missing adatom defect-like features.
2. Individual bright adatoms.
3. A pair of bright adatoms.
4. Individual darker adatoms.
5. A pair of darker adatoms.
6. Multiple dark adatoms, i.e. three or more adjacent adatoms.

These features are identified in figures 3.18 and 3.19. Comparing to published data for similar molecules[70, 81, 125], bright atoms are most likely to be a sulphur bond to the surface, pairs of bright atoms are likely a signature for disulphide fission where the disulphide bond is split upon landing, and both sides of the molecule immediately bond to the surface. Single bright atoms suggest that one half migrated relative to the other, perhaps suggesting the disulphide bond splits before landing. Dull atoms suggest the whole molecule is bonded in some way, and the different configurations of dull atoms may be different bonding geometries or a clustering of individual molecules.

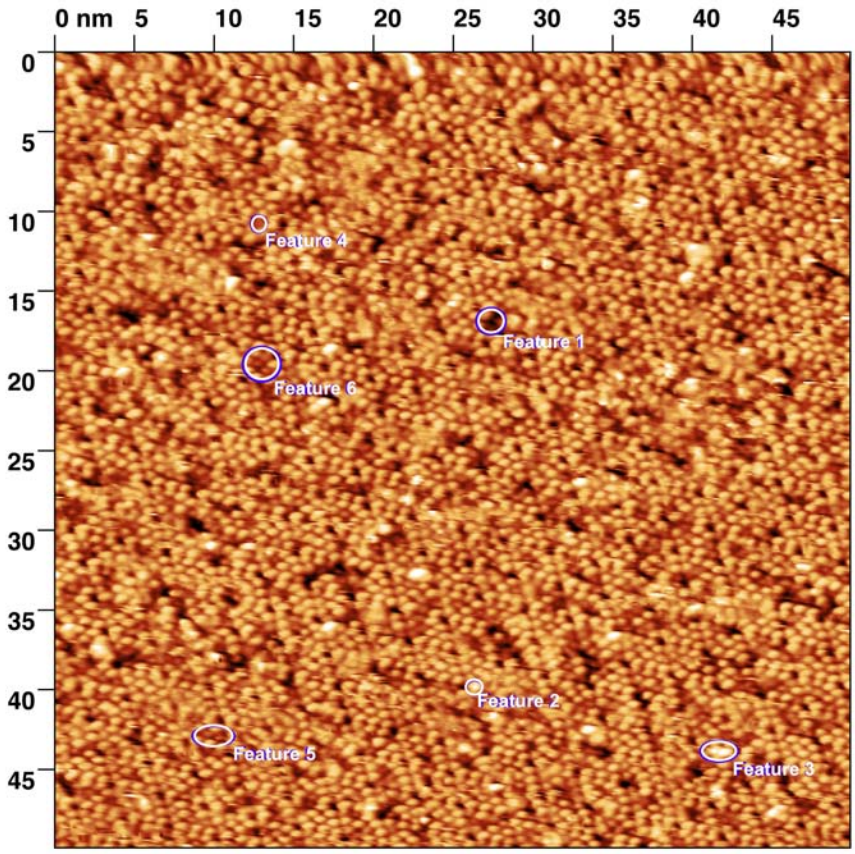

FIGURE 3.18: In this STM image (50 nm by 50 nm, 1.5 V, 120 pA) some examples of features 1-6 are highlighted. Feature 1 is missing atoms. Feature 2 is individual brighter atoms. Feature 3 is a pair of brighter atoms. Feature 4 is individual dull atoms. Feature 5 is a pair of dull atoms. Feature 6 is multiple dull atoms, i.e. three or more adjacent atoms.

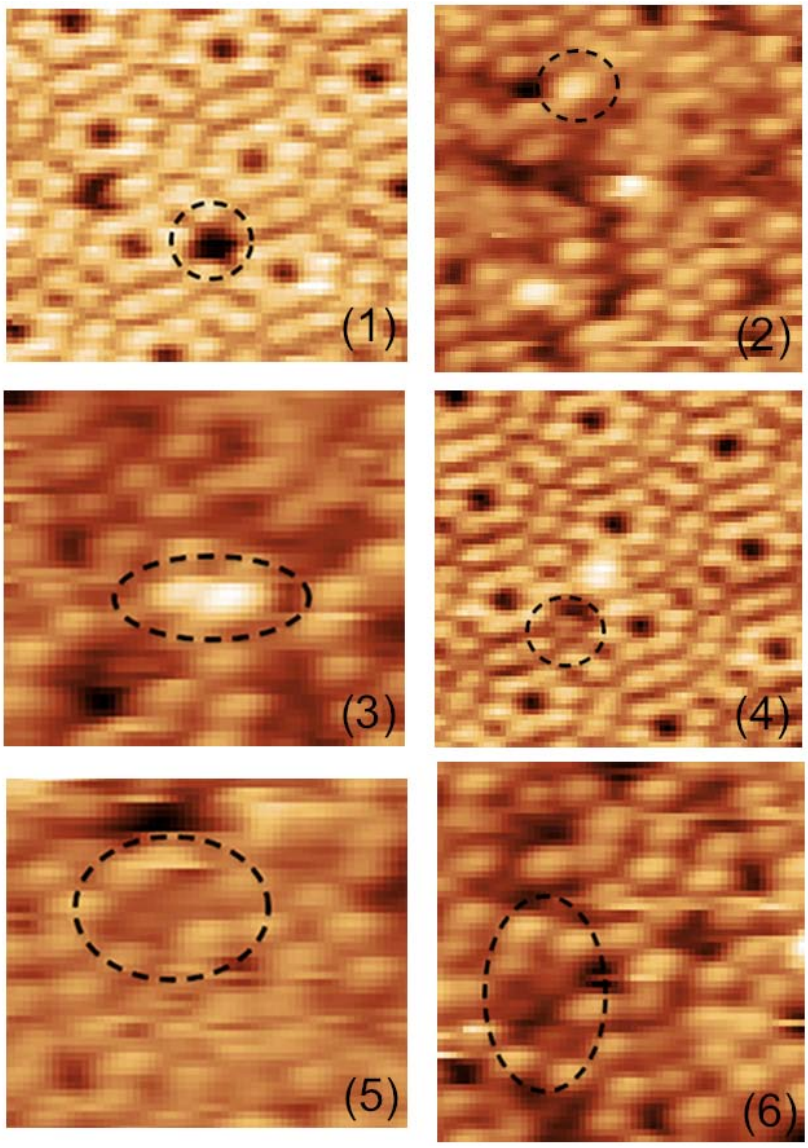

FIGURE 3.19: Some more examples of features 1 - 6, images cropped from larger images similar to the image shown in figure 3.18.

Three different doses of the molecule methylphenyldisulphide were studied in order to explore the change in feature density with dose which, as discussed in chapter 1.2.4, enables conclusions to be drawn about the nature of features in STM images and the bonding of the molecule. The doses were:

1. 130 s at a pressure of 2.1×10^{-9} mbar.
2. 95 s at a pressure of 2.5×10^{-9} mbar.
3. 35 s at a pressure of 2.5×10^{-9} mbar.

Molecular doses are normally represented in Langmuir, L. One Langmuir is defined as the dose required to form one layer of molecules on a surface assuming a sticking coefficient of one, i.e. assuming every molecule sticks when it hits a surface, 1 L = 1×10^{-6} Torr s. One Langmuir corresponds 1×10^{-9} for 750 s. The doses used in Langmuir are therefore (1) 0.321 L, (2) 0.284 L and (3) 0.105 L respectively.

Table 3.2 shows the number of features per unit cell for each type of feature.

TABLE 3.2: The density of features 1-6, number per 7×7 unit cell, as identified in figure 3.18, were manually counted from STM images for three different molecular doses.

Dose (L)	0.105 ±0.005	0.28 ± 0.01	0.321 ± 0.001
Feature 1 (per unit cell)	0.10 ± 0.01	0.10 ± 0.01	0.100 ± 0.009
Feature 2 (per unit cell)	0.052 ± 0.002	0.020 ± 0.001	0.027 ± 0.001
Feature 3 (per unit cell)	0.105 ± 0.006	0.100 ± 0.01	0.060 ± 0.004
Feature 4 (per unit cell)	0.037 ± 0.001	0.015 ± 0.001	0.080 ± 0.006
Feature 5 (per unit cell)	0.012 ± 0.002	0.015 ± 0.001	0.18 ± 0.02
Feature 6 (per unit cell)	0.000 ± 0.001	0.035 ± 0.001	0.11 ± 0.01

No adatom preference is found for the bright features or the pairs of dull adatoms, but the dull single adatom features seem to prefer the middle adatom with a ratio of $\approx$ 2:1. Figure 3.20 plots the density of each type of feature as a function of the dose. The most obvious conclusions are that the defect like features, feature 1, do not appear to be molecules as the number is constant and are, therefore, just defects. The dull features increase with increasing dose while the bright features do not seem to change as much. It may be that the majority of bright features are molecules deposited by the tip (discussed later) and therefore this number may be fairly consistent despite the dose. This would suggest that the dull features are the molecular adsorbates. Middle adatom site preference for single dull adatoms, feature 4, suggests that the molecule enters a precursor state upon landing on the surface and is then able to find it's minimum energy position. The fact that pairs of dull adatoms, feature 5, do not have a preference of adatom site suggests a different bonding geometry that does not have a precursor state, or perhaps a tendency to cluster in the precursor state before final adsorption. This may explain the dramatic increase in multiple dull atoms found together for increased dose.

Feature 5 is seen to increase more than features 4 and 6 with increasing molecular dose which suggests that this is a preferred bonding geometry. Figure 3.21 shows possible bonding geometries for features 4 and 5. Feature 4 appears as a darker adatom, it is probable that this is a product of the fission of the disulphide bond. The molecule is most likely to split at the disulphide bond than anywhere else.[81] This suggests that the two products SCH_3 and C_6H_5S are the most common fission products. The appearance of C_6H_5S would be similar to Chlorobenzene which

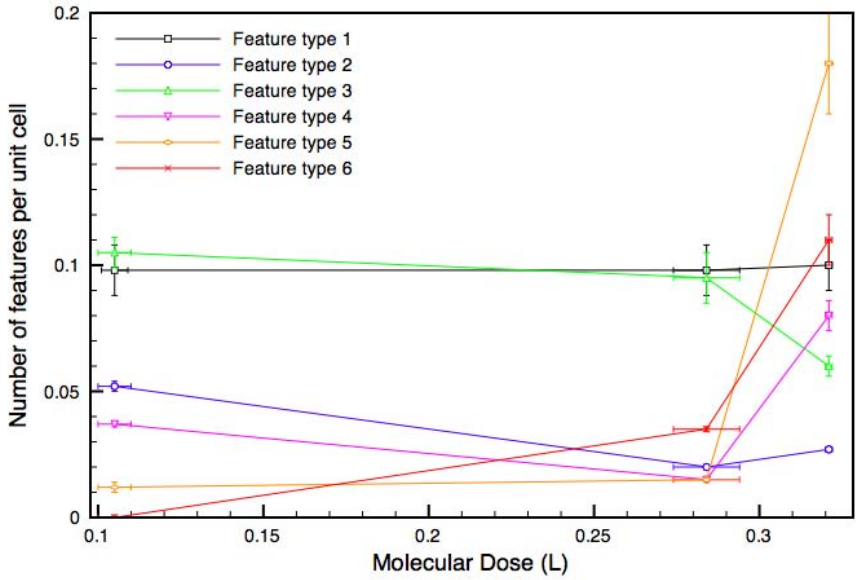

FIGURE 3.20: Density of features 1-6, as identified in figure 3.18. Feature type 1, the defect like feature is not seen to change with dose and remains similar to clean Si(111)-7 × 7. An overall increase is seen for feature types 4-6, the number of dull atoms, as the molecular dose is increased.

appears as a dark adatom adjacent a darker adatom at voltages between 1–2 V.[70] This suggests the single dark atom is most likely SCH_3 and not C_6H_5S. The double dull atom feature, feature 5, may well be the full molecule or C_6H_5S as a product of the fission of the disulphide bond. However, if it were the C_6H_5S product then the feature expected would be more like a chlorobenzene feature and the density per unit cell of the feature would be expected to track that of the other fission product feature 4 in figure 3.20. As the denisty per unit cell of feature 5 increases more rapidly with increasing dose than feature 4 in figure 3.20 it is unlikely to be a fission product related to feature 4 and is assumed to be the full molecule $C_6H_5S_2CH_3$. It is possible that the phenyl ring will bond as the benzene ring of chlorobenzene does,[70, 81] whilst the CH_3 bonds to the surface through the carbon atom and the disulphide bond twists accordingly. However,

it could be that a sulphur atom is instead involved in the bonding. Feature 6, which is multiple darker atoms clustered together, may be due to the clustering of molecules while in the precursor state, however, as the density as a function of dose of feature 6 tracks the trend of the single atom features, feature 4, in figure 3.20, it may be that these multiple atoms are due to fission products next to each other.

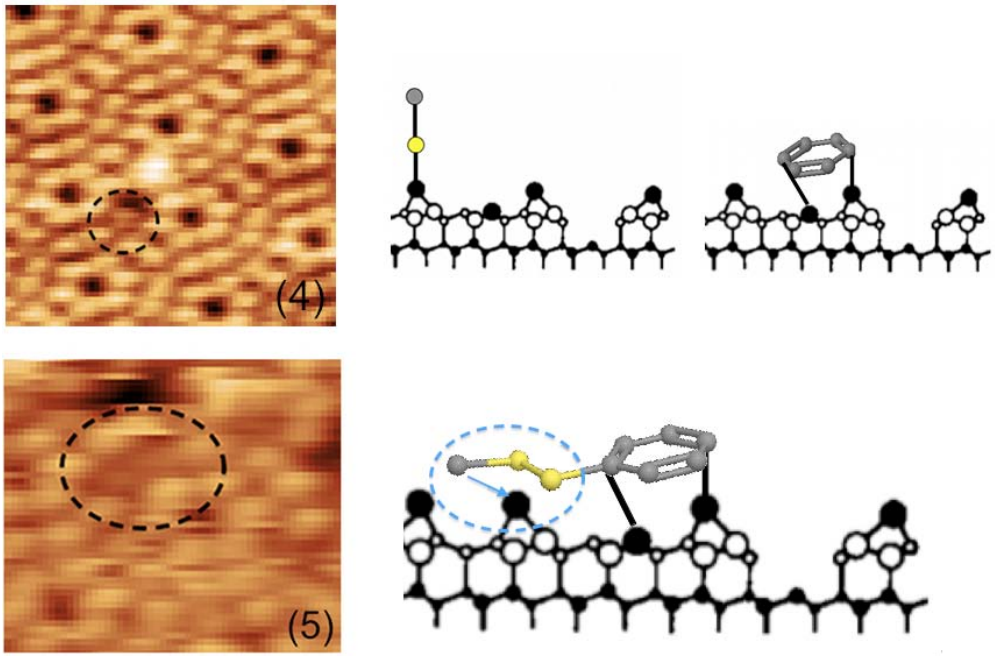

FIGURE 3.21: Features 4 and 5, the dull adatom and the adjacent dull adatoms with suggested bonding configurations represented on half Si 7×7 unit cell. The yellow balls represent sulphur and the grey balls represent the carbon. Feature 4 is most likely due to products of the fission of the disulphide bond. Feature 5 is most likely the entire molecule, with the part circled with blue dashed line twisting and bonding through the carbon as indicated by the arrow. The bonding geometries shown are estimated on assumptions that the molecule will bond in a similar way to chlorobenzene calculated by Cao et al.[126]

3.2.2 Results and Discussion: Deposition of Molecules from an STM Tip

In experiments where the UHV system, described in chapter 2.5, has been dosed with the molecule, methylphenyldisulphide, the molecule has been found to readily attach to the tip. This is seen as the tip appears to deposit features on the surface. These bright features are not seen to increase when the system has not had any molecule introduced and the tip and sample are clean. Figure 3.22 demonstrates the increase in bright features that occurs in consecutive images.

A molecule bonded to the surface appears as a darker atom but if the molecule is weakly bonded to the surface it could appear as a brighter i.e. higher feature on the surface, therefore the first assumption that could be made is that the tip excites the molecule from a strongly bonded, chemisorbed state to a weakly bonding physisorbed state. However this was tested by dosing the UHV system with the molecule and then cleaning the surface. When the surface has been cleaned there should be no molecules present, therefore no dark features or bright features should be observed upon scanning. No dark features were observed, confirming a clean surface but the increase in bright features was still observed. Therefore the bright features are molecules that have reacted with the tip and then are deposited on the surface during imaging, see figure 3.23.

In order to see the continual increase in bright features seen in figures 3.22 and 3.23, there must be a large reservoir of molecules on the tip created upon dosing the system. The most likely cause is the splitting of the disulphide bond upon contact with the Tungsten tip. The tip could then become coated, or passivated,

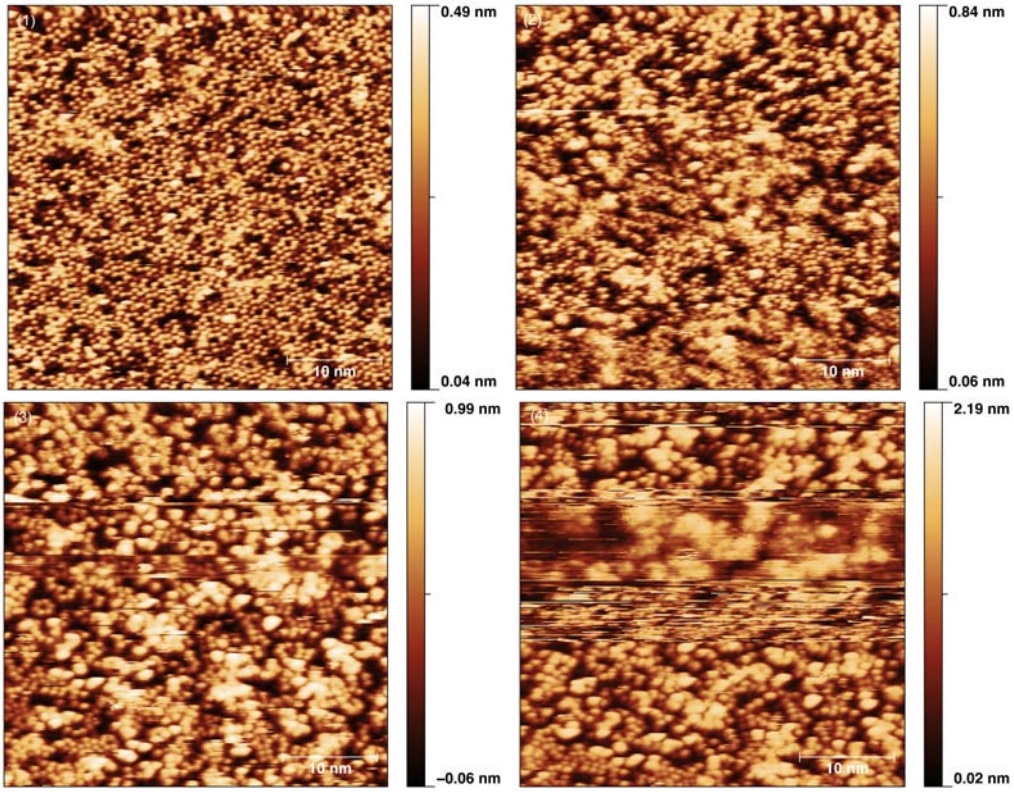

FIGURE 3.22: The four images presented here are sequential images. The voltage for these images is 1.27 V with a tunnelling current set to 40 pA, a low current was used to try to avoid any possibility of mechanical interaction between the tip and the molecules adsorbed on the surface. An increase in bright features and overall height of the sample is observed, suggesting a build up of material on the surface. The dose of molecules here was 130 s at 2.1 $\times 10^{-9}$ mbar.

with the products of the split molecule, $C_6H_5 - S$ and $S - CH_3$, further molecules may then weakly bond, perhaps not splitting, which then readily fall off the tip.

The molecular products from the tip appear bright on the surface and not dark as the molecule adsorbed upon initial dosing. This means that the state of the molecule is different. If the molecule splits upon reacting with the tip, then the products could be expected to be dipoles which would then be affected by the field between the tip and sample. This hypothesis is supported by the voltage dependence of the amount of white features seen in experiments, shown in fig 3.24. Below

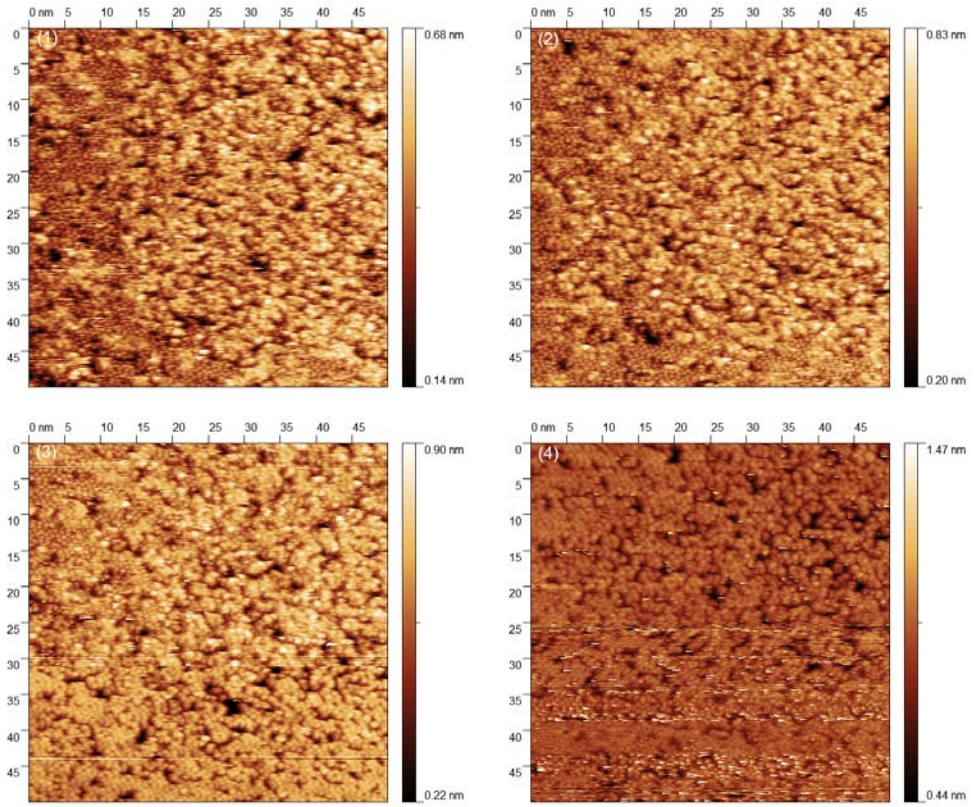

FIGURE 3.23: The four images presented here are sequential images taken with a voltage of 1.04 V and a tunnelling current of 120 pA. The system has been dosed with the molecule MPDS and the sample has been cleaned by resistive heating before scanning. Even though there is no molecule on the sample from initial deposition a build up of bright features is still seen. The dose of molecules in this experiment was 105 s at 2.5×10^{-9} mbar.

1.5 V the amount of bright features does not appear to increase dramatically but above 1.5 V a large increase is seen in subsequent images. This would suggest a similar situation to dipped pen lithography where molecules are picked up with a tip, normally an Atomic Force Microscope (AFM), and are then deposited at specific places on a surface. In electrochemical AFM the bonding of a molecule to the surface is modified by the application of a field between the tip and sample. This modification of bonding by application of a field may explain why the molecules from the gas phase appear dark while the molecules from the tip appear bright,

for example $C_6H_5 - S$ is a dipole and as such may be aligned in the field between the tip and sample forcing the bonding geometry upon deposition. [127–130]

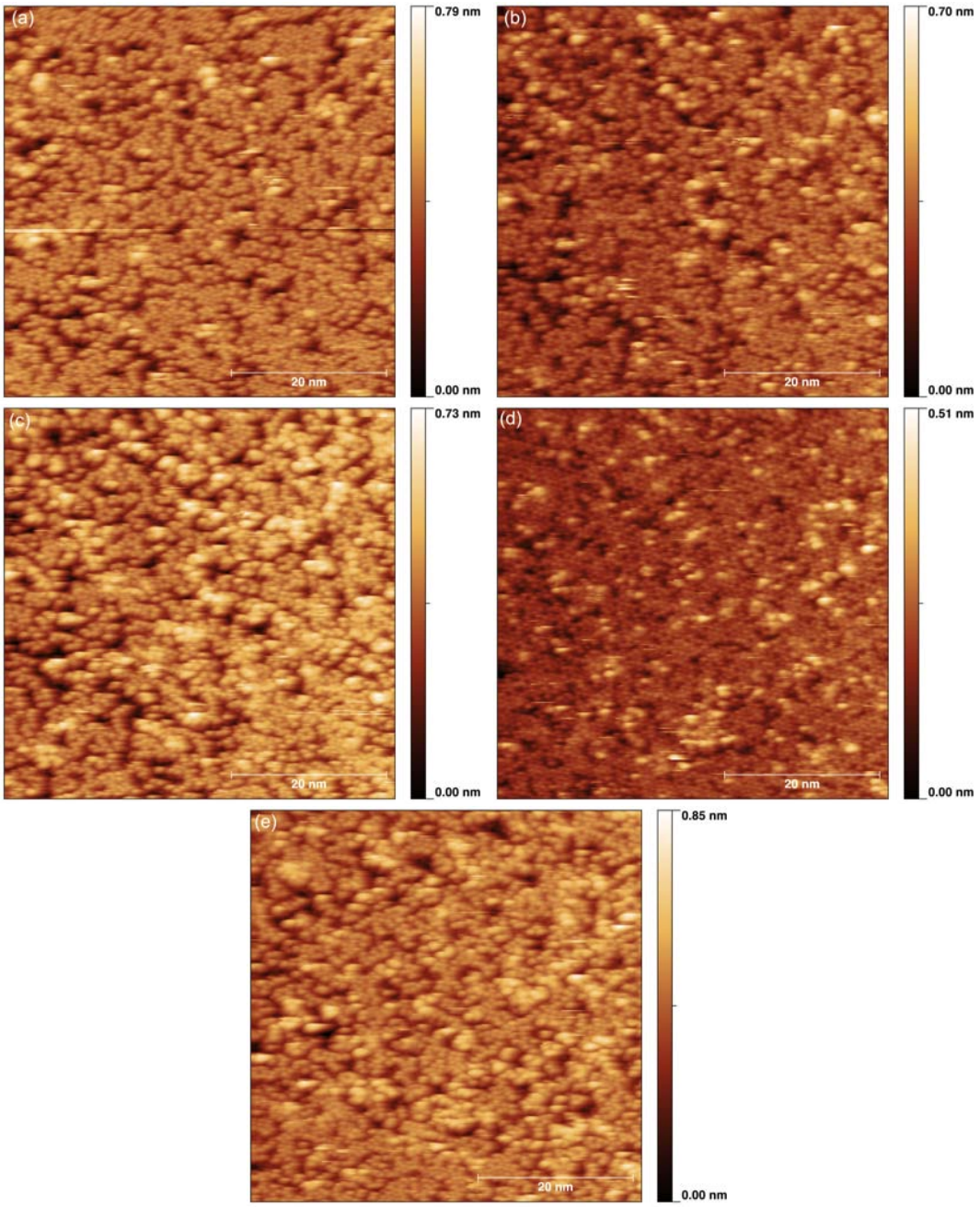

FIGURE 3.24: Images a-c are the same area. In the first image the voltage applied is 1.20 V, for the second image this is increased to 1.5 V, in the third image the voltage is reduced back down to 1.20 V. Images d and e are taken from the same area, a different area from a-c. In the fourth image the voltage is 1.89 V, in the final image the voltage is reduced to 1.19 V. In all images the tunnelling current is 22 pA.The dose of molecules in this experiment was 130 s at 2.1×10^{-9} mbar, the base pressure being 2.5×10^{-10} mbar.

Chapter 4

Scanning Probe Electron AnalyseR (SPEAR)

The Scanning Probe Electron Analyser (SPEAR) is a technique under development that aims to combine photoelectron spectroscopy and scanning tunnelling microscopy. It has already been discussed, in chapter 1, that the mapping of electronic states at the nanometre scale is a very attractive prospect. First photoelectron spectroscopy will be reviewed, then, the technique chosen to achieve nanometre resolution will be discussed.

4.1 Photoelectron Spectroscopy (PES)

Spectroscopy is used to determine the nature of the energy levels of a sample or subject by studying the transition of electrons from one orbital to another. These transitions are induced by either the emission or absorption of a quanta of energy in the form of an electron or photon.[14]

Photoelectron spectroscopy relies on the photoelectron effect first observed by Heinrich Hertz in 1887. In 1905 Einstein produced a mathematical and physical description of how photoemission was due to the absorption of photons. In Einstein's theory, the energy of emitted photoelectrons depends linearly on photon frequency and is independent of photon intensity. In 1915 Robert Millikan showed this linearity experimentally and in 1921 Einstein was awarded the Nobel prize for his explanation of the photoelectric effect.[14, 15, 17, 18]

To understand the photoelectric effect first consider an electron sitting at an energy below the Fermi level, E_F, in a metal. To detect an electron away from the metal, enough energy has to be supplied to remove the electron from the metal. The work-function, Φ, of a metal is the minimum energy required to promote an electron sitting at the Fermi level to the vacuum level.

An electron that has escaped to the vacuum due to photon absorption is known as a photoelectron. This photoelectron will have a kinetic energy, T, which can be measured and is given by equation 4.1.

$$T = \hbar\omega - e\Phi - E \tag{4.1}$$

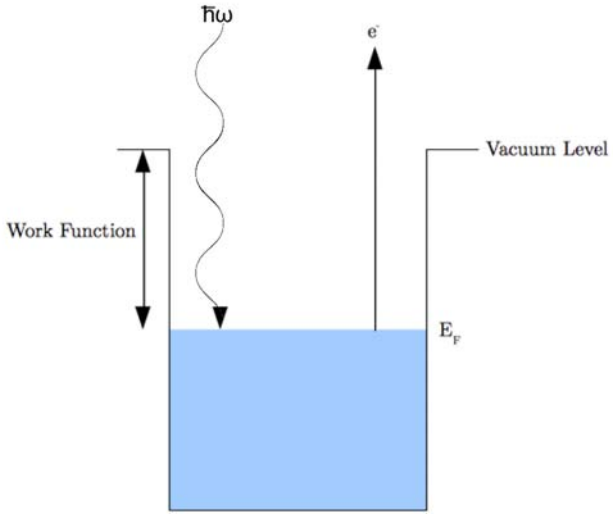

FIGURE 4.1: A photon with energy, $\hbar\omega$, can excite an electron from the sea of electrons below the Fermi level, E_F, if the energy is larger than the sum of the workfunction and the energy difference between the initial state of the electron and E_F. At the simplest level, if this requirement is met an electron can escape to the vacuum level, from where it might be detected in a photoelectron spectroscopy experiment.

where E is the electron energy below E_F, $\hbar\omega$ is the energy of the photon and $e\Phi$ is the energy required to escape into the vacuum from E_F. Since $e\Phi$ and $\hbar\omega$ are known, measuring T provides information about the energy distribution of electrons in a system. If $e\Phi$ is unknown then T would give the energy distribution relative to the vacuum level and $e\Phi$ could be found from the Fermi-edge cut-off observed in the spectra.[14, 15, 17–19, 131]

Photoemission can occur if two conditions are met:[19]

1. The initial state and the final state conserve the wave-vector, k, and are separated by energy $\hbar\omega$. i.e. $E_f(k) - E_i(k) = \hbar\omega$ where i denotes the initial state and f the final state.

2. The energy of the final state corresponds to the energy, T, at which the electrons are collected. i.e. $E_f(k) - e\Phi = T$

The two conditions ensure the conservation of both energy and momentum.

The three-step model, discussed in more detail in section 4.3 and shown in figure 4.2, describes the process of photoemission. The first step is the photoionisation itself where a photon is absorbed and an electron excited. In the second step the electron travels through the sample to the surface, during which secondary electrons may be produced. These secondary electrons are generated by the interaction of the excited electron travelling to the surface with other electrons in the sample. If the excited electron has enough energy, in much the same way as the photon excites electrons, this electron can excite further electrons. Finally the electron escapes into the vacuum and is detected.

A typical photoemission experiment consists of just three components, (I) a source of monochromatic photons, for example a He discharge lamp or a synchrotron source, which illuminate (II) a sample of interest, photoelectrons from the sample are then analysed with respect to kinetic energy and possibly angle by (III) an electrostatic analyser. Typically experiments are performed with the analyser or detector at a set angle, or the angle may be varied within a range of angles and such experiments are said to be angle resolved. If a detector has a large acceptance angle experiments would not be angle resolved. The acquired spectrum may depend on the angle if the sample is a crystal, in which case it may be possible to resolve the DOS of individual planes in an angle-resolved experiment.[14–19, 131] A typical set-up is shown in figure 4.3.

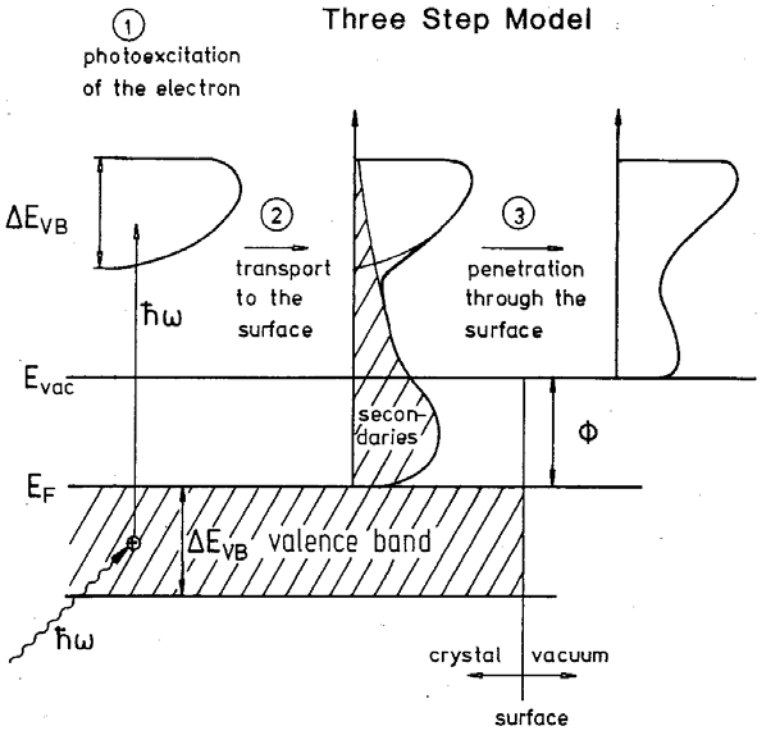

FIGURE 4.2: Photoelectron spectroscopy can be viewed as a three step process: (1) photoexcitation of electrons; (2) travel to surface with associated production of secondary electrons; (3) escape into the vacuum and detection. Figure from reference [17]

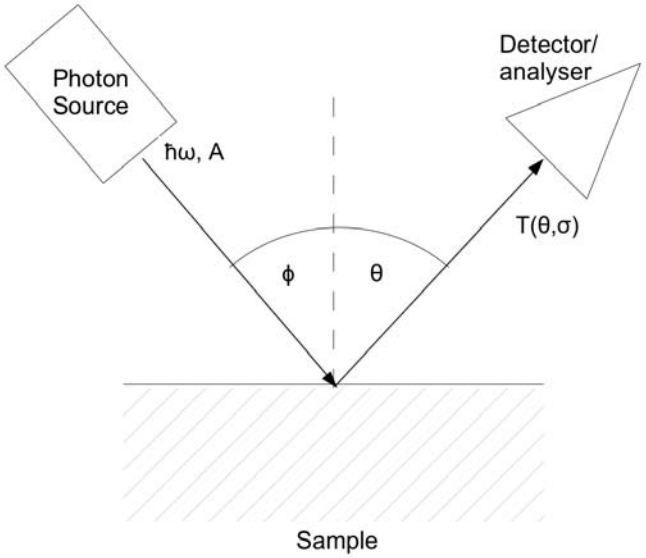

FIGURE 4.3: Monochromatic photons with energy, $\hbar\omega$, (A is the vector potential of the electromagnetic field) impinge upon a sample with angle, ϕ, with respect to the surface normal. The kinetic energy, T, of the photoelectrons should be analysed as a function of the experimental parameters, for example emission angle, θ, or spin orientation σ, by an electrostatic analyser.[14–19]

Figure 4.4 shows a simple view of the energetics of a photoemission experiment. Here photons excite electrons from a metal and the resultant spectrum of the photoelectrons measured at the detector is simply an image of the occupied DOS of the sample.[16, 17]

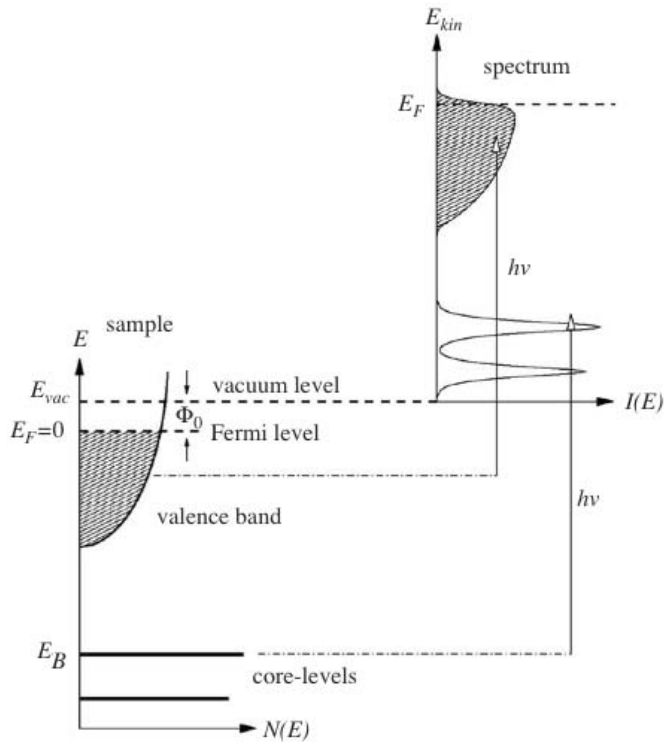

FIGURE 4.4: Electrons from a state with binding energy, E_B, are excited above the vacuum level by photons with energy greater than the sum of the binding energy of the originating state and the work function of the metal. The photoelectron distribution, $I(E_{kin})$, is to first order, an image of the occupied density of states, $N(E_B)$, of the sample. The apparent broadening of the features in the spectrum is due to the resolution of the detector. Figure from reference [17].

To obtain a valence band spectrum Vacuum Ultra Violet (VUV) energies are used to maximise the energy and momentum resolution, as x-ray energies are not required simple noble gas discharge lamps can be used which provide a narrow line width of radiation and a high flux of photons.[16, 17] Figure 4.5 shows an angle-resolved spectra, taken with a photon energy of 21.2 eV, of a Cu(111) surface.

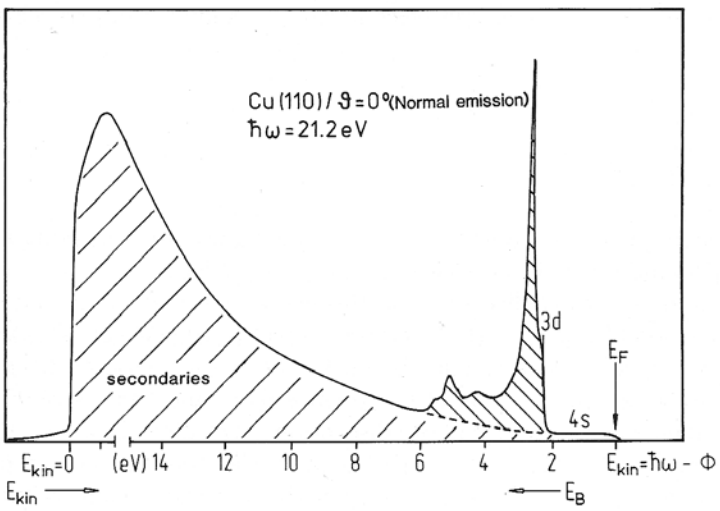

FIGURE 4.5: PES spectra of a Cu(111) surface, photon energy = 21.2 eV, spectra taken at normal emission and polar angle zero with respect to the surface normal. The 3d band of the Cu(111) surface is clearly resolved. A large secondary electron feature is observed. Figure from reference [17]

The structure of the 3d band between 2-6 eV below E_F is quite clear. Between 0-2 eV is the flat 4s band, although this is difficult to resolve from the background created by the secondary electrons. The secondary electron feature has a sharp cut-off at $E_{kin} = 0$, this cut-off energy can be used to measure the work-function using equation 4.1.[16, 17]

4.2 Photoemission

In the previous section the basic process of photoemission was described in order to explore spectroscopy, here a more rigorous treatment of the photoemission process relevant to PES, using VUV light, is presented.

The calcuation of the photocurrent measured, J, starts from the first-order time-dependent pertubation theory. Assuming a small perturbation, H_{PE}, the transition probability per unit time, w, between two N-electron states such as the initial state, i, with wave function, ψ_i, and the final state, f, with wavefunction, ψ_f, is given by equation 4.2.[16, 17, 131, 132]

$$w = \frac{2\pi}{\hbar}|\langle\psi_f|H_{PE}|\psi_i\rangle|^2\delta(E_f - E_i - \hbar\omega) \tag{4.2}$$

The perturbation operator, H_{PE}, describes the interaction of an electron with the electromagnetic field.[16, 17, 131]

The unperturbed Hamiltonian is given by:

$$H = \frac{p^2}{2m_e} + eV(r) \tag{4.3}$$

where p is the momentum operator, $p = -\hbar\nabla$, the scalar potential, $V(r)$, can be neglected by an appropriate choice of gauge.[16, 17, 131, 132]

H_{PE} is given by the transformation of the momentum operator $p \rightarrow p - \frac{e}{c}A$, where A is the vector potential of the electromagnetic field, such that:

$$H = \frac{1}{2m_e}[p - \frac{e}{c}A]^2 + eV(r) \tag{4.4}$$
$$= \frac{p^2}{2m_e} + \frac{e}{2m_e c}(A.p + p.A) + \frac{e^2}{2m_e c^2}A^2 + eV(r)$$
$$= H_0 + H_{PE}$$

the perturbation operator is therefore:

$$H_{PE} = \frac{e}{2m_e c}(A.p + p.A) + \frac{e^2}{2m_e c^2}A^2 \tag{4.5}$$

The quadratic term in A relates to two photon processes and is only relevant at high photon intensities.[131] $A.p + p.A = 2A.p + i\hbar(\nabla.A)$ and ignoring surface effects$\Delta\ A = \nabla.A = 0$.[16, 17, 131, 132] H_{PE} therefore becomes:

$$H_{PE} = \frac{e}{m_e c}A.p \tag{4.6}$$

For valence band photoemission from a crystal, the matrix element, $|\langle\psi_f|H_{PE}|\psi_i\rangle|$, is calculated by using the periodicity of the Bloch function with respect to the lattice vector, G.[16, 17, 131, 132] This results in a photocurrent, I, proportional to:

$$I \propto |\tilde{M}^1_{if}|^2\delta(k_{i\|} - k_{f\|} + G_\|)\delta(k_i - k_f + G)\delta(E_f - E_i - \hbar\omega)\delta(E - E_f + \Phi) \tag{4.7}$$

The matrix element in equation 4.7, is written as $\tilde{M}^1_{if}$ to indicate that momentum conservation is explicitly written out and that it is taken between Bloch states.[17, 131, 132]

Photoexcited electrons have a relatively short inelastic mean free path in the bulk of the solid. This can be taken into account by assuming a complex wave vector perpendicular to the surface:

$$k_\perp = k_\perp^{(1)} + ik_\perp^{(2)} \tag{4.8}$$

This smears the momentum conservation, and the photocurrent is modified as follows:

$$I \propto \frac{|\tilde{M}^1_{if}|^2}{(k_{i\perp}^{(1)} - k_{f\perp}^{(1)})^2 + (k_{f\perp}^{(2)})^2}\delta(k_{i\parallel} - k_{f\parallel} + G_\parallel)\delta(k_i - k_f + G)\delta(E_f - E_i - \hbar\omega)\delta(E - E_f + \Phi) \tag{4.9}$$

Equation 4.13 does not explicitly include electron-electron interactions. If electron-electron interactions are considered, the final hole state of the system is not merely a hole in a ground state created by photoionisation, but can be in any of, s, possible final states of the many electron system.[17, 18, 131, 132] In this case the final state of an N electron system can be written as:

$$\psi_f(N) = \phi_{f,E_{kin}}(k_f).\sum_s \psi_{f,s}(N-1) \tag{4.10}$$

and the initial state is given by

$$\psi_i(N) = \phi_i(k_i)\psi_i(N-1) \tag{4.11}$$

where the initial state $\psi_i(N)$ has the energy $E_0(N)$ and the final states, s, have energies $E_s(N-1)$.[17, 18, 131, 132]

The photocurrent from all possible states of the system is now given by:[16, 17, 132]

$$\begin{aligned} I \propto & \\ & \sum_{s,i} |\langle \phi_{f,E_{kin}} | \tilde{M}_{i,f} | \phi_i \rangle|^2 |\langle \psi_{f,s}(N-1) | \psi_i(N-1) \rangle|^2 \\ & \times \frac{1}{(k_{i\perp}^{(1)} - k_{f\perp}^{(1)})^2 + (k_{f\perp}^{(2)})^2} \\ & \times \delta(k_{i\parallel} - k_{f\parallel} + G_\parallel)\delta(k_i - k_f + G)\delta(E_f - E_i - \hbar\omega)\delta(E - E_f + \Phi) \end{aligned} \tag{4.12}$$

4.3 Photoemission: Three Step Model

The three step model, developed by Berglund and Spicer, is the most commonly used model.[16, 17, 132] It is a phenomenological model that splits the photoemission process into three parts, (I) the excitation of an electron, (II) the journey of the electron through the solid and (III) the escape of the electron into the vacuum. Whilst a more accurate model of photoemission is given by the one step model, the three step model in splitting each part, allows a detailed description of the phenomena involved.[16, 17]

A complication can arise in defining the wave vector, k. Band structures are often plotted in the reduced zone scheme, which means that the bands outside the first Brillouin zone are folded back in by adding an appropriate reciprocal lattice vector, G, see figure 4.6.[16, 17] In the reduced zone scheme an optical transition is 'vertical' if $k_i = k_f$. In the non-reduced or extended zone scheme $k_f = k_i + G$. In order to distinguish between the wave vector of the crystal itself and the wavevector of the photoexcited electron within the crystal they shall be denoted as k and K respectively, where $K = k_i + G$. If E_f is given as a function of the wavevector of the photoelectron the momentum can be denoted K_f. Outside the crystal the wave vector of the photoelectron is given by $p/\hbar$ where p is the electrons momentum in free space.

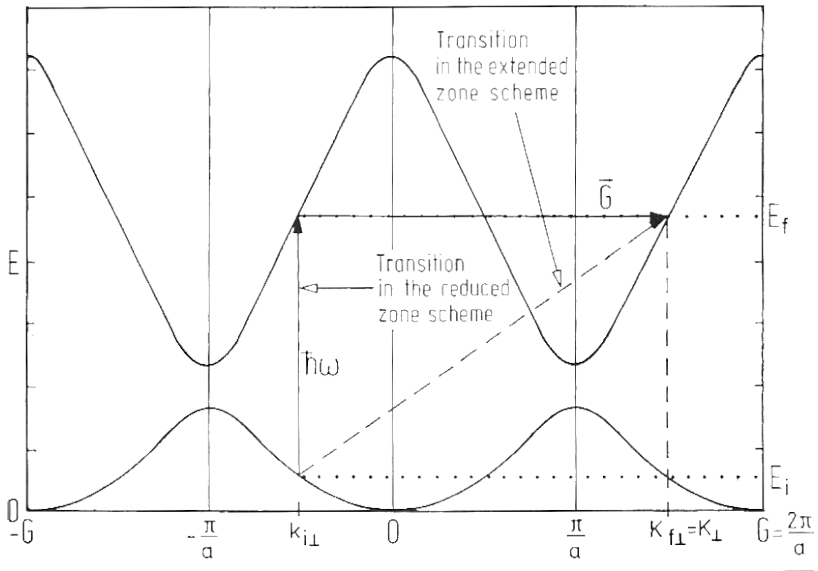

FIGURE 4.6: The transition of an excited electron in the reduced zone scheme is vertical, that same transition can be seen to be non-vertical in the extended zone scheme. In the extended zone scheme the transition occurs between two points connected by the reciprocal lattice vector, G. Figure from reference [17]

4.3.1 Step One: Photoexcitation

The electronic states of a solid are described by bands. Neglecting the momentum of the incoming photon, optical excitation of an electron is a vertical (momentum conserving) transition in the reduced zone scheme, see figure 4.7. After the electron has escaped into vacuum it has an energy dispersion relation as shown in figure 4.7(b).[16, 17]

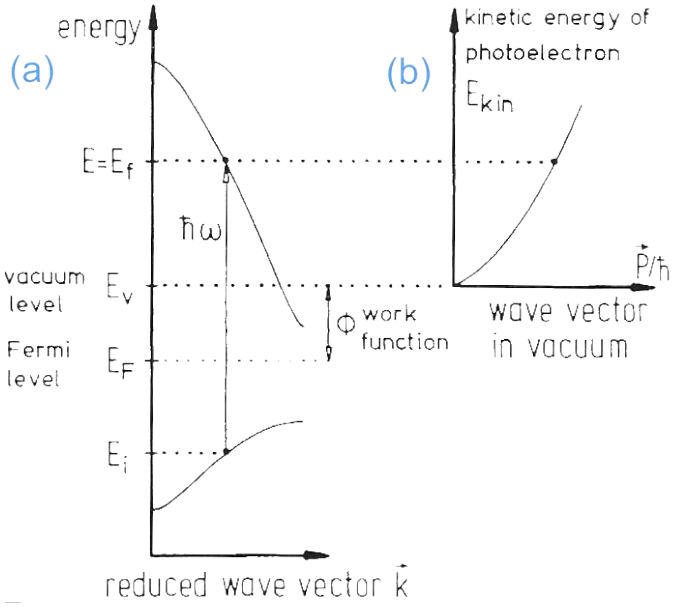

FIGURE 4.7: (a) An optical, photon excited, transition between two bands, the final state being above vacuum level, i.e. the electron escapes the solid into the vacuum. (b) The kinetic energy of an electron in the vacuum is a function of the wave vector $p/\hbar$. Figure from reference [17]

The internal energy distribution of photoexcited electrons $N_{int}(E, \hbar\omega)$, where E is the final kinetic energy, is given by equation 4.13 in the case of the reduced zone scheme:[16, 17]

$$N_{int}(E,\hbar\omega) \propto \sum_{f,i} |M^1_{fi}(k_i,k_f)|^2 \delta(E_f(k_f) - E_i(k_i) - \hbar\omega) \times \delta(E - [E_f(k_f) - \phi]) \quad (4.13)$$

where $E_f(k_f)$ and $E_i(k_i)$ denote the energies of the final bands $|f,k_f\rangle$ and the initial bands $|i,k_i\rangle$, respectively. $|M^1_{fi}(k_i,k_f)|^2$ is the square of the transition matrix element as given in equation 4.5.[16, 17]

The first delta function in equation 4.13 imposes the conservation of energy during the first (excitation step), while the second delta function ensures that the kinetic energy, once the electron has left the sample, equals the final state energy minus the work function.[16, 17]

4.3.2 Step Two: Transport of Electrons to the Surface

Electron-electron interactions dominate the scattering of electrons and reduce the total number of photoelectrons that reach the surface. If the scattering frequency, $1/\tau$ where τ = lifetime, is isotropic and depends only on E, the electron inelastic mean free path $\Lambda(E,k)$ is given by equation 4.14:[16, 17, 132]

$$\Lambda(E,k) = \tau v_g = \frac{\tau}{\hbar}\frac{dE}{dk} \tag{4.14}$$

where v_g is the group velocity in the final state. The transport of the photoelectrons can be described classically by a coefficient, $d(E,k)$, which describes the total number of photoelectrons created within one mean free path, Λ, from the surface. The coefficient $d(E,k)$ is given by equation 4.15:[16, 17, 132]

$$d(E,k) \simeq \frac{\alpha\Lambda}{1+\alpha\Lambda} \tag{4.15}$$

where α is the optical absorption coefficient of the light. These interactions with other electrons during transport to the surface generate a sea of secondary electrons.

4.3.3 Step Three: Escape of the Electron into the Vacuum

If the component of the electrons kinetic energy perpendicular to the sample surface is greater than the surface potential barrier, then an electron may escape into the vacuum, all other electrons will be totally reflected back into the bulk. This is known as the escape-cone argument. Inside the crystal an electron travels in a potential with depth $E_v - E_0$ where E_v is the vacuum level, and E_0 is the lowest energy of the valence band. According to the escape-cone argument an electron must have perpendicular kinetic energy, $K_\perp$, satisfying the condition given by equation 4.18 in order to escape into the vacuum.[16, 17]

$$(\frac{\hbar^2}{2m}K_\perp^2 \geq E_v - E_0) \tag{4.16}$$

The parallel component of the electrons wave vector should be conserved according to figure 4.8 such that:[16, 17]

$$\frac{p_\parallel}{\hbar} = K_\parallel = k_\parallel + G_\parallel \tag{4.17}$$

where p is the momentum of the photoelectron in the vacuum, $K_\parallel$ is the parallel component of the wave vector K.[16, 17]

The escape direction of an electron makes a larger angle with the surface normal outside the crystal than inside, as given by equation 4.18:[16, 17, 132]

$$k_{f\parallel} = \sin\theta(\frac{2m}{\hbar^2}E_{kin})^{1/2} = \sin\acute{\theta}[\frac{2m}{\hbar^2}(E_f - E_0)]^{1/2} \tag{4.18}$$

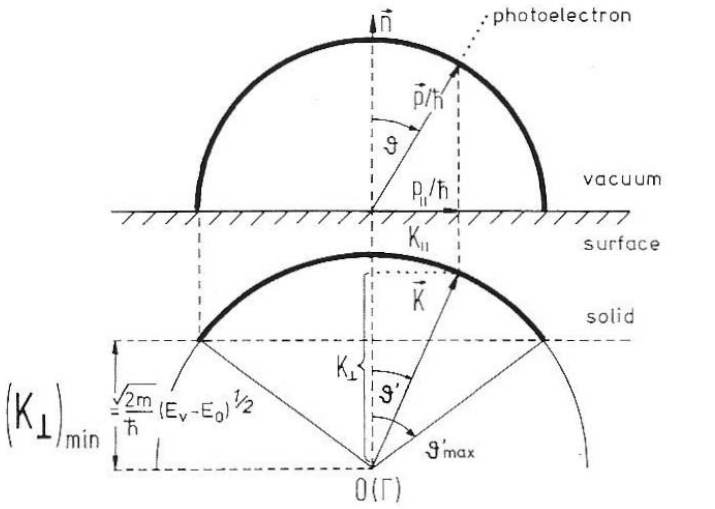

FIGURE 4.8: Escape conditions for a photoexcited electron. The thick solid lines show the internal and external escape cones for electrons with momentum on a circle with radius $|K|$ = constant and $|p|/\hbar$ = constant. Figure from reference [17]

where θ is the angle outside the sample and $\acute{\theta}$ is the angle inside the sample as shown in figure 4.8. For every final state energy, $E_f(\theta \leq \pi/2)$, there is a maximum angle, $\acute{\theta}_{max} < \pi$ /2, inside the sample, at which electrons excited inside the sample can cross the surface:[16, 17, 132]

$$\sin\acute{\theta} = (\frac{E_{kin}}{E_f - E_0})^{1/2} \tag{4.19}$$

The angular region $\acute{\theta} \leq \acute{\theta}_{max}$ is known as the escape cone. This can be taken further and in angular resolved spectra the originating wavevector can be calculated from the emission angle, experiments presented in this thesis are not angle resolved so it is sufficient to say that an excited electron can escape within a set range of angles.[16, 17, 132]

4.4 The Principle of the Scanning Probe Electron AnalyseR (SPEAR)

Photoelectron spectroscopy is, in general, a non-local technique. A spectrum will be an ensemble average of all the features on the surface within the spot size of the excitation source. There are two ways in which the spatial resolution of PES can be increased. The excitation beam can be focused or the analyser can be shrunk. It is non-trivial to focus a Vacuum Ultraviolet (VUV) beam, and to scan such a beam to create a spatially resolved map of electronic spectra would be even more complicated as all the optics would need to be very precisely controlled whilst managing any heating effects. The structure of a Retarding Field Analyser is however quite simple and seems a good candidate for shrinking. In its simplest form all that is required is a collecting layer, a retarding layer and preferably some shielding layer see figure 4.9 for a typical layout.

It has been demonstrated that it is possible to shrink such an analyser onto a microfabricated Si tip.[133–135] Work by Song et al showed that a microfabricated co-axial tip can be used as a field emitter for an Electron Energy Loss Spectroscopy (EELS) like experiment, multilayer tips have also been made.[133–135]

The principle, therefore, in the SPEAR technique is to use the tip of an STM as a detector in a photoelectron set-up. In the SPEAR, VUV light is shone upon the sample producing photoelectrons, which can then be retarded by a bias applied to the sample, and collected with the tip, see figure 4.10. Recall that for the nanograph STM the bias voltage is applied to the tip and the tunnelling current is measured between the STM tip and ground, here the retarding bias is applied

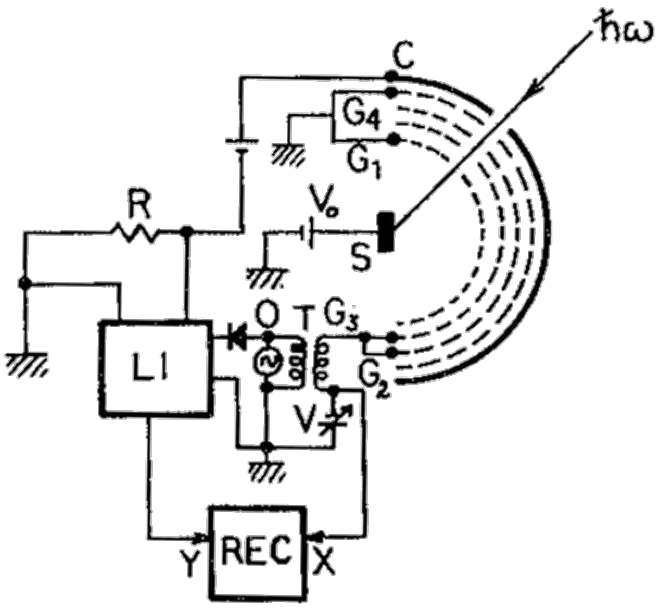

FIGURE 4.9: A retarding voltage V_R is applied to grids G_2 and G_3. There are two grids for the retarding voltage here for improved energy resolution. Grids G_1 and G_4 are grounded to provide a field free region between the sample and retarding grids. Photoelectrons of energy greater then eV_R are collected by the collector and give a current to the load resistor, R. The oscillator, O, adds a small modulation to the retarding field through transformer, T. This gives a modulation to the voltage drop across R, which is detected by a lock-in amplifier. [19]

to the sample and the photocurrent is measured at the tip, between the tip and ground using the same electronics but bypassing the feedback loop that would otherwise reposition the tip. Electrons generated at the sample by an incoming photon can exit with an angle governed by the escape-cone argument but, as the current is measured between the tip and ground, only those electrons reaching the tip contribute to the photocurrent signal, conversely, as the current is measured between the tip and ground, all electrons generated by a photon hitting the tip contribute to the photocurrent signal. By using a smaller detector better spatial resolution is achieved. However, spatial resolution should be enhanced by field

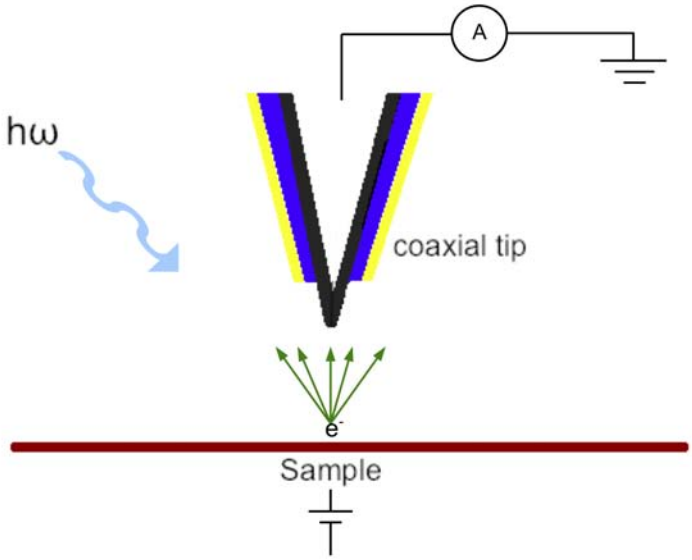

FIGURE 4.10: VUV light excites photoelectrons from a surface which are analysed with a microfabricated tip. In this case an open coaxial tip is shown. Electrons are collected by the central layer having been retarded by a field between the tip and the sample. The yellow outer layer is a shield layer which acts to avoid the collection of electrons from a wider area and also avoids the excitation of electrons from the tip. The blue layer is a dielectric separating the working layers. Here the voltage is applied to the sample and the current is measured at the tip wth comparison to ground as shown in figure 2.12 in chapter Experimental.

effects at the tip, it is expected that the photocurrent directly under the tip will be enhanced by the presence of the tip itself. Imagine the tip as a perfect conductor illuminated by light; by solving Maxwell's equations Crozier et al. and Novotny et al. showed that current must be induced at the end of the tip in order to satisfy the requirement that the tangential component of the electric field at the conductor surface is zero.[136, 137] Current induced in the tip generates a field with tangential components that are equal and opposite in magnitude to the incident field. The induced current must decrease in magnitude toward the apex of the tip to conserve charge but this leaves a net charge at the apex. This means there is a maximum in the surface charge density and therefore the normal component of the electric

field at the apex of the tip, see figure 4.11 as an example. This enhanced field directly under the tip should translate to an enhanced photocurrent under the tip, and, if the effect is strong enough, an enhanced spatial resolution.[136, 137]

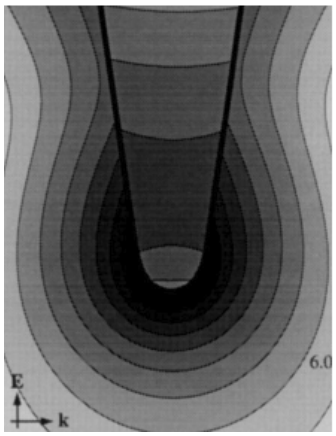

FIGURE 4.11: Simulations by Novotny et al show that for electromagnetic field of wavelength, $\lambda = 810$ nm there can be a large enhancement at the apex of a Au tip. Here the tip is illuminated from the side with the polarisation parallel to the tip axis. The contours are of E^2 (factor of 2 between successive lines). From reference [137].

In the SPEAR experiments the spectra are an angle-integrated measurement, in this case the spectra taken are directly proportional to the combined density of states (DOS). The combined density of states ($D(E, \hbar\omega)$) is given by:[16, 17]

$$D(E, \hbar\omega) = \frac{1}{(2\pi)^3} \sum_{i,f} \int \Omega_{fi}(k) \delta(E - E_f + \Phi) d^3k \tag{4.20}$$

where$\Omega_{fi}(k)$ defines a surface in k-space over which the density of states is integrated. The allowed transistions are selected by $\delta(E - E_f + \Phi)$ at photon energy $\hbar\omega$.[16, 17]

Optical transitions are expected to be direct, that is to say, vertical in the reduced zone scheme and therefore $k_f = k_i = k$. The first step in comparing the measured photocurrent to the theoretical photocurrent is the integration of equation 4.2 over the total solid angle:[16, 17]

$$N_{direct}(E, \hbar\omega) \propto \sum_{i,f} \int d^3k_f d^3k_i |M^1_{fi}(k_f, k_i)|^2 \delta(E_f(k_f) - E_i(k_i) - \hbar\omega) \times \delta(E - E_f + \Phi) \tag{4.21}$$

Relating equation 4.21 to the dielectric constant $\varepsilon = \varepsilon_1 + i\varepsilon_2$ yields:[16, 17]

$$\varepsilon_2 w^2 \propto \sum d^3k |M^1_{fi}(k_f, k_i)|^2 \delta(E_f(k_f) - E_i(k_i) - \hbar\omega) \tag{4.22}$$

According to equation 4.22 the photoemission measures the imaginary part of the dielectric constant, ε, multiplied by w^2. Assuming that the matrix element,

$|M^1_{fi}(k_f, k_i)|^2$, is a constant and remembering that $k_f = k_i = k$ equation 4.22 becomes:[16, 17]

$$N_{direct}(E, \hbar\omega) \propto \sum_{i,f} \int d^3k \delta(E_f(k_f) - E_i(k_i) - \hbar\omega)\delta(E - E_f + \Phi) \tag{4.23}$$

From equation 4.23 and using equations 4.20 and 4.2, it can be seen that for direct transitions and polycrystalline samples, or the case where angle integrated spectra are aqcuired, a photoemission experiment like the SPEAR technique measures the energy distribution of the joint or integrated density of states:[16, 17]

$$N_{direct}(E, \hbar\omega) \propto D(E, \hbar\omega) \tag{4.24}$$

4.5 SPEAR Design

4.5.1 Requirements of the System

SPEAR must be operated at Ultra High Vacuum (UHV) pressures, preferably around 1×10^{-10} mbar. This is necessary for two main reasons:

1. Samples must be kept clean, contaminants on the surface could complicate the interpretation of results.[17]

2. The absorption mean free path of light in the VUV range in atmosphere is 100-1000 Å, thus UHV is needed for light to reach the sample.[17, 19]

VUV light could be supplied by either a discharge lamp or a laser. The system must be able to accept either, therefore ports must be available for either on the chamber. Pumping systems must be flexible to cope with either and the system must be set at the same height as the laser system currently in use within the research group.

If using a femtosecond laser, many experiments are possible either involving the STM or just a sample mounted on the STM. The STM needs to be open in order to allow light in and out, it should also be possible to introduce other analysers to the system, therefore an open STM is required along with a spacious chamber and extra ports.

4.5.2 Vacuum System

An STM vacuum system normally consists of a load lock for putting STM tips and samples in the system without opening the entire system to atmosphere. Then STM tips and samples are moved into the preparation chamber for any preparation that is required and for storage. From the preparation chamber tips and samples can be moved to the STM chamber, which houses the STM itself.

Figure 4.12 shows the design of the STM chamber. As can be seen in table 4.1 this chamber was designed to provide additional ports for other potential experiments, including ports that could be used for electron analysers or time-of-flight, TOF, apparatus.

TABLE 4.1: The original designation of each port of the STM chamber

Port	**Size (inch)**	**Length (mm)**	**Height (mm)**	**Function**
A	6.0	200	151.5	For ion pump
B	2.75	185	141.5	Ion gauge
C	2.75	185	141.5	Laser reflection
D	6.0	200	151.5	To preparation chamber
E	2.75	185	151.5	View window
F	2.75	185	151.5	Transfer arm
G	2.75	185	151.5	View window
H	2.75	170	141.5	Laser reflection
I	4.5	140	141.5	TOF
J	2.75	125	141.5	Laser beam
K	2.75	185	141.5	View window
L	2.75	145	/	View window

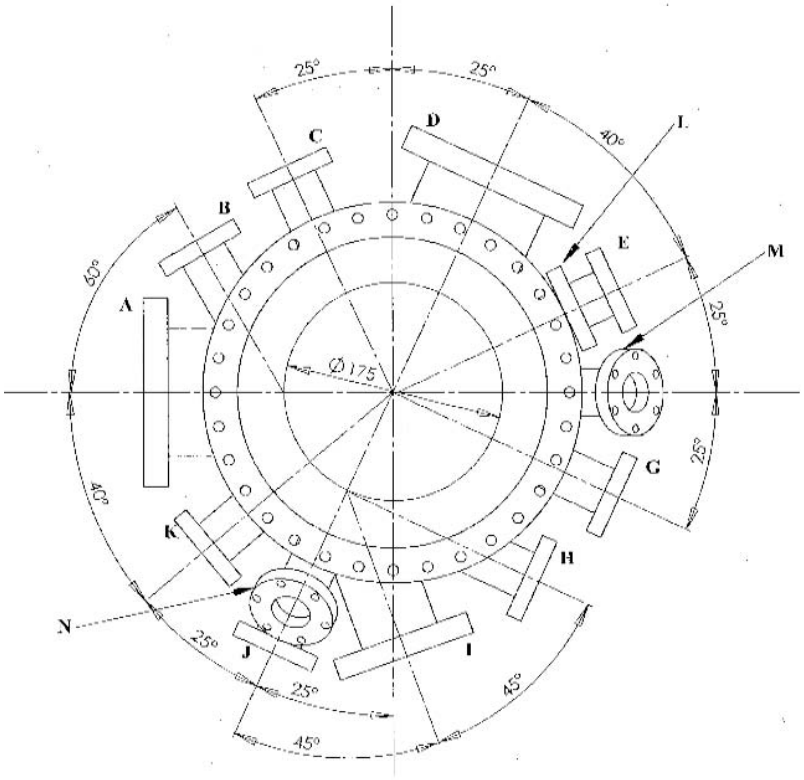

FIGURE 4.12: A top view of the STM chamber, please refer to table 4.1 for the port designations and sizes. For a sense of scale, the inner diameter is given as 175 mm.

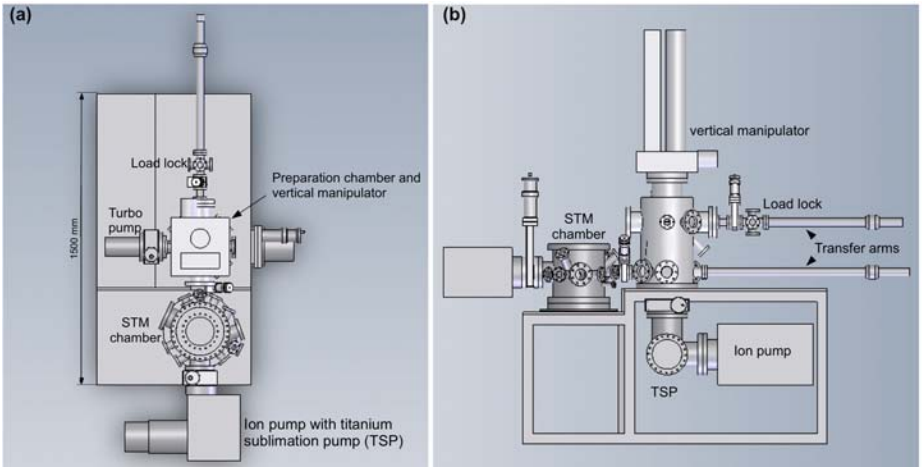

FIGURE 4.13: (a) Top view of the system design, not shown: support for ion pump with combined, Titanium Sublimation Pump, TSP, VUV source and pumping system of VUV source. The STM chamber has it's own ion pump directly connected which in turn has a TSP directly connected. This maximise the pumping for the STM chamber when at UHV pressures. The STM chamber is pumped by the turbo pump mounted at the preparation chamber. (b) Side view of the system design, not shown: support for ion pump with combined TSP, VUV source and pumping system of VUV source. The connection of the load lock, preparation chamber and STM chamber is seen showing the two level transfer system which requires a vertical manipulator. Also visible is the 'lower pumping system', the ion pump and TSP, used to keep the preparation chamber at UHV.

The STM chamber and preparation chamber were not designed by the author, however, the UHV system, given those chambers and the restraints laid out in section 4.5.1, was designed and assembled by the author. The STM chamber was mounted with the preparation chamber and load lock as indicated in figure 4.13. The position of pumps can also be seen in these images. Using the smallest port for tip and sample transfer is not ideal and causes complications, it also limits pumping speed, but the chamber was mounted this way to give access for the laser light as required.

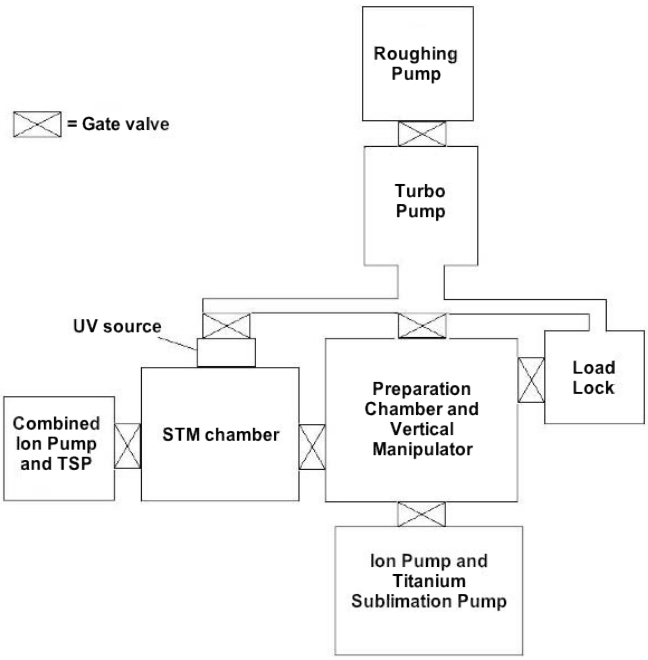

FIGURE 4.14: Pumping diagram for the systems current configuration. The vertical manipulator has a rotation stage which must be connected to the roughing pump, this line is not shown. Ideally the VUV source would have its own pumping station but in this case it is pumped by a turbo pump connected to the preparation chamber.

A pumping diagram is shown in figure 4.14, this shows the locations of pumps and valves in relation to each other. This configuration was thought to be optimal in meeting the requirements with the equipment available.

In order to achieve UHV the system must be baked. Water and oil from pumps, or where people have touched, will naturally be adsorbed on internal chamber walls and equipment. These materials will slowly desorb and readsorb keeping the pressure at high vacuum rather than Ultra High Vacuum. Baking the system, by heating it to 120°C, removes these adsorbates and allows them to be pumped away before readsorbing, therefore reducing the overall base pressure of the system. For this reason bake out shields, which seal the system and maintain heat within it during the baking process, were designed and assembled by the author.

4.5.3 Operation

The design of tip holders and sample holders provided with the Nanograph STM, described in section 2.4 are shown in figures 4.15 and 4.16. The tip holders screw into the STM head by use of a screw thread on the reverse of the tip holder. The sample holder has wings with holes that lock onto sapphire bearings on the sample mount shown in figure 2.11.

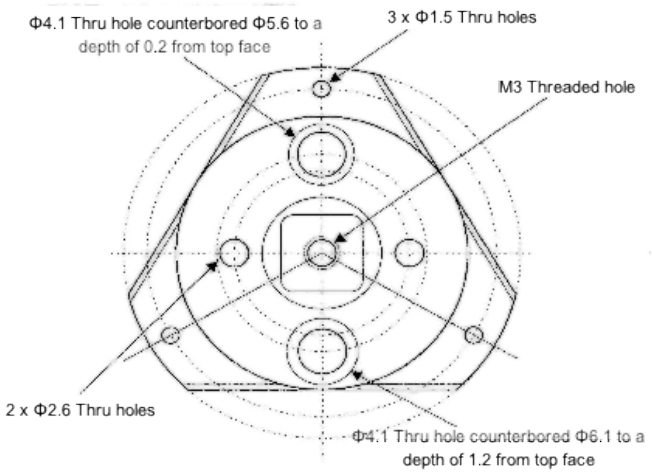

FIGURE 4.15: A schematic of the sample holder used in the nanograph STM. Samples are clamped, with metal clips, onto a quartz plate which raises them up from the rest of the sample holder. The three wings have holes of 1.5 mm diameter which lock onto sapphire bearings in the sample mount of the STM. Drawing provided by Nanograph, all measurements are in mm.

Tips and samples are transferred by the use of magnetic transfer arms, at the end of each transfer arm is a transfer fork, supplied with the transfer arm, as shown in figure 4.17. The transfer fork can directly pick up a sample mount by insertion into holes on the back side of the sample mount. The tip holder is much smaller than the sample mount and a further tool is required. The transfer fork is used to pick up a tip tool, designed by the author, based on designs from other STM

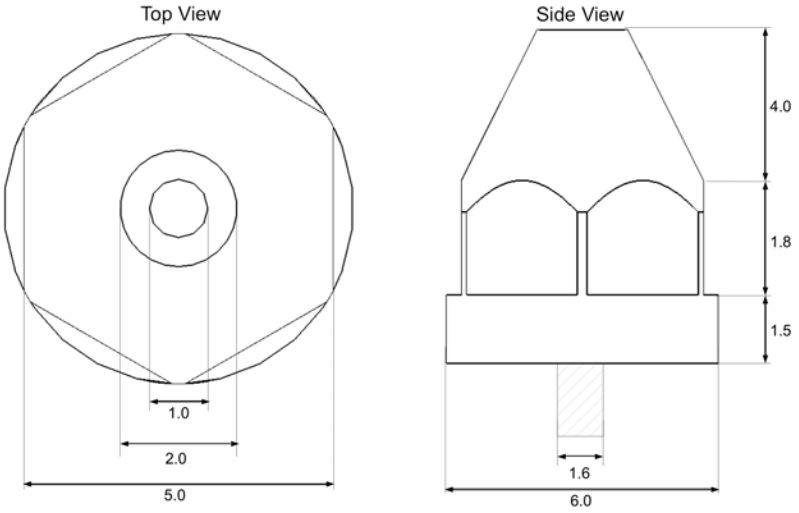

FIGURE 4.16: The tip holder used with the nanograph STM is screwed into the STM via a 1.6 mm thread. The holder has a 5 mm hexagon shape so that it can be screwed into and unscrewed from the STM. A 1 mm hole passes through the entire structure and tip wire is held in place by friction in this hole, for example 0.5 mm wire might be doubled over at the end or 1 mm wire may be used for an exact fit. All measurements are in mm.

systems, shown in figure 4.18. The tip tool has a hex-key structure at one end such that it can be used to screw in and unscrew the tip holders.

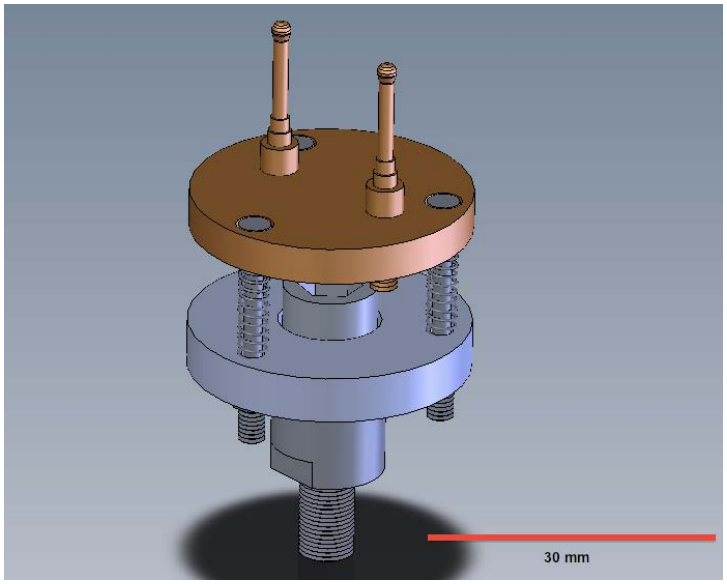

FIGURE 4.17: A 3-D rendering of the transfer fork. The transfer fork uses two lantern-style pins, which insert into the holes of the sample holder and tip holder to pick them up. These pins have some spring like wings which create friction stopping the tip tool or sample mount from slipping off. The transfer fork has three sprung connections in order to give it some flexibility, this allows for some small mis-alignment in the system.

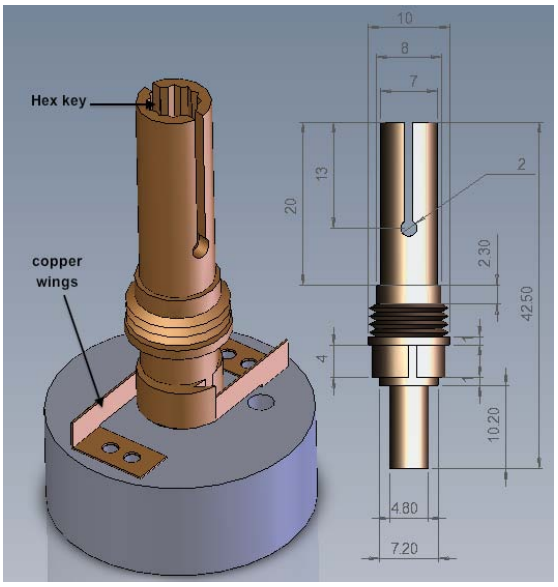

FIGURE 4.18: The tip tool has a hex key like structure at one end in order to screw tip holders in and out of the STM. The base has holes of the correct size for the transfer fork. The main copper part, dimension shown in mm, has a sprung section with copper wings which avoids over-tightening the tip holder in the STM. The bottom of the main copper section also has a threaded part for securing the tip tool within the UHV system. The split in the main body is to allow the tool some flexibility over the tip holder, each tip holder may not be exactly 5 mm across, this is also why copper was chosen as the material.

The system was designed, by the author, with a two level transfer system. Tips and samples are introduced to the upper level of the preparation chamber and a vertical manipulator is used to move them down to the level of the STM, this manipulator is moved out of the way while transferring any tip or sample to the STM. A steel block, designed by the author, shown in figure 4.19 at the end of the manipulator holds one sample and a tip transporter, also designed by the author, shown in figure 4.20, the tip tool is also housed in this steel block. Tip holders are mounted on the tip transporter, the tip transporter goes into the load lock and is moved to the steel block using the transfer arm on the load lock. The vertical manipulator allows tips to be moved to the lower transfer arm. The lower transfer arm picks up the tip tool then picks up tips to transfer to the STM. Sample transfer is done in much the same way. There was some difficulty in transferring samples through the small 2.75" port being used, this was made easier with a specially designed tapered Teflon collar, designed by the author, to guide the transfer arm through.

The tip transporter was originally designed to carry six tips, three on each side, and could be picked up with a transfer fork from either side. The tip holders could screw into 1.6 mm threaded holes in the recesses either side of the transporter. These recesses protect the tip from the transfer fork. This original design could be picked up from either side without the tips being damaged but the tips could not be seen in the vacuum system due to the high sides. There was an unacceptable risk of hitting tips with the tip tool when trying to transfer them, so the high sides were removed from one side and more threaded holes were added on the same side to hold more tips, as shown in figure 4.21. This meant that the tip transporter

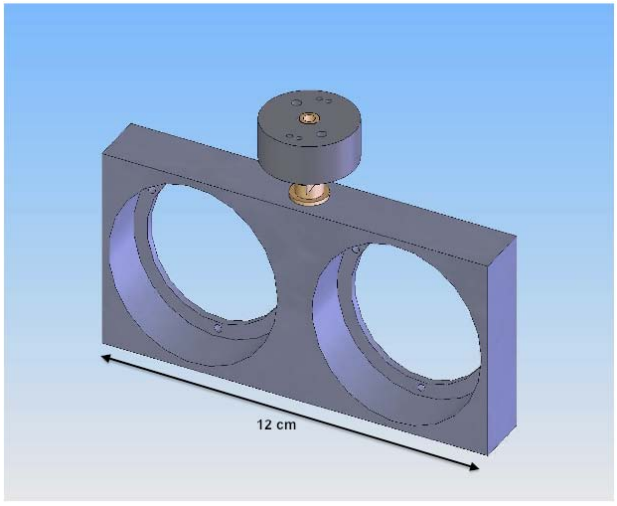

FIGURE 4.19: A 3-D rendering of the steel block, the large holes house a sample mount or the tip transporter. The tip tool is shown in its place on the side of the steel block. When not in use the tip tool sits here, when needed the block is rotated on the vertical manipulator and rotated again to the tip transfer position, the tip tool can then pick a tip up from the tip transporter and move it to the STM or vice versa.

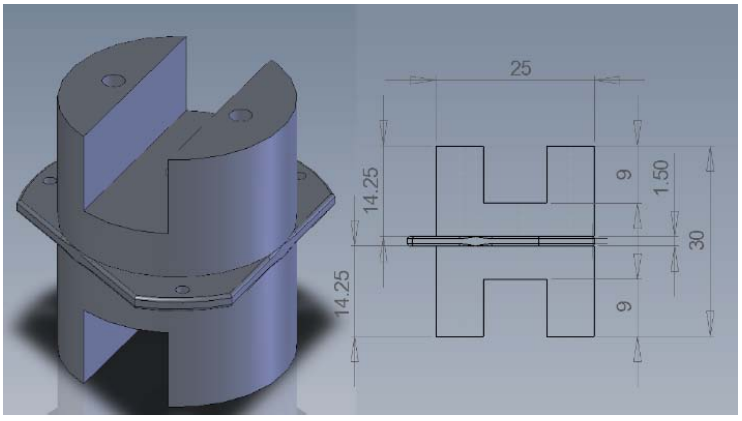

FIGURE 4.20: The original tip transporter carried six tip holders three in each of the two recesses seen. The raised sections have holes for the transfer fork so the tip transporter can be removed from the system to loaded with six tips if required. In practise, tips were usually loaded and used one at a time. The recesses protect the tips from the transfer fork when moving the tip transporter. All measurements are in mm.

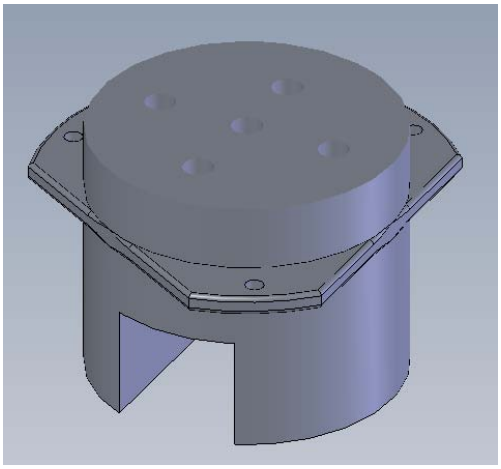

FIGURE 4.21: With the original tip transporter design the recesses reduced the line of sight to the tip holders making it harder to pick up a tip holder without damaging the tip. This was rectified by removing the ability to pick the transporter up with the transfer fork from one side by flattening one side. This flattened side now holds five tips.

had to be picked up form the same side each time, but ensured ease of tip transfer from the preparation chamber to the STM. The tip transporter was used mostly for storage, it was unusual to remove it from vacuum so the inconvenience of rotating the steel block to remove it was minimal, compared to the risk of destroying tips when attempting to pick one up with the tip tool unsighted. The refinement of designs due to the complication of working in UHV is typical. Many small modifications and repairs were carried out during the course of the thesis in order to maintain a working system.

The transfer system was designed, by the author, along with the UHV system, baring in mind the requirements of the system set out in section 4.5.1. The author assembled the UHV system and the transfer system, individual parts designed by the author for tip and sample transfer/storage were machined by the School of Physics and Astronomy Workshop and assembled by the author.

4.5.4 The Excitation Source

A VUV discharge lamp (UVS-300) from SPECS, figures 4.22 and 4.23 is used as the excitation source. The UVS-300 generates a high density plasma by guiding electrons emitted by a hot cathode filament along the lines of a highly inhomogeneous magnetic field towards a small discharge region along the axis of the source.[138] The VUV radiation emitted by the plasma is extracted through a quartz capillary with a 0.1 mm diameter bore.[138]

The nominal output at 3 A current and constant pressure is roughly 1015 photons/sec.steradians as measured with an ion chamber.[138] The non Helium lines contribute less than a fifth of a percent to the HeI discharge line (21.2 eV).[138] The UVS 300 can be operated with other gases to make other wavelengths/energies available.[138]

The UVS 300 requires pumping at all times and should be kept at 6×10^{-5} mbar at all times, however, the UVS 300 can be pumped and opened to atmosphere separate to the STM chamber thanks to a valve which closes the quartz capillary. The capillary is the only entry point into the STM chamber.[138]

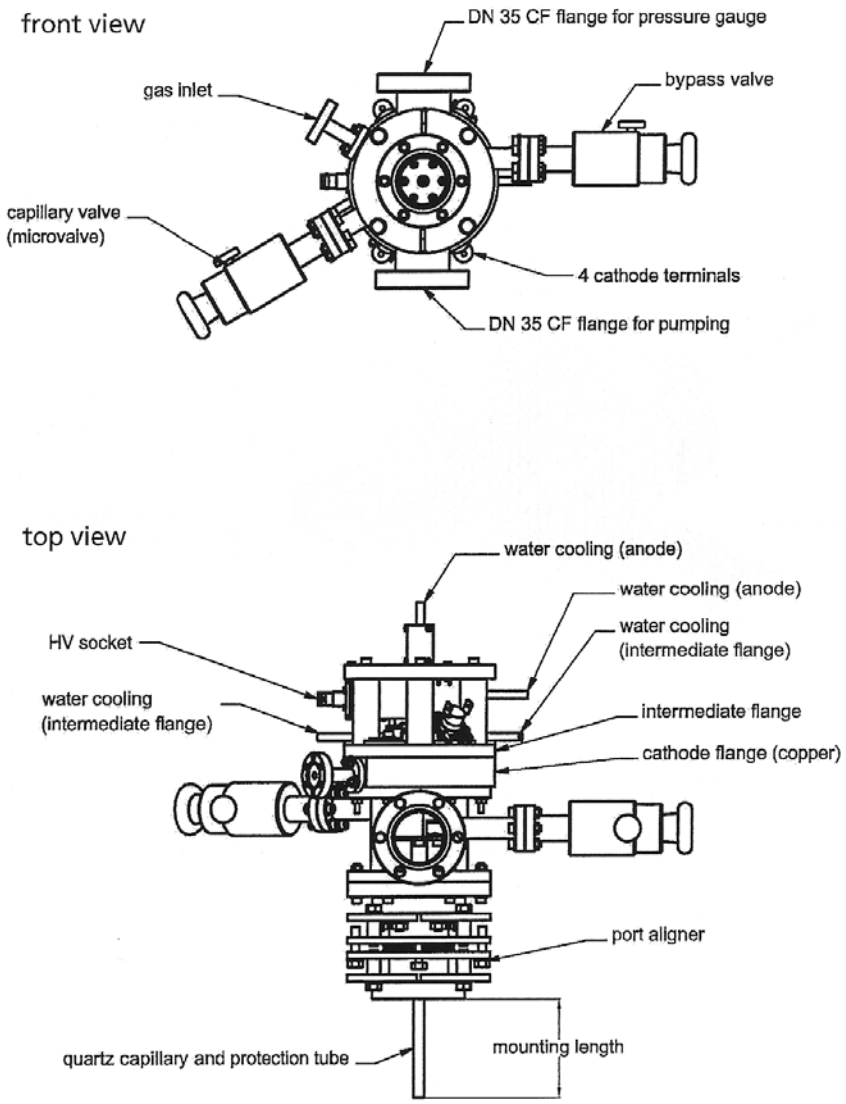

FIGURE 4.22: A schematic of the UVS-300 gas discharge lamp. In the top view the water cooling for the anode and cathode is visible. The anode and cathode are used to generate the hot electrons that ignite the He plasma. The port aligner allows the angle of the quartz capillary, and therefore VUV beam, to be adjusted. In the front view the bypass and capillary valves are highlighted, this allows the source to be pumped and vented separately to the STM chamber. The capillary valve is used to close the quartz capillary from the discharge chamber, this provide the option to operate the source without illuminating the sample. Image from reference [138]

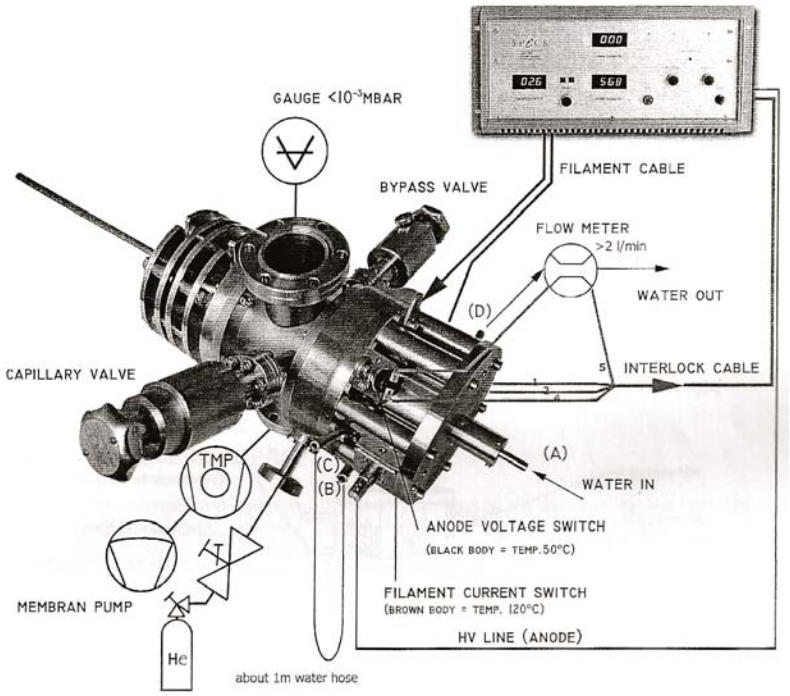

FIGURE 4.23: Image of the UVS-300 He gas discharge lamp, showing the ports for the pressure guage, pumps connection and He gas input. Also shown is the water cooling line and connections to the power supply. Image from reference [138]

4.6 Experimental Method

The UVS-300 helium discharge lamp, described in section 4.5.4, is operated with Helium gas and is set up to provide 21.2 eV photons. In order to maintain a plasma, the UVS-300 must be constantly pumped, and these pumps generate noise in the signal being measured with the STM.

The UVS-300 is aligned with the sample, in these experiments graphite or Au film, by looking at the reflection on the sample surface. This also gives some indication of the spot size of the beam. The capillary has a 0.1 mm bore but the spot size was of the order of a few mm so a cap with a 0.1 mm bore was added to the end to act as a diaphragm giving a smaller spot size. A focussing mirror set-up was considered, but the most efficient UV mirrors available have reflection efficiencies between 10 - 20 % and considering the noise from the pumps a loss in signal would not be acceptable. Ideally the tip would not be illuminated at all, but clearly, even if the spot size was reduced further, reflections from the sample would still cause photoexcitation at the tip. For experiments the tip was bought into tunnelling contact with the surface then retracted until no tunnelling current was observed, and would typically be $\approx$ 200 nm from the surface, the feedback loop is switched off during SPEAR measurements in order to maintain a constant distance. Some data was taken at much greater distances on the order of microns in an attempt to get the tip out of the light.

The UVS-300 requires pumping at all times. Having these pumps running produces both mechanical and electrical noise in the signal. A lock-in amplifier technique was used in single measurements to enhance the signal to noise ratio. Where a

lock-in technique was not used, multiple measurements were taken in order to get an average. To improve the signal quality a laser system should be used instead of the discharge lamp or, at least, the light beam should be collimated. If using the UVS-300 a quiet pumping station that sat separate from the rest of the system would decouple the majority of the noise.

In the measurements made for this thesis the modulation for the lock-in amplifier is made to the retarding voltage applied to the sample, meanwhile the photocurrent is recorded by the lock-in amplifier as measured at the tip. Typical settings for the oscillation amplitude and frequency would be 0.01–0.2 V and 150–300 Hz respectively. The lock-in amplifier interfaces with the RHK SPM software which logs all the data. Using this software it is possible to set-up multiple voltage sweeps and adjust the timing between voltage steps, size of voltage steps, time between sweeps etc. So a typical measurement would be a sweep from –20 to +20 V in small increments taking anywhere between 30 seconds and a few minutes depending on the measurement time at each voltage. Spectra were typically taken in batches of 10-100 which could then be compared for reproducibility or averaged to reduce any noise.

4.7 Results

4.7.1 Acquiring a Photocurrent

A sharp W tip and a HOPG sample were used to test the detection of a photocurrent. The first step is to verify that a photocurrent can be measured at all. Measurements of current-voltage (I(V)) curves were taken with no light on the sample, figure 4.24 and with light applied to the sample, figure 4.25. I(V) curves were also taken with the VUV source running but with the aperture shut to check that any signal acquired was not merely noise from the running of the source.

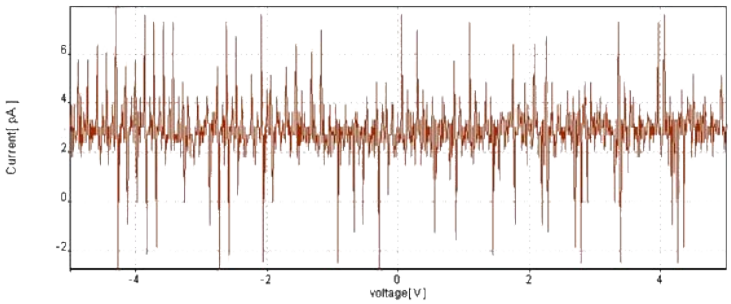

FIGURE 4.24: With the VUV source switched off only noise on the order of a few pA is observed in the signal measured by the STM tip. The tip in this case is retracted far from the surface, this is not a tunnelling current noise. The main contribution to this signal is the pumps that must be run on order to operate the VUV source.

Positive and negative biases were applied to the HOPG sample in order to characterise the photocurrent contribution from the illuminated tip and sample. A positive field at the HOPG sample would stop photoelectrons from the sample reaching the tip and being detected as a photocurrent, a negative field applied to the sample should stop electrons from leaving the tip and being counted as a photocurrent signal.

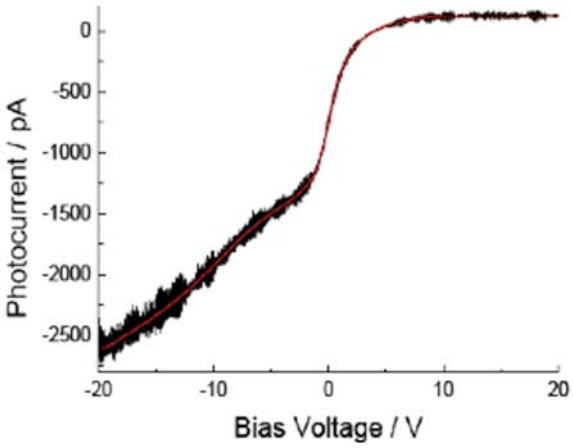

FIGURE 4.25: The black data is from sixteen I(V) curves of the HOPG–W tip system. The red curve shows an average of those spectra. The obvious features are the large negative signal at negative voltage, the abrupt changes in signal around 0 V, and the difference in gradient of the negative and positive side.

Figure 4.24 shows the noise in the system when no light is shining on the sample, this noise is due to the pumps running to maintain operational pressure within the VUV source. Figure 4.25 shows the signal aquired when the VUV light illuminates the sample. It is clear from the comparison of figure 4.24 to figure 4.25 that there is a measurable photocurrent produced. Features in I(V) curves should correspond to features in the density of states, as the negative voltage applied to the sample acts to retard photoelectrons emitted at the tip. A positive voltage retards photoelectrons emitted by the sample. Therefore, features on the negative bias side are due to the tip and features on the positive bias side are due to the sample. The differential of the I(V) curves, dI/dV, is directly proportional to the density of states and features are much clearer.

4.7.2 Highly Oriented Pyrolytic Graphite Sample and Tungsten Tip.

The junction between a Tungsten tip and a HOPG surface was illuminated by VUV light generated by a He discharge lamp as described in section 4.6. Multiple spectra were acquired and a number of techniques were used to try and improve the signal-to-noise ratio or to average out the noise as can be seen in figures 4.26 to 4.28. Figure 4.26 was produced by averaging ≈ 100 I(V) curves without any further filtering, figure 4.27 is the average of 10 I(V) curves and has been smoothed using a moving window average, the key features are still seen, this method is quicker than averaging over many more curves. Finally, figure 4.28 is a single spectrum taken using the lock-in amplifier technique, described in section 4.6, again a faster method whilst retaining key features.

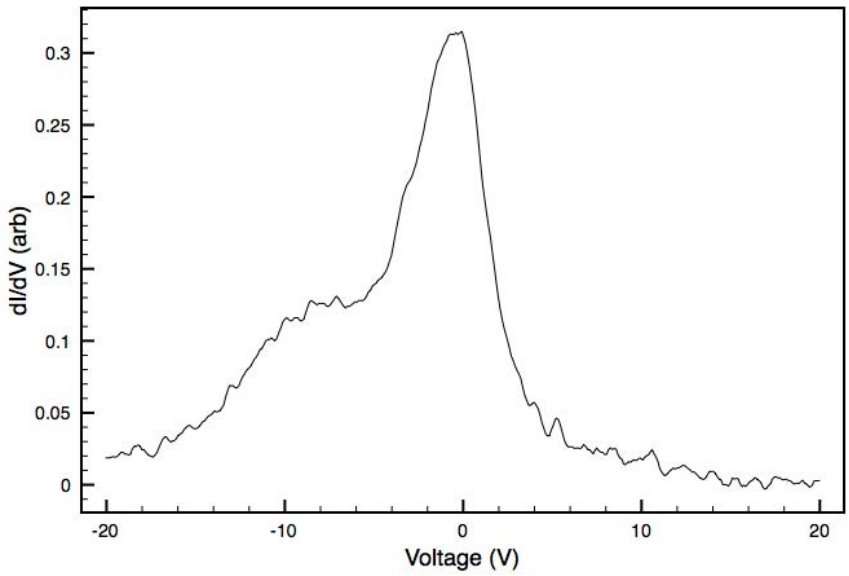

FIGURE 4.26: This spectrum, for the HOPG–W tip system, was produced by averaging over many I(V) curves without any smoothing involved. The voltage is applied to the sample and at negative voltage a large feature is seen. A large feature is seen around 0 V. The negative bias features are attributed to the tip, as negative bias on the sample should retard photoelectrons generated at the tip, but will only accelerate electrons generated at the sample.

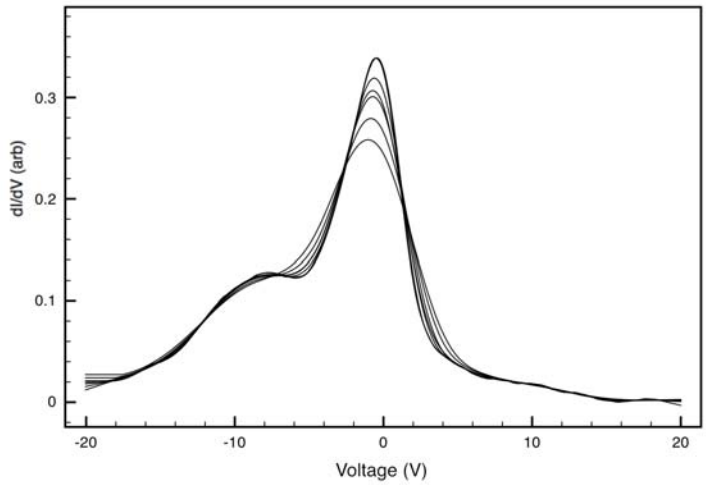

FIGURE 4.27: These 10 spectra, for the HOPG–W tip system, were produced by smoothing 10 I(V) curves by a moving window average technique, and taking the differential of the average of those curves. Each spectra presented is from a different day showing the reproducibility of the features. Again the voltage is applied to the sample and a feature is seen at negative bias and at 0 V. In this data there is some suggestion of a broad feature at +10 V.

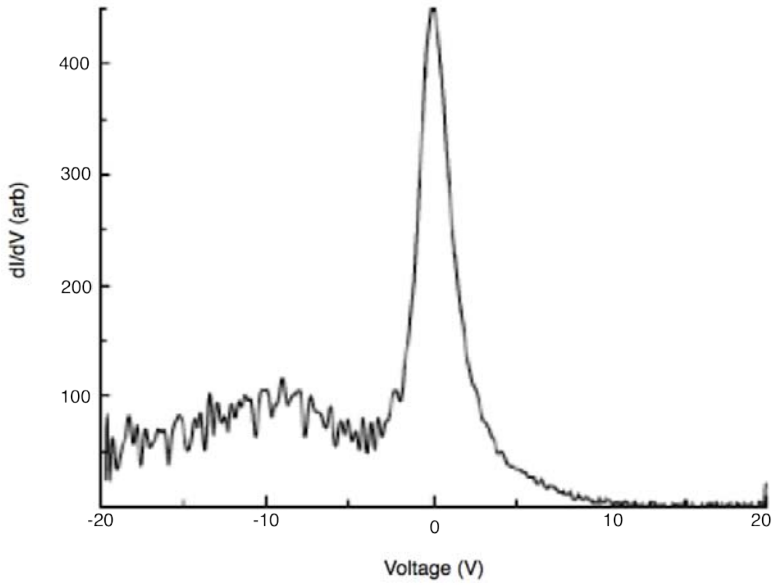

FIGURE 4.28: This spectrum, for the HOPG–W tip system, was measured directly by lock-in amplifier technique. The voltage is applied to the sample, the feature at negative bias is still present as is the feature at 0 V. The positive bias side appears very flat and featureless especially after 10 V.

In figures 4.26 to 4.28, a clear feature is seen at 0 V, this peak at around 0 V can be attributed to the low energy secondary electrons and is a standard feature in PES.[14, 15, 17, 18] The other recurring feature is a peak at negative bias, where the bias is applied to the sample. In the negative voltage regime electrons from the sample would be accelerated while electrons from the tip should be stopped from exiting the tip depending on energy. In the positive bias regime, electrons from the tip will be accelerated and electrons from the sample will be retarded by the positive bias. Therefore, features in figure 4.26 at negative bias correspond to features in the electronic structure of the tip. The positive bias side, where photoelectrons from the sample are retarded, shows no unambiguous features. It is suggested that the illumination of the tip gives rise to a large photocurrent from the tip, this contribution to the overall signal from the tip does not allow the resolution of sample features. It is expected that the field created by the presence of the tip, discussed in chapter 4, forces the trajectories of many sample electrons away from the tip, therefore, the contribution to the signal by the sample may be considerably smaller than the contribution by the tip. Any electron that leaves the tip contributes to the signal but an electron from the sample must reach the tip in order to be counted.

Figure 4.26 can be rearranged using equation 4.1 to represent the data with respect to kinetic energy for the side of the spectra related to the tip, see figure 4.29.

The feature seen in the side of the spectra related to the tip appears at 8.4 eV kinetic energy according to figure 4.29. This kinetic energy corresponds to an energy below vacuum of 12.8 eV, given by the difference of the photon energy used and the kinetic energy. Tungsten has a work function of $\approx$ 4.6 eV which

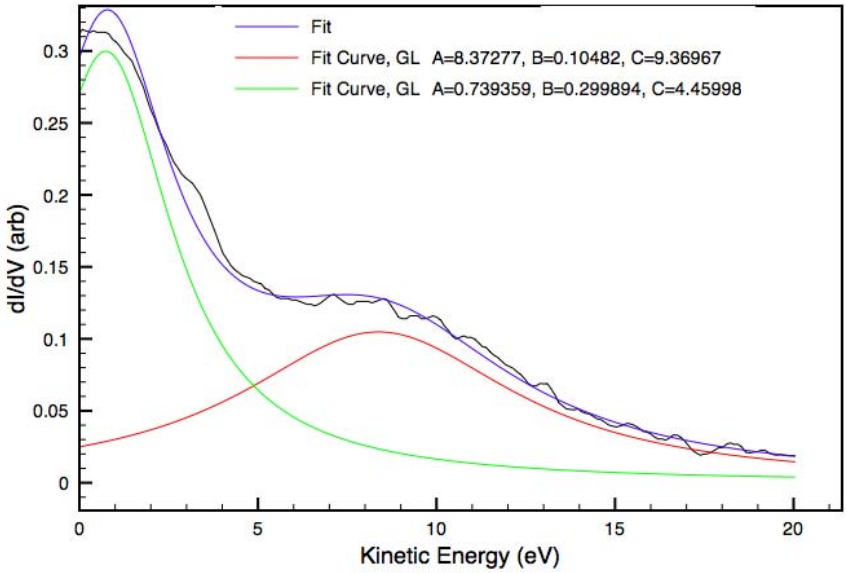

FIGURE 4.29: Using equation 4.1 the axis has been rearranged from figure 4.26 to present the negative side of figure 4.26 with respect to the kinetic energy of photoelectrons emitted from the tip. Gaussian curves have been fitted to find the centre of the peak of the features. The parameters A, B, C are the centre, height and full width at half maximum of a Gaussian function of the form $Ae^{-\frac{(x-B)^2}{2c^2}}$

gives an energy, using equation 4.1, of $\approx$ 8.2 eV below E_F.[17] For clean W(110) a peak is expected for 10.1 eV below the Fermi level, the Tungsten tip should not have a large (110) surface so this could be the same feature. Looking at the integrated density of states for the bcc Tungsten crystal, figure 4.30, peaks are expected at $\approx$2, $\approx$3.5 and $\approx$5-8 eV below E_F.[139] Again it should be remembered that the W tip is polycrystalline and so a direct comparison is not possible but it is likely the feature in the SPEAR spectra relates to the very broad feature seen between 5 and 8 eV.

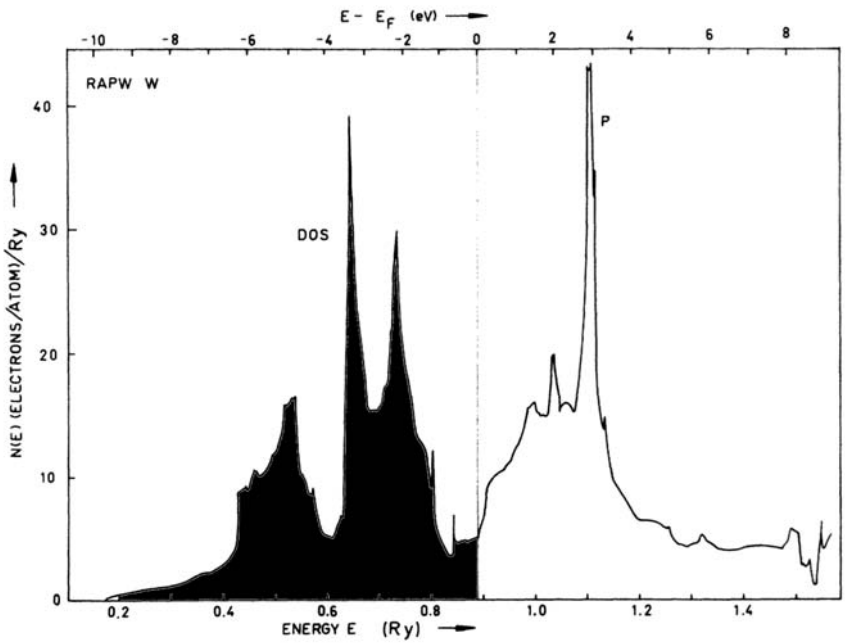

FIGURE 4.30: The integrated density of states for the bcc W crystal, shown is the total density of states. A peak is seen starting at 5 eV and ending around 8 eV below the Fermi level for the integrated density of states, this may correspond in part to the peak seen at 8.2 eV below the Fermi level in the SPEAR spectra. The shaded area represents the occupied electronic states. Figure from reference [140]

Looking instead at oxidised Tungsten, valence band features shift by ≈ 1 eV with respect to Fermi energy. In work by Bullett the first conduction band in WO_3 appears between 6.1 - 8.7 eV below E_F, see figure 4.31.[141] It is very easy for Tungsten to oxidise, after electrochemical etching, W tips are cleaned by resistive heating to remove as much oxygen as possible, it is however quite possible for an oxide layer, or some fraction of a monolayer, to remain.[142–144]

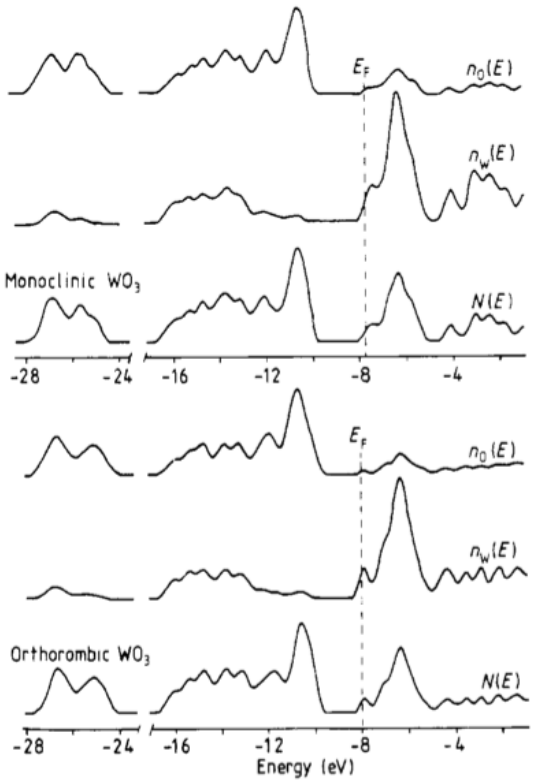

FIGURE 4.31: The spectrum of electron states calculated for the full monoclinic and orthorhombic crystal structures of WO_3. The oxide acts to shift features considerably compared to pure Tungsten. The onset of the conduction band is expected between 6.1 - 8.7 eV below the Fermi level which does directly correspond to features found for the Tungsten tip. Figure from reference [141]

4.7.3 Gold Sample and Tungsten Tip

A set of experiments was performed using the same Tungsten tip with a sample of Au sputtered onto HOPG. Since it is far more common to calibrate PES experiments with Au or Ag than with HOPG, Au can be expected to yield a stronger signal compared to the HOPG sample.[17] Figure 4.32 shows the resultant spectrum.

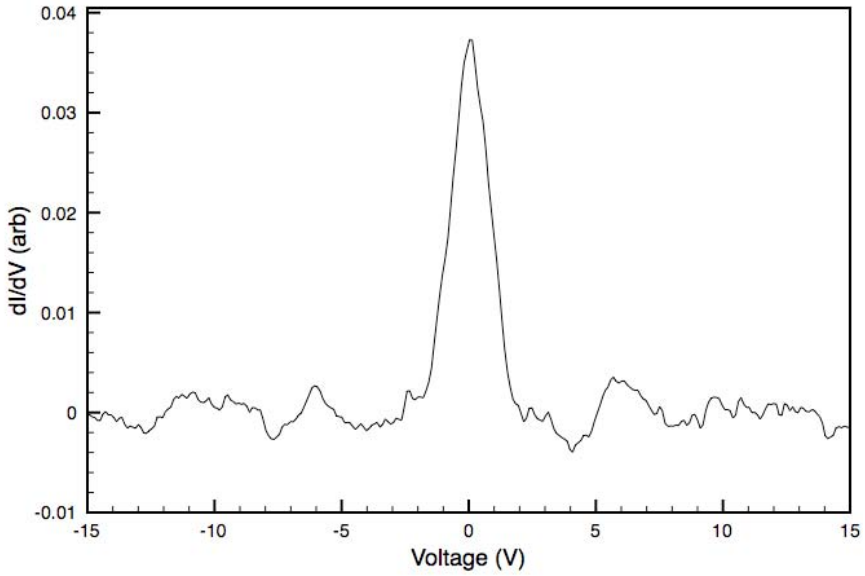

FIGURE 4.32: A spectrum taken with the Au sample and Tungsten tip, bias voltage applied to the sample. The spectrum is a result of ≈ 50 I(V) curves, averaged, smoothed with a moving window average and then differentiated. There is again a central peak around 0 V applied to the sample, then features at 6 V either side of zero. The negative bias side appears different to the negative bias side for the bare HOPG sample.

Figure 4.32 can be rearranged using equation 4.1 to represent the data with respect to kinetic energy for the side of the spectra related to the tip and the sample, figures 4.33 and 4.34 respectively.

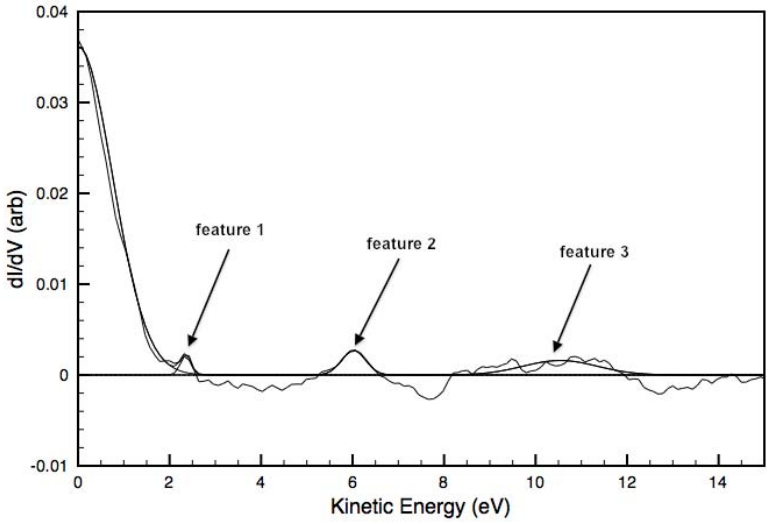

FIGURE 4.33: The axis of the dI/dV spectra in figure 4.32 have been adjusted so that the side of the spectra related to the tip is presented with respect to kinetic energy of photoelectrons from the tip, this is done using equation 4.1. Gaussian curves are fitted to identify features 1, 2 and 3.

In the side of the spectra related to the tip, more than one peak is seen, as shown in figure 4.33. Peaks are seen at 2.34 eV, 6.0 eV and 10.5 eV kinetic energy corresponding to 18.86 eV, 15.2 eV and 10.7 eV below the vacuum level, respectively as opposed to the 12.8 eV below vacuum level seen on plain HOPG. It may be that the tip had picked up some Au as this tip was used to check the quality of the Au film before taking spectra. It is quite easy to pick Au atoms up with a tip while scanning.[145]

A peak is seen at 6 eV kinetic energy in the side of the spectra related to the sample, figure 4.34, identical to one of the peaks seen in the tip side, adding credence to the idea that the tip is covered in Au. If the tip had picked up a large amount of Au and increased in size, that would give a larger signal from the sample also. The work function for Au is $\approx$ 5.1 eV giving an energy of 10.1 eV below E_F for this feature. The 5d band feature of Au should be $\approx$ 5 eV wide and

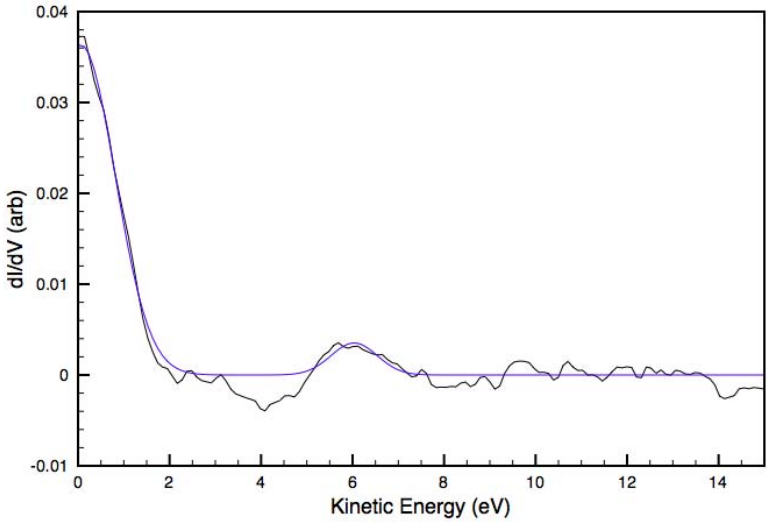

FIGURE 4.34: The axis of the dI/dV spectra in figure 4.32 have been adjusted so that the side of the spectra related to the Au sample is presented with respect to kinetic energy of photoelectrons generated by the sample, this is done by the use of equation 4.1. The main feature is a peak at 6 V resolved by the use of Gaussian curve fitting.

centred around 5 eV below E_F perhaps the feature seen here is due to the onset of this valence band feature.[17]

This result was checked by Dr Feng Yin who took spectra of a Au coated HOPG sample using a pure Au wire, rather than Tungsten. The wire was flat at the end, instead of a sharp tip, to pick up more photoelectrons generated by the sample by presenting a larger collection area and reducing the curvature of the field. The acquired spectrum is presented in figure 4.35.[146]

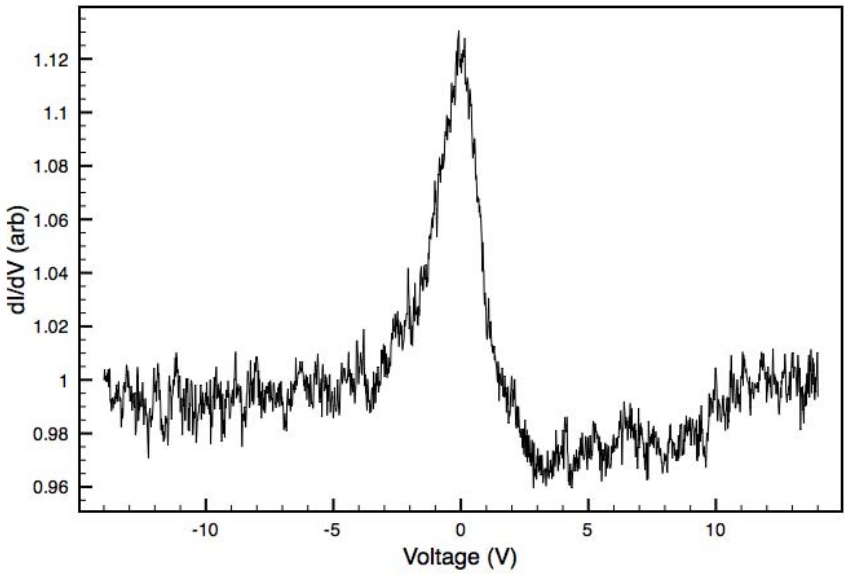

FIGURE 4.35: A spectrum, taken using the lock-in amplifier technique, of a Au coated HOPG sample with a Au wire used as the tip. Bias voltage was applied to sample. The negative bias side appears flat and featureless, the positive bias side shows a feature at around 6 eV, and another feature at 10 eV. Figure courtesy of Dr Feng Yin.[146]

Interestingly, features in the tip side are not as clear in figure 4.35, perhaps because Au reflects a larger amount of light than W or perhaps, as the Au wire was flat, there was less enhancement of the photoemission at the tip. Either way the 6 eV feature is seen again in the sample side although perhaps not exactly at 6 eV. It seems that more structure in the spectrum can be resolved with the flat tip, obviously all spatial resolution is sacrificed.

4.7.4 Conclusions

The SPEAR system has succesfully resolved features in the energetic structure of a Tungsten tip. Using this technique it is possible to see that the tip picked up some Au, which contributed to the signal enough to change the spectra acquired. It may be possible to improve this technique and use it to characterise tips for the purpose of Scanning Tunneling Microscopy and Scanning Tunneling Spectroscopy (STS). In the case of STS the tip is assumed, more often that not, to have a flat DOS. To be able to resolve the DOS of the tip, and deconvolute that from spectra and indeed from images, could be very useful.[13, 20]

Using sharp tips it is seemingly not possible to resolve the photoelectron spectra of nanostructured surfaces due to the large amount of photoelectrons generated at the tip. If the tip is removed from the beam then light reflected by the sample still causes photoelectrons to be generated at the tip. When this experiment was proposed it was expected that the sharp tip would help provide resolution, as field enhancement would cause more photoelectrons to be generated directly under the tip. This same effect also causes more photoelectrons to be generated from the tip, contributing a signal from the tip to the spectra. The same field will push electrons from the sample away from the tip reducing the signal that can be acquired from the sample. This is why the flat tip is seemingly more successful. This field problem is analysed further by simulating this system in chapter 5.

4.8 Proposed Improvements

Using the set-up in figure 4.14 a base pressure of 5×10^{-10} mbar was achieved. This pressure is higher than intended but is good enough for experiments, so whilst further baking of the system would help, it was thought better to carry on with experiments. The pressure could be further improved by using a smaller preparation chamber, perhaps by changing from a two level system with a large vertical manipulator, to a system with a carousel of tips and samples on one level that has clearance through for tip and sample transfer. The most obvious thing to do would be to use larger ports for the pumps, and to attempt to shorten pumping routes.

A second generation SPEAR could benefit from an optimised STM chamber. See figure 4.36. This design for the STM chamber has only ports specific to the SPEAR technique. This design would make sample transfer easier, and optimises pumping speeds with two 6" ports opposite each other, it also has access for laser light from any of four ports, with four more ports for viewing and for gauges.

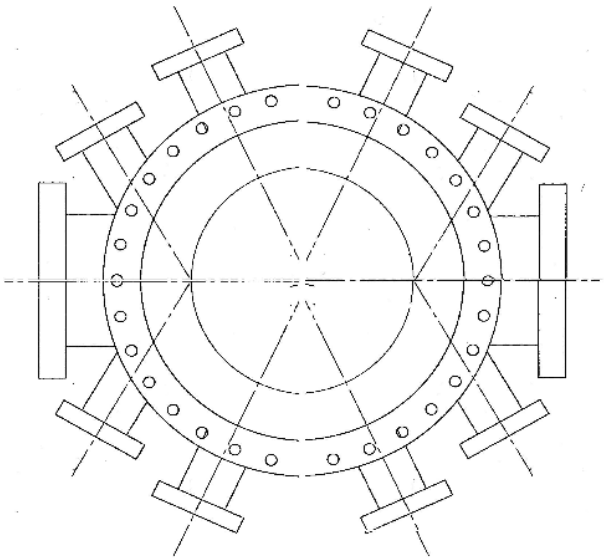

FIGURE 4.36: A top view of an alternative STM chamber design, as less room is required if it is known that other equipment will not be used in the STM chamber. The main chamber could be 10" diameter rather than the 12" diameter of the current system. Large 6" ports provide easy sample transfer and pumping options, while the amount of other ports is reduced to eight, which could be reduced to four if a specific side is chosen for the excitation source.

Chapter 5

Simulations of the Scanning Probe Electron AnalyseR

It has been demonstrated in chapter 4 that, by illuminating an STM junction between a simple W tip and a HOPG sample, it is possible to resolve electronic states of the tip. However it is not possible to unambiguously resolve the electronic states of the sample due to the large contribution to the signal made by photoelectrons generated at the tip. To investigate the cause of this a simulation was written in Matlab. This simulation calculates the field between a tip and a sample, then generates electrons and tracks the movement of these electrons until they hit the tip or sample or leave the simulation domain. Electrons are generated with a set energy. The current at the tip/collector is recorded as a function of retarding bias to determine whether these I(V) spectra exhibit features which can provide information about the tip(collector), sample or shield. The code is included in appendix A.

5.1 Simulation Method

Electrodes are set up for a type of tip, by defining the electrodes in the class 'tip' any kind of tip can be simulated. Each electrode is generated separately and contains all the information needed to know where it is, what it's voltage is at a given point and what it's workfunction is and some identifier/name. Figure 5.1 shows an example of the simple tip simulated to act as a model of the experimental work from chapter 4.

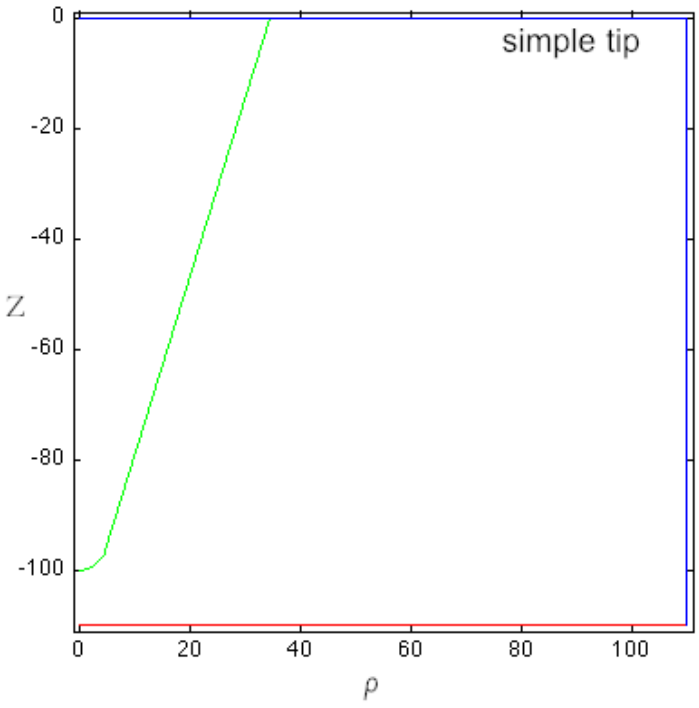

FIGURE 5.1: A simple tip. The components of the tip are represented in green, the sample in red and the boundaries are blue. The boundaries are used to determine if an electron leaves the simulation area or will continue to be detected by the larger part of the tip. In the simulation domain the tip has a tip radius of 5 nm positioned 10 nm from the surface and has a length of 100 nm.

A grid containing these electrodes is produced in order to solve the field using a finite difference method[147, 148], an example of a solved field is shown in figure 5.2.

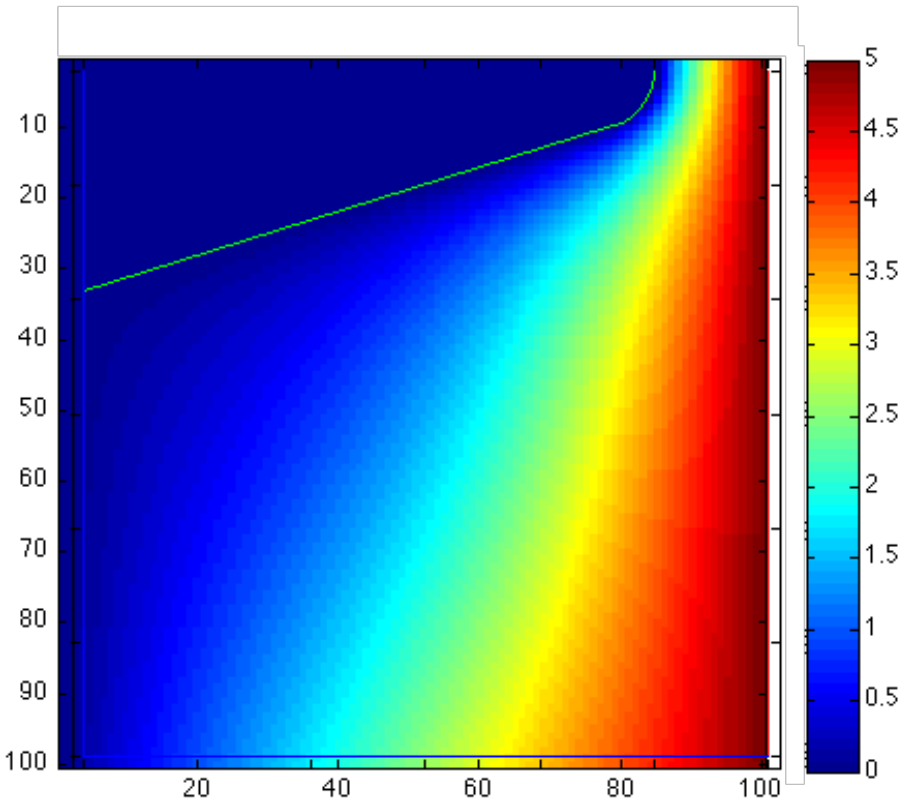

FIGURE 5.2: Here a field has been solved using a 100 by 100 grid, larger grids are used for the purpose of the simulation, the tip/sample positions have been overlaid.

The field between the tip and sample is calculated by solving Laplace's equation in cylindrical coordinates. Laplace's equation in cylindrical coordinates is given as:

$$\nabla^2 V = \frac{\partial^2 V}{\partial \rho^2} + \frac{1}{\rho}\frac{\partial V}{\partial \rho} + \frac{1}{\rho^2}\frac{\partial^2 V}{\partial \phi^2} + \frac{\partial^2 V}{\partial z^2} \tag{5.1}$$

where V is the potential at coordinates ρ, ϕ and z as shown in figure 5.3

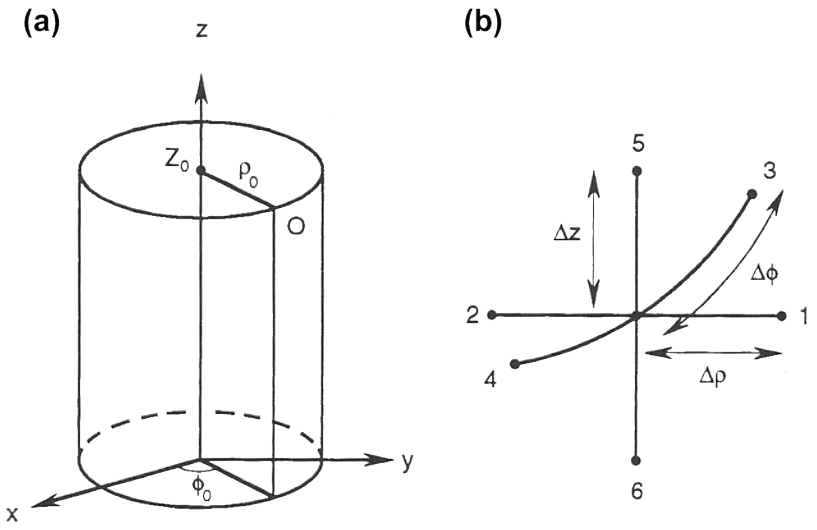

FIGURE 5.3: (a) Cylindrical coordinates system: The point O is at (ρ_O, ϕ_O, Z_O). (b) The point O represented as a node for the purposes of the finite difference method. Figure from reference [147].

In this simulation the system is rotational symmetric around θ, such that $V = V(\rho, z)$. The finite difference approximation of Laplace's equation for a cylindrically symmetric potential, V, is:[147]

$$\frac{V_1 - 2V_0 + V_2}{(\Delta\rho)^2} + \frac{1}{\rho_0}\frac{V_1 - V_2}{2\Delta\rho} + \frac{V_3 - 2V_0 + V_4}{(\Delta z)^2} \tag{5.2}$$

whereΔ ρ andΔ z are the steps along ρ and z respectively, and

$$
\begin{aligned}
V_0 &= V(\rho_O, \phi_O, z_O) \\
V_1 &= V(\rho_O + \Delta\rho, \phi_O, z_O) \\
V_2 &= V(\rho_O - \Delta\rho, \phi_O, z_O) \\
V_3 &= V(\rho_O, \phi_O, z_O + \Delta z) \\
V_4 &= V(\rho_O, \phi_O, z_O - \Delta z)
\end{aligned} \tag{5.3}
$$

In the finite difference grid is split into squares, such that$\Delta\ \rho = \Delta z = h$, as shown in figure 5.4. Equation 5.2 becomes:[147]

$$(1 + \frac{h}{2\rho_O})V_1 + (1 - \frac{h}{2\rho_O})V_2 + V_3 + V_4 - 4V_0 = 0 \tag{5.4}$$

In figure 5.4 $\rho_O = ih$ and $z_O = jh$ therefore equation 5.4 becomes:

$$V(i,j) = \frac{1}{4}[V(i,j-1)+V(i,j+1)+(\frac{2i-1}{2i})V(i-1,j)+(\frac{2i+1}{2i})V(i+1,j)] \tag{5.5}$$

At $\rho_O = 0$, i.e. on the ρ axis, equation 5.4 has a singularity, however, by symmetry, all odd order derivatives are zero:[147]

$$\frac{\partial V}{\partial \rho}|_{\rho=0} = 0 \tag{5.6}$$

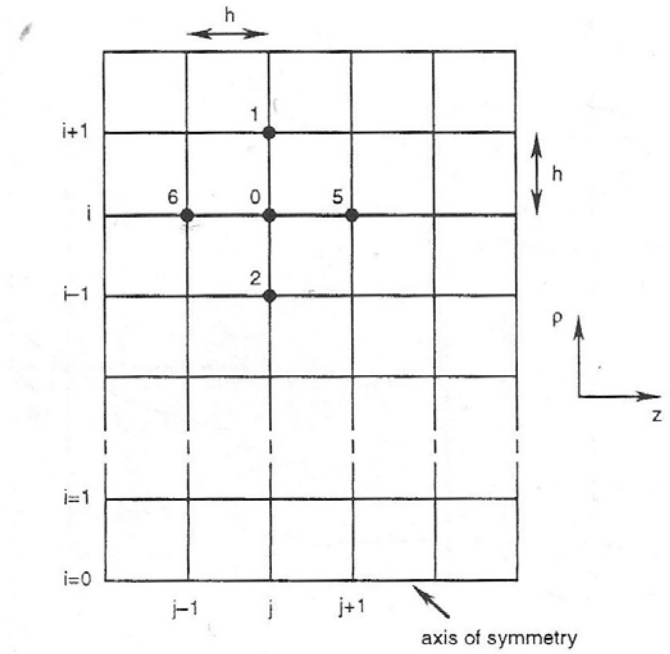

FIGURE 5.4: Finite difference grid for a cylindrical coordinate system with symmetry about the z axis. Figure from reference [147].

since

$$V(\Delta\rho, z_o) = V(-\Delta\rho, z_O) \tag{5.7}$$

by L'Hopital's rule the Laplace becomes:[147]

$$2\frac{\partial^2 V}{\partial\rho^2} + \frac{\partial^2 V}{\partial z^2} = 0 \tag{5.8}$$

which for the purpose of the finite difference method is given as:[147]

$$V(0,j) = \frac{1}{6}[V(0,j-1) + V(0,j+1) + 4V(1,j)] \tag{5.9}$$

It is equations 5.5 and 5.9 that are used to solve the field between the tip and sample. Coordinates i and j are chosen randomly and V(i,j) is set using equations 5.5 and 5.9, this is repeated until the Laplace is zero everywhere. Once the field has been solved an electron can be generated at random, the probability of an electron being generated at a given point is proportional to the area that point represents in the cylindrical coordinate system. An electron is generated with an angle from the surface that follows a cos^2 distribution around the surface normal.[149] Once an electron has been generated the path of the electron is solved, see figure 5.5 for examples.

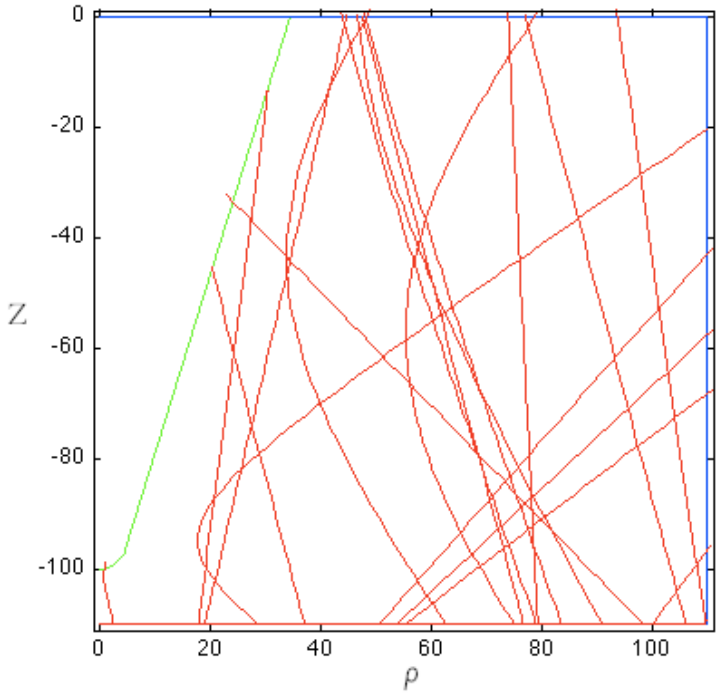

FIGURE 5.5: Electron paths for the simple tip, scale in nm, only electrons from the sample are shown. A retarding bias of 5 V has been applied to the sample, the electrons have an energy of 8 eV. Some electrons are pushed away from the tip by the field but some, depending on initial angle would be detected.

The particle begins at Cartesian coordinates x, y and z with velocity in components v_x, v_y and v_z the path of the electron is calculated over a period of time split into

steps,$\Delta\ t$, until the electron collides with an electrode. The electric field in the three coordinates is interpolated from the grid values of the solution of the field in the cylindrical coordinates:

$$\begin{aligned} E_x &= V(\rho)\cos(\phi) \\ E_y &= V(\rho)\sin(\phi) \\ E_z &= V(z); \end{aligned} \tag{5.10}$$

The field is used to calculate the acceleration ($a_{x,y,z}$) in the Cartesian coordinate system, which in turn determines the velocity and the path the electron takes:

$$
\begin{aligned}
a_x &= \Delta t(q_e/m_e)E_x \\
a_y &= \Delta t(q_e/m_e)E_y \\
a_z &= \Delta t(q_e/m_e)E_z
\end{aligned}
\tag{5.11}
$$

$$
\begin{aligned}
v_x &= v_x + \Delta t a_x \\
v_y &= v_y + \Delta t a_y \\
v_z &= v_z + \Delta t a_z
\end{aligned}
$$

$$
\begin{aligned}
x &= x + \Delta t v_x \\
y &= y + \Delta t v_y \\
z &= z + \Delta t v_z
\end{aligned}
$$

where q_e is the charge of an electron and m_e is the mass of an electron. These Cartesian coordinates are then transformed into the cylindrical coordinates to find $V(\rho, z)$ for the next step.

$$
\begin{aligned}
\rho &= \sqrt{x^2 + y^2} \\
z &= z
\end{aligned}
\tag{5.12}
$$

Energy conservation is maintained at each step by adjusting the kinetic energy using the factor, F, given by:

$$F = \sqrt{\frac{(K_{init} + E_{vacuum} - V(r,z))^2}{K_{elec}^2}} \tag{5.13}$$

where K_{init} is the kinetic energy the electron started with, E_{vacuum} is the vacuum energy of the electrode the electron originated from and K_{elec}^2 is the kinetic energy the electron has according to it's velocity, v(x,y,z), this velocity can be adjusting using the factor, F as in equation 5.15.

$$\begin{aligned} v_x &= Fv_x \\ v_z &= Fv_z \\ v_y &= Fv_y \end{aligned} \tag{5.14}$$

Electrons that leave the tip/collector contribute a negative current to the overall signal while electrons that hit the tip/collector contribute a positive current. By monitoring where the electrons go it is possible to get an understanding of signal intensities and demonstrate an ability to resolve electronic features of the tip and the sample.

5.2 Simulation Results

5.2.1 Simple Tip

The simple tip is set-up with electrodes as per figure 5.1. The simulations should test whether a given tip can identify features in the tip or sample. For simplicity the electrons from the tip and sample were given a feature at 5 eV kinetic energy, with a flat spread of energies between 0 and 15 eV, this is equivalent to a flat DOS with a single feature. The 5 eV feature has 100 times the height of the rest of the density of states. The bias voltage, applied to the sample, is scanned between -7 V and 7 V in steps of 0.5 V in order to test the tips ability to resolve it's own energy states and those of the sample. Each data point represents 10000 electrons. The field calculations were performed on grids of size 200 by 200, and solved over 1000 iterations. Electron paths were calculated until the electron hit an electrode, the time steps were 10^{-15} s when electrons were measured to be more than 2 nm from any electrodes, time steps were reduced to 10^{-17} s when the electron-electrode distance became less than 2 nm. Secondary electrons are not considered and so only features at 5 eV can be expected. The photocurrent is measured at the tip and the bias is applied to the sample as a direct comparison to the experimental work of chapter 4.

Figure 5.6 shows the calculated photocurrent for the simple tip. The main points to note are that the features at -5 V and +5 V correspond to the tip and sample respectively and are well resolved, the second thing to note is that the photocurrent is predominantly negative, meaning that the majority of the signal is coming from the tip. Although the majority signal is from the tip, the retardation of electrons

due to the main feature of the sample, at 5 V, gives a measurable change in photocurrent. Features from the sample were not well resolved in the experimental work in chapter 4.

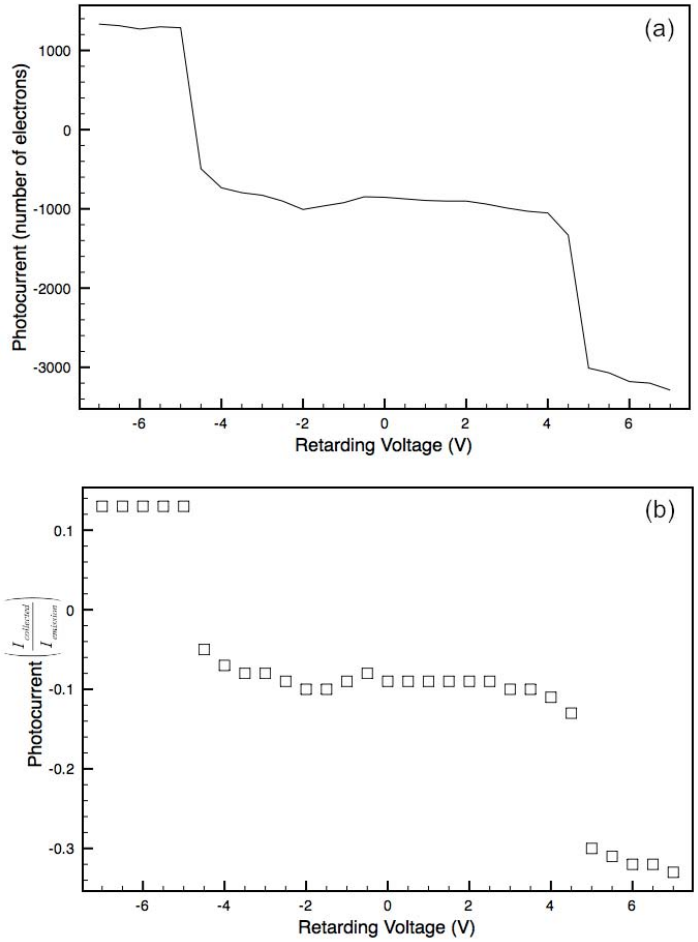

FIGURE 5.6: A simulated I(V) curve for the simple tip shown in figure 5.1. The retarding voltage is applied to the sample, therefore, the feature on the negative voltage side is due to the tip. On the positive voltage side, electrons from the sample are retarded, and the feature is from the DOS of the sample. (a) The photocurrent here is the photocurrent which is electrons hitting the tip minus electrons leaving the tip, i.e. electrons that leave the tip contribute a negative signal. Notice that the signal is mostly negative and is therefore dominated by the signal from the tip. (b) The signal has been normalised to the total number of electrons emitted.

Figure 5.7 shows the differential of the simulated I(V) signal in figure 5.6. Figure 5.7 shows clearly the features resolved from the tip and sample.

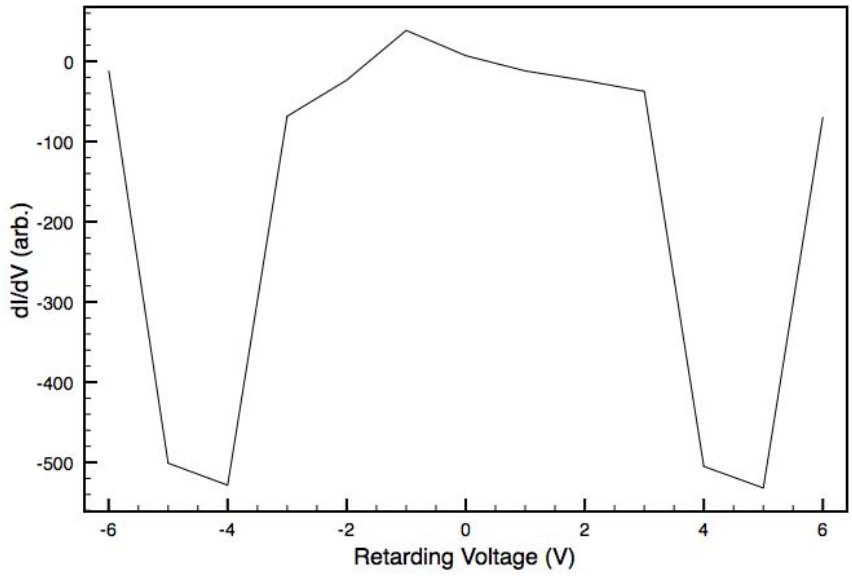

FIGURE 5.7: Simulated dI/dV spectrum for the simple tip shown in figure 5.1. The retarding voltage is applied to the sample. The feature in the negative voltage side is due to the feature in the tip's DOS. The feature seen in the positive side of the spectrum is due to the feature in the DOS of the sample.

The simulation suggests that a tip of this type could resolve sample features in the experiments performed in chapter 4, however, this is not a perfect simulation of the experiment. In the case of the simulations an ideal scenario has been imagined, where only 100 nm of the tip and sample is illuminated, this is done to keep the number of electrons manageable but flatters the real scenario in which at least 0.1 mm of the tip and sample is illuminated. In this case, the contribution to the signal from the tip scales with the size, but the contribution to the sample does not increase simply because there are more electrons. To understand why the spotsize is so important, consider again figures 5.2 and 5.5, the field created by the tip causes the majority of electrons to be pushed away from the tip, electrons

further away from the tip will not contribute to the signal, this is advantageous in terms of spatial resolution but it means that the signal from the sample is, in reality, much weaker than the signal from the tip.

By choosing a single energy, and simulating only electrons generated at the sample, it is possible to test the percentage of sample electrons the simple tip actually collects, given the size of the simple tip it would be expected to be very high. The spatial resolution can also be tested in this way. Therefore the simulation was run for a single voltage of 3 V and a single electron energy of 5 eV, only sample electrons were generated and the origin of every electron that reaches the tip is recorded, 50000 electrons were simulated for four different tip-sample distances (10 nm, 100 nm, 500 nm and 1000 nm). The percentage of sample electrons detected is given as a function of tip-sample distance in figure 5.8.

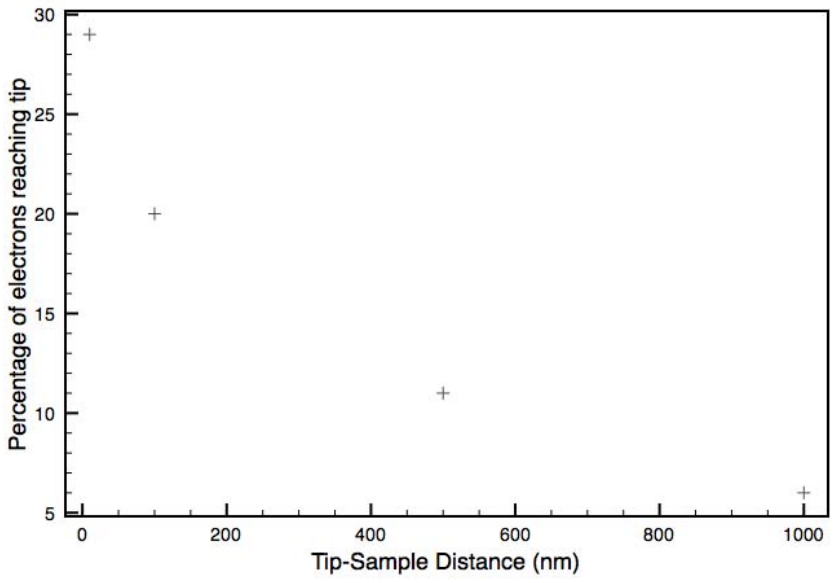

FIGURE 5.8: The percentage of electrons generated at a sample surface detected by the simple tip, figure 5.1, as a function of tip-sample separation. As the distance between the tip and the sample is increased the amount of electrons that the tip actually detects decreases.

The percentage signal that a simple tip can detect decreases as a function of the distance between the tip and sample according to figure 5.8. The experimental work was performed at large, 100-1000 nm, tip-sample distances, this would mean a drop is signal intensity from the sample compared to the simulation presented in figures 5.6 and 5.7. The decrease in signal intensity as a function of tip-sample separation is due to the trajectories of electrons being pushed away from the tip, at larger separations there is more time for the field to act upon the electron trajectories and less electrons actually reach the tip.

Figure 5.9 shows the resolution for the four different tip-sample distances. 50000 electrons generated at the sample surface with energy of 5 eV are simulated, for each that is detected by the simple tip the origin position is recorded, this is plotted as a histogram to give some indication of the resolution of the simple tip.

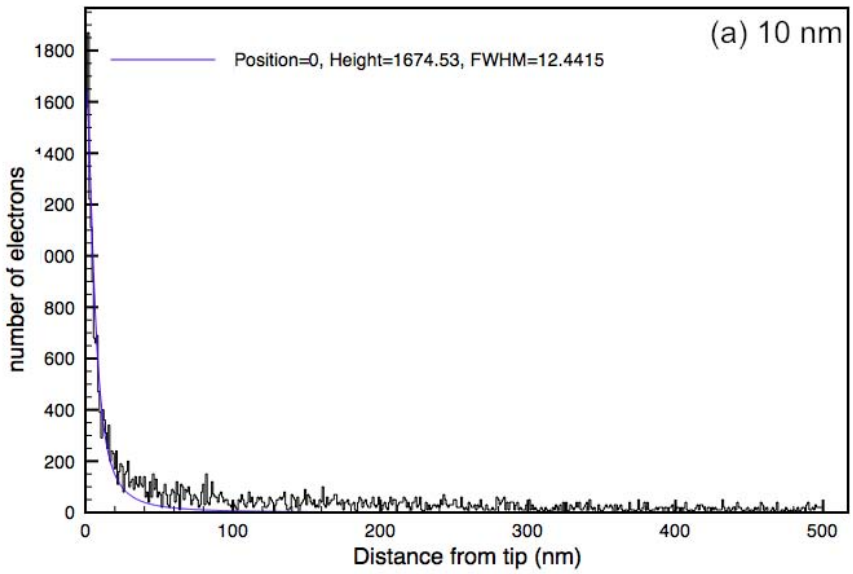
(a) 10 nm
Position=0, Height=1674.53, FWHM=12.4415
number of electrons
Distance from tip (nm)
0
100
200
300
400
500

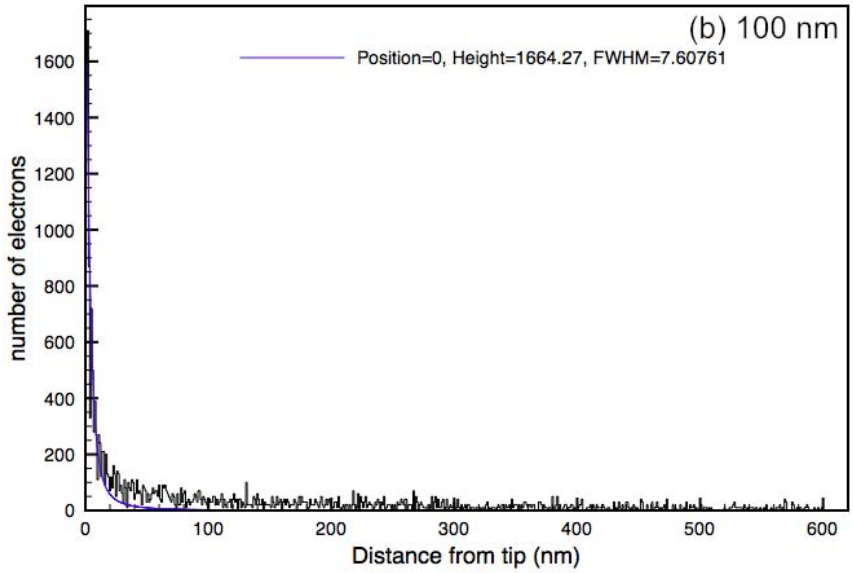
(b) 100 nm
Position=0, Height=1664.27, FWHM=7.60761
number of electrons
Distance from tip (nm)
0
100
200
300
400
500
600

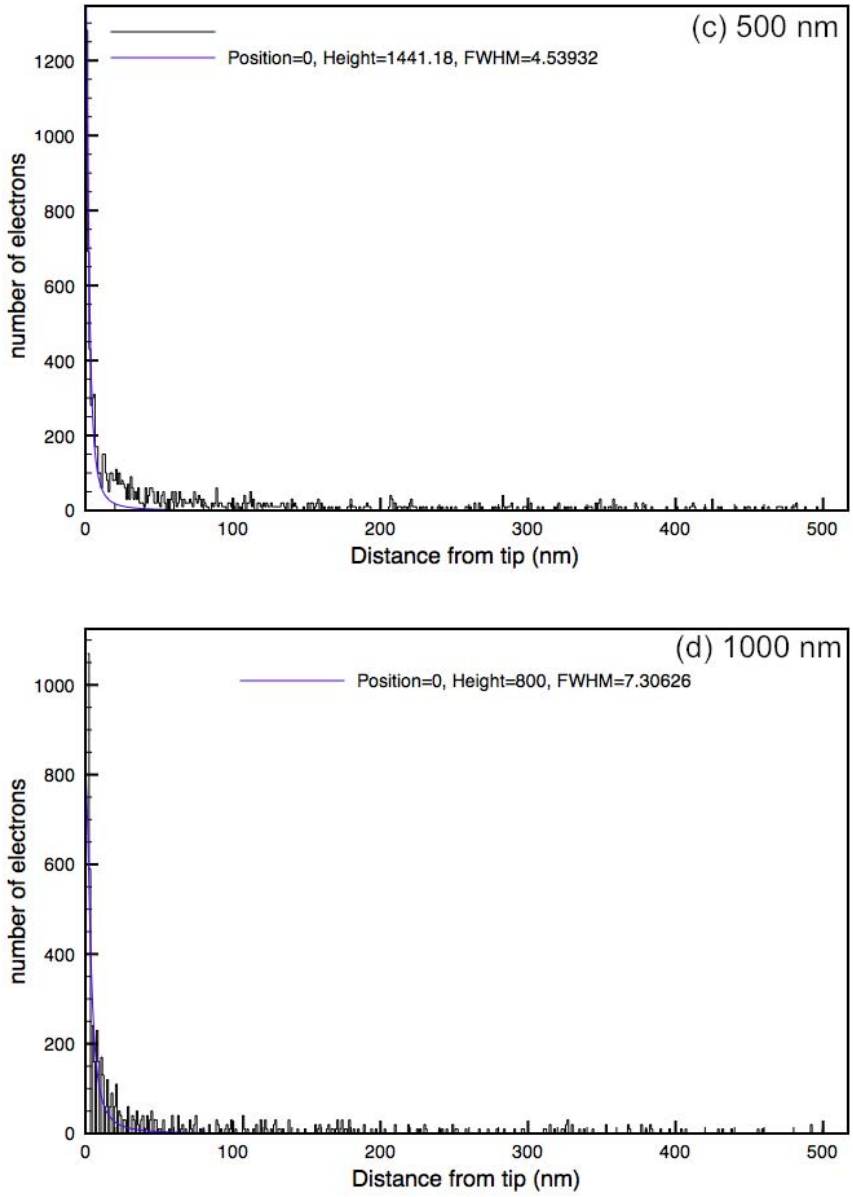

FIGURE 5.9: The resolution of the simple tip for four different tip-sample distances (a) 10 nm and (b) 100 nm (c) 500 nm (d) 1000 nm. 50000 electrons were simulated and the position of each detected electron recorded, these positions are binned into a histogram with 1 nm bin size. A Gaussian curve is fitted and the Full Width Half Maximum (FWHM) of the curve gives some indication of the resolution.

Figure 5.10 shows the resolution of the simple tip as a function of tip sample separation, the resolution is obtained from curve fitting to the histograms presented in figure 5.9. The resolution is assumed to be the FWHM of a Gaussian curve, however, it may be more realistic to consider the resolution to be the size of the base of the Gaussian which would encompass about 95% of the electrons detected, in which case the resolutions presented here should be multiplied by ≈1.7.

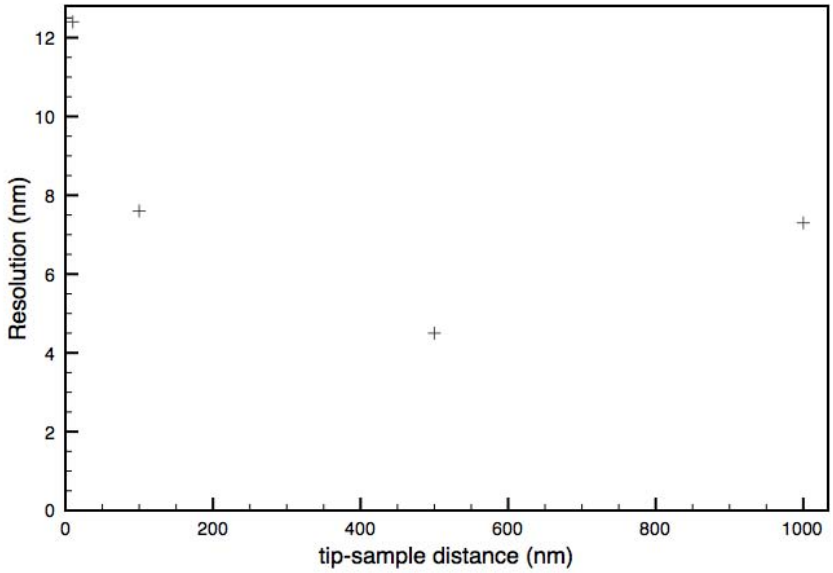

FIGURE 5.10: The resolution of the simple tip as a function of tip-sample separation. In general the resolution tends to improve with increasing tip-sample distance.

According to figure 5.10 there is some general trend to improving resolution, i.e. collecting electrons from a smaller area, with increasing tip-sample distance. When the tip signal is dominant it would be preferable to collect electrons from a larger area. Experiments were performed with large tip-sample separations, at large separation there is more time for the field to affect the electron paths and push electrons away from the tip, reducing the signal detected.

5.2.2 Coaxial Tip

In order to successfully resolve electronic states of a sample the contribution to the signal made by the tip must be reduced. This could be done by focusing the beam under the tip, but to improve spatial resolution the tip should be placed as close to the surface as possible without being in tunnelling contact, a distance of 5 - 10 nm would be reasonable, it is not possible to focus a VUV beam this much. The simpler option is to shield the tip and thus a microfabricated coaxial tip is proposed. A coaxial tip could be a tungsten tip coated with a shield layer or a microfabricated silicon tip as discussed in chapter 4. Schematics of the simple W tip and coaxial tip are shown in figure 5.11. It is expected that reducing the size of the tip/collector will increase the spatial resolution, this can be seen by looking at a simple geometrical picture as in figure 5.11. Photoelectrons are generated with a range of angles, ignoring field effects, the furthest electrons reach the tip from a 45° angle. A simple W tip, electrochemically etched, can at best have a size and corresponding collection area of $\approx$ 3 mm, as shown in figure 5.11(a), whereas a microfabricated Si tip can have a geometry and collection area less than 50 nm as shown in figure 5.11(b).

A coaxial tip can be designed to collect electrons from a smaller area than a non-coaxial tip, the shielding of the tip will reduce the tip signal, but would the reduction in sample signal, due to reduction in collection area, hinder or improve the resolution of a sample's electronic features?

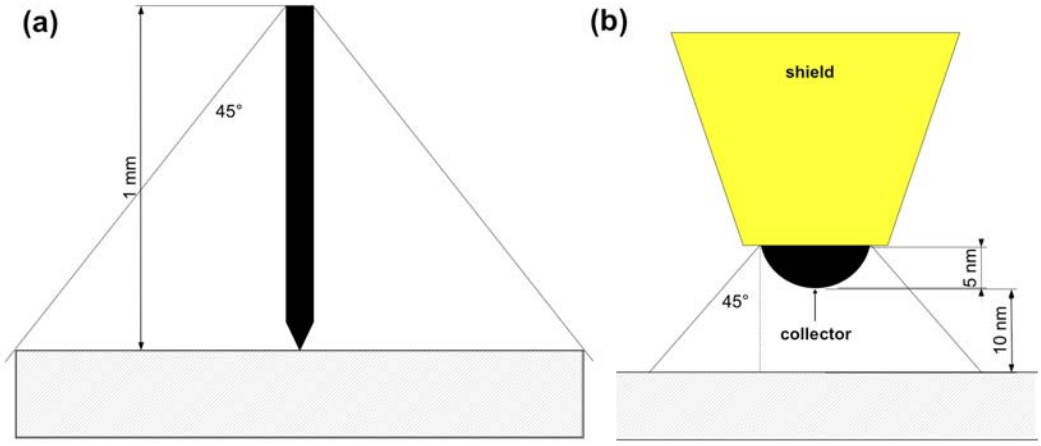

FIGURE 5.11: Electrons leave the surface with a range of angles therefore the area from which a tip collects electrons can be determined by the dimensions of the tip. (a) Electrochemical etched W tip: Assuming a best case scenario where the tip holder is shielded and the tip is as short as possible the tip can be expected to have a resolution of ≈ 3 mm. (b) Microfabricated coaxial tips: Using techniques available at NPRL a tip radius of 5 nm on the coaxial tip is achievable[135], such a coaxial tip can be expected to have a resolution of ≈ 50 nm.

The coaxial tip was simulated using the same simulation as for the simple tip, the simulation domain of the coaxial tip is shown alongside the simple tip in figure 5.12.

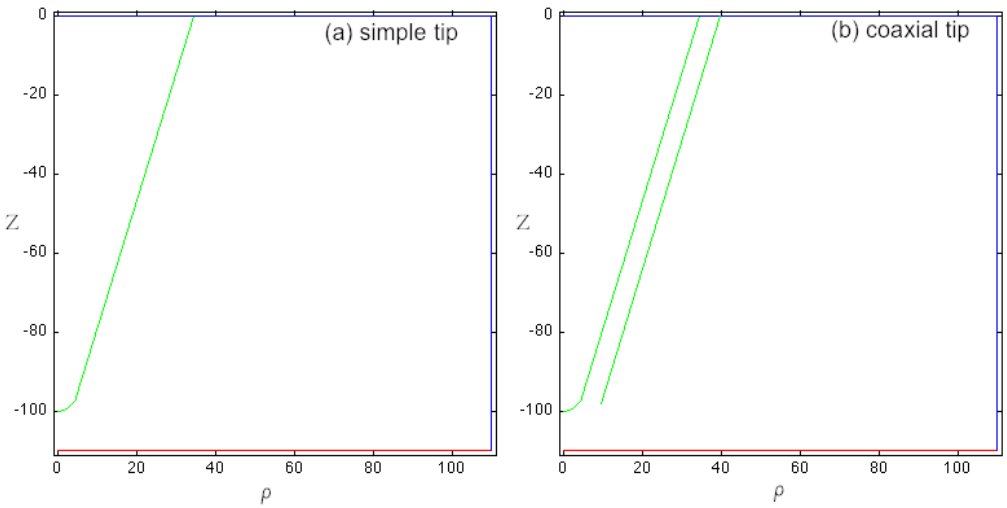

FIGURE 5.12: A non-coaxial and coaxial tip. The components of the tip are represented in green, the sample in red and the boundaries are blue. The boundaries are used to determine if an electron leaves the simulation area or will continue to be detected by the larger part of the tip in the case of a non-coaxial tip. (a)Simple/non-coaxial tip: In this case a non-coaxial tip with tip radius 5 nm is positioned 10 nm from the surface with a length of 100 nm. (b) Coaxial tip: The coaxial tip has a grounded layer that acts as a shield. The tip radius is 5 nm, the tip is 10 nm from the surface with a length of 100 nm, the shield length is 95 nm. The dielectric that would be required between the tip and the shield is not included in simulations.

For the coaxial tip the density of states from the tip and sample were given a feature at 5 eV kinetic energy, with a flat spread of energies between 0 and 15 eV, the same as the simple tip, the shield of the tip is given a feature at 3 eV. The bias voltage, applied to the tip, is scanned between -7 V and 7 V in steps of 1 V in order to test the tips ability to resolve it's own energy states and those of the sample. Each data point represents 10000 electrons. The field calculations were performed on grids of size 200 by 200, and solved over 1000 iterations. Electron paths were calculated until the electron hit an electrode, the time steps were

10^{-15} s when electrons were measured to be more than 2 nm from any electrodes, time steps were reduced to 10^{-17} s when the electron-electrode distance became less than 2 nm. Secondary electrons are not considered neither is the dielectric that would be required between the tip/collector and the shield. The coaxial tip has the retarding bias applied to the tip/collector while the shield and sample are grounded, the current is measured at the collector. For easy comparison of spectra, from the coaxial tip to the simple tip, the data for the coaxial tip is presented as a function of retarding bias as though it were applied to the sample in figure 5.13.

In figure 5.13(a) the feature highlighted in red is very clearly from the sample, as the retarding voltage increases the electrons from the sample are retarded and when the electrons from the feature with 5 eV kinetic energy are unable to reach the tip a large change in signal is seen. The feature highlighted in blue in figure 5.13(a) is not so obvious, it appears around the energy of the feature in the shields density of states, but does not appear to be from the retardation of these electrons but rather the attraction. It is possible that with high enough positive voltage on the tip (negative retarding voltage) the electrons from the shield are attracted to the tip and so a feature is seen once the energy is high enough to attract the bulk of these electrons, this also explains why the feature is not at exactly 3 V. Although the coaxial tip collects electrons from a smaller area the signal is still dominated by electrons from the sample and the sample feature can be clearly resolved.

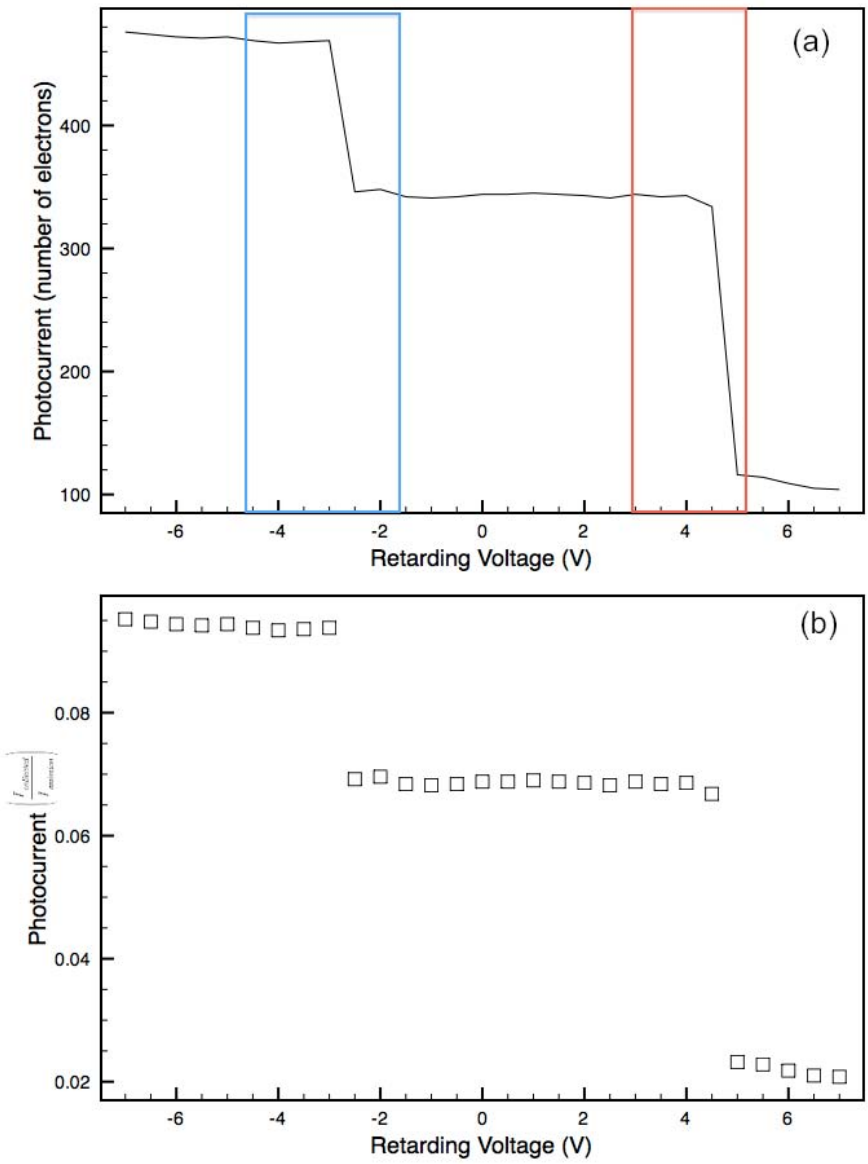

FIGURE 5.13: A simulated I(V) curve for the coax tip shown in figure 5.12. The retarding voltage is applied to the tip but the data has been rearranged for direct comparison with the simple tip. Therefore, the feature on the negative voltage side would be due to the tip and features on the positive voltage side are due to the sample. (a) The photocurrent is the number of electrons hitting the tip minus those electrons that leave the tip, notice that the photocurrent is entirely positive, the photocurrent signal is dominated by the sample. (b) The signal has been normalised to the total number of electrons emitted.

Figure 5.14 shows the differential of the simulated I(V) signal in figure 5.13. Figure 5.14 shows clearly the feature of the tip and the feature attributed to the shield.

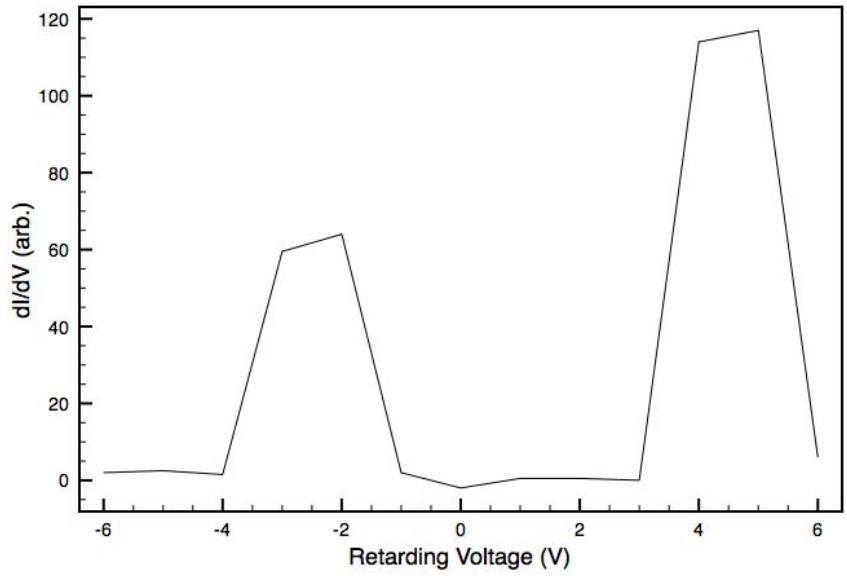

FIGURE 5.14: Simulated dI/dV spectrum for the coax tip shown in figure 5.12. The retarding voltage is applied to the tip but, as in figure 5.13, the x-axis has been reversed for direct comparison to the simple tip.

It is expected that, due to the shielding, the amount of electrons generated at the tip will be greatly reduced. However, the smaller collection area will also reduce the amount of electrons, collected by the tip, that have been generated at the sample. To investigate this the simulation was run for a single voltage of 3 V and a single electron energy of 5 eV, only sample electrons were generated and the origin of every electron that reached the tip was recorded, 50000 electrons were simulated for four different tip-sample distances (10 nm, 100 nm, 500 nm and 1000 nm). At 500 and 1000 nm the signal is found to drop to a negligible amount. The percentage of sample electrons detected is given as a function of tip-sample distance in figure 5.15.

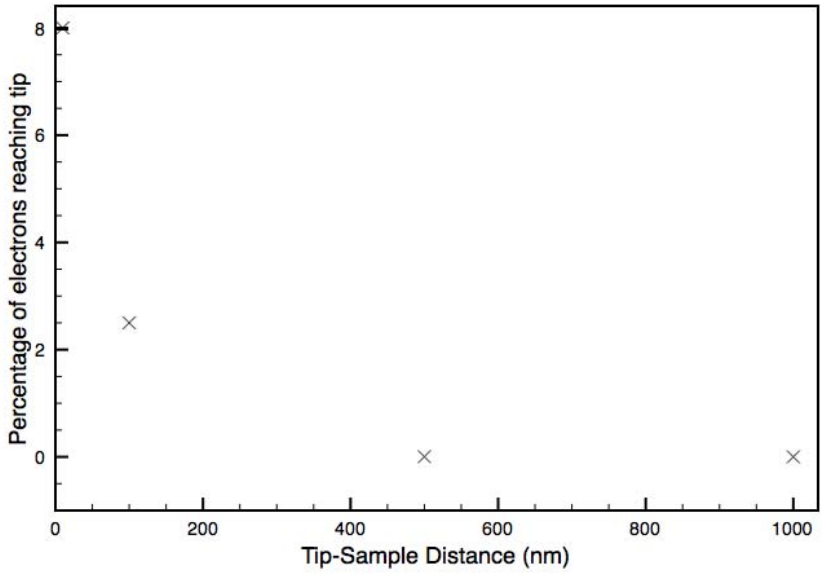

FIGURE 5.15: The percentage of electrons collected by the tip/collector of the coaxial tip, shown in figure 5.12(b), as a function of tip-sample separation. As the tip is moved away from the surface the signal intensity drops.

The percentage of photoelectrons generated at a sample collected by the coaxial tip is very low, just a couple of percent, and drops dramatically with increasing distance. However, operating the tip within 10 nm of a surface is not a problem, this kind of tip-sample distance is ideal for imaging a surface and quickly taking spectra at predefined spots.

Figure 5.16 shows the resolution for two different tip-sample distances, the data for 500 nm and 1000 nm is not shown as the signal is so low. 50000 electrons generated at the sample surface with energy of 5 eV are simulated, for each that is detected by the coaxial tip the origin position is recorded, this is plotted as a histogram to give some indication of the resolution of the coaxial tip.

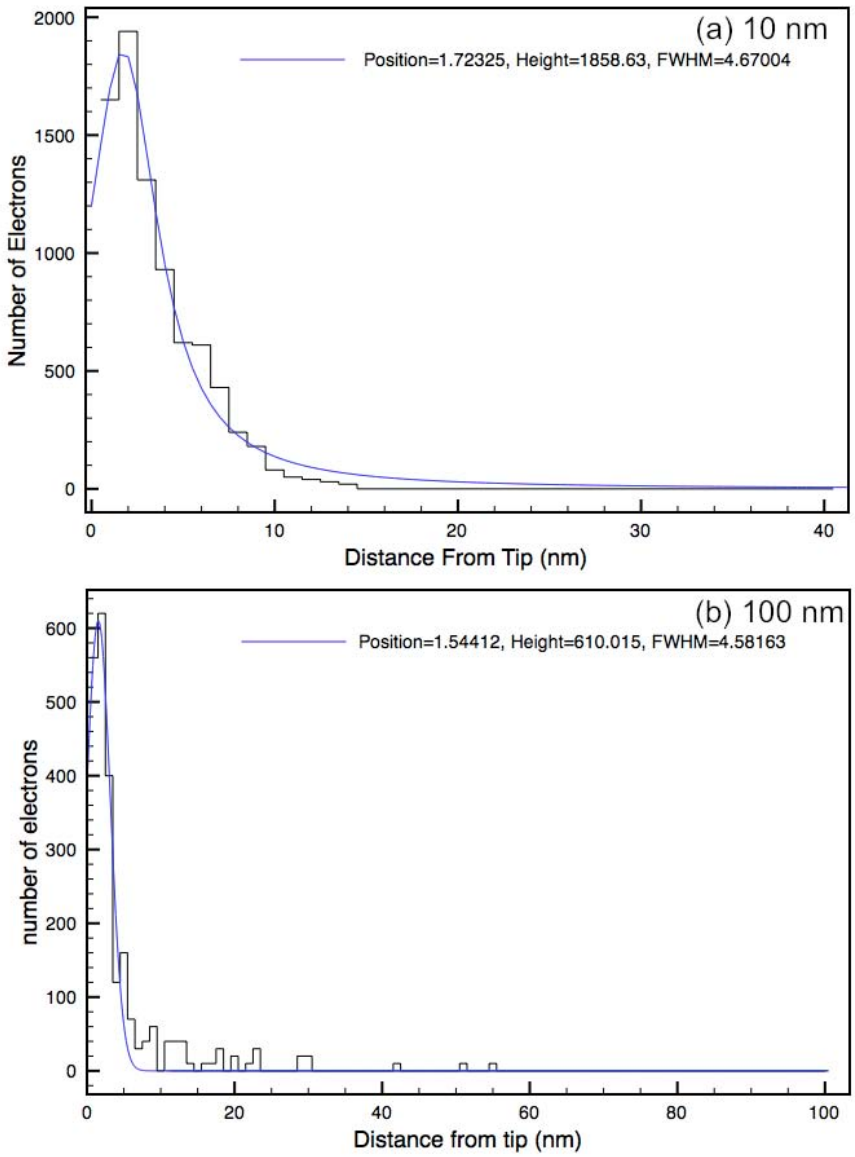

FIGURE 5.16: The resolution of the coaxial tip for two different tip-sample distances (a) 10 nm and (b) 100 nm. 50000 electrons were simulated and the position of each detected electron recorded, these positions are binned into a histogram with 1 nm bin size. A Gaussian curve is fitted and the Full Width Half Maximum (FWHM) of the curve gives some indication of the resolution.

Figure 5.17 shows the resolution of the coaxial tip as a function of tip sample separation, the resolution is obtained from curve fitting to the histograms presented in figure 5.16. For simplicity and consistency the resolution is assumed to be the FWHM of a Gaussian curve, as with the simple tip.

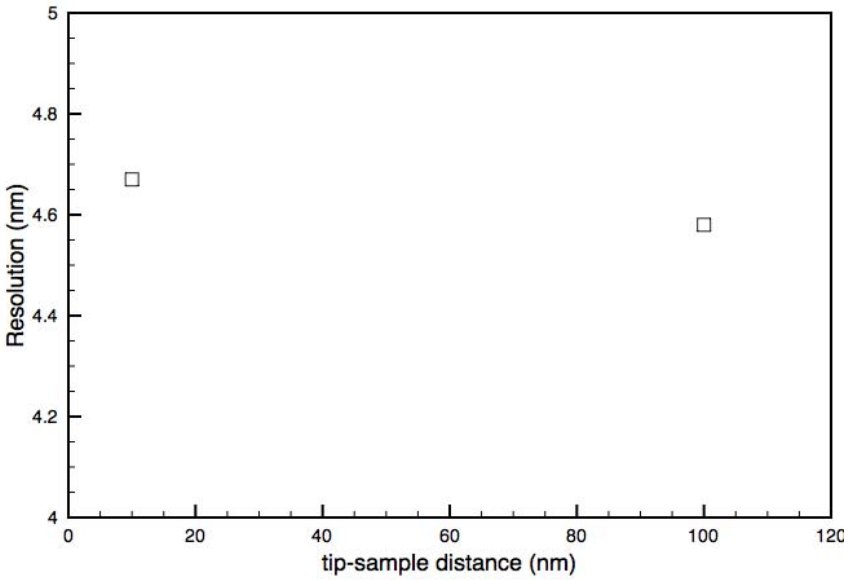

FIGURE 5.17: The resolution of the coaxial tip as a function of tip-sample separation. Only two data points are shown as for larger tip-sample separation the signal intensity is found to be negligible.

The resolution for the coaxial tip is around 5 nm between 10 – 100 nm tip-sample distance, this resolution is due to the field at the tip curving the trajectories of electrons improving the resolution when compared to the simple picture presented in figure 5.11.

5.3 Conclusions

The simulation of the simple tip presented here assumed a VUV spotsize of 500 nm, in reality the spotsize is more like 1 mm. The simulation suggested that with a smaller spotsize it should be possible to resolve the features on the sample. In the experimental work presented in chapter 4 this is not the case. Two reasons are proposed for this:

- Figure 5.8 shows that the amount of electrons collected from the sample reduces with increasing tip-sample distance, the experimental work was performed at larger tip-sample separations than the simulation.
- The area of the tip illuminated in the experimental work presented in chapter 4 was seven orders of magnitude larger than the assumed area in the simulations. All electrons generated at the tip contribute to the signal.

The points raised above combine to create a low sample signal with a much larger tip signal compared to simulations, this explains why the tip signal is so dominant. The simulation suggests that one solution is to reduce the spotsize but another solution is to use coaxial tips. The simulations of the coaxial tips show that features in the density of states in a sample can be resolved, and, according to figure 5.18, the coaxial tip offers improved spatial resolution. The area of the coaxial tip exposed to illumination is eight orders of magnitude smaller than the tip used in experimental work in chapter 4, therefore the contribution from the tip will be much smaller, this calculation is based on the area of tip exposed in

figure 5.12(b) which is a reasonable experimental aim according to work by Song et al.[133–135]

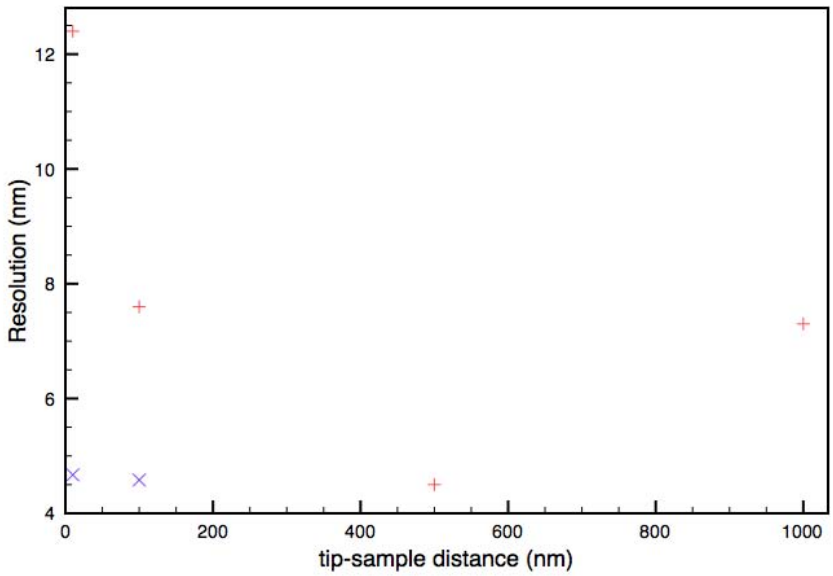

FIGURE 5.18: A comparison between the resolution offered by the coaxial tip, blue ×, and the simple tip, red +. The coaxial tip offers superior resolution.

The tip signal for the coaxial tip compared to the real tip should be eight orders of magnitude lower based on the surface area exposed. Figure 5.19 shows a direct comparison of the amount of electrons collected from the sample, i.e. the sample signal intensity, as a function of tip-sample separation.

Figure 5.19 suggests that the coaxial tip collects about five times less sample electrons than the simple tip, therefore the intensity of the signal can be expected to be five times less, however, the coaxial tip generates eight orders of magnitude less photoelectrons at the tip/collector. The signal from the coaxial tip is dominated by the sample, while the signal from the simple tip may be dominated by the tip itself in a real experimental set-up.

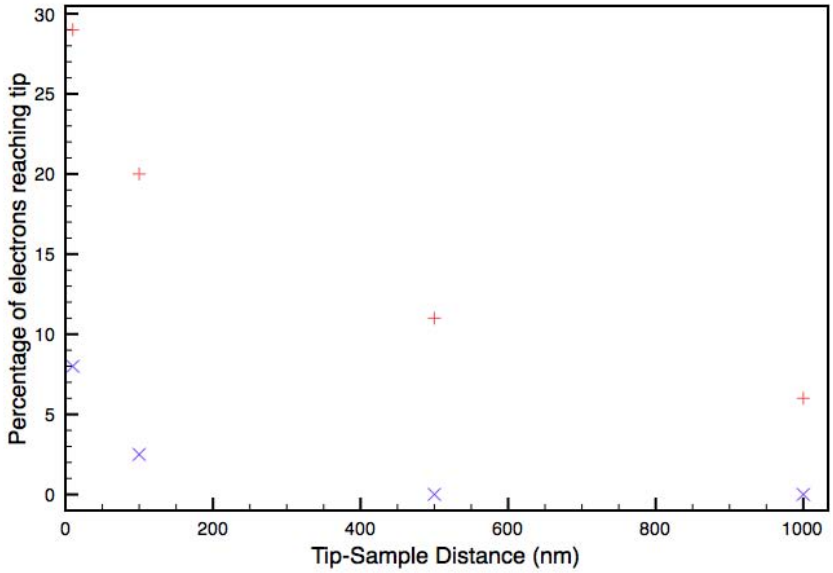

FIGURE 5.19: A comparison between the sample signal received by the coaxial tip, blue ×, and the simple tip, red +. The simple tip collects four or five times more electrons than the coaxial tip.

The simulation of the simple tip presented here does not exactly represent the set-up used in chapter 4, but rather a best case scenario, with a VUV spot-size on the tip of 500 nm, i.e. only 500 nm of the tip is exposed to light. In reality $\approx$ 1 mm of the tip was exposed to light and the contribution from the tip to the overall signal was far higher. It is possible to run these simulations taking into account the full tip contribution, but, for speed and simplicity this was not done here. The simulation of the coaxial tip is an experimentally possible situation, these simulations suggest that a coaxial tip would be capable of resolving features, in the DOS of states of a nanostructured surface, with a resolution approaching 5 nm, despite the illumination of the tip.

By using a coaxial tip the SPEAR technique would be able to resolve the electronic structure of individual nanoscale features on a surface, such as the elongated clusters discussed in chapter 3.1. Such an instrument would offer new insight, and new understanding, into the role that physical structure plays in the electronic structure of clusters. Understanding the electronic structure of clusters could lead to improvements in the fields of photonics, plasmonics, catalysis and more. This technique could probe the role of interfaces between materials, or different crystal orientations. Any structure on the scale of a few nanometres could be probed using the SPEAR technique combined with nanofabricated coaxial tips.

Chapter 6

Conclusions and Outlook

In chapter 1.3 the aims of the thesis were decribed as follows

- Design and construction of an Ultra High Vacuum system for the SPEAR technique.
- STM studies of nanostructured surfaces that may be suitable and interesting candidates for SPEAR measurements.
- Demonstrate the detection of a photocurrent with an STM tip.
- Demonstrate the ability to obtain photoelectron spectra of large flat samples of HOPG and Au using the SPEAR technique.
- Obtain SPEAR spectra of samples identified as suitable candidates by STM studies.

A UHV system was succesfully designed as outlined in chapter 4.5 this system was used for the SPEAR experiments, chapter 4 and experiments on size-selected clusters, chapter 3.1.

Two model surface structural systems, suitable for future SPEAR experiments, were identified and studied; size-selected clusters on Highly Oriented Pyrolytic Graphite (HOPG), 3.1, and methylphenyldisulphide on Si(111)-7×7, 3.2.

In chapter 3.1 large size selected clusters (3500 atoms and above) of Pd and Au on HOPG were found to exhibit non-spherical shapes through experiments performed with UHV-STM. The aspect ratios of these clusters increases with increasing cluster size. The non-spherical nature of these clusters is traced back to the aggregation regime in the gas condensation cluster source. The size and temperature of the clusters are believed to create a slow coalescence process that, given a high enough collision rate, leads to non-spherical clusters. If the non-spherical shape can be manipulated by the cluster source conditions, then the distinctive cluster properties could be controlled in novel electronics or media storage employing cluster plasmons or in catalysis/sensors.[94, 95, 150]

The molecule methylphenyldisulphide contains an S-S bond of great interest in nature, specifically in the stabilisation of folded proteins. The molecule was studied on Si(111)-7×7 by UHV-STM in chapter 3.2. Features corresponding to different bonding geometries were identified. The molecule was found to bond either as an intact molecule or as fragments after fission of the S-S bond upon landing. The molecule exhibits a 2:1 preference for the middle adatom of the 7×7 unit cell suggesting it enters a precursor state before adsorbing on the surface. The molecule also bonds to the STM tip in such a way that a reservoir is created which under

certain conditions paints the surface with molecules, a similar process to dipped pen lithography.[129]

In order to probe the local electronic structure of nanostructured surfaces like methylphenyldisulphide on Si(111)-7×7 and clusters on HOPG, scanning probe spectroscopy is required. The new SPEAR technique uses an STM tip to collect photoelectrons generated at a surface. The detection of a photocurrent, under illumination of the STM with vacuum ultraviolet light of 21.2 eV, with a W tip was demonstrated in chapter 4. In the case of a bare HOPG surface, electronic states of the tip are partially resolved. However, the large signal generated by photoelectrons from the tip does not allow the unambiguous resolution of the states of the surface at this point. It is therefore not possible to obtain SPEAR spectra on the samples identified in this thesis as potentially interesting with a normal STM tip. In order to achieve spectroscopy on the scale of nanometres a coaxial tip is required, this was demonstrated in chapter 5 using simulations written in Matlab. These simulations show that the difficulty in resolving electronic states of a surface with an ordinary tip is due to the large signal generated at the tip and the field in the system bending the electron paths away from the tip. The simulations demonstrate that a coaxial tip cuts out the majority of the tip signal, a coaxial tip is therefore able to resolve electronic states from the surface. The simulations demonstrate that the SPEAR technique could be improved upon, using coaxial tips, and achieve the spatial resolution required to resolve the electronic states of individual clusters on a surface. In particular this technique could be used to probe the non-spherical clusters identified in chapter 3.1, as mentioned previously such clusters will have unique optical and electronic properties that vary with size

and shape, by controlling the shape and probing the change in electronic struture using the SPEAR technique new avenues of investigation for catalysis, plasmonics and other cutting edge fields, become available.

Appendix A

Matlab Code

This code was written primarily by the author with input from Dr Wolfgang Theis. Dr Theis wrote some of the code for setting up the electrodes, in particular the setofelectrodes class, the initial set-up of the field from electrodes and the smoothfield function, all of which have since been corrected or edited by the author. The rest of the code, i.e. the solving of the field, the random generation of electrons and the calculation of electron energies and trajectories were written solely by the author.

A.1 Defining the Tip

```
classdef tip < handle

properties (SetAccess = protected)
listofelsets = []; overallsize;
areas =[];

end

properties (SetAccess = 'public')
voltage = [];
tiptype;

end

methods

function obj = tip()
end

function setupcoaxtip(obj,tipvol, samplevol, radius, dist, tiplen,ang,shieldvol)



obj.overallsize = tiplen+dist;

sam = setofelectrodes('sample');
el = electrode('sample', [0,0]);
el.setelectrode([0,obj.overallsize], [obj.overallsize,obj.overallsize], samplevol, samplevol, 1, 5);
sam.addelectrode(el);
obj.listofelsets = [obj.listofelsets sam];
```

```
stip = setofelectrodes('tip');
pmatch= [radius*sin(pi/2-ang), tiplen-radius+radius*cos(pi/2-ang)];
rtop = pmatch(1)+pmatch(2)*tan(ang);
el = electrode('tip side',[rtop+5,0]);
el.setelectrode(pmatch, [rtop,0], tipvol, tipvol, 1, 4);
stip.addelectrode(el);
el = electrode('tip apex', [0,0]);
el.setsphericalelectrode(tiplen-radius, radius, ang, tipvol, 4);
stip.addelectrode(el);
obj.listofelsets = [obj.listofelsets stip];



boun = setofelectrodes('bounding');
el = electrode('rmax bound',[0,0]);
el.setelectrode([obj.overallsize,0], [obj.overallsize,obj.overallsize], tipvol, samplevol,
1, 0);
boun.addelectrode(el);
el = electrode('top bound',[0,10]);
el.setelectrode([0,1/obj.overallsize], [obj.overallsize,1/obj.overallsize], tipvol, tipvol,
1, 4);
boun.addelectrode(el);
obj.listofelsets = [obj.listofelsets boun];

sshield = setofelectrodes('shield');
pmatch= [(radius+5)*sin(pi/2-ang), tiplen-radius+(radius+5)*cos(pi/2-ang)];
rtop = pmatch(1)+pmatch(2)*tan(ang);
el = electrode('shield side',[rtop+5,0]);
el.setelectrode(pmatch, [rtop,0], shieldvol, shieldvol, 1, 4);
sshield.addelectrode(el);
obj.listofelsets = [obj.listofelsets sshield];

obj.areas(1) = sam.area;
obj.areas(2) = stip.area;
```

```
obj.areas(3) = 0;
obj.areas(4) = sshield.area;

end

function setupsimpletip(obj,tipvol, samplevol, radius, dist, tiplen,ang)


obj.overallsize = tiplen+dist;

sam = setofelectrodes('sample');
el = electrode('sample', [0,0]);
el.setelectrode([0,obj.overallsize], [obj.overallsize,obj.overallsize], samplevol, samplevol, 1, 5);
sam.addelectrode(el);
obj.listofelsets = [obj.listofelsets sam];

stip = setofelectrodes('tip');
pmatch= [radius*sin(pi/2-ang), tiplen-radius+radius*cos(pi/2-ang)];
rtop = pmatch(1)+pmatch(2)*tan(ang);
el = electrode('tip side',[rtop+5,0]);
el.setelectrode(pmatch, [rtop,0], tipvol, tipvol, 1, 4);
stip.addelectrode(el);
el = electrode('tip apex', [0,0]);
el.setsphericalelectrode(tiplen-radius, radius, ang, tipvol, 4);
stip.addelectrode(el);
obj.listofelsets = [obj.listofelsets stip];


boun = setofelectrodes('bounding');
el = electrode('rmax bound',[0,0]);
el.setelectrode([obj.overallsize,0], [obj.overallsize,obj.overallsize], tipvol, samplevol, 1, 0);
boun.addelectrode(el);
```

```
el = electrode('top bound',[0,10]);
el.setelectrode([0,1/obj.overallsize], [obj.overallsize,1/obj.overallsize], tipvol, tipvol,
1, 4);
boun.addelectrode(el);
obj.listofelsets = [obj.listofelsets boun];

obj.areas(1) = sam.area;
obj.areas(2) = stip.area;
obj.areas(3) = 0;

end

function dist = distancefrom(obj,r,z)
d1 = obj.listofelsets(1).distancefrom(r,z);
n = 1;
for i=2:length(obj.listofelsets)
d2 = obj.listofelsets(i).distancefrom(r,z);
if abs(d2(3)) < abs(d1(3))
d1 = d2;
n = i;
end
end
dist = [n, d1];
end


function draw(obj, sn)
obj.listofelsets(1).draw('r', sn);
hold on
obj.listofelsets(2).draw('g', sn);
hold on
obj.listofelsets(3).draw('b', sn);
hold on
try
```

```
obj.listofelsets(4).draw('g', sn);
end
hold off
axis([-1 obj.overallsize+1 -obj.overallsize-1 1])
axis square
end


function y = randomelectrodeset(obj)
y = randsample(length(obj.areas),1, true,obj.areas);


end


end


end
```

A.2 Defining Electrodes

```
classdef electrode < handle


properties (SetAccess = protected)


pst = [];
pend = [];
vst = 0;
vend = 0;
nrpositive = true;
zcentre;
radius;
theta;
isspherical;
wf;
elname;
outside;
snplusminus;


end


methods
function obj = electrode(elname, outside)
obj.elname = elname;
obj.outside = outside;
end

function setelectrode(obj,pst,pen,vst,vend,sn,wf)

obj.pst = pst;
obj.pend = pen;
```

```
obj.vst = vst;
obj.vend = vend;
obj.nrpositive = sn;
obj.isspherical = false;
obj.snplusminus = 1;
obj.wf = wf;
d = obj.distancefrom(obj.outside(1),obj.outside(2));
if d(2) < 0
obj.snplusminus = -1;
end



end

function setsphericalelectrode(obj, zc, rad, thet, volt, wf)

obj.zcentre = zc;
obj.radius = rad;
obj.theta = thet;
obj.vst = volt;
obj.vend = volt;
obj.isspherical = true;
obj.snplusminus = 1;
obj.wf = wf;
end



function y = vacuumlevel(obj, lam)

y = obj.vst *(1-lam)+ obj.vend*lam + obj.wf;v
end

function y = rzof(obj, lam)
```

```
if obj.isspherical == true
y = [obj.radius*sin((pi/2-obj.theta)*lam'), obj.radius*cos((pi/2-obj.theta)*lam')+obj.zcentre];
else y = [obj.pst(1) *(1-lam')+ obj.pend(1)*lam', obj.pst(2) *(1-lam')+ obj.pend(2)*lam'];
end

end



function y = surfnormal(obj, lam)

if obj.isspherical == true
m = obj.rzof(lam)-[0,obj.zcentre];
y = m/sqrt(m*m');
else
d = obj.pend - obj.pst;
m = [d(2),-d(1)];
y = m/sqrt(m*m').*obj.snplusminus;
end

end

function y = tangent(obj, lam)

if obj.isspherical == true
m = obj.rzof(lam)-[0,obj.zcentre];
y = m/sqrt(m*m')*obj.radius*(pi/2-obj.theta);
y = [y(2),-y(1)];
else
y = obj.pend - obj.pst;
end

end
```

```
function y = area(obj)

if obj.isspherical == true
y = 2*pi*obj.radius*sin(obj.theta)^2;
else
y = pi*(obj.pst(1)+obj.pend(1)) *sqrt((obj.pst(1)+obj.pend(1))^2+(obj.pst(2)-
obj.pend(2))^2);
end
end



function y = randomlam(obj)
if obj.isspherical == true
lam = 0:1/1000:1;
weight = sin(lam*obj.theta);
y = randsample(length(lam),1,true,weight)/1000;

else
lam = 0:1/1000:1;
r = obj.pst(1):(obj.pst(2)-obj.pst(1))/1000:obj.pst(2);

weight = 2*pi*r;
y = randsample(length(lam),1,true,weight)/1000;
end
end

function draw(obj,c)
if obj.isspherical == true
lam = 0:1/100:1;
pa = obj.rzof(lam);
r = pa(:,1);
z = pa(:,2);
```

```
else
z = [obj.pst(2) obj.pend(2)];
r = [obj.pst(1) obj.pend(1)];

end
plot(r,-z,c)
hold on;
end

function drawsurfacenormals(obj,c)
for lam = 0:1/10:1
obj.drawsurfacenormalat(c,lam);
end
end

function drawsurfacenormalat(obj,c,lam)
pa = obj.surfnormal(lam);
rz = obj.rzof(lam);
r = [rz(1), rz(1) + pa(1)];
z = [rz(2), rz(2) + pa(2)];
plot(r,-z,c)
hold on;
end

function dist = distancefrom(obj,r,z)
if obj.isspherical == true
ra = sqrt((z-obj.zcentre)^2+(r^2));
lam = 0.5;
if lam > 1
d = [r,z]-obj.rzof(1);
dist = [1, d*d'];
else
```

```
dist = [lam, ra-obj.radius];
end
else
ta = obj.tangent(0.5);
lam = (ta*[r,z]' - ta*obj.pst')/(ta*ta');
if lam < 0
lam = 0;
d = [r,z]-obj.pst;
s = d*obj.surfnormal(lam)';
d = sign(s)*sqrt(d*d');
else
if lam > 1
lam = 1;
d = [r,z]-obj.pend;
s = d*obj.surfnormal(lam)';
d = sign(s)*sqrt(d*d');
else
d = [r,z]-obj.pst;
d = d*obj.surfnormal(lam)';
end
end
dist = [lam, d];
end
end



end


end


classdef setofelectrodes < handle

properties
```

```
electrodelist = [];
ar = [];
setelname;

end



methods

function obj = setofelectrodes(name)
obj.setelname = name;

end


end


methods
function y = area(obj)


y = 0;


for n=1:length(obj.electrodelist)
y = y + obj.electrodelist(n).area;
end
end



function y = randomelectrode(obj)

w = obj.ar;
```

```
w(3) = 0;
y = randsample(length(w),1,true,w);


end


function addelectrode(obj, electr)
obj.ar = [obj.ar electr.area];
obj.electrodelist = [obj.electrodelist electr];


end


function draw(obj,c, sn)
for n=1:length(obj.electrodelist)
obj.electrodelist(n).draw(c);
if sn
obj.electrodelist(n).drawsurfacenormals(c);
end
hold on;
end
end


function dist = distancefrom(obj,r,z)


dmin = [1 obj.electrodelist(1).distancefrom(r,z)];


for n=2:length(obj.electrodelist)
d1 = obj.electrodelist(n).distancefrom(r,z);
if abs(d1(2)) < abs(dmin(3))
dmin = [n d1];
end
```

```
end
dist = dmin;
end



end


end
```

A.3 Solving Electric Field

```
classdef electricfield < handle

properties

gridsize = 100;
potential;
isfixed;
gamma = 1;
scalingfactor;
tipgeom;
lapl;
end


methods

function obj = electricfield(tipgeom, gridsize, usediff)


obj.tipgeom = tipgeom;
obj.gridsize = gridsize;
obj.scalingfactor = obj.tipgeom.overallsize/obj.gridsize;


obj.potential = zeros(obj.gridsize,obj.gridsize);
obj.isfixed = zeros(obj.gridsize,obj.gridsize);
obj.lapl = zeros(obj.gridsize,obj.gridsize);

if usediff
obj.setfixedandpotentialfromdiff();
else
obj.setfixedandpotentialstepalong();
```

```
end


end



function setfixedandpotentialfromdiff(obj)
for i = 1:obj.gridsize
for j =1:obj.gridsize

d = obj.tipgeom.distancefrom((i-1)*obj.scalingfactor,(j-1)*obj.scalingfactor);

if abs(d(4)) < obj.scalingfactor*1.5
obj.potential(i,j) = obj.tipgeom.listofelsets(d(1)).electrodelist(d(2)).vacuumlevel(d(3));
obj.isfixed(i,j) = d(1);

end
end
end
end


function setfixedandpotentialstepalong(obj)
si = obj.tipgeom.overallsize;
for s = 1:length(obj.tipgeom.listofelsets)
for e =1:length(obj.tipgeom.listofelsets(s).electrodelist)
el = obj.tipgeom.listofelsets(s).electrodelist(e);
for lam = 0:1/2/obj.gridsize:1
rz = el.rzof(lam);
sn = el.surfnormal(lam);
for f = 0:10
ij = round(rz/obj.scalingfactor - sn*si/obj.gridsize);
i = ij(1);
j = ij(2);
```

```
if (i>0) && (i<=obj.gridsize) && (j>0) && (j<=obj.gridsize)
obj.potential(i,j) = obj.tipgeom.listofelsets(s).electrodelist(e).vacuumlevel(lam);
obj.isfixed(i,j) = s;
end
end
end
end
end
end

function y = mylaplace (obj,r,z)

a = obj.potential(r,z-1);
b = obj.potential(r,z+1);
c = obj.potential(r-1,z);
c = c - c/(2*r);
d = obj.potential(r+1,z);
d = d + d/(2*r);

y = -4*obj.potential(r,z) +(a + b + c + d);
end

function showlapl(obj)

for i = 2:obj.gridsize-1
for j =2:obj.gridsize-1
obj.lapl(i,j) = obj.mylaplace(i,j);
end
imagesc(obj.lapl), colorbar
axis square
end

end
```

```
function y = calcpotential(obj,itmax, gamma,myTolerance)


check = 0;


iteration = 1;


test = 1;
test1 = 1:10;


stop = 0;


while ((test > myTolerance && stop ~=1) && (iteration < itmax)),


C = obj.potential;


for i = 1:obj.gridsize^2



r = randsample(obj.gridsize-1,1);
z = randsample(obj.gridsize-1,1);


if z == 1
z = 2;
end

if obj.isfixed(r,z) == 0
if r == 1
v = obj.potential(r,z+1)/4 + (obj.potential(r,z-1)/4) + obj.potential(r+1,z)/2;
```

```
else
a = obj.potential(r,z-1);
b = obj.potential(r,z+1);
c = obj.potential(r-1,z);
c = c - c/(2*r);
d = obj.potential(r+1,z);
d = d + d/(2*r);


v = (a + b + c + d)/4;
end
obj.potential(r,z) = obj.potential(r,z) + gamma*(v-obj.potential(r,z));


end


end


D = C-obj.potential;
if iteration > 100
for jj = 1:1:length(test1)
check = check + test1(jj);
end
check = check/10;
check = check/test;
if check == 1;
stop = 1;
end
check = 0;
end
test = max(max(abs(D)));
if mod(iteration,10) ~= 0
test1(mod(iteration,10)) = test;
else
```

```
test1(10) = test;
end


iteration = iteration + 1;


y = obj.potential;


end


end


function disp(obj)

imagesc(obj.potential), colorbar
axis square

end


function f = smoothfield(obj, x , y)


y = y/obj.scalingfactor+1;
x = x/obj.scalingfactor+1;
nrx = obj.gridsize;
nry = obj.gridsize;
nx = floor(x);
ny = floor(y);
if(nx<1)
nx=1;
end
if(ny<1)
```

```
ny=1;
end
if(nx>=nrx)
nx=nrx-1;
end
if(ny>=nry)
ny=nry-1;
end

dx = x-nx;
dy = y-ny;

sv = obj.potential(nx,ny) + dx*(obj.potential(nx+1,ny)-obj.potential(nx,ny)) +
dy*(obj.potential(nx,ny+1)-obj.potential(nx,ny))+
dx*dy*(obj.potential(nx+1,ny+1)-obj.potential(nx,ny+1) - obj.potential(nx+1,ny)
+ obj.potential(nx,ny));

Er = (obj.potential(nx+1,ny)-obj.potential(nx,ny)) + dy*(obj.potential(nx+1,ny+1)-
obj.potential(nx,ny+1) - obj.potential(nx+1,ny) +
obj.potential(nx,ny));

Ez = (obj.potential(nx,ny+1)-obj.potential(nx,ny)) + dx*(obj.potential(nx+1,ny+1)-
obj.potential(nx,ny+1) - obj.potential(nx+1,ny) +
obj.potential(nx,ny));

f = [sv, Er,Ez];



end


end
end
```

A.4 Generating a Random Electron

```
classdef energydist < handle

properties
sample;
tip;
shield;
feature_ tip = 8;
feature_ sam = 8;
feature_ shi = 5;
ephot = 21;


end

methods
function obj = energydist(f_ tip, f_ sam, f_ shi)
obj.feature_ tip = f_ tip;
obj.feature_ sam = f_ sam;
obj.feature_ shi = f_ shi;
i = 0;
for energy = 0:0.1:obj.ephot
i = i+1;
obj.sample(i,1) = energy;
obj.sample(i,2) = 1;
end
k = round(obj.feature_ sam/0.1);
obj.sample(k,1) = obj.feature_ sam;
obj.sample(k,2) = 10;


i = 0;
for energy = 0:0.1:obj.ephot
i = i+1;
```

```
obj.tip(i,1) = energy;
obj.tip(i,2) = 1;
end
k = round(obj.feature_ tip/0.1);
obj.tip(k,1) = obj.feature_ tip;
obj.tip(k,2) = 10;



i = 0;
for energy = 0:0.1:obj.ephot
i = i+1;
obj.shield(i,1) = energy;
obj.shield(i,2) = 1;
end
k = round(obj.feature_shi/0.1);
obj.shield(k,1) = obj.feature_shi;
obj.shield(k,2) = 10;


end


function x = getkinenerg(obj, n, vacuum)
x = 0;


if n == 1
x = 8 - vacuum;
if x < 0
x = 0;
end
end
if n == 4
x = 5 - vacuum;
if x < 0
```

```
x = 0;
end

end
if n == 2
x = 8 - vacuum;
if x < 0
x = 0;
end
end


end


end


end


classdef randelec < handle


properties


vr;
vz;
vtheta;
orig_electrode;
startpos = [];
kin_energy;
charge = 1.60217646*10^(-19);
mass = 9.10938188*10^(-31);
elsetnr;
elnr;
```

```
iscos2;
vacuumlevel;
originating_position;



end

methods
function obj = randelec(tipgeom, energ_dist)

obj.elsetnr = tipgeom.randomelectrodeset();
obj.elnr = tipgeom.listofelsets(obj.elsetnr).randomelectrode();
obj.orig_electrode = tipgeom.listofelsets(obj.elsetnr).electrodelist(obj.elnr);
obj.originating_position = obj.orig_electrode.randomlam();
obj.startpos = obj.orig_electrode.rzof(obj.originating_position);
obj.kin_energy = energ_dist.getkinenerg(obj.elsetnr,
obj.orig_electrode.vacuumlevel(obj.originating_position));

norm = obj.orig_electrode.surfnormal(obj.originating_position);
anglenorm = atan2(norm(1),norm(2));
anglerange = -pi/2+anglenorm:0.1:pi/2+anglenorm;
w = cos(anglerange).^2;
k = randsample(length(anglerange),1,true,w);
angle = anglerange(k);
k = randsample(length(anglerange),1,true,w);
anglephi = anglerange(k);
v = sqrt((2*obj.kin_energy*obj.charge)/obj.mass)*(10^9);
obj.vz = v*cos(angle);
obj.vr = v*sin(angle)*cos(anglephi);
obj.vtheta = v*sin(angle)*sin(anglephi);

obj.iscos2 = angle-anglenorm;
```

```
obj.vacuumlevel = obj.orig_electrode.vacuumlevel(obj.originating_position);

end



end

end
```

A.5 Solving Paths

```
classdef elecpath

properties

elp = [];
sethit;
electronleavestip = 0;

tf = 10000000;
tdelta = 10^(-16);
charge = -1.60217646*10^(-19);
mass = 9.10938188*10^(-31);


end

methods
function obj = elecpath(ef, tipgeom, rand_elec)

vacuumlevel = rand_elec.vacuumlevel;
kinetic = rand_elec.kin_energy;


distcheck = 100000;


obj.sethit(1) = 0;
obj.sethit(2) = 0;
obj.sethit(3) = 0;
obj.sethit(4) = 0;
if rand_elec.elsetnr == 2
obj.electronleavestip = 1;
```

```
end


r = rand_elec.startpos(1);
z = rand_elec.startpos(2);
theta = 0;
vr = rand_ elec.vr;
vz = rand_ elec.vz;
vtheta = rand_ elec.vtheta;

vx = vr;
vy = vtheta;
x = r;
y = theta;

t = 0;
n = 0;
collision = 0;

while(collision ~= 1)

V = ef.smoothfield(r,z);

Ex = V(2)*cos(theta);
Ey = V(2)*sin(theta);
Ez = V(3);

neg = kinetic+vacuumlevel-V(1);
kenerg = (10^-18)*(vx^2 + vy^2 + vz^2)*obj.mass/(abs(obj.charge)*2);

fa = sqrt(neg^2/kenerg^2);

obj.elp = [obj.elp,r,z];
```

```
vx = fa*vx;
vz = fa*vz;
vy = fa*vy;

ax = obj.tdelta*(obj.charge/obj.mass)*Ex;
az = obj.tdelta*(obj.charge/obj.mass)*Ez;
ay = obj.tdelta*(obj.charge/obj.mass)*Ey;
n = n+1;


vx = vx + obj.tdelta*ax;
vz = vz + obj.tdelta*az;
vy = vy + obj.tdelta*ay;

x = x + obj.tdelta*vx;
z = z + obj.tdelta*vz;
y = y + obj.tdelta*vy;

r = sqrt((x^2) + (y^2));

theta = atan2(x,y);


if mod(n,distcheck) ~= 0
dist = tipgeom.distancefrom(r,z);
if dist(4) >= 2
distcheck = 100000;
obj.tdelta = 10^(-15);
end
if 0.5 < dist(4) < 2
distcheck = 100;
end
if dist(4) < 0.5

distcheck = 10;
```

```
obj.tdelta = 10^(-17);

if dist(1) == 1 && dist(4) <= 0
collision = 1;
obj.sethit(2) = 1;
end
if dist(1) == 2 && dist(4) <= 0
collision = 1;
obj.sethit(1) = 1;
end
if dist(1) == 3 && dist(4) <= 0
if abs(r) < = tipgeom.overallsize
obj.sethit(4) = 1;
else
obj.sethit(3) = 1;
end
collision = 1;
end
if dist(1) == 4 && dist(4) < = 0
obj.sethit(4) = 1;
collision = 1;
end


end


end


t = t+obj.tdelta;

end
```

```
end

function drawpaths(obj, randelec)

A = reshape(obj.elp,2,[]);

if randelec.elsetnr == 1

plot(A(1,:), -A(2,:), 'r')

end

if randelec.elsetnr == 2

plot(A(1,:), -A(2,:), 'b')

end

if randelec.elsetnr == 4

plot(A(1,:), -A(2,:), 'c')

end
drawnow

hold on
end

end
```

```
end
```

A.6 running the code (coaxial tip)

```
clear
fid = fopen('simpletip.txt', 'w');
fprintf(fid, '%s', 'voltage');
fprintf(fid, '\t');
fprintf(fid, '%s', 'current'); fprintf(fid, '\n');


gridsize = 100;
retarding = 20.0;
voltsteps = 1.0;
Nelectrons = 100000;
maxiter = 1000;


energy_ dist = energydist(10,8,11);

tipgeom = tip();
for v = -retarding:voltsteps:retarding


I = 0;


tipgeom.setupcoaxtip(v,0,5,10,30,0.3,0);


ef = electricfield(tipgeom, gridsize, true);
ef.calcpotential(maxiter,1,-1);



for n = 1:Nelectrons

tipside = 0;
```

```
rand_ el = randelec(tipgeom, energy_ dist);

if rand_ el.elsetnr == 2
if rand_ el.elnr == 1
tipside = 1;
end
end


while rand_ el.kin_ energy <= 0 —— tipside == 1
rand_ el = randelec(tipgeom, energy_ dist);
if rand_ el.elsetnr == 2
if rand_ el.elnr == 1
tipside = 1;
else
tipside = 0;
end

end
if rand_ el.elsetnr ~= 2
tipside = 0;
end
end

path = elecpath(ef,tipgeom, rand_ el);
I = I + path.sethit(1) - path.electronleavestip;
clear path
clear rand_ _ el


end

clear ef

M = [v I];
```

```
fid = fopen('coaxtip1.txt', 'a');
dlmwrite('coaxtip1.txt', M, 'delimiter', '\t', '-append')
fclose(fid);


end

fclose(fid);
```

Bibliography

[1] J.R. Hook and H.E. Hall. *Solid state physics*. Wiley, 2nd edition, 1991.

[2] S. Link, M. B. Mohamed, and M. A. El-Sayed. Simulation of the optical absorption spectra of gold nanorods as a function of their aspect ratio and the effect of the medium dielectric constant. *The Journal of Physical Chemistry B*, 103(16):3073–3077, 1999.

[3] C. Burda, X. Chen, R. Narayanan, and M. A. El-Sayed. Chemistry and properties of nanocrystals of different shapes. *Chemical Reviews*, 105(4):1025–1102, 2005.

[4] K. L. Kelly, E. Coronado, L. Zhao, and G. C. Schatz. The optical properties of metal nanoparticles: The influence of size, shape, and dielectric environment. *The Journal of Physical Chemistry B*, 107(3):668–677, 2002.

[5] S. Eustis and M. A. El-Sayed. Why gold nanoparticles are more precious than pretty gold: Noble metal surface plasmon resonance and its enhancement of the radiative and nonradiative properties of nanocrystals of different shapes. *Chemical Society Reviews*, 37(25):209–217, 2006.

[6] J. Jortner. Cluster size effects. *Zeitschrift für Physik D Atoms, Molecules and Clusters*, 24(3):247–275, 1992.

[7] H. Liu, B. S. Mun, G. Thornton, S. R. Isaacs, Y-S. Shon, D. F. Ogletree, and M. Salmeron. Electronic structure of ensembles of gold nanoparticles: Size and proximity effects. *Phys. Rev. B*, 72(15):155430, 2005.

[8] Z. Hao, L. An, J. Zhou, and H. Wang. A supported gold catalyst for the elimination of hydrogen from co2 feed gas in the production of urea. *Reaction Kinetics and Catalysis Letters*, 59(2):295–300, 1996.

[9] M. Turner, V. B. Golovko, O. P. H. Vaughan, P. Abdulkin, A. Berenguer-Murcia, M. S. Tikhov, B. F. G. Johnson, and R. M. Lambert. Selective oxidation with dioxygen by gold nanoparticle catalysts derived from 55-atom clusters. *Nature*, 454(7207):981–983, 2008.

[10] A Z Moshfegh. Nanoparticle catalysts. *Journal of Physics D: Applied Physics*, 42(23):233001, 2009.

[11] G. E. Johnson, R. Mitrić, V. Bonaĉić-Koutecký, and A.W. Castleman Jr. Clusters as model systems for investigating nanoscale oxidation catalysis. *Chemical Physics Letters*, 475(1-3):1 – 9, 2009.

[12] S. N. Rashkeev, A. R. Lupini, S. H. Overbury, S. J. Pennycook, and S. T. Pantelides. Role of the nanoscale in catalytic co oxidation by supported au and pt nanostructures. *Phys. Rev. B*, 76(3):035438, 2007.

[13] R. Wiesendanger. *Scanning Probe Microscopy and Spectroscopy: Methods and Applications*. Cambridge University Press, 1994.

[14] T.G. Wright A. M. Ellis, M. Fehér. *Electronic and photoelectron spectroscopy : fundamentals and case studies.* Cambridge University Press., 2005.

[15] D. Briggs. *Handbook of X-ray and ultraviolet photoelectron spectroscopy.* Hayden and Sons Ltd, 1977.

[16] S. Hüfner, S. Schmidt, and F. Reinert. Photoelectron spectroscopy–an overview. *Nuclear Instruments and Methods in Physics Research Section A: Accelerators, Spectrometers, Detectors and Associated Equipmen*, 547(1):8 – 23, 2005.

[17] S. Hüfner. *Photoelectron spectroscopy : principles and applications.* Springer, 3rd rev. and enlarged ed edition, 2003.

[18] J.W. Rabalais. *Principles of ultraviolet photoelectron spectroscopy.* Wiley, 1977.

[19] M.G. Lagally and R.L. Park. *Solid state physics : surfaces. Methods of experimental physics.* Academic Press., 1985.

[20] R J Hamers. Atomic-resolution surface spectroscopy with the scanning tunneling microscope. *Annual Review of Physical Chemistry*, 40:531–539, 1989.

[21] J. Lehmann, M. Merschdorf, W. Pfeiffer, A. Thon, S. Voll, and G. Gerber. Surface plasmon dynamics in silver nanoparticles studied by femtosecond time-resolved photoemission. *Phys. Rev. Lett.*, 85(14):2921–2924, 2000.

[22] J. Lehmann, M. Merschdorf, W. Pfeiffer, A. Thon, S. Voll, and G. Gerber. Silver nanoparticles on graphite studied by femtosecond time-resolved multiphoton photoemission. *The Journal of Chemical Physics*, 112(12):5428–5434, 2000.

[23] I Yamamoto, N Matsuura, M Mikamori, R Yamamoto, T Yamada, K Miyakubo, N Ueno, and T Munakata. Imaging of electronic structure of lead phthalocyanine films studied by combined use of PEEM and Micro-UPS. *Surf Sci*, 602(13):2232–2237, 2008.

[24] M Munzinger, C Wiemann, M Rohmer, L Guo, M Aeschlimann, and M Bauer. The lateral photoemission distribution from a defined cluster/substrate system as probed by photoemission electron microscopy. *New Journal of Physics*, 7(68):1–17, 2005.

[25] M. Cinchetti, A. Oelsner, G. H. Fecher, H. J. Elmers, and G. Schonhense. Observation of cu surface inhomogeneities by multiphoton photoemission spectromicroscopy. *Applied Physics Letters*, 83(8):1503–1505, 2003.

[26] R. J. Hamers and D. G. Cahill. Ultrafast time resolution in scanned probe microscopies: Surface photovoltage on Si(111)–(7 × 7). *J. Vac. Sci. Technol. B*, 9(2):514–518, 1991.

[27] N. N. Khusnatdinov, T. J. Nagle, and Jr. G. Nunes. Ultrafast scanning tunneling microscopy with 1 nm resolution. *Applied Physics Letters*, 77(26):4434–4436, 2000.

[28] G. M. Steeves, A. Y. Elezzabi, and M. R. Freeman. Nanometer-scale imaging with an ultrafast scanning tunneling microscope. *Applied Physics Letters*, 72(4):504–506, 1998.

[29] V. Gerstner, A. Knoll, W. Pfeiffer, A. Thon, and G. Gerber. Femtosecond laser assisted scanning tunneling microscopy. *J. Appl. Phys.*, 88(8):4851–4859, 2000.

[30] S. Grafström. Photoassisted scanning tunneling microscopy. *J. Appl. Phys.*, 91(4):1717–1753, 2002.

[31] V. Gerstner, A. Thon, and W. Pfeiffer. Thermal effects in pulsed laser assisted scanning tunneling microscopy. *J. Appl. Phys.*, 87(5):2574–2580, 2000.

[32] Y. Hasegawa, K. Tsuji, K. Nakayama, K. Wagatsuma, and T. Sakurai. X-ray source combined ultrahigh-vacuum scanning tunneling microscopy for elemental analysis. *J. Vac. Sci. Technol. B*, 18(6):2676–2680, 2000.

[33] A. Saito, J. Maruyama, K. Manabe, K. Kitamoto, K. Takahashi, K. Takami, M. Yabashi, Y. Tanaka, D. Miwa, M. Ishii, Y. Takagi, M. Akai-Kasaya, S. Shin, T. Ishikawa, Y. Kuwahara, and M. Aono. Development of a scanning tunneling microscope for *in situ* experiments with a synchrotron radiation hard-X-ray microbeam. *Journal of Synchrotron Radiation*, 13(2):216–220, 2006.

[34] T. Matsushima, T. Okuda, T. Eguchi, M. Ono, A. Harasawa, T. Wakita, A. Kataoka, M. Hamada, A. Kamoshida, Y. Hasegawa, and T. Kinoshita. Development and trial measurement of synchrotron-radiation-light-illuminated scanning tunneling microscope. *Rev. Sci. Instrum.*, 75(6):2149–2153, 2004.

[35] K. Tsuji and K. Hirokawa. Characteristics of an x-ray excited current detected with a scanning tunneling microscope tip. *Rev. Sci. Instrum.*, 67(10):3573–3577, 1996.

[36] C-Y. Chiu, Y-L. Chan, Y. J. Hsu, and D. H. Wei. Collecting photoelectrons with a scanning tunneling microscope nanotip. *Applied Physics Letters*, 92(10):103101, 2008.

[37] T. Okuda, T. Eguchi, K. Akiyama, A. Harasawa, T. Kinoshita, Y. Hasegawa, M. Kawamori, Y. Haruyama, and S. Matsui. Nanoscale chemical imaging

by scanning tunneling microscopy assisted by synchrotron radiation. *Phys. Rev. Lett.*, 102(105503), 2009.

[38] I Schmid, J Raabe, C Quitmann, S Vranjkovic, H J Hug, and R H Fink. NanoXAS, a novel concept for high resolution microscopy. *Journal of Physics: Conference Series*, 186(1):012015, 2009.

[39] G. Binnig, H. Rohrer, Ch. Gerber, and E. Weibel. Surface studies by scanning tunneling microscopy. *Phys. Rev. Lett.*, 49(1):57–61, 1982.

[40] R. Young, J. Ward, and F. Scire. Observation of metal-vacuum-metal tunneling, field emission, and the transition region. *Phys. Rev. Lett.*, 27(14):922–924, 1971.

[41] M. Schmid. Tu wien. http://upload.wikimedia.org/wikipedia/commons/f/f9/.

[42] I. H. Musselman and P. E. Russell. Platinum/iridium tips with controlled geometry for scanning tunneling microscopy. *Journal of Vacuum Science and Technology A: Vacuum, Surfaces, and Films Technology A: Vacuum, Surfaces, and Films*, 8(4):3558–3562, 1990.

[43] P. A. Tipler. *Physics for Scientists and Engineers*. W. H. Freeman, 2003.

[44] J. Hoffman. http://hoffman.physics.harvard.edu/research/, 2010.

[45] J. Bardeen. Tunnelling from a many-particle point of view. *Phys. Rev. Lett.*, 6(2):57–59, 1961.

[46] J. Tersoff and D. R. Hamann. Theory of the scanning tunneling microscope. *Phys. Rev. B*, 31(2):805–813, 1985.

[47] S. Park and C. F. Quate. Theories of the feedback and vibration isolation systems for the scanning tunneling microscope. *Rev. Sci. Instrum.*, 58(11):2004–2009, 1987.

[48] Chunli Bai. *Scanning tunneling microscopy and its applications*. Springer, 2000.

[49] M. Fotino. Tip sharpening by normal and reverse electrochemical etching. *Rev. Sci. Instrum.*, 64(1):159–167, 1993.

[50] I. Ekvall, E. Wahlström, D. Claesson, H. Olin, and E Olsson. Preparation and characterization of electrochemically etched W tips for STM. *Measurement Science and Technology*, 10(1):11–18, 1999.

[51] G. Binnig and D. P. E. Smith. Single-tube three-dimensional scanner for scanning tunneling microscopy. *Rev. Sci. Instrum.*, 57(8):1688–1689, 1986.

[52] Y. Kuk and P. J. Silverman. Scanning tunneling microscope instrumentation. *Rev. Sci. Instrum.*, 60(2):165–180, 1989.

[53] K. Wegner, P. Piseri, H. Vahedi Tafreshi, and P. Milani. Cluster beam deposition: a tool for nanoscale science and technology. *Journal of Physics D - Applied Physics*, 39(22):R439–R459, 2006.

[54] S. Pratontep, S. J. Carroll, C. Xirouchaki, M. Streun, and R. E. Palmer. Size-selected cluster beam source based on radio frequency magnetron plasma sputtering and gas condensation. *Rev. Sci. Instrum.*, 76(4):045103, 2005.

[55] S. K. Friedlander. *Smoke, Dust, and Haze*. Oxford University Press, second edition edition, 2000.

[56] M. R. Zachariah and M. J. Carrier. Molecular dynamics computation of gas-phase nanoparticle sintering: A comparison with phenomenological models. *Journal of Aerosol Science*, 30(9):1139–1151, 1999.

[57] S Arcidiacono, NR Bieri, D Poulikakos, and CP Grigoropoulos. On the coalescence of gold nanoparticles. *International Journal of Multiphase Flow*, 30(7-8):979–994, 2004.

[58] F. Y. Huang and M. J. Kushner. Shapes of agglomerates in plasma etching reactors. *J. Appl. Phys.*, 81(9):5960–5965, 1997.

[59] T Hawa and MR Zachariah. Coalescence kinetics of unequal sized nanoparticles. *Journal of Aerosol Science*, 37(1):1–15, 2006.

[60] M. M. Lunden. *Sintering of aerosol agglomerates*. PhD thesis, Caltech, 1995.

[61] S. K. Friedlander and M. K. Wu. Linear rate law for the decay of the excess surface area of a coalescing solid particle. *Phys. Rev. B*, 49(5):3622–3624, 1994.

[62] G. Binnig, H. Rohrer, Ch. Gerber, and E. Weibel. 7×7 reconstruction on Si(111) resolved in real space. *Phys. Rev. Lett.*, 50(2):120–123, 1983.

[63] R. E. Palmer, P. A. Sloan, and C. Xirouchaki. Decoration of surfaces with size-selected clusters and molecular manipulation at room temperature: precision and uncertainty in organizing atoms. *Phil. Trans. R. Soc. Lond. A*, (362):1195–1205, 2004.

[64] D. M. Eigler and E. K. Schweizer. Positioning single atoms with a scanning tunnelling microscope. *Nature*, 344(6266):524–526, 1990.

[65] D. M. Eigler, C. P. Lutz, and W. E. Rudge. An atomic switch realized with the scanning tunnelling microscope. *Nature*, 352(6336):600–603, 1991.

[66] T. W. Fishlock, A. Oral, R. G. Egdell, and J. B. Pethica. Manipulation of atoms across a surface at room temperature. *Nature*, 404(6779):743–745, 2000.

[67] P. A. Sloan and R. E. Palmer. Two-electron dissociation of single molecules by atomic manipulation at room temperature. *Nature*, 434(7031):367–371, 2005.

[68] D. F. Padowitz and R. J. Hamers. Voltage-dependent STM images of covalently bound molecules on Si(100). *The Journal of Physical Chemistry B*, 102(43):8541–8545, 1998.

[69] K. D. Brommer, M. Galván, A. Dal Pino Jr., and J.D. Joannopoulos. Theory of adsorption of atoms and molecules on Si(111) $-$ (7 $\times$ 7). *Surface Science*, 314(1):57 – 70, 1994.

[70] P. A. Sloan, M. F. G. Hedouin, R. E. Palmer, and M. Persson. Mechanisms of molecular manipulation with the scanning tunneling microscope at room temperature: Chlorobenzene/Si(111)-(7 $\times$ 7). *Phys. Rev. Lett.*, 91(11):118301, 2003.

[71] C. L. Teague and J. J. Boland. STM study of multiple bonding configurations and mechanism of 1,3-cyclohexadiene attachment on Si(100) - 2x1. *The Journal of Physical Chemistry B*, 107(16):3820–3823, 2003.

[72] http://www.chem.qmul.ac.uk/surfaces/scc/scat1_6a.htm.

[73] Dimitri Petrovych. http://nanowiz.tripod.com/sisteps/si7×7model.gif.

[74] T.H. Andersen, I.-H. Svenum, A. Gabrielsen, and A. Borg. Investigation of 1,1-dichloroethene interacting with the Si(1,1,1)-7 x 7 surface studied by scanning tunneling microscopy. *Surface Science*, 603(1):84 – 90, 2009.

[75] Y. Cao, X. M. Wei, W. S. Chin, Y. H. Lai, J. F. Deng, S. L. Bernasek, and G. Q. Xu. Formation of di-σ bond in benzene chemisorption on Si(111)-7×7. *The Journal of Physical Chemistry B*, 103(27):5698–5702, 1999.

[76] S. Frokjaer and D. E. Otzen. Protein drug stability: a formulation challenge. *Nat Rev Drug Discov*, 4(4):298–306, 2005.

[77] R. M. Cooke, B. G. Carter, P. Murray-Rust, M. J. Hartshorn, P. Herzyk, and R. E. Hubbard. The solution structure of echistatin: evidence for disulphide bond rearrangement in homologous snake toxins. *Protein Eng.*, 5(6):473–477, 1992.

[78] R. B. Freedman. Native disulphide bond formation in protein biosynthesis: evidence for the role of protein disulphide isomerase. *Trends in Biochemical Sciences*, 9(10):438 – 441, 1984.

[79] R. A. Zubarev, N. L. Kelleher, and F. W. McLafferty. Electron capture dissociation of multiply charged protein cations. A nonergodic process. *Journal of the American Chemical Society*, 120(13):3265–3266, 1998.

[80] R. A. Zubarev, N. A. Kruger, E. K. Fridriksson, M. A. Lewis, D. M. Horn, B. K. Carpenter, and F. W. McLafferty. Electron capture dissociation of gaseous multiply-charged proteins is favored at disulfide bonds and other sites of high hydrogen atom affinity. *Journal of the American Chemical Society*, 121(12):2857–2862, 1999.

[81] P. Maksymovych, D. C. Sorescu, and J. T. Yates. Gold-adatom-mediated bonding in self-assembled short-chain alkanethiolate species on the Au(111) surface. *Phys. Rev. Lett.*, 97(14):146103, 2006.

[82] W.C. Bigelow. *Vacuum methods in electron microscopy.* Practical methods in electron microscopy. Portland, 1994.

[83] A.H. Turnbull. *An introduction to vacuum technique.* Newnes, 1962.

[84] G.F. Weston. *Ultrahigh vacuum practice.* Butterworths, 1985.

[85] http://www.lesker.com/newweb/gauges/.

[86] A. Berman. *Total pressure measurements in vacuum technology.* Academic Press. Press., Orlando, 1985.

[87] I. M. Goldby, B. von Issendorff, L. Kuipers, and R. E. Palmer. Gas condensation source for production and deposition of size-selected metal clusters. *Rev. Sci. Instrum.*, 68(9):3327–3334, 1997.

[88] B. von Issendorff and R. E. Palmer. A new high transmission infinite range mass selector for cluster and nanoparticle beams. *Rev. Sci. Instrum.*, 70(12):4497–4501, 1999.

[89] D. Cattaneo, S. Foglio, C.S. Casari, A. Li Bassi, M. Passoni, and C.E. Bottani. Different W cluster deposition regimes in pulsed laser ablation observed by in situ scanning tunneling microscopy. *Surface Science*, 601(8):1892 – 1897, 2007.

[90] S. J. Carroll, R. E. Palmer, P. A. Mulheran, S. Hobday, and R. Smith. Deposition and diffusion of size-selected (Ag400+) clusters on a stepped graphite surface. *Applied Physics A: Materials Science & Processing*, 67(6):613–619, 1998.

[91] F Claeyssens, S Pratontep, C Xirouchaki, and R E Palmer. Immobilization of large size-selected silver clusters on graphite. *Nanotechnology*, 17(3):805–808, 2006.

[92] Z. Q. Yu, C. M. Wang, Y. Du, S. Thevuthasan, and I. Lyubinetsky. Reproducible tip fabrication and cleaning for uhv stm. *Ultramicroscopy*, 108(9):873 – 877, 2008.

[93] A S Lucier, H Mortensen, Y Sun, and P Grutter. Determination of the atomic structure of scanning probe microscopy tungsten tips by field ion microscopy. *Phys. Rev. B*, 72(235420), 2005.

[94] L. Douillard, F. Charra, Z. Korczak, R. Bachelot, S. Kostcheev, G. Lerondel, P-M. Adam, and P Royer. Short range plasmon resonators probed by photoemission electron microscopy. *Nano Letters*, 8(3):935–940, 2008.

[95] P. Zijlstra, J. W. M. Chon, and M. Gu. Five-dimensional optical recording mediated by surface plasmons in gold nanorods. *Nature*, 459(7245):410–413, 2009.

[96] M. Haruta. Size- and support-dependency in the catalysis of gold. *Catalysis Today*, 36(1):153 – 166, 1997. Copper, Silver and Gold in Catalysis.

[97] V. Bonaĉić-Koutecký, J. Burda, R. Mitric, M. Ge, G. Zampella, and P. Fantucci. Density functional study of structural and electronic properties of bimetallic silver–gold clusters: Comparison with pure gold and silver clusters. *The Journal of Chemical Physics*, 117(7):3120–3131, 2002.

[98] S. Vajda, M. J. Pellin, J. P. Greeley, C. L. Marshall, L. A. Curtiss, G. A. Ballentine, J. W. Elam, S. Catillon-Mucherie, P. C. Redfern, F. Mehmood, and P. Zapol. Subnanometre platinum clusters as highly active and selective catalysts for the oxidative dehydrogenation of propane. *Nat Mater*, 8(3):213–216, 2009.

[99] H-J Freund. Clusters and islands on oxides: from catalysis via electronics and magnetism to optics. *Surface Science*, 500(1-3):271 – 299, 2002.

[100] M. Lyubovsky and L. Pfefferle. Methane combustion over the α-alumina supported Pd catalyst: Activity of the mixed Pd/PdO state. *Applied Catalysis A: General*, 173(1):107 – 119, 1998.

[101] M. Lyubovsky and L. Pfefferle. Complete methane oxidation over Pd catalyst supported on α-alumina. influence of temperature and oxygen pressure on the catalyst activity. *Catalysis Today*, 47(1-4):29 – 44, 1999.

[102] T. Ressler, M. Hagelstein, U. Hatje, and W. Metz. In situ x-ray absorption spectroscopy studies on chemical oscillations in the CO/O_2 system on

supported Pd catalysts. *The Journal of Physical Chemistry B*, 101(34):6680–6687, 1997.

[103] K. Okamoto, R. Akiyama, H. Yoshida, T. Yoshida, and S. Kobayashi. Formation of nanoarchitectures including subnanometer palladium clusters and their use as highly active catalysts. *Journal of the American Chemical Society*, 127(7):2125–2135, 2005.

[104] C Vinod, G Kulkarni, and C Rao. Size-dependent changes in the electronic structure of metal clusters as investigated by scanning .... *Chemical Physics Letters*, 289:319–323, 1998.

[105] B. Palpant, B. Prével, J. Lermé, E. Cottancin, M. Pellarin, M. Treilleux, A. Perez, J. L. Vialle, and M. Broyer. Optical properties of gold clusters in the size range 2–4 nm. *Phys. Rev. B*, 57(3):1963–1970, 1998.

[106] H Hövel and I Barke. Large noble metal clusters: electron confinement and band structure effects. *New J Phys*, 31(5):1–14, 2003.

[107] P. Alivisatos. The use of nanocrystals in biological detection. *Nat Biotech*, 22(1):47–52, 2004.

[108] R. H. Magruder III, L. Yang, R. F. Haglund Jr., C. W. White, L. Yang, R. Dorsinville, and R. R. Alfano. Optical properties of gold nanocluster composites formed by deep ion implantation in silica. *Applied Physics Letters*, 62(15):1730–1732, 1993.

[109] J. P. Wilcoxon, J. E. Martin, and P. Provencio. Optical properties of gold and silver nanoclusters investigated by liquid chromatography. *The Journal of Chemical Physics*, 115(2):998–1008, 2001.

[110] R. D. Averitt, S. L. Westcott, and N. J. Halas. Linear optical properties of gold nanoshells. *J. Opt. Soc. Am. B*, 16(10):1824–1832, 1999.

[111] D. E. Aspnes, E. Kinsbron, and D. D. Bacon. Optical properties of au: Sample effects. *Phys. Rev. B*, 21(8):3290–3299, 1980.

[112] D. Pearmain. Private communication. Colleague at UoB, 2010.

[113] N. P. Young, Z. Y. Li, Y. Chen, S. Palomba, M. Di Vece, and R. E. Palmer. Weighing supported nanoparticles: Size-selected clusters as mass standards in nanometrology. *Phys. Rev. Lett.*, 101(24):246103, 2008.

[114] L. Miao, V. R. Bhethanabotla, and B. Joseph. Melting of Pd clusters and nanowires: A comparison study using molecular dynamics simulation. *Phys. Rev. B*, 72(13):134109, 2005.

[115] H Yasumatsu, T Hayakawa, and T Kondow. Electronic structures of size-selected single-layered platinum clusters on silicon(111)-7x7 surface at a single cluster level by tunneling spectroscopy. *J Chem Phys*, 124(1):014701, 2006.

[116] M. Hupalo, C. Z. Wang, B. J. Min, K. M. Ho, and M. C. Tringides. Electronic structure of stepped $Si(111) - (7 \times 7)$: theory and experiment. *Phys. Rev. B*, 67(11):115333, 2003.

[117] G-X. Qian and D. J. Chadi. Si(111)-7×7 surface: Energy-minimization calculation for the dimer–adatom–stacking-fault model. *Phys. Rev. B*, 35(3):1288–1293, 1987.

[118] K. Takayanagi, Y. Tanishiro, S. Takahashi, and M. Takahashi. Structure analysis of Si(111)-7×7 reconstructed surface by transmission electron diffraction. *Surface Science*, 164:367–392, 1985.

[119] I. Chizhov, G. Lee, and R. F. Willis. STM study of room temperature adsorption of Au on the $Si(111)(7 \times 7)$ surface: evidence for the reaction of Au atoms with Si rest atoms. *Applied Physics A: Materials Science and Processing*, 66(0):1003–1006, 1998.

[120] T. Zhang, E. Bertelsen, and T. Alber. Entropic effects of disulphide bonds on protein stability. *Nat Struct Mol Biol*, 1(7):434–438, 1994.

[121] G. Bulaj. Formation of disulfide bonds in proteins and peptides. *Biotechnology Advances*, 23(1):87 – 92, 2005.

[122] C. J. Camacho and D. Thirumalai. Modeling the role of disulfide bonds in protein folding: Entropic barriers and pathways. *Proteins: Structure, Function, and Genetics*, 22(1):27–40, 1995.

[123] L. Masip, J. L. Pan, S. Haldar, J. E. Penner-Hahn, M. P. DeLisa, G. Georgiou, J. C. A. Bardwell, and J-F. Collet. An Engineered Pathway for the Formation of Protein Disulfide Bonds. *Science*, 303(5661):1185–1189, 2004.

[124] Jmol: an open-source java viewer for chemical structures in 3d. http://www.jmol.org/.

[125] S. Dobrin, K. R. Harikumar, and J. C. Polanyi. An STM study of the localized atomic reaction of 1,2– and 1,4–dibromobenzene at Si(111)-7×7. *Surface Science*, 561(1):11 – 24, 2004.

[126] Y. Cao, J. F. Deng, and G. Q. Xu. Stereo-selective binding of chlorobenzene on si(111)-7 x 7. *The Journal of Chemical Physics*, 112(10):4759–4767, 2000.

[127] Y. Cai and B. M. Ocko. Electro pen nanolithography. *Journal of the American Chemical Society*, 127(46):16287–16291, 2005.

[128] K-B. Lee, J-H. Lim, and C. A. Mirkin. Protein nanostructures formed via direct-write dip-pen nanolithography. *Journal of the American Chemical Society*, 125(19):5588–5589, 2003.

[129] Y. Li, B. W. Maynor, and J. Liu. Electrochemical AFM "dip-pen" nanolithography. *Journal of the American Chemical Society*, 123(9):2105–2106, 2001.

[130] C. A. Mirkin D. S. Ginger, H. Zhang. The evolution of dip-pen nanolithography. *Angewandte Chemie International Edition*, 43(1):30–45, 2004.

[131] J. C. Green. Photoelectron spectroscopy: Study of valence bands in solids. *Annual Review of Physical Chemistry*, 28(1):161–183, 1977.

[132] C. N. Berglund and W. E. Spicer. Photoemission studies of copper and silver: Theory. *Phys. Rev.*, 136(4A):A1030–A1044, 1964.

[133] M. Y. Song, A. P. G. Robinson, and R. E. Palmer. Fabrication of co-axial field emitter tips for scanning probe energy loss spectroscopy. *Nanotechnology*, 21(15), 2010.

[134] M. Y. Song, J. J. Lawton, A. P. G. Robinson, and R. E. Palmer. Scanning probe energy loss spectroscopy with microfabricated coaxial tips. *Phys. Rev. B*, 81(16):161411, 2010.

[135] M. Y. Song. Private communication. Colleague at UoB, 2009.

[136] K. B. Crozier, A. Sundaramurthy, G. S. Kino, and C. F. Quate. Optical antennas: Resonators for local field enhancement. *J. Appl. Phys.*, 94(7):4632–4642, 2003.

[137] L. Novotny, R. X. Bian, and X. S. Xie. Theory of nanometric optical tweezers. *Phys. Rev. Lett.*, 79(4):645–648, 1997.

[138] SPECS GmbH, Germany. *Manual UVS 300 UV Lamp/ UVS 300-A Power Supply.*

[139] D. A. Papaconstantopoulos. *Handbook of the band structure of elemental solids.* Plenum Press, 1986.

[140] N. Egede Christensen and B. Feuerbacher. Volume and surface photoemission from tungsten. i. calculation of band structure and emission spectra. *Phys. Rev. B*, 10(6):2349–2372, 1974.

[141] D W Bullett. Bulk and surface electron states in WO_3 and tungsten bronzes. *Journal of Physics C: Solid State Physics*, 16(11):2197–2207, 1983.

[142] R. Opila and R. Gomer. Adsorption of oxygen on the tungsten (110) plane at low temperatures; spectroscopic measurements. *Surface Science*, 105(1):41 – 47, 1981.

[143] W. Lisowski, A. H. J. Berg, G. A. M. Kip, and L. J. Hanekamp. Characterization of tungsten tips for STM by SEM/AES/XPS. *Fresenius' Journal of Analytical Chemistry*, 341(3):196–199, 1991.

[144] W. F. Lisowski, A. H. J. van den Berg, L. J. Hanekamp, and A. van Silfhout. Distribution and thickness of the surface contaminations on STM tungsten tips, studied by AES/SEM and ARXPS. *Microchimica Acta*, 107(3):189–196, 1992.

[145] Z. Wang and M. Moskovits. Scanning tunneling microscope-promoted growth of nanometer-scale, uniform gold stripes on reconstructed Au(111) surfaces. *J. Appl. Phys.*, 71(11):5401–5409, 1992.

[146] F. Yin. Private communication. Colleague at UoB, 2010.

[147] M. N. O. Sadiku. *Numerical Techniques in Electromagnetics*. CRC Press, 1992.

[148] G. Lindfield and J. Penny. *Numerical Methods Using Matlab*. Prentice Hall, 2nd edition, 1999.

[149] Milton A. Chaffee. The angular distribution of photoelectrons ejected by polarized ultraviolet light in potassium vapor. *Phys. Rev.*, 37(10):1233–1237, 1931.

[150] S. Kim, K. L. Shuford, H-M. Bok, S. K. Kim, and S. Park. Intraparticle surface plasmon coupling in quasi-one-dimensional nanostructures. *Nano Letters*, 8(3):800–804, 2008.